HYBRID SYSTEMS FOR WATER OXIDATION CATALYSIS

Marta Ventosa Rosquelles

UNIVERSITAT ROVIRA i VIRGILI

Hybrid Systems for Water Oxidation Catalysis

Marta Ventosa Rosquelles

DOCTORAL THESIS
2021

Marta Ventosa Rosquelles

Hybrid Systems for Water Oxidation Catalysis

DOCTORAL THESIS

Supervised by

Prof. Antoni Llobet and Dr. Carolina Gimbert-Suriñach

Institute of Chemical Research of Catalonia

Tarragona

2021

ICIQ - Institut Català d'Investigació Química

Avinguda Països Catalans 16,

43007 Tarragona (Spain)

Prof. Antoni Llobet, Group Leader at the Institute of Chemical Research of Catalonia, and Dr. Carolina Gimbert,

We STATE that the present study, entitled "*Hybrid Systems for Water Oxidation Catalysis*" presented by Marta Ventosa Rosquelles for the award of the degree of Doctor, has been carried out under our supervision at the group of Antoni Llobet in the Institute of Chemical Research of Catalonia.

Tarragona, February 1st, 2021

Doctoral Thesis Supervisors

Prof. Antoni Llobet Dr. Carolina Gimbert-Suriñach

Acknowledgments & agraïments

Personally, the following section has been the most challenging among all, without wanting to underestimate the rest. There are no words that can describe the felt gratitude towards every single person and emotion that has helped me in achieving this climb.

First of all, I would like to thank the supervisors of my thesis, Antoni Llobet and Carolina Gimbert-Suriñach. I could not have asked for better belayers, that is, in climbing terms, the person on the ground that secures the climber. Every time I would fall, they would tense the rope by giving me advice and directing me on all possible ways to reach the summit. From them, I learned both science and humbleness, which I will bring as a toolkit in my professional and personal life. Thank you very much Toni for allowing me to join your group and for your supervision of great value. Carolina, thank you for being an example to follow, as a person and as a woman in science. Your caring, calmness, never-ending curiosity, together with your vast memory, critical thinking, and scientific knowledge are truly inspiring. Moreover, I would like to acknowledge Mª José, whose patience, efficiency, and listening skills have been essential to soften the hard climb.

I have had the great opportunity to share this journey with several collaborators and mentors, who kindly taught me and helped to shape this work. Special thanks to Prof. Caramori, Dr. Berardi, and Martina Salati (University of Ferrara) for our fruitful collaboration and your insights, resulting in a challenging noble-metal-free photoanode. Besides, thanks to Prof. Puntes, Dr. Bastús, and Jana Oliveras (ICN2) for teaming up with us to achieve an elaborated molecular colloidal photocatalyst, which happily turned out to be the first publication of this thesis. Finally, I would like to thank Dr. de la Peña-O'Shea's group at IMDEA Energía and Prof. Eder's group at TU Wien for all the lessons learned and the warm welcoming received in my short stays there.

I cannot imagine completing this journey without my roped comrades, in labcoat! From absolutely each and one of you I learned how to be more humble and compassionate, dealing with different cultures and ways of thinking. Moreover, all that spiced up with lots of fun and laughter! Thank you both Dr. Marcos and Dr. Sergi for your scientific and personal support, and for creating the cheerfulness union of the lab. Thank you Dr. Holub for being a harsh climber and scientist, you have been necessary and motivating in several ways. Jan O. and Isabel, I always say that when I grow up I want to be like you. Do not get angry for

considering you too old for gin tonics, what I mean is that you are an example to follow (individually and as a couple), and for sure you will be the best parents for little Felix. And how to forget the eSCALED crew? Ludo, Robin, and both Andrews, you were the true laughter of my journey and all of you have enlightening life stories. I am sad that the speed of your research stays brought you away from Tarragona, but I hope that you bring with you the same positive energies everywhere you go. Thank you Asmaul, Roc, and Pablo for being an example inside and outside the lab. And the same gratitude to the rest of the team: Primavera, Abi, Tingting (the CTF partner in crime), Navid, Andrey, Alice, Yuanyuan, Laura (the BODIPY master), and Vasilis-Marco (the pair that will keep the group alive). I want to highlight the bright students that I have had the luck to (co)supervise. Truly, they gave me a reason to keep passionate and motivated. My very best wishes to Martina Salati, Jana Oliveras, Florian Dorchies, and Irene Ligiélli. Last but not least, all my gratitude to Dr. Nataliia. Your professionalism, inner strength, but especially your humanity, have been a source of inspiration in life. Together we learned, helped each other, and enjoyed uncountable life moments. “Tia” you will have a friend in Tarragona whenever you want to come back.

The rock is easier when you have already the bolts settled. These bolts are the different people that constitute ICIQ’s support areas, such as NMR, XRD, Mass, Chemical Reaction unit, High-throughput unit, Photophysical unit, the glassblower/mechanical workshop, reception and the administration. Without their patience and help, this thesis would not be half of what it is. I would like to acknowledge Frederic Ratel for allowing me to participate in the different courses bridging science and business. The last of the bolts, called the anchor, is formed by the Green ICIQ team. All my special gratitude to the founders and major contributors, Berta, Ariadna, and Xavi. Your positivity and pushing energies have been a source of motivation and honesty that I will bring to my next stage. Thank you for your time and your willingness to improve the sustainability and health of ICIQ and its workers, but most of all, the Earth. Please do not lose any glimpse of energy or smile.

To extend even more this Mediterranean soap opera, let me mention ICIQ’s climbers (especially Cristina), a team of good people addicted to adrenaline and passion for life. The after-work climbs or our weekends in nature have been the best reboot after hard days inthe lab. I cannot miss mentioning my Chemistry family, formed by all my University friends, who were the ones expanding my mind, heart and laughter, and for whom I wish health,

love and lots of spicy life. And to my dear fellows and mentors of “la Caixa” fellowship. At the beginning I was reluctant to meet those brains, but they truly exceeded my expectations: highly skilled people driven by the motivation to make a change. I cannot name all of them (maybe I should allow the kindest and strongest delegate, Elena, to do it) and all their paths, but I can ensure that meeting you has been one of the most precious things of this Ph.D. I hope one day I can see all of you taking more or less important roles, but utterly happy in your life paths.

But… wait! What are the most essential tools for a climb? The harness and the quickdraws, which represent the people with whom, I am lucky to say, I love. Per a tots els meus amics de Tarragona. Compartim la vida des dels tres anys i mai ens diem lo molt que ens estimem. Potser, en part, perquè som una pinya que actuem enlloc d’ensucrar-nos amb paraules. Sóc molt afortunada de compartir inexhaurable humor i somriures, espatlles per a plorar, orelles per a escoltar i cames per a ballar i perdre’s. Gràcies Sílvia per aguantame el dia a dia amb el teu positivisme i bones energies per encarar la vida. Són les teves millors qualitats i ho comparteixes amb tothom que et rodeja. Gràcies per haver-me donat un gran bocí de la teva bondat i espero que no parem de fer “silviades & martades” per molts anys més. Espero que construeixis un bonic i feliç camí juntament amb el Pere, la gran persona i artista de la portada d’aquesta tesi. Albert, gràcies a tu també per saber escoltar, profunditzar i alegrar a qualsevol, amb aquelles cerveses post-estudi tan necessàries. Espero continuar creixent juntament amb tots vosaltres, en aquesta aventura que vam heretar dels millors pares. De fet, agraeixo a la meva mare Carme i al meu pare Alfred, unes de les persones més bondadoses que conec. Ja ho demostra el fet que us coneguessiu de voluntariat, i gràcies al vostre coratge i amor, el Pau, l’Aina i jo us devem la vida. Gràcies per ser sempre el pal de paller i espero, algun dia, estar a la vostra alçada i transmetre el que ens vau ensenyar. Però tampoc heu estat tant bons… i per això he tingut la sort de tenir dos germans! Pau, sempre has sigut el meu exemple, veient com evolucionaves fins a convertir-te en qui ets ara, una persona impressionant. També tu Aina, per haver fet de germana gran, per tota la teva tranquilitat, compassió i bondat, estàs feta per ser la millor mare de la nova incorporació a l’equip, juntament amb el Ion. Tu petita Àlix, sense saber-ho, has sigut la millor mestra de tots. M’omple d’amor i sentit vital veure els teus ulls curiosos descobrint el món des de la més bondadosa ment lliure de lligams i prejudicis.

To Ιωάννα, who has been my lifeline. It looks like I am good at filling pages with corny gratitude messages for all, but for you, no words can describe the love I feel. Thank you for taking the courageous step to embark with me on all our adventures in the inner and outer world. Your true kindness, sparking caring eyes and deeply curious mind have the best ripple effect on anyone around. Utterly, you have been the best present that this Ph.D. has given to me. Our memories will fill me with love and light, and I hope we continue experiencing many more in this wild, wild world.

The work performed in the present doctoral thesis has been possible thanks to the Institute of Chemical Research of Catalonia (ICIQ), Universitat Rovira i Virgili (URV) and the funding of MINECO/MICINN, FEDER (CTQ2016-80058-R,CTQ2015-73028-EXP, SEV 2013-0319), AGAUR (2014 SGR-915, 2017- SGR-1631). Special thanks to the support of the fellowship from "la Caixa" Foundation (ID 100010434). The fellowship code is LCF/BQ/DI17/11620036. This project has received funding from the European Union´s Horizon 2020 research and innovation programme under the Marie Skłodowska-Curie grant agreement No. 713673.

Finally, to mother Earth, Pachamama, Gaia, God, or who/whatever is out there telling the best of the jokes. Thank you for allowing me to laugh about it, and I hope to return it in the most kind and humble way.

List of publications

1. Ventosa, M.; Oliveras, J.; Bastús, N. G.; Gimbert-Suriñach, C.; Puntes, V.; Llobet, A. Nanocrystal-Molecular Hybrids for the Photocatalytic Oxidation of Water. *ACS Appl. Energy Mater.* **2020**, *3* (10), 10008–10014. https://doi.org/10.1021/acsaem.0c01685.

Table of Contents

Abstract

Chapter 1. General Introduction

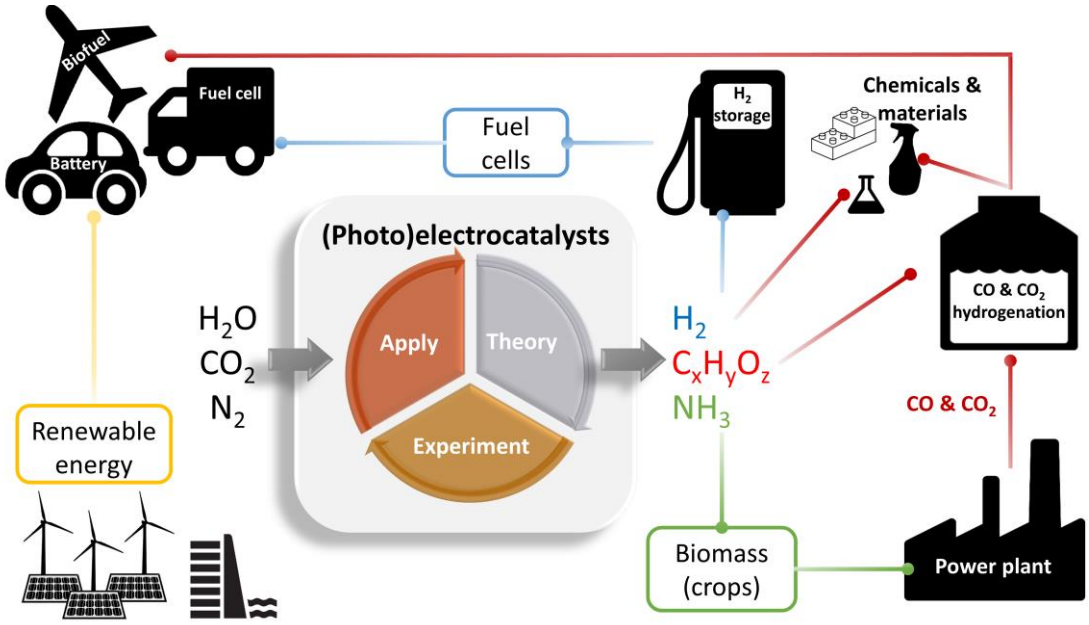

This chapter provides the motivation for the research disclosed in the present thesis. The irreversible effects of the current energy system based on fossil fuels are discussed on the verge of climate change. Artificial photosynthesis aims to substitute fossil fuels by developing photoabsorbing materials that drive the oxidation of water and subsequent reduction of protons or CO_2 into new energy vectors. A brief discussion of the processes involved in artificial photosynthesis is given, from light-absorption, to charge transfer and final catalysis. From all, one of the remaining challenges is to find efficient and stable (photo)catalytic materials for water oxidation. Finally, the most relevant (photo)catalysts reported up to date are analyzed, highlighting molecular (photo)anodes as new promising candidates to fulfill this goal.

Chapter 2. Objectives

Following the review in the variety of scientific and technical solutions awarded by the field of artificial photosynthesis, the main objectives of this thesis are unfolded in the present chapter. The main purpose is to bring the robust base of fundamental knowledge to practical devices for light-driven water oxidation.

Chapter 3. An anode based on a molecular Ru water oxidation catalyst covalently bonded to polythiophene

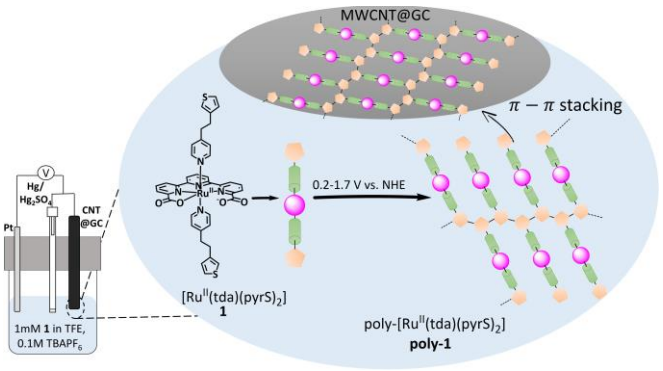

The current chapter introduces a promising strategy to incorporate homogeneous water oxidation catalysts into photoelectrochemical cells. In this direction, a derivative of Ru-tda complexes (tda^{2-} is [2,2':6',2"-terpyridine]-6,6"-dicarboxylate) with thiophene groups at the axial ligands is presented. The electropolymerization of the thiophene groups leads to the corresponding polythiophene functionalized with Ru-tda active sites. After an activation step, it achieves current densities of 90 mA·cm^{-2} at 1.45 V (V vs. NHE) and Turnover Numbers (TONs) over 20,000 in 4 h, which ranks among the best molecular anodes described up to now.

Chapter 4. Visible-light oxygen evolution at neutral pH by an organic dye/molecular catalyst homogeneous system

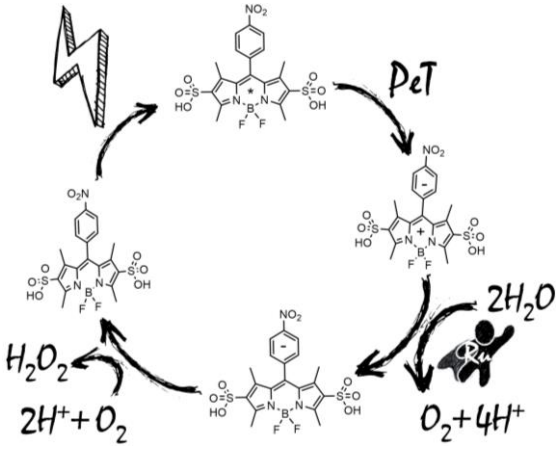

This chapter presents the homogenous interaction of two 4,4-Difluoro-4-bora-3a,4a-diaza-s-indacene (BODIPY) dyes with a Ru-based water oxidation catalyst. The constraints of light-driven water oxidation are overcome through the rational design of the organic dye and the molecular catalyst. Specifically, substitution in the BODIPY's aryl moiety leads to a robust organic dye even under harsh oxidative conditions, which is an alternative to the widespread but unstable ruthenium tris(bipyridine), $[Ru(bpy)_3]^{2+}$. Oxygen detection experiments, together with spectroscopic and electrochemical characterization techniques have revealed the complex mechanistic scenario, which surprisingly consists of simultaneous water oxidation and oxygen reduction.

Chapter 5. Noble-metal-free organic dye-sensitized photoanode with a molecular Cu water oxidation catalyst

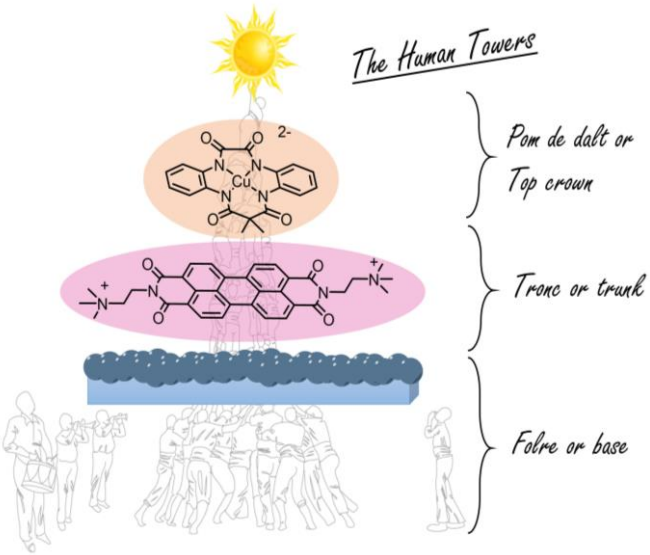

The present work introduces a system towards Dye-Sensitized Photoelectrochemical Cells (DSPECs) to generate solar fuels. Most of the published photoanodes for water oxidation are constituted of ruthenium tris(bipyridine) photosensitized semiconductors coupled to noble-metal catalysts. In this chapter, a hybrid molecular photoanode has been assembled by the combination of a macrocyclic Cu-complex and an organic dye of the perylendiimide family, all based on earth-abundant materials. Charge transfer between the different components as well as significant photocurrents are proven by photoelectrochemistry, Nuclear Magnetic Resonance (NMR), UV-Vis, and X-ray Absorption Spectroscopy (XAS).

Chapter 6. Functionalized covalent triazine frameworks for water oxidation photocatalysis

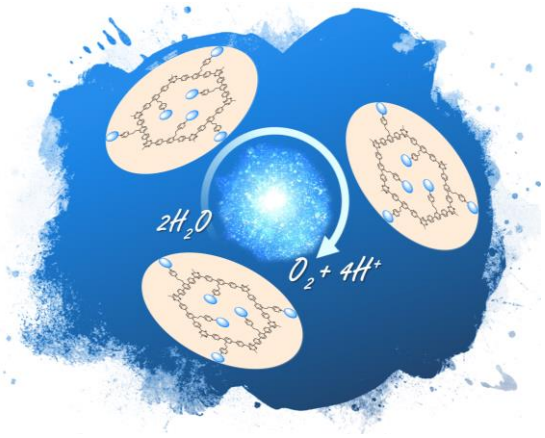

The following chapter is a contribution to the reduced pool of published colloidal photocatalysts for light-driven water oxidation. Herein, four novel covalent triazine frameworks are synthesized and characterized, designed to increase the oxidation potential energy and to serve as an anchor to molecular catalysts. In this line, a highly active Ru-based molecular water oxidation catalyst has been covalently attached to one of them. As a result, the first hybrid system molecular catalyst/organic photocatalyst is reported, with activities of 54 turnover numbers towards water oxidation.

Chapter 7. Nanocrystal–molecular hybrids for the photocatalytic oxidation of water

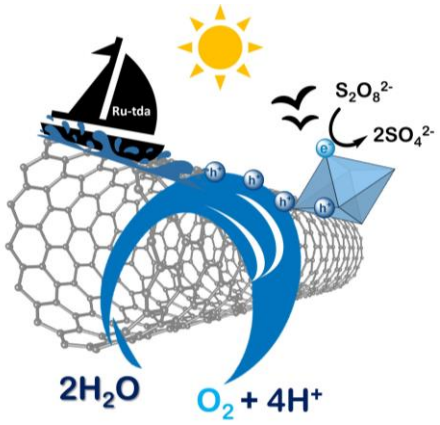

The reported work exposes a modular molecular hybrid colloidal photocatalyst composed of TiO_2 nanocrystals, as light-absorbers, and a molecular water oxidation catalyst from the Ru-tda family (tda^{2-} is [2,2':6',2"-terpyridine]-6,6"-dicarboxylate), both anchored onto Single-walled Carbon Nanotubes (SWCNTs). The molecular hybrid material is capable of achieving at neutral pH the photocatalytic oxidation of water to dioxygen under 3 suns illumination, giving the benchmark turnover number of 229. This unique architecture allows rational adjustments of each component independently, creating the path to future systems.

Chapter 8. Conclusions

Considering the initial objectives and the results obtained, this chapter unveils the main conclusions and outcomes of the present doctoral thesis.

Glossary of terms and abbreviations

Abs	Absorbance
bda^{2-}	[2,2'-bipyridine]-6,6'-dicarboxylate
bpy	2,2’-bipyridine
COSY	Correlation Spectroscopy
CB	Conduction Band
CV	Cyclic Voltammetry
CE	Counter Electrode
δ	Chemical shift
DCM	Dichloromethane
DFT	Density Functional Theory
DMSO	Dimethyl sulfoxide
DPV	Differential Pulse Voltammetry
DSPEC	Dye-Sensitized Photoelectrochemical Cell
ΔG°	Gibbs free energy
E	Potential
E°	Standard potential
$E_{½}$	Thermodynamic redox potential calculated as $(E_{p,a} + E_{p,c})/2$
$E_{p,a}$	Anodic peak potential
$E_{p,c}$	Cathodic peak potential
$E_{cat,onset}$	Onset potential of the catalysis
E_F	Fermi level
E_{fb}	Flatband potential
ε	Extinction coefficient
EC	Electrochemical Cell (electrolyzer)
ESI-MS	Electrospray Ionization Mass Spectrometry
EtOH	Ethanol
FE	Faradaic Efficiency
FOWA	Foot of the Wave Analysis
GC	Glassy Carbon
G-C	Generator-Collector method
HER	Hydrogen Evolution Reaction
hv	Light
λ	Wavelength
M	Molar
I	Ionic strength
IEM	Ionic Exchange Membrane
I2M	Interaction of two M-O groups
i	Current
j	Current density
m/z	Mass-to-charge ratio
MLCT	Metal to Ligand Charge Transfer
MS	Mass Spectrometry
MSE	Mercury-mercurous Sulfate Electrode
MeCN	Acetonitrile

MeOH	Methanol
mol-WOC	Molecular Water Oxidation Catalyst
η	Overpotential
NHE	Normal Hydrogen Electrode
NMR	Nuclear Magnetic Resonance
NCs	Nanocrystals
OEC	Oxygen-Evolving Center
PCET	Proton Coupled Electron Transfer
PEC	Photoelectrochemical cell
ppm	Parts per million
PS	Photosensitizer
PSI	Photosystem I
PSII	Photosystem II
PV	Photovoltaic
PRR	Proton reduction reaction
PXRD	Powder X-Ray Diffraction
py	Pyridine
phbf	Phosphate buffer
rds	Rate determining step
RE	Reference Electrode
RT	Room Temperature
RRDE	Rotating Ring Disk Electrode
S	Surface of the electrode
SEM	Scanning Electron Microscopy
$TBAPF_6$	Tetra(N-butyl)ammonium hexafluorophosphate
tda^{2-}	[2,2’:6’,2’’-terpyridine]-6,6’’-dicarboxylate
tPa^{4-}	[2,2':6',2''-terpyridine]-6,6''-diphosphonate
TEM	Transmission Electron Microscopy
TFE	Trifluoroethanol
TOF	Turnover Frequency
TON	Turnover Number
trpy	2,2’:6’,2’’-terpyridine
UV-Vis	Ultraviolet-Visible Spectroscopy
v	Scan rate
VB	Valance Band
vs.	*versus*
WE	Working Electrode
WNA	Water Nucleophilic attack
WO	Water Oxidation
WOC	Water Oxidation Catalyst
XAS	X-ray Absorption Spectroscopy
XPS	X-ray Photoelectron Spectroscopy
XRD	X-Ray Diffraction

Chapter 1

General Introduction

Chapter 1.

I

1.1 The energy challenge

Beyond a shadow of a doubt, we are experiencing a paradigm change. One causality for this statement, for example, is the irruption of the COVID-19 pandemic by the end of 2019.[1] Consequently, a global crisis has struck with 1.5 million deaths reported up to now[1] and the deepest global recession since the Second World War.[2] And yet, society still does not know the outcome of this health crisis. Despite the woes of a recession, the new virus triggered the immersion of technology in our lives affecting how we work and relate, as well as prompted concerns about mental health and environmental consciousness. In fact, the outbreak of COVID-19 converges with climate emergency by being one of the consequences of the impact of globalized human activities on terrestrial ecosystems.[3] This environmental degradation has led the scientific community to propose the beginning of a new geological epoch, the Anthropocene.[4] It differentiates from the Holocene by a stratigraphic signature of the sediments (hydrocarbons, pesticides, nitrates and phosphates, toxic heavy metals…), by an increase of greenhouse gases in the atmosphere, ocean acidification, or temperature increase, among others.[4] All these can lead to the transgression of the planetary boundaries[5] with irreversible consequences as collected by the report of the Intergovernmental Panel on Climate Change (IPCC) on the impacts of 1.5˚C increase.[6]

One of the main contributors to this situation has been our energy system based on fossil fuels.[7] Thus far, crude oil was an easy and cheap source of energy centralized in the hands of a few governments and companies.[8] Besides, fossil fuel combustion has led to unprecedented CO_2 concentration in the atmosphere.[6] This, along with the estimated increase in the world population to 9.4 billion by 2050,[9] will create a demand of 27.6 TW.[10] Therefore, the resulting trajectory of satisfying this demand with fossil fuels would likely cause serious disruptions to ecosystems, society, and economies.[11] Without getting carried away by pessimism, positively, interdisciplinary research has come together to find scientific and technological solutions for clean and renewable energy sources. For example, after years of research, the price of the electricity generated by solar and wind technologies is reaching values below fossil fuels.[12] Moreover, COVID-19 has evoked a collapse in oil demand and price. For the first time in history, in April 2020,

I

United States' crude oil briefly went negative in price.[13] As a result, the irruption of solar and wind power has impacted the markets as shown in Figure 1 (data from the *World Energy Outlook 2020,*[14] based on three case scenarios depending on the COVID-19 measures applied). Besides, the climate emergency is taking a big role in the global political arena. For example, in November 2016, 195 countries signed the Paris Agreement to set the threshold of temperature increase below 2°C from pre-industrial levels.[15] Actually, the United Nations has established this issue inside their list of Sustainable Development Goals (SDGs) within their Agenda 2030 to ensure access to affordable, reliable, sustainable, and modern energy for all.[16]

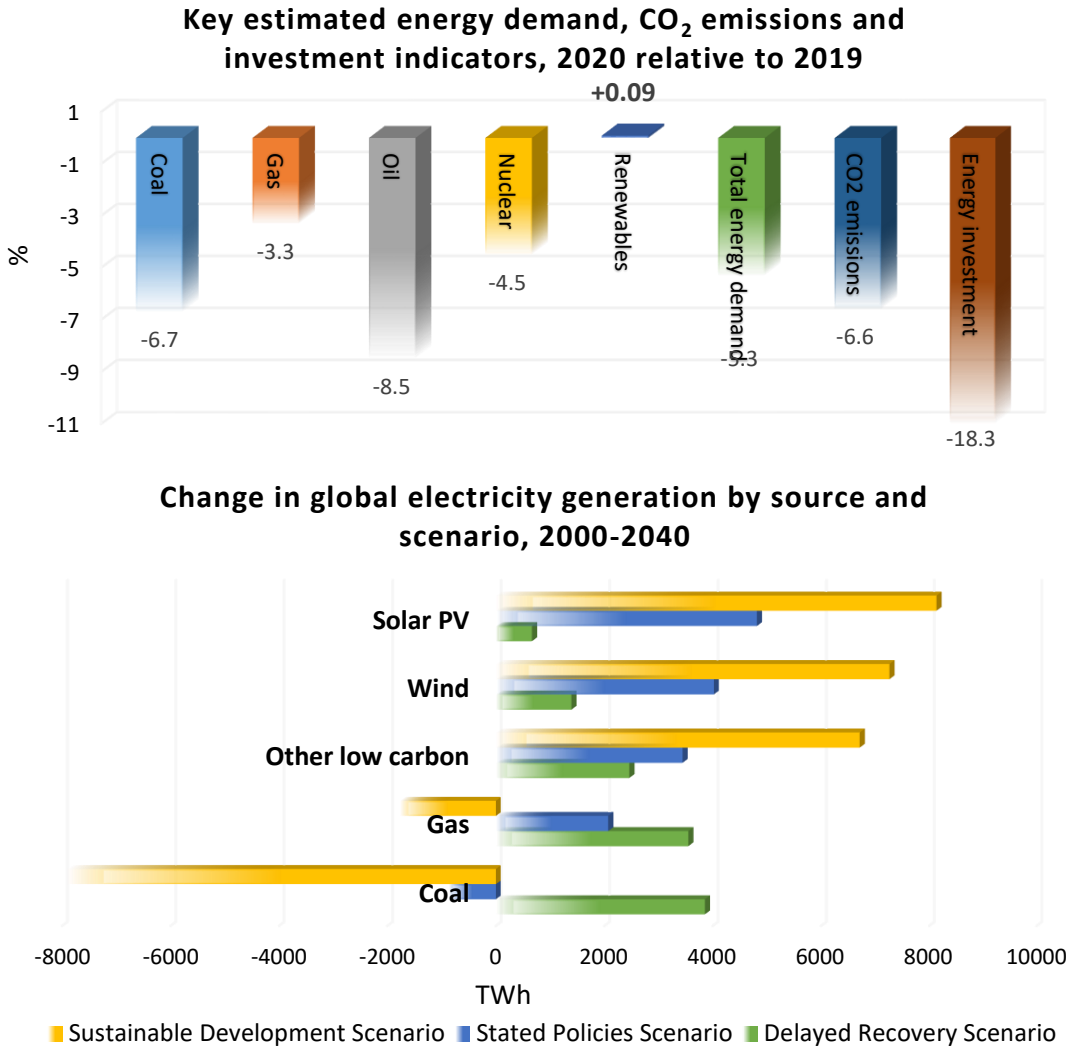

Figure 1. Top, comparative assessment of energy demand, CO_2 emissions, and investment from 2020 relative to pre-COVID-19 (data from World Energy Outlook 2020 report[14] evaluated by the International Energy Agency). Bottom, prognostic of global energy demand per source depending on three case scenarios: (yellow) if a surge in clean policies and investments for economic recovery post-COVID-19; (blue) if policies to control COVID-19 surge effect with the pandemic gradually controlled in 2021, and the global economy gets back to pre-crisis levels; (green) if the same policies are adopted but prolonged pandemic causes economic clash.

In light of this change in paradigm, renewable energy technologies, such as biomass, hydroelectric, geothermal, wind power, and solar energy, have irrupted strongly into the economy. However, these technologies rely on intermittent sources, like solar and wind meteorology, and are based on the direct conversion into electricity with its inherent problems for storage and transport. Second generation of renewable energy technologies is focusing on transforming the "clean" produced electricity into liquid or gas fuels as energy vectors to be used wherever and whenever needed. Other than that, the new fuels would supply other demands in a sustainable fuel-free path to industrial chemicals and materials, such as plastics and fertilizers (Scheme 1).[17]

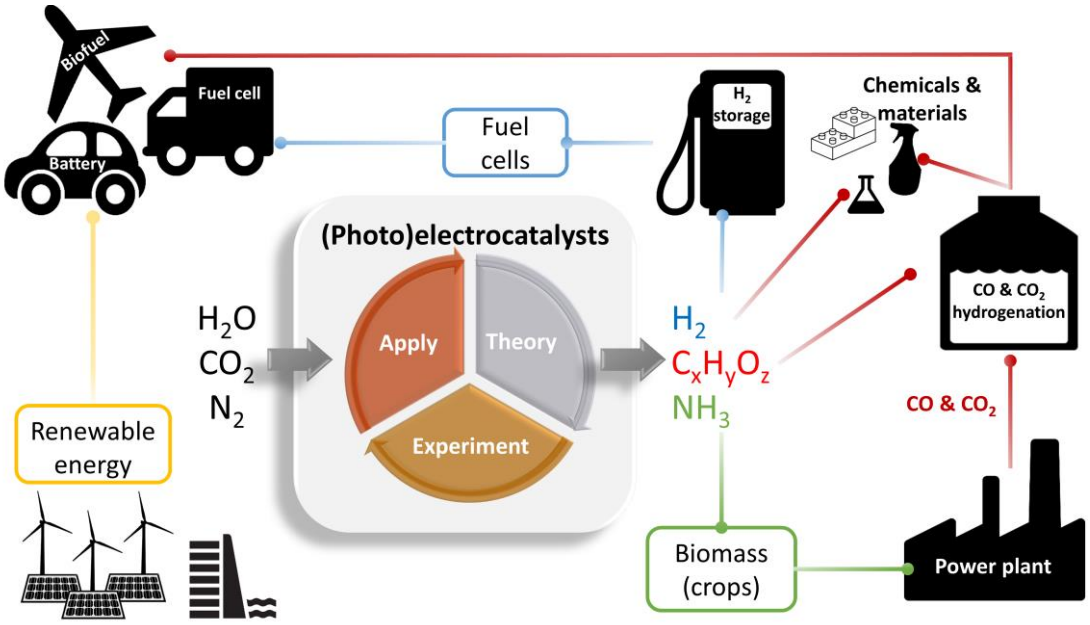

Scheme 1. Schematic representation of energy diversification to attain sustainability based on (photo)electrocatalysts for solar fuel production and usage.

Simpler than that, Nature has attained this goal through one of the most primal but essential of all processes: photosynthesis. The mechanism consists of sunlight-driven reactions that transform water and CO_2 into products that store energy in their chemical bonds. The scientific community has been inspired by Nature to explore the next generation of renewables from the biomimicry of proteins and/or reactions involved.[18–22] Research is focused on the absorption of photons from the spectrum of the Sun's solar radiation, on the efficient charge separation, and the e^- transfer to reduce protons into hydrogen, nitrogen into ammonia or carbon dioxide into carbon monoxide, hydrocarbons, and alcohols. As shown in Scheme 1, these solar fuels would provide a

resilient and diversified energy market breaking the centralization imposed by fossil fuels.

1.2 Natural and artificial photosynthesis

Giacomo Ciamician was aware of human dependence on coal and its consequences. Thus, in his Science paper entitled *The Photochemistry of the Future* (1912),[23] he describes the need "to fix the solar energy through suitable photochemical reactions with new compounds that master the photochemical processes that hitherto have been the guarded secret of the plants".

His visionary mindset inspired other scientists in the quest for biomimicking natural photosynthesis. Photosynthesis is the mechanism by which plants, cyanobacteria, and algae use sunlight energy, water, and CO_2 to obtain oxygen and energy-rich organic compounds. This process, redefined by hundreds of millions of evolution, is based on the light absorption of the solar spectrum to produce oxidation-reduction reactions. Figure 2 depicts a diagram of all the redox reactions and molecules involved in the thylakoid membrane vesicles of chloroplasts.[24] The first step occurs in photosystem II, with the absorption of light by chlorophyll P680 (λ = 680 nm) and the generation of excitons, that is, pairs of electron-hole. After delocalization of the excitons within the "pigment-protein matrix",[25] charge separation occurs with efficient electron transfer to strong reducing agents, such as Plastoquinone (Pq) and Plastocyanin (Pc). Their reduced forms carry hydrogen atoms (PqH_2) and when electrons are transferred between molecules, more protons are pumped to the other side of the membrane, building up a potential difference between both sides. The excitation of P680 and reduction of Pq leaves a positive oxidizing charge in PSII. The catalytic cluster named Oxygen-Evolving Center (OEC) is in charge of accumulating four oxidative charges and splitting water into four protons and a molecular oxygen. This mechanism will provide of more electrons and protons for further reactions. A second light absorption occurs in Photosystem I (PSI, λ = 700 nm) with concomitant electron transfer to Ferredoxin (Fc). Afterward, two reduced ferredoxin molecules transfer two electrons to a molecule of Nicotinamide Adenine Dinucleotide Phosphate ($NADP^+$) resulting in NADPH. Finally, the enzyme ATPase takes the energy from the build-up charge in the membrane to synthesize the

energy-rich Adenosine Triphosphate (ATP). NADPH and ATP are the energy vectors employed in the Calvin cycle, which is the process that fixates carbon dioxide into energy-rich sugar molecules.

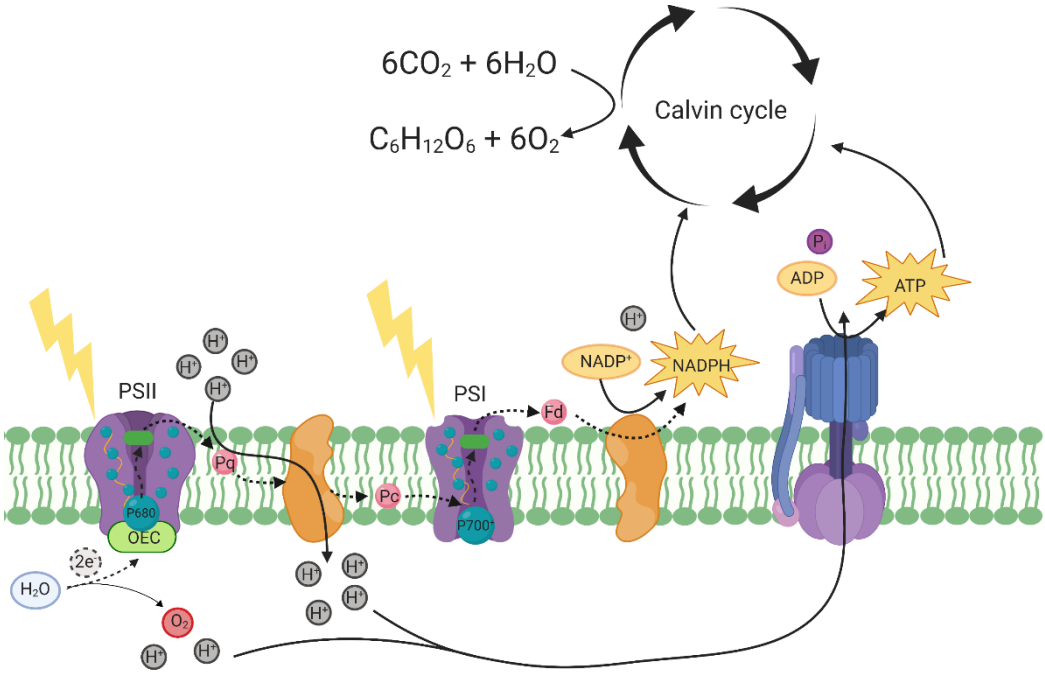

Figure 2. Conceptual illustration of the mechanisms in natural photosynthesis. Briefly, a first absorption by the chlorophyll P680 (λ = 680 nm) of Photosystem II (PSII) with subsequent reduction of Plastoquinone (Pq) and Plastocyanin (Pc). The oxidative charge accumulated in PSII is employed by the Oxygen-Evolving Center (OEC) to split water into protons and electrons. A second light absorption occurs in P700 (λ = 700 nm) in the photosystem I (PSI) which reduces Ferredoxin (Fc). As a result of the electron transfer, a Nicotinamide Adenine Dinucleotide Phosphate ($NADP^+$) gets reduced to NADPH. As a consequence of the proton transfer and build-up charge, Adenosine Triphosphate (ATP) is generated. Both NADPH and ATP are the energy vectors employed in the Calvin cycle for carbon fixation to sugar molecules. Image created with BioRender.com

The key elements of photosynthesis are two separated clusters: the light-harvesting antennas and the catalytic centers. On one hand, chlorophylls P680 and P700 absorb one photon in the visible of the solar spectrum, astonishingly operating at nearly 100% quantum efficiency under optimum conditions.[26] On the other hand, the catalytic centers in charge of water splitting and $NADP^+$ reduction require four-electron/holes and two-electron/protons respectively. For years, research focused on revealing how Nature has managed to combine all the processes with their requirements and optimizations.[27] The first step towards biomimicking materials for photocatalytic water splitting is to understand the actual structure and processes in PSII. One striking

I

discovery was the study of the OEC and its protein environment at a resolution of 1.9 Å by X-ray Absorption Spectroscopy (XAS), X-Ray Diffraction (XRD), and Density Functional Theory (DFT) (Figure 3).[28] As a result, OEC's composition and metric parameters were determined, which consists of a Mn_4O_5 cluster (bottom of Figure 3).[28] Besides, P680 is composed of two chlorophyll dimers (top of Figure 3), whose structures are based on a chlorin ring with a central magnesium atom, and with several other attached side chains and a hydrocarbon tail.[25,28] In addition, the work of Prof. Rienk van Groendelle *et al.*[29] shined light onto the near-unity quantum efficiency by proving quantum coherence between excitons and charge-transfer states by 2-D electronic spectroscopy.

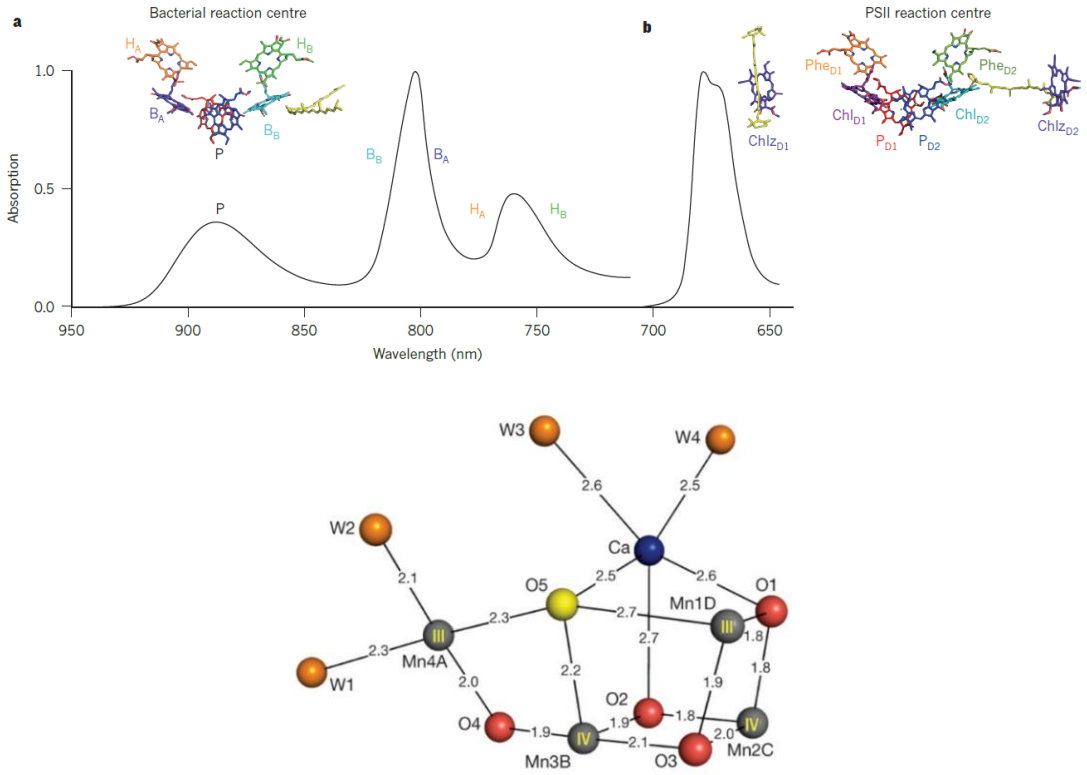

Figure 3. Top, X-ray structure and absorption spectra of (a) the bacterial reaction center and (b) the PII light-harvesting antennas.[25] Bottom, X-ray structure and metric parameters of the Oxygen-Evolving Center in the PSII at 1.9 Å of resolution.[28]

Following the processes of light absorption, there is the electron transfer to a pheophytin molecule and the reduction of $P680^+$ by the OEC. The Mn_4O_5 cluster is responsible to collect all four oxidative charges and oxidize water highly efficiently, with low overpotentials (430 mV) and high turnover frequencies (100-400 s^{-1}).[30,31] All thanks to the oxidation of the Mn^{2+} centers to Mn^{3+} with proton-coupled electron transfer (PCET) catalysis, which is the movement of an electron from one site to another

accompanied by proton transfer.[32] Detailed information on PCET and the key role they have in water oxidation catalysis will be given later. Despite such advancements, the O-O bond formation mechanism is still under investigation. Moreover, all the catalysis is performed at nearly neutral pH values and using earth-abundant elements. Another secret of natural photosynthesis is the catalyst's repairing process (degraded by light or during catalysis), which can occur every 30 min in some organisms.[33]

Inspired by the principles rigid by Nature, scientists have attempted to obtain technologies that harvest sunlight energy into solar fuels.[22,34] Artificial photosynthesis[18,20,21] aims to achieve water splitting to H_2 and O_2 (Equation 1-3 in Table 1) with 1 sun intensity (AM 1.5 G of the solar radiation). Besides, other solar fuels can be obtained by coupling the electron and proton release from water oxidation to the reduction of CO_2 or N_2 into gaseous or liquid fuels (Eq. 4-11, Table 1).

	Reaction	***E° / V vs. RHE or NHE (pH 0)***	***Equation***
Oxidation half-reaction	$2H_2O \rightarrow O_2 + 4H^+ + 4e^-$	1.23 V	(1)
	$2H_2O \rightarrow H_2O_2 + 2H^+ + 2e^-$	1.77 V	(2)
Reduction half-reaction	$4H^+ + 4e^- \rightarrow 2H_2$	0 V	(3)
	$N_2 + 8H^+ + 6e^- \rightarrow 2NH_4^+$	0.275 V	(4)
	$CO_2 + 8H^+ + 8e^- \rightarrow CH_4 + 2H_2O$	0.18 V	(5)
	$CO_2 + 14H^+ + 14e^- \rightarrow C_2H_4 + 4H_2O$	0.14 V	(6)
	$2CO_2 + 12H^+ + 12e^- \rightarrow C_2H_5OH + 4H_2O$	0.08 V	(7)
	$CO_2 + 6H^+ + 6e^- \rightarrow CH_3OH + H_2O$	0.03 V	(8)
	$CO_2 + 2H^+ + 2e^- \rightarrow CO + H_2O$	-0.1 V	(9)
	$CO_2 + 2H^+ + 2e^- \rightarrow HCOOH$	-0.17 V	(10)
	$2CO_2 + 2H^+ + 2e^- \rightarrow H_2C_2O_4$	-0.45 V	(11)

Table 1. Redox reactions and their respective potentials (V vs. RHE) relevant to solar fuel generation in artificial photosynthesis.

Table 1 displays the reduction and oxidation reactions relevant to solar fuel production. As seen, water oxidation is key to provide protons and electrons to reduce H^+, CO_2, and

I

N_2. For this reason, Water Oxidation (WO) is considered one of the "Holy Grails" in chemistry. [34,35] In this line, the focus of this thesis is research on technologies for light-driven water oxidation.

As in Nature, artificial photosynthesis consists of several steps: light absorption, charge separation, electron transfer, and catalysis. Nowadays, several designs have been proposed depending on the integration of light-harvesting units with catalysts and the communication between catalytic reactions (full water splitting or half-reactions). Consequently, the following sections are a tutorial review on the theoretical basis of all the steps involved in sunlight-driven water oxidation catalysis and the state-of-the-art of envisioned technologies.

1.3 Light absorption

Light is the quanta (or photons) of the electromagnetic field propagating through space. In fact, the light visible to the human eye is just a small part of the electromagnetic spectrum. Light interaction with matter is the result of the resonance of an oscillating electromagnetic field with charged particles, mostly electrons. This interaction can give rise to absorption, transmission, or scattering of the incident light. The latter englobes reflection, refraction, and diffraction, in which the light is dispersed by an atom in a different direction. Despite the scattering, the forward light has the same energy (frequency) as the incident light. On the contrary, absorption is the phenomena in which photons are annihilated or created.[36] The energy associated with the photon promotes an electron from its ground state to a molecular orbital higher in energy or excited state. Subsequently, the excited electron goes back to the ground state through a non-radiative decay (heat or phonons) or a radiative decay (light or photons). For example, some semiconductor materials can exhibit both, with a first nonradiative relaxation with a small energy difference between levels and then a higher radiative transition over the bandgap of the semiconductor. This radiative emission of energy can be coupled to suitable co-catalysts to trigger redox reactions. For simplicity, the dynamics of light absorption and electron transfer in discrete molecular systems (similar to proteins) will first be explained. When these molecular systems or atoms are constituting an extensive

lattice, the theory is explained by a continuum of orbitals. Finally, the state-of-the-art of all light-absorbing materials will be expounded.

1.3.1 Molecular dyes

Dyes are discrete molecules with multiple conjugated bonds with π-electrons, as in organic and organometallic molecules. The Pauli exclusion principle dictates that two electrons cannot have the same quantum numbers in a molecule so each atomic orbital splits into two molecular orbitals of different energy, bonding, and anti-bonding orbitals. The molecular orbital splitting allows the movement of electrons between non-degenerate energy levels. Upon absorption of a photon, an electron from the Highest Occupied Molecular Orbital (HOMO) to the Lowest Unoccupied Molecular Orbital (LUMO) (Figure 4). The energy difference between them is the HOMO-LUMO gap, which is the driving force for radiative decay. The advantage of using molecular dyes is that this bandgap can be tuned by rational molecular design to absorb in the visible region of the solar spectrum. Besides, high molar extinction coefficients (ε) are characteristic of these components. ε is a measurement of how strong a species absorbs the light at a given wavelength (λ) expressed in terms of $M^{-1}{\cdot}cm^{-1}$ or $L{\cdot}mol^{-1}{\cdot}cm^{-1}$. The state-of-the-art of molecular dyes for water oxidation purposes will be described below, in section *1.3.4 Light-absorbers for photocatalytic water oxidation*.

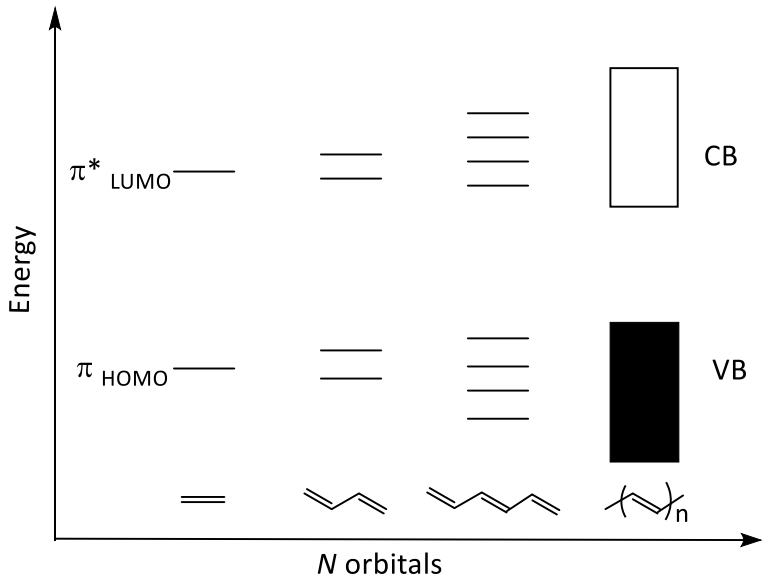

Figure 4. Relationship between π HOMO and π LUMO orbitals of finite molecules and conduction (CB) and valence (VB) band of infinite systems.*

1.3.2 Semiconductors and band theory

When a large number *N* of identical atoms or molecules get together to form a lattice, their orbitals will overlap. This overlap is again ruled by the Pauli principle of exclusion in which each atomic orbital splits into two molecular orbitals. The great amount of adjacent molecular orbitals forms continuum levels of energy bands. In solid-state physics, this is the band theory (Figure 4), in which a periodic lattice of adjacent HOMO orbitals generates a degenerate energy level or valence band (VB); at the same time, the continuum of LUMO orbitals derives to a conduction band (CB).

The difference in energy between bands is called bandgap (E_g), which is the parameter that defines the optical and electronic properties of the materials. In metals (or alloys), E_g is so small that there is an overlap between VB and CB (Figure 5, left). Thus, the outermost electrons in the atoms, or valence electrons, will easily transfer to empty orbitals with low energy such as thermal k_bT (product of Boltzmann's constant and temperature). The electrons in higher orbitals are "delocalized" in the crystal moving freely between the orbitals. On the other hand, if $E_g > 9$ eV as for insulators, the bands are too separate to allow electron promotion between orbitals, and thus, the solid will have no conductivity (Figure 5, middle). In the mid-term, there are semiconductor materials, in which the promotion of valence electrons to CB will be allowed by absorption of thermal, electrical, or optical energy depending on the E_g value (Figure 5, right). Moreover, the promotion of an electron will create a "hole" that can be occupied by another electron from neighboring bands. In all solids, valence electrons follow the Fermi-Dirac distribution, f(ϵ), which defines the particle distribution over energy states of a system with thermodynamic equilibrium. Equation 12 is the mathematical expression of f(ϵ), in which ϵ is the energy of a state occupied by an electron, E_F is the Fermi level, k_b is the Boltzmann's constant, and T is the temperature. If there is a state at the Fermi level ($\epsilon = E_F$) then this state will have 50% chances to be occupied. For conductor materials, the E_F lays in one of the bands, and for insulators, it lays inside of the bandgap (Figure 5). In the case of semiconductors, E_F position will depend on whether the semiconductor is intrinsic or extrinsic. Intrinsic semiconductors are pure semiconductor materials such as Si or Ge. On the contrary, in extrinsic semiconductors, some impurities are added to increase the number of charge carriers or conductivity.

$$f(\epsilon) = \frac{1}{e^{(\epsilon - E_F)/kT} + 1} \qquad \text{(Equation 12)}$$

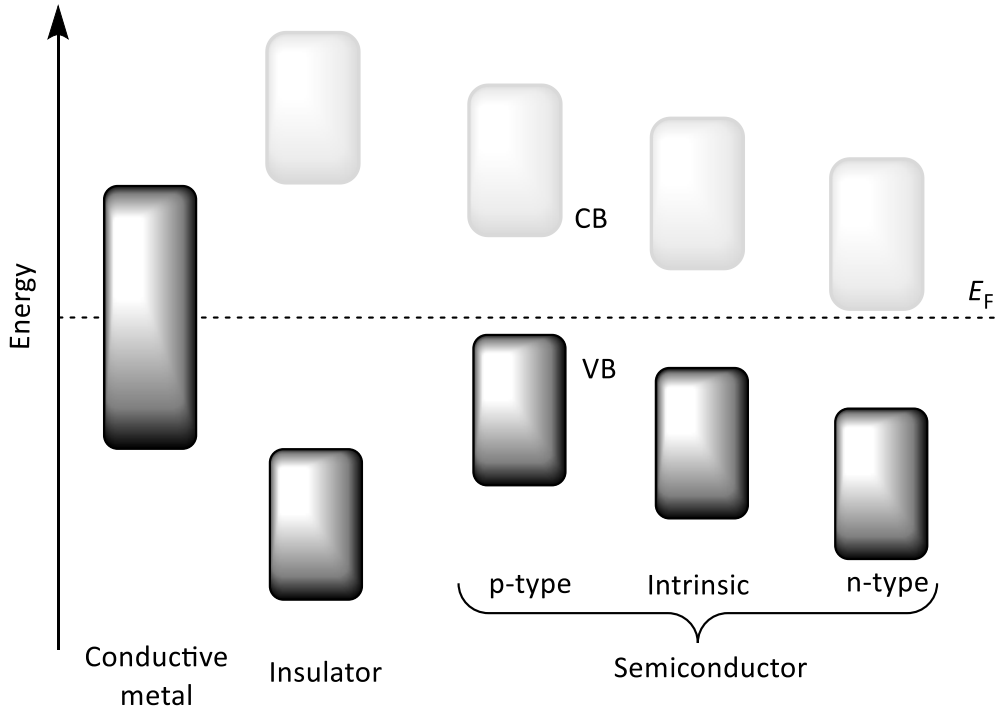

Figure 5. Band and Fermi level positions in a conductive metal, an insulator, and p-, intrinsic, n-type semiconductor materials.

Doping is the addition of electron-rich (donor) or electron-deficient (acceptor) atoms within the lattice of a semiconductor.[37] The concentration of dopants will influence the conductivity and the band structure. Donor impurities will generate n-type semiconductors, in which electrons are the majority of all charge carriers. Acceptor impurities will result in p-type semiconductors since holes are the majority carriers. For example, the addition of phosphorous ([Ne] $3s^2\ 3p^3$) in a silicon material ([Ne] $3s^2\ 3p^2$) increases the number of electrons free to move (n-type semiconductor); these new donor states will shift the E_F near the CB, increasing the conductivity of the material. Conversely, the insertion of boron atoms ([He] $2s^2\ 2p^1$) in a silicon material ([Ne] $3s^2\ 3p^2$) will generate vacancies or holes in the crystal lattice (p-type semiconductor); hence, the empty orbitals will be acceptor states of valence electrons resulting in a shift of the E_F near the VB. Despite these well-known examples, some semiconductors, such as metal oxides or amorphous materials, have not well-defined stoichiometric ratios that can produce the abovementioned electronic structures. Then, trap or intra-bandgap states are generated, which will affect charge carrier mobility or recombination since they act as a "trap". For example in the Fujishima-Honda cell, the first photochemical device for

water splitting in the literature made of a TiO_2 photoanode, an applied bias is needed. The extra energy is required because the electrons in trap states below the CB of TiO_2 are not sufficiently reducing to generate hydrogen in the counter electrode and thus, they recombine.[38,39] Yet, trap states can play different roles depending on their position in the E_g. If they are shallow (near the CB) they will get occupied by electrons that can be useful or otherwise recombined.

In most inorganic semiconductors the approach to charge carrier separation occurs over p-n junctions. When an n-type semiconductor (rich in electrons) gets in contact with a p-type (hole rich), a depletion layer or space charge region at the interface is generated in the absence of light or applied bias. This new distribution creates an electric field through the junction. The created potential difference will physically separate electron-hole pairs, which will feel an opposite force within the same electric field. This effect minimizes recombination and the employment of minority carriers to mobilize to catalytic centers or the electrolyte to perform reactions.

In optoelectronics, the most employed inorganic semiconductors are crystalline or amorphous Si, Ge, GaAs, chalcogenides such as CdTe, and metal oxides such as TiO_2. However, research has gone beyond the classical inorganic semiconductors, in the quest for less scarce materials and higher efficiencies for commercial applications. For example, in the case of solar cells, Figure 6 illustrates that new emerging materials show rapidly growing efficiencies (orange line) to levels competitive with more expensive mature technologies (purple and blue lines).

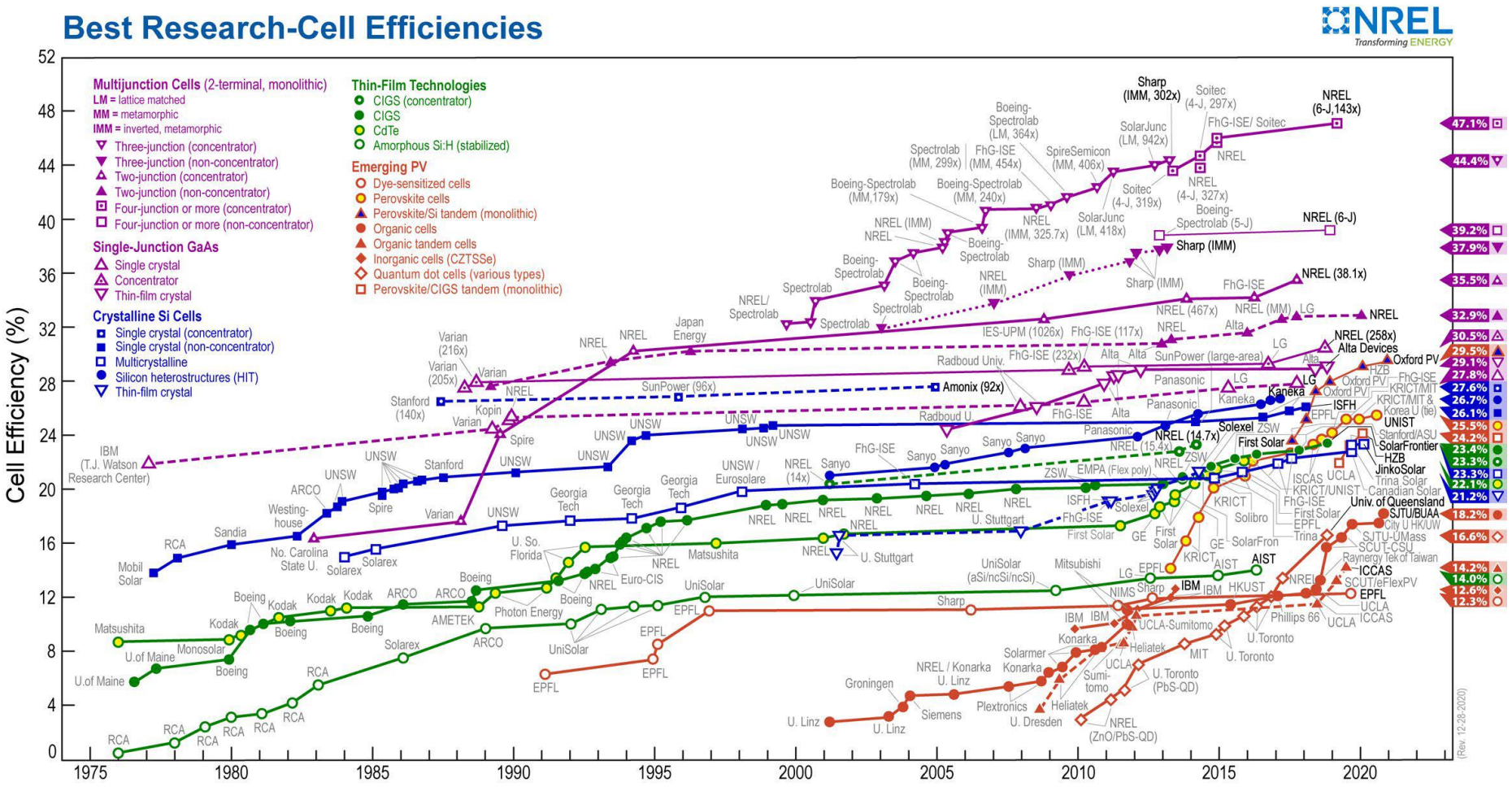

Figure 6. Chart of the highest efficiencies in reported solar cells from 1976 up to now. Different families of semiconductor materials are depicted with a specific color code. This plot is courtesy of the National Renewable Energy Laboratory, Golden, US.

1.3.3 Emerging semiconductors

Solid-state physics theory has focused on bulk inorganic semiconductors. However, new emerging semiconductor materials have irrupted with a variety of electronic, optical, and physical characteristics. For example, when the dimensions of semiconductors or metals are reduced to the nano-scale, new phenomena such as the quantum or plasmon effects give rise to new optophysical properties with enhanced light-matter interactions. Yet, for the scope of this thesis, this subsection will only focus on new semiconductors based on organic solids. They are polymers formed by repetitive building blocks that contribute to an extended π-conjugated system. Comparing to inorganic semiconductors, organics are low in cost materials and have a low temperature of manufacturing (60-120° C), chemical stability, mechanical flexibility, and good tunability of the framework and electronic structures.[40–42] For example, their versatility makes their optical absorption range from 1.7-3 eV which corresponds to 700-400 nm in the visible spectrum.

Previous solid-state theory may not be applied in the same manner for organic semiconductors. Upon optical excitation, electron-hole pairs bonded by electrostatic Coulomb interactions, also known as excitons, are generated. The dielectric constants in organic semiconductors are so low (ε∼ 3-4), that efficient photogeneration is hindered.[43] In fact, proper charge separation occurs in binary systems, between an electron acceptor (A) and an electron donor (D). The D-A configuration can be: (i) intrinsic within the organic polymer, e.g. between different functional groups, (ii) extrinsic by combining two different organic semiconductors. For example, fullerenes are the most common materials employed as A and diketopyrrolopyrrole as D.[44]

The most common organic semiconductors are Conjugated Microporous Polymers (CMP) and Covalent Organic Frameworks (COF). All these are porous materials based on organic building units linked by covalent bonds. Depending on the monomer or co-monomer composition the photophysical properties vary.[45] Besides, size pore, crystallinity, and physical properties, such as wettability, will get affected. Therefore, a huge range of materials has been synthesized by combining infinite possibilities of

monomers, co-monomers, and spacers. Yet in the next section, we will try to focus on those employed for photocatalytic water oxidation applications.

Finally, a new branch in optoelectronics is constituted by organic-inorganic hybrids (OIH). These materials are based on the sensitization of inorganic semiconductors with organic dyes or macromolecules.[46] This strategy brings together the advantages of both fields.[47–49] On one side, inorganic semiconductors bring extended band-states and high charge carrier mobility, which can be increased by electrical injection from a molecular dye or an organic polymer.[47] On the other hand, the energetic states in dyes and polymers are easily tunable by ligand or monomer rational design, making them more efficient in visible-light absorption and efficiency.[50] Besides, they offer other characteristics such as hydrophobicity, hydrophilicity, temperature-responsive, flexibility, among others. Therefore, dye-sensitized semiconductors or hybrid materials based on conjugated polymers and inorganic semiconductors, are new emerging fields with several applications.[46] Therefore, they have attracted much attention in recent years, especially for photocatalytic and environmental applications.[46]

1.3.4 Light-absorbers for photocatalytic water oxidation

Preceding paragraphs summarized a brief overview of light absorption theory. However, in this thesis, we will focus on light-absorbers for water oxidation. Previous cases were all explained in hypothetical thermodynamic equilibrium in the vacuum. However, when molecular dyes or semiconductor materials come into contact with an electrolyte, most likely an aqueous one, the thermodynamic equilibrium must be restored.

For example, the presence of solvent around the molecular dye, also known as the solvation effect, affects its energy, properties, dynamics, and reactivity in the ground and the excited state.[51] The polarization given by solvent molecules or interactions such as hydrogen-bonding will directly affect the excitation energy. As a result, solvatochromic shifts in the absorption spectra will appear, especially in highly polar solvents such as water. Another effect occurring during water oxidation photocatalysis is the quenching effect of molecular oxygen on excited state electrons, which hinders charge transfer to catalytic centers. Besides, photosensitizers for water oxidation are not so common, due to the high oxidation potentials needed and their limited stability

in aqueous media.[52] Moreover, the reported ones rarely digress from the most common ruthenium(II) tris(bipyridine), $[Ru(bpy)_3]^{2+}$, and porphyrin derivatives,[53–55] which are pricey and exhibit stability issues as well as charge recombination (Figure 7). Alternatively, robust organic dyes are suitable candidates to overcome these limitations. For example, various organic dyes were accomplished for the complementary proton reduction reaction, such as fluorescein,[56] eosin,[57] rhodamine,[58] triarylamine,[59] triazatriangulenium,[60] and perylene derivatives (see some examples in Figure 7).[61] Therefore, in the field of light-driven water oxidation further research should focus on: (i) stability of dye molecules (and their anchoring) under water oxidation conditions, (ii) the use of earth-abundant materials, (iii) reach light absorption and charge separation efficiencies as in natural photosynthesis. The pathway is long yet much progress has been achieved in the field of dye-sensitized solar cells,[59,62,63] which is the first milestone towards artificial photosynthesis.

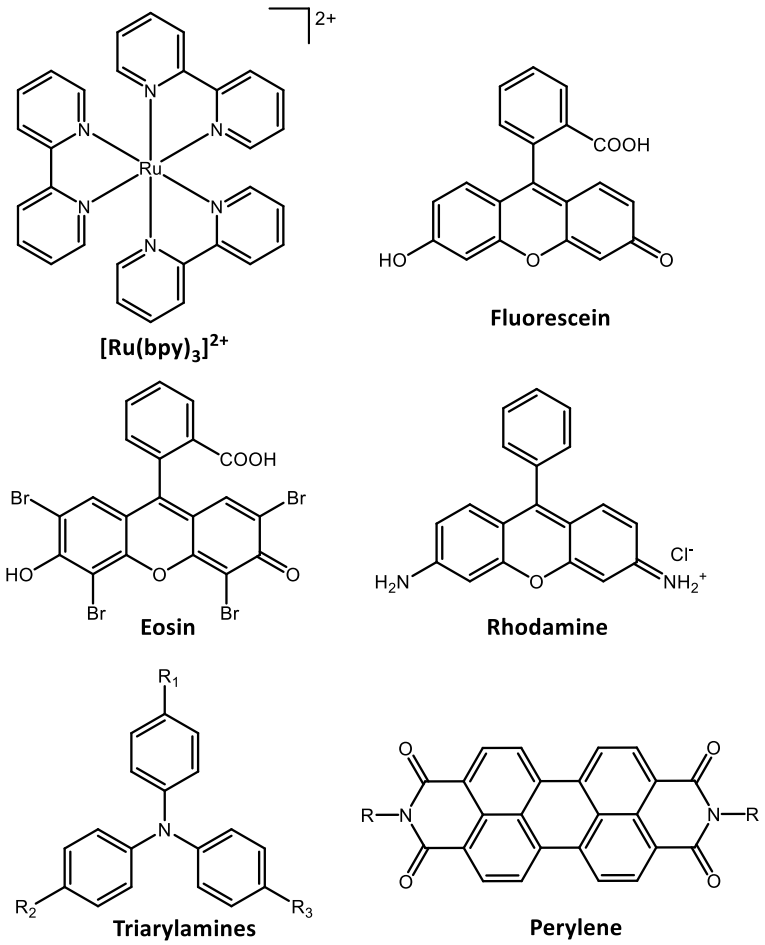

Figure 7. Main organic dyes employed in water splitting photocatalysis: $[Ru(bpy)_3]^{2+}$, fluorescein,[56] eosin,[57] rhodamine dyes,[58] triarylamine,[59] triazatriangulenium[60], and perylene derivatives.[61]

In a similar manner but with other terminology, solid-state semiconductors are also affected by aqueous environments. The immersion of a semiconductor in an electrolyte generates a "build-in" voltage at the semiconductor's interface. In the case of n-type semiconductors for water oxidation, the electrons in the bulk material migrate to the interface to re-establish thermodynamical equilibrium (Figure 8). Thus, a region of positive charges on the semiconductor's surface (depletion layer) and negative charges on the electrolyte's interface (Helmholtz layer) is generated. Then, the E_F of the semiconductor equilibrates with the $E_{F,redox}$ of the A/A^- redox couple in solution, which is considered as constant. The effect of the electric field and the difference in local energy structure is represented by a band bending at the edges of CB and VB. In n-type semiconductors, the band bends upwards to higher energies due to depletion of electrons and generation of holes (Figure 8). Band bending will also occur when a semiconductor comes into contact with another semiconductor or a metal. This concept is important in photocatalytic water splitting, i.e. the bending should align with the potential for water reduction and water oxidation. If we polarize the semiconductor by applying an external potential ($\Delta\phi$), we remove the energy difference and the bands become flat. Thus, by using electrochemical techniques we study E_F at the flatband conditions (E_{Fb}), which in the case of n-type semiconductors lays near the CB.

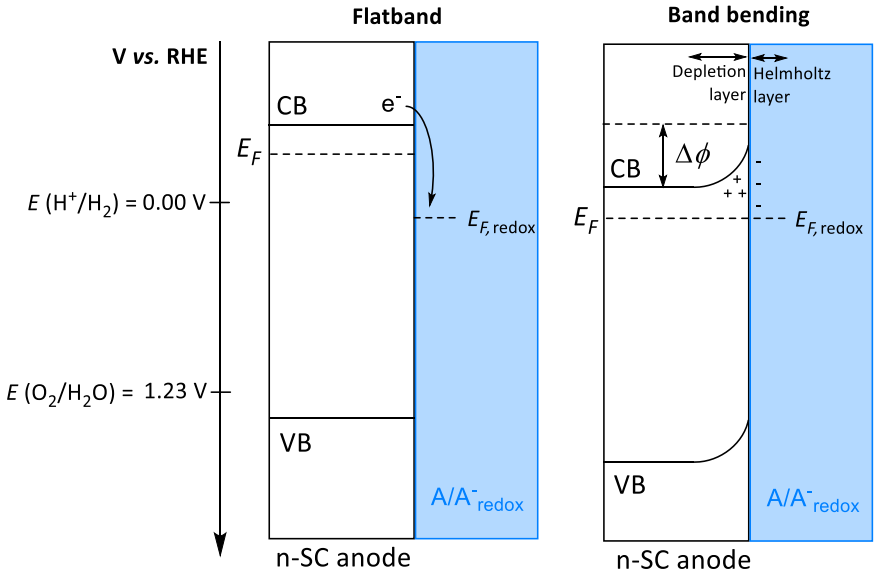

Figure 8. Scheme illustrating the band bending process when an n-type semiconductor comes into contact with an electrolyte. When the electrons in the bulk material migrate to the interface to re-establish thermodynamical equilibrium, a region of positive charges on the semiconductor's surface (depletion layer) and negative charges on the electrolyte's interface (Helmholtz layer) is generated. Then, the E_F of the semiconductor equilibrates with the $E_{F,redox}$ of the A/A^- redox couple in solution. $\Delta\phi$ is the difference in potential between the flat and bent bands. On the left, energy scale (V vs. RHE) for the proton reduction and water oxidation.

I

Years of research in inorganic semiconductors have given fruitful results with a wide range of semiconductors thermodynamically suitable for water oxidation (Figure 9). As previously mentioned, in 1972 Honda and Fujishima reported that water could be split over a TiO_2 photoelectrode.[39] Since then, TiO_2 has been considered the most suitable and well-studied n-type semiconductor for water oxidation photoanodes.[64] As shown in Figure 9 other examples of inorganic semiconductors are metal oxides such as WO_3 or $BiVO_4$,[65,66] and chalcogenides such as CdSe and CdS.[67] Despite their long-term attention, most inorganic semiconductors absorb in the UV, and their activity or stability at neutral pH is questionable.[68] Besides, most of them are made of toxic and/or non-earth abundant materials which result in high costs. Hence, the latest research is focused on: (i) decreasing the bandgap (E_g < 3 eV) for increased visible light absorption of the solar spectrum while keeping VB below water oxidation potential (dashed blue line in Figure 9); (ii) stability in the long-term in aqueous solvents and harsh water oxidation conditions; (iii) final cost of manufacturing. On the right side of Figure 9, the most representative organic semiconductors based on conjugated polymers are shown. Most studies involving conjugated polymers have focused on photocatalytic proton reduction due to the complexity of photocatalytic water oxidation. For example, several works use the well-known carbon nitrides (g-C_3N_4) with this purpose but they show low water oxidation activity and stability.[69–72] The best performing hybrid material up to date is an aza-fused conjugated microporous polymer (aza-CMP) using $Co(OH)_2$ as a cocatalyst (3 wt%) yet with low oxygen production rates.[73] Despite the little amount of literature published, emerging hybrid inorganic-organic materials have a lot of potential in the field of artificial photosynthesis. An infinite number of inorganic-organic combinations bring into play a broad library of materials with advantages from interdisciplinary research and composed of elements more in line with the new upcoming atom-circular economy.[74]

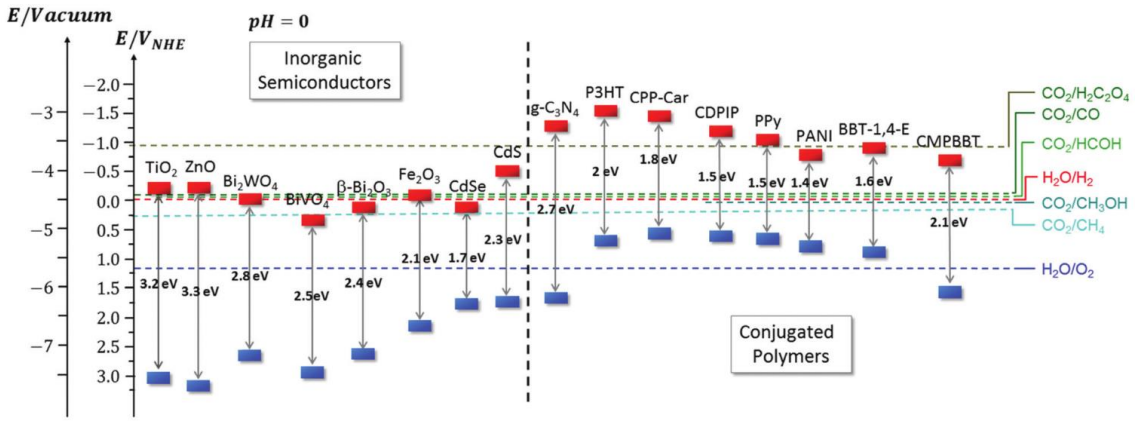

Figure 9. Energy level band diagram of the most representative inorganic and organic semiconductors. Adapted from.[46]

1.4 Catalysts for water oxidation

From all the reactions to obtain solar fuels (see Table 1), Water Oxidation (WO) to dioxygen is fundamental to obtain the electrons for the reduction of protons, carbon dioxide, and/or nitrogen. It is particularly challenging because it involves the removal of four electrons and four protons from two water molecules and the formation of an O-O bond (1.23 V vs NHE at *pH* = 0, ΔG°= 113.5 kcal·mol^{-1}). These steps translate into added kinetic complexity, that is, extra potential (overpotential, η) needed to perform the reaction. Therefore, the discovery of Water Oxidation Catalysts (WOC) at low η ($\Delta G^{\ddagger}_{cat}<\Delta G^{\ddagger}$, Scheme 2) that are fast, selective, active, and stable is a key challenge for the development of photosynthetic devices.

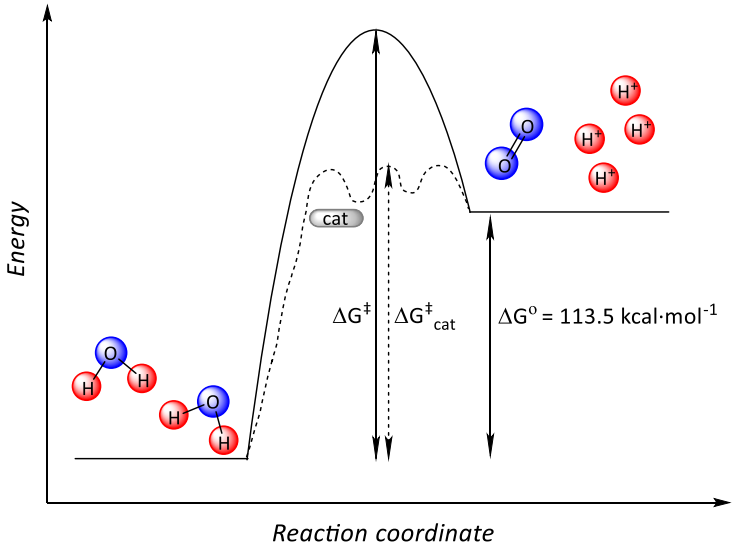

Scheme 2. Schematic illustration of the thermodynamic and kinetic barriers for water oxidation catalysis (solid line). The kinetic barrier is lowered by the water oxidation catalyst (cat, dashed line).

I

Already in 1789, J.R Deiman and A. P. van Troostwijk evolved hydrogen and oxygen by putting gold electrodes in water and discharging them with an electrostatic machine.[75] From then onwards, the field of heterogeneous water oxidation started the search for a suitable electrocatalyst. The first example was back in 1902 when Glazer and Coehn reported a nickel oxide electrode that evolved O_2.[76] More than a century later, huge accomplishments have been achieved towards factual technologies.[77] However, there is still room for improvement so that commercial electrolyzers can compete with fossil fuels in terms of stability and activity. An extensive list of reported heterogeneous electrocatalysts for water oxidation has been reported in the form of volcano plots, which follow the Sabatier principle (Figure 10): ideally, reaction intermediate(s) should bind to the active site(s) of the catalyst neither too strongly nor too weakly ($\Delta G_O < \Delta G_{OH}$). In addition, electrocatalysts should be highly active at the lower overpotentials possible. Among the state-of-the-art of bulk electrocatalysts for WO, we mostly find metal oxides in various surface structures (rutile, perovskite, spinel, rock salt, and bixbyite oxides). By far, the most employed and studied heterogeneous WOC is IrO_2.[78] Despite RuO_2 is more active, it is also more unstable.[17] Yet IrO_2 does not show better stabilities under WO conditions and is an even more scarce element than platinum.[77] The rest of the metal oxides mostly show too high overpotentials 0.35 V < η < 0.5 V (vs. NHE, pH = 0) and mostly restricted to extreme pH[17,77,78] which limits their use in realistic scenarios.

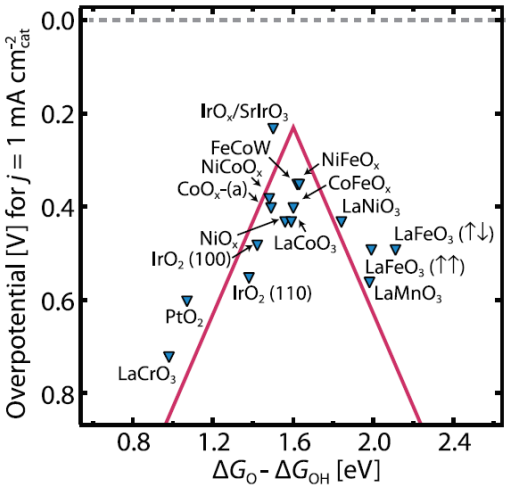

Figure 10. Main reported heterogeneous water oxidation catalysts in the shape of a volcano plot. Adapted from.[17]

Despite their interest over a century of research, further improvement is necessary for scaling-up:[77] (i) reduce the high amounts of scarce noble metals (or toxic ones) by

increasing the number of active sites per gram, (ii) improve the intrinsic activity of each active site, (iii) increase their stability and use in neutral pH.

Another line of research began in 1982 with the discovery of the first molecular catalyst for water oxidation (mol-WOC). T.J. Meyer and co-workers[79] reported the complex *cis,cis*-$[(bpy)_2(H_2O)Ru^{III}(\mu\text{-}O)Ru(H_2O)(bpy)_2]^{4+}$ or blue dimer (bpy is 2,2'-bipyridine), which is a dinuclear Ru-based coordination complex (**1** in Figure 11). Advantageously, its catalytic cycle was fully characterized by a wide range of spectroscopic, electrochemical and analytical techniques. From this first milestone, the field grew exponentially with reported mol-WOC based on metal complexes containing Ru, Cu, Fe, Ir, Mn, and Co. Ru-based complexes are by far the most studied due to their high activity and stability in harsh water oxidation conditions. One of the key features of Ru is its electronic configuration ([Kr] $4d^7\ 5s^1$) which allows several oxidation states from (-II) to (VIII). In particular, oxidation states (II), (III), and (IV) are the most common in six-coordination complexes (O_h geometry), mostly surrounded by polypyridyl ligands, relevant to WO catalysis. Parallel research is focused on first-row transition metals, which are earth-abundant elements that would lower costs. Disadvantageously, they suffer from ligand lability at neutral pH leading to decomposition. Nevertheless, Cu-based complexes have demonstrated good performances and stabilities due to ligand stability. All in all, homogeneous catalysts have the advantage that their O-O mechanism can be well-studied by means of spectroscopic, electrochemical, and analytical techniques. This is key to tune the active centers for better performance, both in homogenous and/or anchored on surfaces. Herein we will focus on the two families of molecular WOCs (mol-WOCs) that have given the best results in the field of homogeneous water oxidation: Ru- and Cu-based complexes. The parameters used for comparison and benchmarking WOCs are:

- Faradaic Efficiency (FE, %): efficiency of charge transfer towards oxygen formation, which is given in percentage (Equation 13).

$$\text{FE}\ (\%) = \frac{\text{Final mols O}_2}{\text{Total mols } e^-/_4} \cdot 100 \qquad \text{(Equation 13)}$$

- Turnover Number (TON): number of chemical conversions per active site of the catalyst before it deactivates (Equation 14). It is a dimensionless parameter that evaluates the robustness and stability of a molecular catalyst.

$$\mathrm{TON} = \frac{\text{mols } O_2}{\text{mols WOC}} \qquad \text{(Equation 14)}$$

- Turnover Frequency (TOF, s^{-1}): activity rate defined by the number of catalytic cycles per catalytic center per unit of time (Equation 15). This parameter evaluates how fast a catalyst is, and normally is presented as the TON divided by time (s^{-1}).

$$\mathrm{TOF} = \frac{\mathrm{TON}}{\Delta t} \qquad \text{(Equation 15)}$$

- Electrochemical overpotential (η, V): extra potential required to overcome the kinetic barrier imposed by the reaction. Mathematically is defined as the difference between the thermodynamic potential in standard conditions (E°) and the actual potential needed to perform the reaction (E).

$$\eta = E - E^{\circ} \qquad \text{(Equation 16)}$$

1.4.1 Ru-based mol-WOC

The first studies of Ru-based WOCs were focused on obtaining derivatives of the blue dimer as the earliest benchmark in the field (**1** in Figure 11). At that time, it was believed that dinuclear Ru complexes were the only ones able to accumulate four oxidative equivalents, needed for the reaction. However, there have been several turning points throughout the short timeline of mol-WOC as summarized in Figure 11. In this initial context, Llobet and co-workers[80] prepared the complex *in*,*in*-{[Ru^{II}(trpy)(H_2O)]$_2$(μ-bpp)}$^{3+}$ (**2** in Figure 11, bpp^- is 3,5-bis[2-pyridyl]pyrazolate). The insertion of a bpp^- bridge increased rigidity and electronic communication, favoring the coupling between Ru centers. Thus, better efficiencies (70% with respect to the sacrificial oxidant, Ce^{IV}) and TOF 0.014 s^{-1} were achieved although having a moderate catalytic performance. Interestingly, the next pint point in the field occurred in 2005 when Thummel et al.[81] reported the first mononuclear Ru-based complex capable of transferring four electrons/protons process for WO. Complex **3** is [Ru^{II}(npm)(pic)$_2$(OH_2)]$^{2+}$ where npm is 4-t-butyl-2,6-di (1',8'-naphthyrid-2'-yl)pyridine and pic is 4-picoline. Shortly thereafter,

Meyer and co-workers[82] presented another mononuclear catalyst which provided significant input on mechanistic studies, revealing how O-O binding occurs in different Ru-species (see section *1.4.3 Water oxidation mechanisms in mol-WOC* below). The discovery of single-site Ru-complex did not exceed in efficiency to the dinuclear ones, yet it offered the possibility of easier ligand tuning and synthesis as well as new mechanistic ways for the oxidation of water.

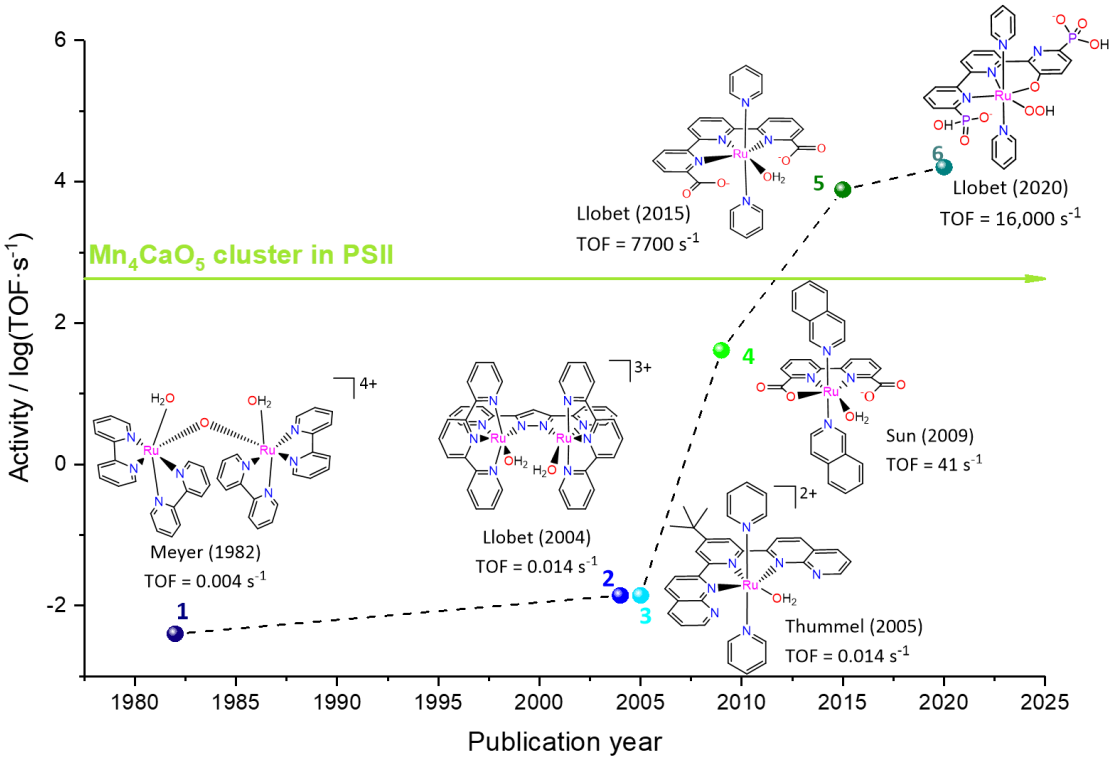

*Figure 11. Timeline of the benchmarking Ru-based complexes over 40 years of homogeneous water oxidation catalysis research. TOF values for complexes were determined at pH 1.0 using Ce^{IV} as a sacrificial oxidant, except in the case of **5** and **6**, for which TOF was determined electrochemically at pH 7.0.*

A step forward in increasing overall efficiency was made in 2009 when Sun *et al.*[83] introduced two carboxylate ligands to a mononuclear Ru complex (**4** in Figure 11). The introduction of electron-donating negatively charged ligands to the first coordination sphere stabilizes the high oxidation states of the metal center. Subsequently, this complex established a new efficiency benchmark with reported TOF values of 41 s^{-1}. This discovery was followed up by a series of Ru-bda complexes (bda^{2-} is [2,2'-bipyridine]-6,6'-dicarboxylic) achieving TOF up to 380-1000s^{-1} by tuning the second coordination sphere.[84] In that case, axial ligands enhanced supramolecular π–π interactions or hydrogen bonding, which influenced the kinetics and the mechanism of the reaction.[85] Besides, Ru-bda complexes represented a breakthrough in terms of overpotential with

η = 300 mV at pH 7.[86] These advancements surpassed the threshold set by Mn_4CaO_5 cluster (with TOF_{MAX} around 400 s^{-1}). This overtaking became evident with the irruption of a new Ru mononuclear complex based on the tda^{2-} ligand (tda^{2-} is [2,2':6',2"-terpyridine]-6,6"-dicarboxylate), from the groups Llobet, Sala and co-workers.[87] By far, $[Ru^{II}(tda\text{-}\kappa\text{-}N^3)(py)_2(OH_2)]$ (**5** in Figure 11) represented the best-reported mol-WOC with TOF values of 7,700 s^{-1} at pH 7.0 and with η = 600 mV. Briefly, the high activity is due to the Ru seven coordination environment stabilized by anionic terpyridine and the presence of a dangling carboxylate group which acts as a base (proton acceptor) during the critical O-O bond formation step (*vide infra*). In this case, the axial ligands are not playing a central role in catalysis and thus, their tuning has been used to successfully attach the complex to substrates to generate anodes and photoanodes for commercial applications.[88] At the time of writing, the best mol-WOC in terms of TOFs has been recently reported by Llobet and co-workers.[89] Inspired by tda^{2-}, the new complex contains an equatorial ligand with two phosphonate groups (tPa^{4-} or [2,2':6',2''-terpyridine]-6,6''-diphosphonate), which give high electron density to the metal center and high versatility towards PCET. These dangling phosphonates are responsible for the low energy towards the formation of the active catalyst or $[Ru^{III}(OOH)(tPa\text{-}\kappa\text{-}N^2O)(py)_2]^{2-}$ (**6** in Figure 11). Also, they act as pendant bases enhancing the intramolecular proton transfer and O-O bond formation. This renders **6** with TOF_{max} of 16,000 s^{-1} and with an overpotential of 530 mV at pH 7.[89] Overall, the key features associated with bda^{2-}, tda^{2-} and tPa^{4-} are their flexibility, adaptability, multidenticity, and equatorial coordination, thus they are referred to as FAME ligands.[90] As seen, the TOF reported over the past years have increased exponentially and surpassed the OEC in natural photosynthesis with thoroughly reported mol-WOC fully characterized by means of spectroscopic, electrochemical techniques, X-ray diffraction analysis, and DFT calculations. This is an excellent base in which to build molecular (photo)anodes for real devices.

1.4.2 Copper complexes mol-WOC

The exponential increase in terms of TOFs and overpotential made by Ru-based mol-WOC motivated the study of first-row transition metal complexes for WO. Complexes based on Fe, Cu, Co, and Mn attracted much attention as they are earth-abundant metals and less toxic for the environment. This young field has experienced fast

development, yet a lot of work must be done to avoid several issues concerning first-row transition metals, such as: (i) the difficult access to high oxidation states without catalyst deactivation; (ii) the lack of mechanistic information; (iii) normalization of TON and TOF across the literature; (iv) stability issues due to ligand lability or oxidation at neutral pH. In this regard, we should emphasize the critical review of some of the published complexes based on Fe, Co, and Mn, which are metal oxides instead of the reported molecular complexes.[91–95] In this thesis we will focus on Cu complexes, which are present in natural biological systems for O_2 activation[96] and have more examples compared to Ni or Fe. Prior to that, the reader should bear in mind that Cu(IV) complexes are unstable and that Cu(III) might sometimes not have enough potential to oxidize water.

The first homogeneous copper WOC was $[(bpy)Cu(\mu\text{-}OH)]_2^{2+}$, reported by Mayer *et al.*[97] in 2012 achieving a first TOF mark of 100 s^{-1} at pH 12.5 and 750 mV overpotential (**I** in Figure 12). In terms of overpotential is far from the Ru-based complexes with η = 300 mV as its best (Ru-bda, **4** in Figure 11). Yet, it was just the first step in the development of Cu complexes for WO with TOF of 100 s^{-1} and recent in time. Thereafter, Meyer and co-workers[98] developed a Cu complex with a triglycylglycine macrocyclic ligand (H_4TGG) lowering the overpotential mark to 520 mV at pH 11 (**II** in Figure 12). Besides, it is important to highlight that this WOC displayed 5 h of stability with 99% Faradaic efficiencies despite a moderate TOF of 33 s^{-1}. Though being a striking success, the lack of studies on the mechanism makes it still uncertain. In 2014 Lin *et al.*[99] developed a biomimetic Cu-WOC (**III** in Figure 12) introducing redox-active ligands or "non-innocent" ligands, which were involved in the charge accumulation within the complex. In this manner, Cu(IV) complexes difficult to stabilize were avoided. Subsequently, Llobet and co-workers[100] prepared a new family of Cu complexes containing tetradentate amidate ligands (**IV** in Figure 12). The scaffold surrounding the metal center acts as a non-innocent ligand by being redox-active in the mechanism of water oxidation and stabilizes high oxidation states of the Cu. Besides, π-delocalization of the ligand enhances the stability on a pH range from neutral to basic. In this manner, a striking overpotential of just 170 mV was achieved by inserting pyridine and pyrene substituents in the ligand (**V** in Figure 12).[101] Moreover, these substituents can serve as an anchor point on graphitic

surfaces, which has proven no decomposition to CuO and high activities.[101] Recently, a breakthrough was established by a Cu complex featuring a tetraamidate macrocyclic ligand, labeled as Cu-MAC (**VI** in Figure 12). The "macrocyclic effect" of the surrounding ligand acts through metal-ligand cooperativity by accommodating the different oxidative charges to promote water oxidation. This translates to high activities (140 s^{-1}) and low overpotential (200 mV) at neutral pH. Therefore, the latter examples are suitable candidates for (photo)anode preparation.

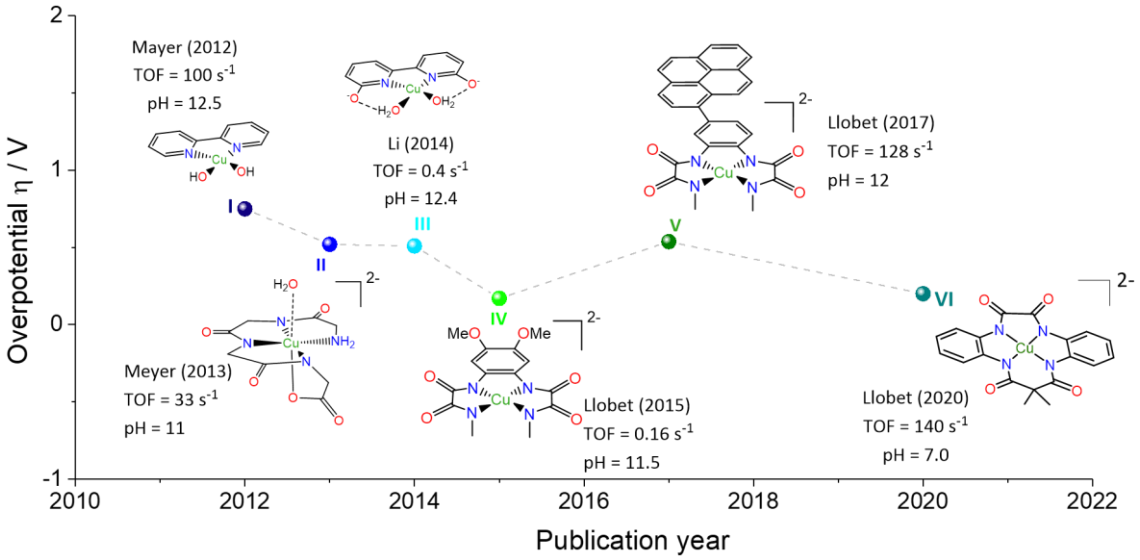

Figure 12. Diagram depicting the recent field of copper mol-WOC comparing published complexes by their overpotential.

1.4.3. Water oxidation mechanisms in mol-WOC

The field of homogeneous molecular catalysts awakens special attention because of the availability of a wide range of spectroscopic, electrochemical, and computational techniques to study the different mechanisms and intermediates involved in the reaction. With this information, rational design and synthetic versatility of molecular chemistry can lead to highly active, selective, and stable WOCs. A brief description of the mechanistic information known up to date will be given below to explain the sparking interests of molecular catalysts.

In 1970, before the discovery of the blue dimer, the group of Prof. Thomas J. Meyer postulated the theory of Proton-Coupled Electron- Transfer (PCET)[102] after observing the interesting redox behavior of a water molecule when bonded to a metal center in transition metal complexes. PCET is a reaction mechanism in which a proton and an

electron are exchanged in a concerted manner. As seen in Scheme 3 the loss of an electron is linked to the loss of a proton thanks to the acidity of the coordinated aqua ligand.[102] This mechanism allows the total charge of a complex to remain constant while increasing the oxidation state of the metal center and thus, avoiding the accumulation of charge and generation of high-energy intermediates. Due to this stabilization, the potential to obtain highly oxidized species is decreased. Actually, this process is indispensable for many natural enzymes and electrochemical systems.[103,104]

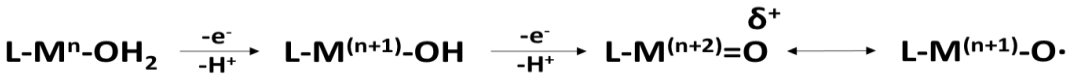

Scheme 3. Proton-Coupled Electron-Transfer (PCET) for a transition metal complex with an aquo group (M-OH_2). L stands for ligands completing the metal coordination sphere.

Besides, the potential $E_{1/2}$ of molecular complexes dependence versus the pH follows the Nernst equation (Equation 17). Therefore, for each electron/proton transfer the potential diminishes 59 mV per pH unit.[105] This *E vs.* pH dependence is represented in Pourbaix diagrams.

$$E = E° + \frac{RT}{nF} ln \frac{(ox)}{(red)} = E° + 2.3026 \frac{RT}{nF} log_{10} \frac{(ox)}{(red)} = E° - 0.059\, pH \qquad \text{(Equation 17)}$$

The elucidation of O-O bond formation and thus, water oxidation mechanism, came along with the discovery of the reviewed molecular catalysts. Two general mechanisms have been proposed: Water Nucleophilic Attack (WNA) and Inter/Intramolecular coupling of two M-O units (I2M).[21,76,90] Scheme 4 displays a graphical representation of both pathways.

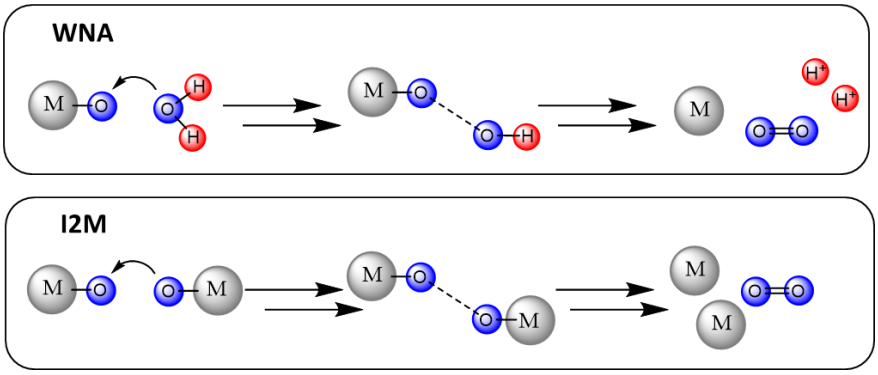

Scheme 4. Conceptual illustrations depicting pathways for O-O formation in molecular water oxidation catalysts: Water Nucleophilic Attack (WNA) and Inter/Intramolecular coupling (I2M).

WNA mechanism is the nucleophile attack of a water molecule to the electrophilic M-O species. Subsequently, M-O-OH forms, which after further oxidation releases molecular

oxygen. Mononuclear complexes are the most representative examples of WNA, such as the abovementioned Ru-tda, Ru-tPa, or Cu-MAC (**5** and **6** in Figure 11, and **VI** in Figure 12).[89,106] In some cases, redox-active ligands or "non-innocent" ligands[100] can get reversibly oxidized to assist the metal center and avoid detrimental high oxidation states, e.g. in Cu complexes avoiding unstable Cu(IV) states (**IV**, **V** and **VI** in Figure 12). On the other hand, the I2M is a mechanism in which two intra/inter M-O centers are involved in the O-O formation. Most of the reported dinuclear complexes follow a 1st order kinetics I2M mechanism, studied by oxygen labeling experiments and theoretical calculations (**1** and **2** in Figure 11).[90] Besides, mononuclear complexes such as Ru-bda (**4** in Figure 11) follow a 2nd order kinetics I2M (k_{obs} depends on catalyst concentration).[84] The O-O formation is usually the rate-determining step and thus, molecular catalysts allow the rational design of the active centers to enhance it and reduce the activation energy. For example, seven coordination of ligands to the metal center, pendant bases in the 1st or 2nd coordination sphere to favor PCET are among the studied options to enhance O-O formation.[76] Therefore, it is non-trivial the mechanistic, electronic, and structural studies due to their influence in the mol-WOC, which will have a direct effect on its performance when anchored on solid supports for device fabrication.[88]

1.5 Envisioned technologies for energy production

The current challenge in the water oxidation field is to build photo(electro)chemical cells for solar fuel generation that would supply constant power for transport, industry, and/or households (Scheme 1). There are several strategies to fulfill this target as illustrated in Figure 13. This section will cover the economic and technical feasibility of each prototype together with the avant-garde reported systems. To be cost-competitive with fossil fuels, the target set by the US Department Of Energy (DOE) is to produce hydrogen at 2-4 USD·kg^{-1} with moderate Solar-To-Hydrogen conversion efficiencies (STH) and moderate lifetimes. For clarity, STH is defined as:

$$\text{STH}\ (\%) = \frac{\text{output energy as } H_2}{\text{energy of incident solar light}} = \frac{(\text{mol } H_2 \cdot s^{-1})\ \text{x}\ (237000\ \text{J} \cdot \text{mol}^{-1})}{(100\ \text{mW} \cdot \text{cm}^{-2})\ \text{x area}\ (\text{cm}^2)}\ \text{x}\ 100 \quad \text{(Equation 18)}$$

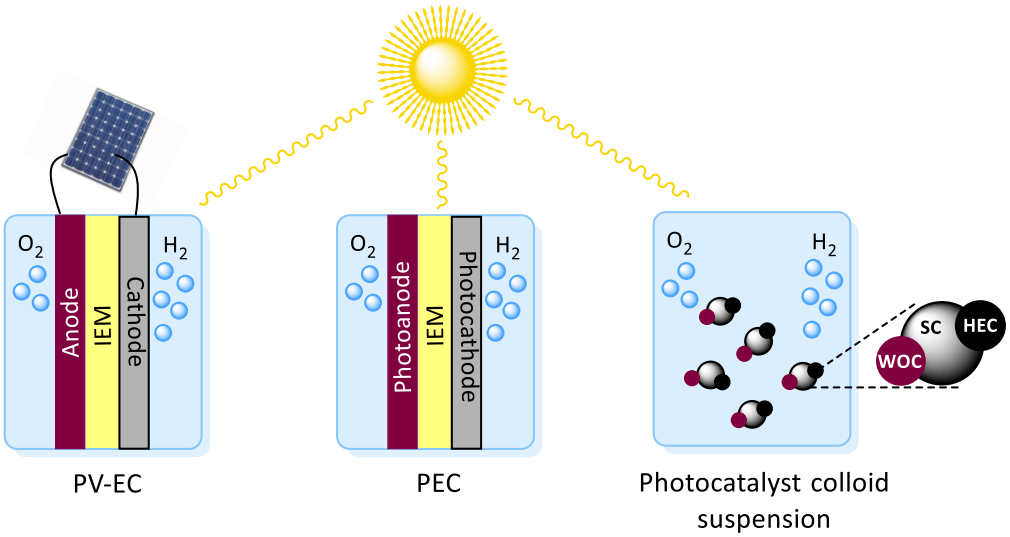

Figure 13. Technologies for water splitting: left, Photovoltaic Cell (PV) coupled with an Electrochemical Cell (EC); center, Photoelectrochemical Cell (PEC); right, photocatalysts colloid suspension. All these can be coupled to (photo)electrocathodes or catalysts for N_2 or CO_2 reduction instead of H^+ reduction. IEM is Ion-Exchange Membrane; WOC is Water Oxidation Catalyst; HEC is Hydrogen Evolution Catalyst; SC is Semiconductor.

Figure 13 illustrates the design of three different prototypes for hydrogen production plants, yet the generation of other solar fuels can be projected. In that case, (photo)anodes for water oxidation can be coupled to (photo)cathodes for the reduction of N_2 or CO_2. Due to their ubiquitous presence in all systems, (photo)anodes for water oxidation are paramount to develop such technologies and are the focus of the present thesis. As seen in previous sections, molecular catalysts have achieved TOFs higher than the Oxygen-Evolving Complex in Photosystem II (Figure 11). Despite their synthetic versatility, molecular (photo)anodes are at their beginning compared to those based on other materials. Typical devices are composed of metal oxides with a planar 2-D surface. Despite the numerous investigations, no feasible (photo)anode has been achieved, especially at neutral pH.[77] Moreover, the field has diverged from the classical 2-D approach of high-loading of precious metals towards the fine-tuning of nanoparticles.[107] Current research focuses on changes in size and morphology, in single-atom-sites on specific supports, and in ligand effect, all in all, trying to mimic the lock-key model of natural enzymes. Therefore, both heterogeneous and homogeneous catalysis are conveying, and in fact, they are two sides of the same coin. To that end, "heterogenization"[108,109] of molecular catalysts on (semi)conductive supports is on the emerge and the following sections will be dedicated to molecular (photo)anodes.

1.5.1 PV-EC

The first model is the integration of mature technologies consisting of a Photovoltaic cell (PV) and an electrolyzer or Electrochemical Cell (EC). The latter is composed of an anode and a cathode immersed in the electrolyte solution and separated by an ion-exchange membrane. Separation of the products is necessary for efficient performance and the anionic or cationic nature of the membrane will depend on the optimal working pH of the catalyst. The advantage of this design is that both light absorption and catalysis are separated, with available commercial materials for both PV and EC. Nonetheless, separated processes are detrimental to the overall efficiency and material costs. As a set-point, only PV-EC systems with Solar-to-Hydrogen (STH) efficiencies close to the theoretical limit (> 25%) are considered to be competitive for commercial applications.[110–112] The reason to set such a high STH is to balance the high costs of manufacturing precious metal materials for both PV and EC. In line with this requirement, oxide electroanodes[17,78] need to have current densities in the range of 0.2-1.0 A·cm^{-2} to operate in commercial electrolyzers.[113,114] Currently, stability issues, high overpotential or extreme pH oxidations are still prevailing and need to be surpassed for scaling-up these systems. The emerging field of molecular anodes still presents moderate current densities for practical applications, although they show promising characteristics such as high activities (TOF > 50,000 s^{-1}) and low overpotentials (η < 400 mV). Furthermore, high intrinsic activities are in accordance with the atom (circular) economy,[107] i.e. molecular anodes do not need high loadings of precious metals compared to anodes based on metal oxides, where just 0.1-1% of material is active.[115] Additionally, most metal oxides are efficient at extreme pH ranges, hazardous for other components or structures.[77]

1.5.1.1 Strategies for anchoring molecular catalysts on solid surfaces

The first step towards a molecular anode is to anchor the homogeneous mol-WOC on a substrate. Figure 14 illustrates the different strategies employed for heterogenization on (semi)conducting supports. Both substrates have analogous anchoring strategies, thus we can also apply them for Photoelectrochemical Cells (PEC, in the next section). Also, all the covalent strategies can be applied to anchor dye molecular complexes on semiconductors as will be explained in section *1.5.2 PEC*.

The anchoring strategies followed by the research community are based on covalent (top of Figure 14) or non-covalent interactions (bottom left of Figure 14) depending on the surface chemistry of the support material (bottom right of Figure 14). Certain properties of the substrate need to be controlled such as conductivity, morphology, and stability against oxidation conditions.[116] Besides, a suitable anchoring group requires robust attachment to the surface, the transmission of injected electrons, survival at working oxidizing conditions, stability through a wide range of pHs, and survival of prolonged solar irradiation in the case of PEC.[116] In addition, the linker should not be strongly electronically coupled to avoid recombination because the catalyst needs to accumulate oxidative charges.[117] On the other hand, molecular catalysts should incorporate specific functional groups on the ligand sphere for anchoring. Covalent strategies can lead to more stable anchoring but can also involve slightly harsher synthetic conditions than non-covalent ones. These modifications should not affect the mol-WOC behavior, which should be at least equally active and robust than the reported homogeneous homologue.

Most of the molecular anodes reported in the literature are based on covalent bonds to carbon or metal oxide surfaces (top of Figure 14).[109,116–119] To guarantee electron/hole communication between the catalyst and the substrate, the nature of the covalent anchor can have electronic communication by generating a dipole, breaking orbital overlap, releasing protons, or blocking the surface from the solvent.[120]

I

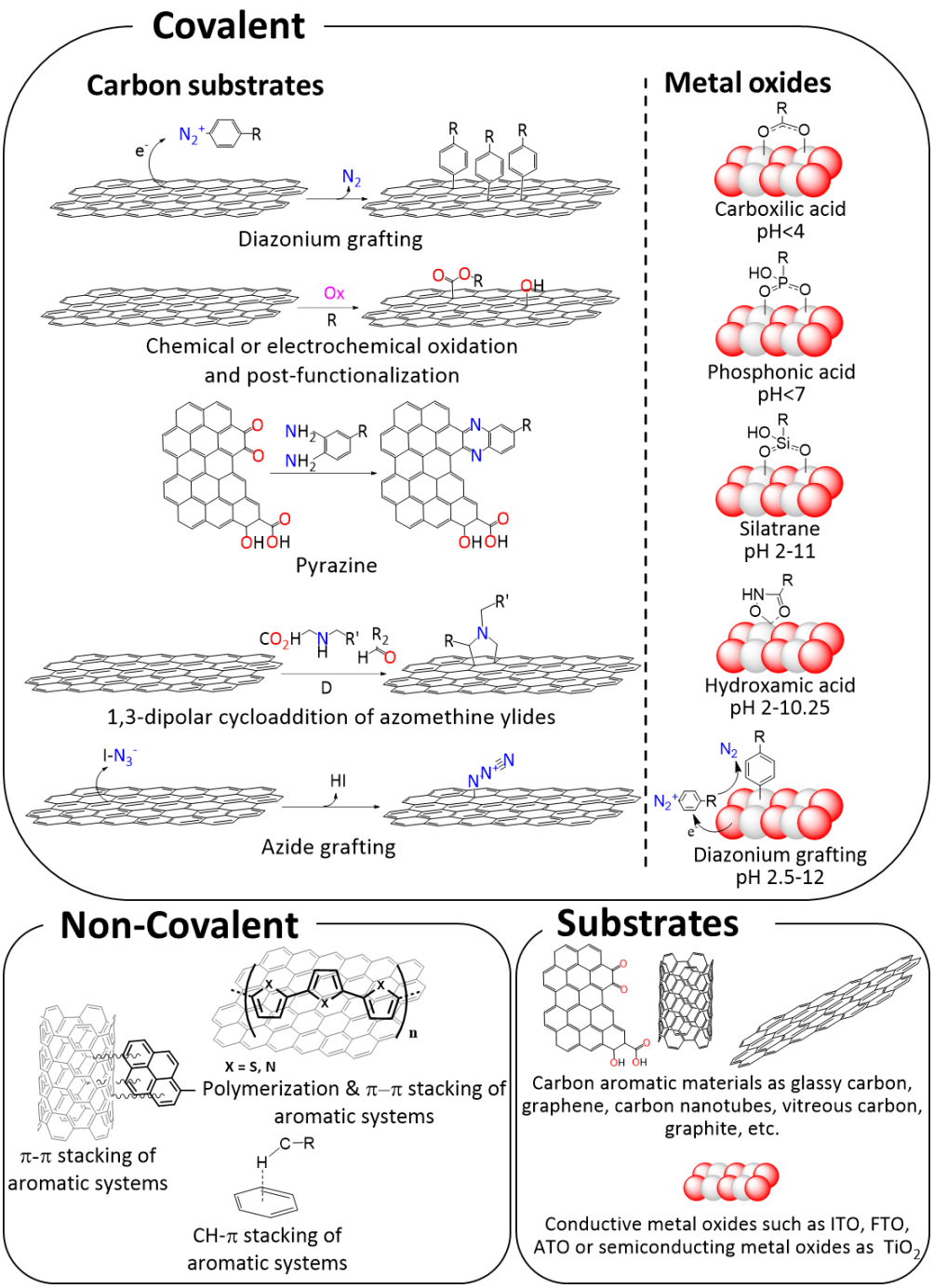

Figure 14. Strategies to anchor molecular catalysts on (semi)conducting supports.

Graphitic materials are cheap and have good electronic conductivity, and they are already used in electrochemistry and optoelectronic devices. Carbon-based materials range from flat glassy carbon to nanostructured carbon materials such as widely used multi-wall carbon nanotubes (bottom right in Figure 14). Normally, they present high surface area, electrical conductivity, high thermal and chemical stability. Covalent bonds on graphitic surfaces can be achieved in several ways:

i. Diazonium grafting by electroreduction of diazonium salts, forming a C-C bond which is highly stable in aqueous solution at a wide potential window.[88]
ii. Redox modification of the substrate, such as in reduced Graphene Oxide (rGO). Consecutive redox processes generate defects on graphene layers that are suitable for post-functionalization with the carboxylates, phosphonates, or other functional groups at the molecular catalysts.[121]
iii. Pyrazine formation by condensation of ortho-phenylenediamines on ortho-quinone moieties on graphite edge planes.[122] The result is Graphite Conjugated Catalysts (GCCs), mainly reported for oxygen and CO_2 reduction but promising candidates for water oxidation. The advantage of this strategy is the coupling between the appended molecule and the surface of the electrode.
iv. 1,3-dipolar cycloaddition of azomethine ylides or Prato's reaction, which introduces two different chemical functions (R and R') onto the surface of graphitic materials such as carbon nanotubes.[123,124]
v. Azide grafting that can subsequently react with alkyne derivatives linked to molecular catalyst via "click" chemistry methodology.[125,126]

All these covalent strategies can also be applied on Transparent Conductive Oxides (TCO) such as Fluorine doped Tin Oxide (FTO), Indium doped Tin Oxide (ITO), or other oxides in the form of nanoparticles (e.g. TiO_2 or In_2O_3).[127] Generally, molecular catalysts with specific functional groups (carboxylates, phosphonates, hydroxamate, or siloxanes) can bind to the surface atomic oxygen in a mono-, bi-, tri-dentate fashion.[128,129] However, when employing these anchoring groups one should be aware of their hydrolysis at certain pHs, as indicated in Figure 14.[117]

Another simple but successful way of anchoring is through supramolecular structures based on non-covalent π-π stacking (bottom left of Figure 14). The functionalization of the mol-WOC with a pyrene derivative group can enhance the attachment to the π-system of any nanostructured graphite material. In comparison with covalent bonding, it requires easier synthetic modifications, and it shows high stability in aqueous electrolytes due to the hydrophobic effect. This route was the one used to anchor the best mol-WOCs such as Ru-bda, Ru-tda, or Cu-based complexes, resulting in the improvement of their activities and stabilities.[88,101,130] Analogously, CH-π interactions

I

work similarly, with the C-H groups of the ligands contacting with the substrate's π-system. In fact, the best molecular anode in terms of activity and stability at pH 7 is based on CH-π interactions.[131] Reported by Llobet *et al.* in 2020, it consists of an oligomeric Ru-tda complex anchored on multiwall carbon nanotubes that sustains current densities of 32 $mA \cdot cm^{-2}$ for 12 hours. Hence, its oligomeric nature is also disruptive. Polymers based on molecular catalysts as monomers can be used to increment the number of active sites and stability of molecular anodes like metal oxides. Another way of polymer formation and non-covalent interaction is the polymerization of molecular catalysts on top of graphitic surfaces (Figure 15). Three different types of polymerization can be found in the literature, depending on the functionalization group in the backbone of the molecular catalysts: thiophene, pyrrole, and vinyl-pyridyl. The latter consists of the formation of a polyvinyl pyridine film at the surface of the electrode by UV-light.[132] On the other hand, the first two are known anodic electropolymerizations of R-substituted pyrroles[133,134] or R-substituted thiophenes.[135] Thiophene-based polymers have a wide range of applications in the field of organic electronic devices, such as transistors, light-emitting diodes, solar cells, sensors, and capacitors.[136] Specifically in our case, they are of particular interest because of their good conductivity and high resistance to oxidation,[137] and of further interest because of the semiconductive nature of some polythiophenes.[138]

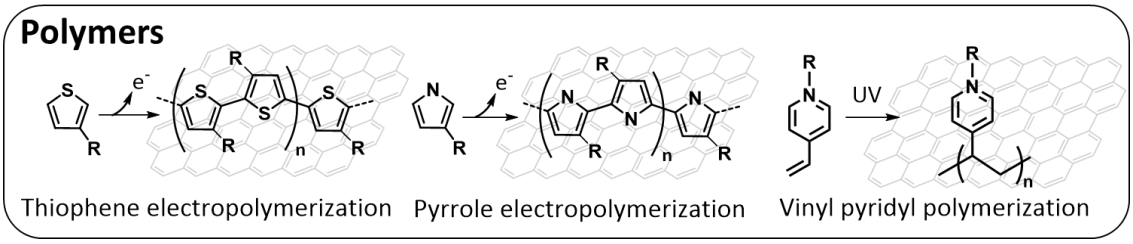

Figure 15. Chemical and electropolymerization of functional groups R containing the molecular complexes.

1.5.1.2 Molecular anodes

So far, we have reviewed all the different strategies employed to anchor mol-WOC on conductive surfaces to build EC for water oxidation. Table 2 below is a summary of the state-of-the-art in molecular electroanodes. An overview of the table shows the variety of anchoring methods and substrates used. Interestingly, non-covalent techniques are the majority (entries 1- 4, 6 and 8) from which entries 3, 4 and 8 are polymers formed by anodic polymerization of the mol-WOC. Besides, some of the literature focuses on covalent techniques (entries 5 and 7) despite giving rise to low activities and low

stability, on the contrary of what was sought. For example, the reported Ru-bda complex covalently anchored on glassy carbon substrates showed modest catalytic activities because of the constraints imposed on I2M encounters, highlighting the importance of mechanistic understanding for device design. In the end, this hindrance results in its decomposition to RuO_2.[139] Moreover, other published Ru-bda covalent bonds, such as phosphonates, have been proven to be hydrolyzed at pH < 7 (entries 5 and 7).[140] Entry 2 consists of a Ru-tda functionalized with pyrene units in the axial positions. It represents the first molecular anode to achieve a million turnover numbers over a period of 12 h with moderate current densities of 10.5 $mA \cdot cm^{-2}$ at 1.4 V vs RHE. This benchmark has recently been pushed to higher activities by its oligomeric version (entry 1). As previously mentioned, Llobet and co-workers[131] synthesized a 15-unit Ru-tda connected by bipyridines and anchored through CH-π interactions on multi-wall carbon nanotubes. As a result, current densities of 240 $mA \cdot cm^{-2}$ and TONs of 200,000 over 12 h were achieved. This is the best molecular anode reported up to date, establishing a precedent to future and applicative devices. In parallel, the same group in collaboration with F. Würthner published a cyclic trimer of the Ru-bda complex achieving excellent performances (entry 6).[141] This work represents the first time that the electrochemical transformation of Ru-bda generates a more active species that follow a WNA mechanism. Subsequently, striking activities of 3,200 s^{-1} and TONs of 1.8 million over 6 hours are reported. Overall, all these impressive results are elevating the role of molecular anodes in the quest for efficient and highly active electrolyzers.

Entry[ref, a]	Catalyst or Catalyst precursor[b]	Anchoring group[c]	Electrode[d]	pH	Γ / nmol·cm^{-2}	J (mA·cm^{-2}) @ E_{cat} (V)[e]	J / mA·nmol^{-1},[f]	E vs RHE	TOFs[j] / s^{-1}	TONsx10^{-3}
1[131]	{[Ru(tda)(4,4'-bpy)]$_{15}$(4,4'-bpy)}	π-CH	CNT@GC	7.0	16.0	240 (1.40)	16.5	1.86	8.1x10^3	200 (12h)
2[142]	[Ru(tda)(OH)(pypA)$_2$]	Pyrene	CNT@GC	7.0	0.55	10.5 (1.40)	19.1	1.86	8.9x10^3	1000 (12h)
3[135]	poly-[Ru(bda)(F-Isoq)(pyrS)]	Poly-S	BPG	7.2	0.96	2.0 (1.20)	2.8[g]	1.65	3.98	5.2 (7h)
4[134]	poly-[Ru(bda)(py-pyr)$_2$]	Poly-P	BPG	7.2	0.42	2.8 (1.30)	6.6[g]	1.6	10.47	31.6 (1h)
5[143]	[Ru(bda)(4-(C_5H_{11})-py)$_2$]/[Ru(4,4'-(C_7H_{15})$_2$-bpy)(4,4'-(PO_3H_2)$_2$-bpy)$_2$]$^{2+}$	R-PO_3^{2-}	n-TiO_2/n-SnO_2/FTO	4.6	21.0	1.8 (1.40)[h]	0.1	1.3	5x10^{-5},[i]	0.53 (3h)[i]
6[141]	[($Ru(H_2O)_2$(bda-κ-NO)(bpb)]$_3$	π–π & CH–π	CNT@GC	7.0	8.4	168 (1.40)	20	1.86	3.2x10^3	1800 (6h)
7[144]	[Ru(Mebimpy)(4,4'-(($HO)_2$-$OPCH_2$)$_2$-bpy)(OH_2)]$^{2+}$	R-PO_3^{2-}	n-ITO/FTO	5.0	0.12	0.015 (1.85)	0.13	2.15	0.36	11 (8h)
8[133]	[Ru_2(μ-bpp)(μ-OAc)(t-trpy)$_2$]$^{2+}$	Poly-P	VCS	1.0	4.6	--	--	--	--	0.041

Table 2. [a]References [b]bpy, 2,2'-bipyridine; pypA, 4-(pyren-1-yl)-N-(pyridin-4-ylmethyl)butanamide; bpy-$CH_2PO_3H_2$, ([2,2'-bipyridine]-4,4'-diylbis(methylene))bis(phosphonic acid); bda, 2,2'-bipyridine–6,6'–dicarboxylate; F-Isoq, 6-fluroisoquinoline; pyrS, 4-(2-(thiophen-3-yl)ethyl)pyridine; py-pyr is 4-(pyren-1-yl)pyridine; py, pyridine; 4,4'-PO_3H_2-bpy, 4,4'-diphosphonate- 2,2'-bipyridine; bpb, 1,2-bis(pyridine-2-carboxamido)benzenate(2−); Mebimpy, 2,6-bis(1-methylbenzimidazol-2-yl)pyridine; bpp, 3,5-bis(2-pyridyl)pyrazolato; μ-OAc, acetato bridging ligand; t-tpy, 4'-(p-pyrrolylmethylphenyl)-2,2':6',2''-terpyridine. [c]Poly-P, polypyrrole; Poly-S, polythiophene; R-PO_3^{2+}, phosphonate covalent bond. [d]CNT, Multi Walled Carbon Nanotubes; GC, Glassy Carbon; BPG, Basal-plane Pyrolytic Graphite; n-TiO_2, nano-TiO_2; FTO, Fluorinated Tin Oxide; n-ITO, nano-Indium Tin Oxide; VCS, Vitreous Carbon Sponge. [e]Taken from the top of the electrocatalytic wave (E vs. NHE, pH 7). [f]Intrinsic activity. [g]Orientative only, because key data is not available or reliable. [h]Corrected value removing the intensity associated with [Ru(bpy)$_3$] moiety in Figure S6a. [i]TOFs and TONs based on photocatalytic experiments. [j]Measured using FOWA for entries 1-2 and 6, and other methodologies for the rest.

Despite the level of maturity achieved in the field of EC cells, the coupling with PV cells generates high costs and low efficiencies. Thus, a great body of research focuses on PEC, where both light-absorber and catalyst units are integrated into the same cell aiming for simplicity and lower costs.

1.5.2 PEC

Photoelectrochemical Cells have all the components incorporated to perform light-driven water splitting. Those constituents need good coordination to perform light absorption, charge separation, and catalysis. Several configurations for PEC water splitting systems[109,145] are common across the literature (Figure 16): (i) SC photoelectrode submerged in the electrolyte with a metal counter electrode; (ii) n-SC photoanode with a p-SC photocathode; (iii) p-n junction photoanode with a metal cathode; (iv) dye-sensitized metal oxide photoanode with a metal cathode. Models i-iii are mainly based on semiconductors with wide-bandgaps, and therefore with lower absorbance of the visible part of the solar spectrum. In the case of PEC, only systems with STH efficiencies between 10-15% are considered to be competitive for commercial applications.[110–112] If we assume that only UV light is absorbed (<400 nm) with 100% of quantum efficiency, then a maximum STH of 2% is possible. If we extend the absorption to the visible light (up to 700 nm or 1000 nm), then we could achieve the ideal STH of 25% and 47% respectively.[146] Therefore, it is essential to absorb the full range of visible light for commercial applications.

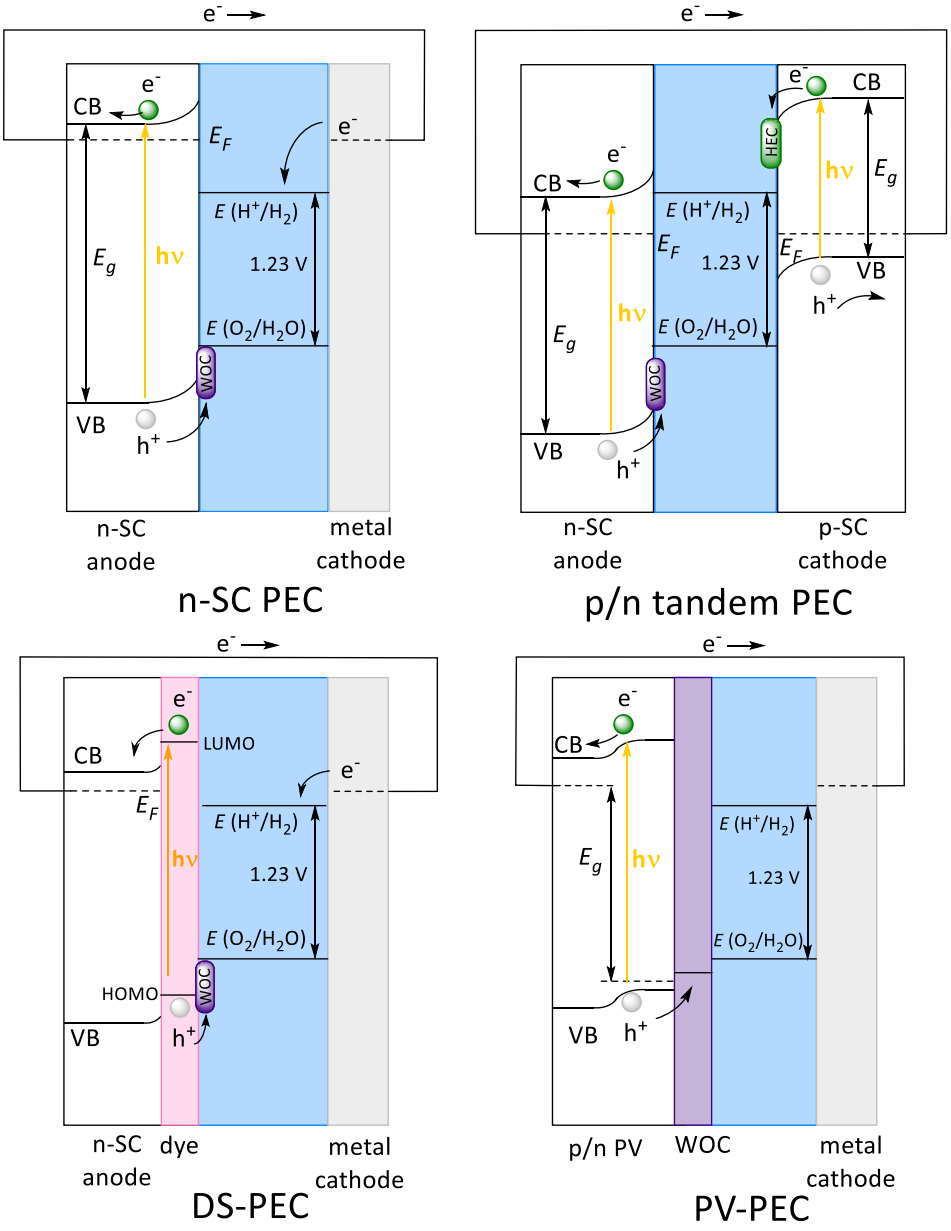

Figure 16. Different configurations of Photoelectrochemical Cells (PEC): n-SC PEC (top left) is the combination of a photoanode with a metal cathode; p/n tandem PEC (top right) consists of both photoanode and photocathode; DS-PEC (bottom left) is a Dye-Sensitized photoanode in a PEC; PV-PEC (bottom right) is the coupling between a p-n photovoltaic solar cell with an electroanode and a metal cathode. For clarity: WOC is Water Oxidation Catalyst, which refers to the active centers in photoanodes or independent co-catalysts; HEC is Hydrogen Evolution Catalyst; n-SC is n-type Semiconductor; p-SC is p-type Semiconductor.

One strategy towards this goal is dye sensitization of wide-bandgap SC (type iii). The concept of a Dye-Sensitized Solar Cell (DSSC) was proposed by Grätzel in 1991 as a new type of solar cell with Ru dyes on TiO_2.[147] The evolving concept of a Dye-Sensitized Photoelectrochemical Cell (DSPEC)[59] is just the anchoring of (molecular) catalysts on the dye-sensitized semiconductors to use the separated charges to perform catalytic

reactions in a highly efficient manner. The main components[62] of these devices are: catalysts for water oxidation, proton or CO_2 reduction, light-harvesters, semiconductors for electron-hole transportation, and a membrane. Bottom left of Figure 16 represents the scheme of the electron transfer in a DSPEC for water oxidation. Firstly, light excitation of the dye (D) generates its excited state (D*) which will transfer an electron to the conduction band of the semiconductor, being TiO_2 the most used.[64,148] Subsequently, the positively charged dye (D^+) is reduced by the electrons from the molecular catalyst for water oxidation. Then the electrons flow to the counter electrode consisting of a metal or molecular cathode.

The first DSPEC cell for water oxidation was reported in 1999 when Meyer *et al.* [149] integrated a Ru-Ru chromophore-catalyst dyad on TiO_2. This first two-compartment cell displayed no oxygen and low photocurrents, yet it was the first stone on the field. Right after ten years, in 2009, Mallouck and co-workers[38] reported the first functional device. Their DSPEC was composed of a Ru-based chromophore with an IrO_2 WOC with photocurrents of 30 μA. To overcome these low photocurrents, an electron-transfer mediator was introduced with the result of a three-fold enhanced performance. Subsequently, with the improvement of molecular dyes, catalysts, and anchoring strategies, several DSPECs have been published in the last decade (Table 3). To the date of writing, the best photoanode reported is entry 1, which consists of a phosphonate-derivatized $[Ru(bpy)_3]^{2+}$ chromophore and a pyridyl-derivatized $Ru(bda)(4,4'\text{-}bpy)_2$ on TiO_2. The reported photoanode showed impressive Incident Photo-to-Current Efficiency (IPCE) of 25%, yet the photocurrent reduced to the half after 1 h of performance. For the viability of this technology increasing the STH but especially extending the cell life are key.[150]

Entry[ref]	***Chromophore****	***Catalyst[$]***	***SC substrate***	***pH***	***IPCE / %***	***Maximum stable photocurrent density / mA·cm^{-2}***
1[52]	RuP^{2+}	$Ru(bda)(4,4'\text{-}bpy)_2$	TiO_2	5.8	25	1.7
2[151]	RuP^{2+}	$Ru(bda)(L_{C10})$	SnO_2/TiO_2 core-shell	7.0	24.8	1.4
3[152]	RuP^{2+}	$Ru(bda)(4\text{-}O(CH_2)_3P(O_3H_2)\text{-}pyr)_2]$	SnO_2/TiO_2 core-shell	4.7	17.1	0.85
4[153]	RuP^{2+}	$(Ru(bda)(4\text{-}vinylpy)_2)$	SnO_2/TiO_2 core-shell	7.0	3.1	0.4
5[154]	TA	$Ru(bda)(pyP)_2$	SnO_2/TiO_2 core-shell	4.8	0.3	0.4
6[155]	Zn porphyrin	IrCp*	$nanoTiO_2$	7.0	-	0.03
7[156]	RuP^{2+}	IrO_2	TiO_2	5.8	-	0.08
8[157]	RuP^{2+}	$Zr^{4+}\text{-}Ru(bda)(4\text{-}O(CH_2)_3P(O_3H_2)\text{-}pyr)_2]$	SnO_2/TiO_2 core-shell	5.7	-	1-1.5

*Table 3. Main photoanodes for water oxidation with DSPEC configuration reported in the literature.[52] * RuP^{2+} is $[Ru(bpy)_2(4,4'\text{-}PO_3H_2\text{-}bpy)]^{2+}$.[$] bda is 2,2'-bipyridine-6,6'-dicarboxylate; bpy is 2,2'-bipyridine; L_{c10} is an aliphatic chain of 10 C; pyr is pyridine; pyP is (3- (pyridin-4-yloxy)propyl)phosphonic acid; TA is triarylamine; IrCp* is $[(C_5(CH_3)_5IrCl_2)]_2$.*

1.5.3 Photocatalyst colloid suspensions

The third category of water splitting devices is suspended or colloidal photocatalysts.[112] They are the simplest in design but the less matured technology among all. However, hybrid colloidal photocatalysts enclosed in aqueous reactor beds are highly promising due to their simplicity in reactor design, economic viability, and scalability.[9] In fact, bed particle suspensions with STH values of 5-10% and lifetimes of 5 years could produce hydrogen at 1.6-3.5 USD·kg^{-1}, making them cost-competitive *vs.* fossil-based fuels.[158] On the other hand, panel array PEC systems are estimated to produce hydrogen at 4.0-10.4 USD·kg^{-1} if STH values are 10-15% and lifetimes of 10 years. The lower price of suspended systems versus array PEC is due to the lower capital costs of plant installation. Inspired by techno-economical reports, particulate semiconductor materials as photocatalysts have received a lot of attention.[146] These systems involve colloidal photocatalysts based on wide band-gap semiconductors on top of which specific metal oxide domains, such as iridium, ruthenium, nickel, or cobalt oxides, are deposited as co-catalysts.[146] As said, UV light absorption can allow a maximum of 2% STH. To pursue the absorption of visible-spectrum, several examples of oxides, (oxy)nitrides, (oxy)sulfides, (oxy)halides, and chalcopyrites have reached lower bandgaps. Despite the efforts, average STH values lay between 0.1-2%. Thus, further improvement, in terms of visible light absorption and efficient co-catalysts, is necessary to go beyond the current proof-of-concept stage. It is noteworthy that the reported efficiencies vary a lot depending on the light source and hence, standard protocols should be stablished across the literature.[159]

Molecular catalysts have shown high efficiencies at mild pH, close or equal to neutral pH on the contrary of their metal oxide analogs, as previously explained.[77] Besides, their high activity can act as a protective shield for the accumulation of oxidative holes on the SC or avoiding recombination, as has been shown in recent molecular hybrid systems.[159] Despite these advantages, Table 4 displays just a few examples of published hybrid systems, which denote the hitch of these materials. Attention to visible light absorption, quantum efficiency, charge separation, and transport avoiding trapping or recombination, and surpassing the high kinetic barrier for WO are some of the challenges. Moreover, as for EC and PEC, the performance of mol-WOCs anchored on surfaces will be strongly related to the stability of the bond.[128]

Entry[ref]	*Photo-absorber*	*WOC[§]*	*Anchor*	*Loading*	*TON (h)*	*Apparent Quantum Yield (%)[$]*	*Electrolyte (pH)*	*Sacrificial electron acceptor*	*Source of illumination*
1[161]	$BiVO_4$	$[Co_4O_4(O_2CMe)_4CNpy_4$	Physi-adsorption	5 wt%	11.6 (5.83)	4.5	Water (4.0)	$Na_2S_2O_8$ (10 mM)	300 W Xe lamp, $\lambda \geqslant 420$ nm
2[162]	n-Fe_2O_3	CoSlp	Physi-adsorption	n/a	33(72 h)	n/a	Phosphate buffer (7.0)	$Na_2S_2O_8$	300 W Xe lamp, $\lambda \geqslant 420$ nm
3[162]	p-Co_3O_4	CoSlp	Physi-adsorption	n/a	35 (72h)	n/a	Phosphate buffer (7.0)	$Na_2S_2O_8$	300 W Xe lamp, $\lambda \geqslant 420$ nm
4[159]	CdS nanorods	Ru(tpy)(bpy)Cl_2	Covalent bond	3 mg hybrid*	0.16 (1h)	0.27	Water (6.0)	TEOA	Xe lamp, $\lambda = 460 \pm 50$ nm at 20 mW cm^{-2}

*Table 4. State-of-the-art colloidal photocatalysts based on mol-WOC at semiconductor nanoparticles. [§] (Slp) Salophen ligand is [N,N'-disalicylal-1,2-phenylenediamine]; tpy is 2,2':6',2''-terpyridine ligand; bpy is 2,2'-bipyridine ligand.*83 molecules Ru/nanorod. [$] Apparent quantum yield (AQY) is defined as the number of reacted electrons per absorbed photon. The final molecular nature of entries 1-3 after photocatalysis has not been demonstrated*

An alternative line of research are Conjugated Microporous Polymer (CMP) photocatalysts because of their synthetic versatility and delocalized π-system. These characteristics allow improved light absorption (in comparison with wide-range SC), tuned electronic properties, and porous structures, that is, increase in surface area. We shall recall the conjugated polymers presented in section *1.3.4 Light-absorbers for photocatalytic water oxidation*. For example, carbon nitrides, g-C_3N_4, show good efficiencies for photocatalytic hydrogen evolution but low water oxidation activity and stability, despite the high co-catalyst loading based on silver or cobalt nanoparticles.[69–72] Other conjugated polymers display the same behavior, with achieved hydrogen evolution but lack of thermodynamic potential or stability under water oxidation conditions. To the best of our knowledge, there is no example in the literature of mol-WOC on CMPs. On the other hand, Wang *et al.*[73] have reported a hybrid system based on low bandgap conjugated microporous polymer nanosheets (aza-CMP) using $Co(OH)_2$ as a cocatalyst (3 wt%) showing the highest O_2 evolution. However, further research is needed to improve the very low rate of oxygen production (0.57 µmol $O_2 \cdot mg_{hybrid}^{-1} \cdot h^{-1}$). Nevertheless, photocatalyst colloidal suspensions are recent and promising materials, with just a few examples in the literature (Table 4) leaving spare room for imminent breakthroughs.

1.6. References

(1) Callaway, E.; Ledford, H.; Viglione, G.; Watson, T.; Witze., A. COVID and 2020: An extraordinary year for science https://www.nature.com/immersive/d41586-020-03437-4/index.html.

(2) Group, W. B. *Global Economic Prospects*; Washington DC, 2020. https://doi.org/10.1596/978-1-4648-1553-9_ch1.

(3) The Lancet. Climate and COVID-19: Converging Crises. *Lancet* **2020**, *2667* (20), 32579. https://doi.org/10.1016/S0140-6736(20)32579-4.

(4) Waters, C. N.; Zalasiewicz, J.; Summerhayes, C.; Barnosky, A. D.; Poirier, C.; Galuszka, A.; Cearreta, A.; Edgeworth, M.; Ellis, E. C.; Ellis, M.; Jeandel, C.; Leinfelder, R.; McNeill, J. R.; Richter, D. d.; Steffen, W.; Syvitski, J.; Vidas, D.; Wagreich, M.; Williams, M.; Zhisheng, A.; Grinevald, J.; Odada, E.; Oreskes, N.; Wolfe, A. P. The Anthropocene Is Functionally and Stratigraphically Distinct from the Holocene. *Science* **2016**, *351* (6269), aad2622–aad2622. https://doi.org/10.1126/science.aad2622.

(5) Rockström, J.; Steffen, W.; Noone, K.; Persson, Å.; Chapin, F. S.; Lambin, E. F.; Lenton, T. M.; Scheffer, M.; Folke, C.; Schellnhuber, H. J.; Nykvist, B.; de Wit, C. A.; Hughes, T.; van der Leeuw, S.; Rodhe, H.; Sörlin, S.; Snyder, P. K.; Costanza, R.; Svedin, U.; Falkenmark, M.; Karlberg, L.; Corell, R. W.; Fabry, V. J.; Hansen, J.; Walker, B.; Liverman, D.; Richardson, K.; Crutzen, P.; Foley, J. A. A Safe Operating Space for Humanity. *Nature* **2009**, *461* (7263), 472–475. https://doi.org/10.1038/461472a.

(6) IPCC, 2018: Global Warming of 1.5°C. An IPCC Special Report on the impacts of global warming of 1.5°C above pre-industrial levels and related global greenhouse gas emission pathways, in the

I

context of strengthening the global response to the threat of climate change, sustainable development, and efforts to eradicate poverty [Masson-Delmotte, V., P. Zhai, H.-O. Pörtner, D. Roberts, J. Skea, P.R. Shukla, A. Pirani, W. Moufouma-Okia, C. Péan, R. Pidcock, S. Connors, J.B.R. Matthews, Y. Chen, X. Zhou, M.I. Gomis, E. Lonnoy, T. Maycock, M. Tignor, and T. Waterfield (eds.)]. In Press.

(7) Lewis, N. S.; Nocera, D. G. Powering the Planet: Chemical Challenges in Solar Energy Utilization. *Proc. Natl. Acad. Sci.* **2006**, *103* (43), 15729–15735. https://doi.org/10.1073/pnas.0603395103.

(8) Rapier, R. The Ten Countries That Dominate World Fossil Fuel Production https://www.forbes.com/sites/rrapier/2019/07/14/ten-countries-that-dominate-fossil-fuel-production/?sh=482c2c375b13.

(9) Hoffert, M. I.; Caldeira, K.; Jain, A. K.; Haites, E. F.; Harveyk, L. D. D.; Potter, S. D.; Schlesinger, M. E.; Schneider, S. H.; G.Watts, R.; TomM.L.Wigley; Donald J.Wuebbles. Energy Implicationsof Future Stabilization of Atmospheric CO2 Content. *Nature* **1998**, *395*, 881–884.

(10) Smalley, R. E. Future Global Energy Prosperity: The Terawatt Challenge. *MRS Bull.* **2005**, *30* (6), 412–417. https://doi.org/10.1557/mrs2005.124.

(11) Steffen, W.; Rockström, J.; Richardson, K.; Lenton, T. M.; Folke, C.; Liverman, D.; Summerhayes, C. P.; Barnosky, A. D.; Cornell, S. E.; Crucifix, M.; Donges, J. F.; Fetzer, I.; Lade, S. J.; Scheffer, M.; Winkelmann, R.; Schellnhuber, H. J. Trajectories of the Earth System in the Anthropocene. *Proc. Natl. Acad. Sci. U. S. A.* **2018**, *115* (33), 8252–8259. https://doi.org/10.1073/pnas.1810141115.

(12) IRENA. *Renewable Power Generation Costs in 2019*; Abu Dhabi, United Arab Emirates 2020.

(13) OECD. *The Impact of Coronavirus (COVID-19) and the Global Oil Price Shock on the Fiscal Position of Oil-Exporting Developing Countries*; 2020.

(14) IEA. *World Energy Outlook 2020*; Paris, France 2020.

(15) United Nations. Adoption of the Paris Agreement. In *Paris Climate Change Conference – COP 21*; Paris, France, 2015.

(16) United Nations. Transforming Our World: The 2030 Agenda for Sustainable Development. *Gen. Assem. 70 Sess.* **2015**, *16301*, 1–35. https://doi.org/10.1007/s13398-014-0173-7.2.

(17) Seh, Z. W.; Kibsgaard, J.; Dickens, C. F.; Chorkendorff, I.; Nørskov, J. K.; Jaramillo, T. F. Combining Theory and Experiment in Electrocatalysis: Insights into Materials Design. *Science* **2017**, *355* (6321). https://doi.org/10.1126/science.aad4998.

(18) Gratzel, M. Artificial Photosynthesis: Water Cleavage into Hydrogen and Oxygen by Visible Light. *Acc. Chem. Res.* **1981**, *14* (12), 376–384. https://doi.org/10.1021/ar00072a003.

(19) Armaroli, N.; Balzani, V. The Future of Energy Supply: Challenges and Opportunities. *Angew. Chemie Int. Ed.* **2007**, *46* (1-2), 52–66. https://doi.org/10.1002/anie.200602373.

(20) Tachibana, Y.; Vayssieres, L.; Durrant, J. R. Artificial Photosynthesis for Solar Water-Splitting. *Nat. Photonics* **2012**, *6* (8), 511–518. https://doi.org/10.1038/nphoton.2012.175.

(21) Berardi, S.; Drouet, S.; Francàs, L.; Gimbert-Suriñach, C.; Guttentag, M.; Richmond, C.; Stoll, T.; Llobet, A. Molecular Artificial Photosynthesis. *Chem. Soc. Rev.* **2014**, *43* (22), 7501–7519. https://doi.org/10.1039/C3CS60405E.

(22) Montoya, J. H.; Seitz, L. C.; Chakthranont, P.; Vojvodic, A.; Jaramillo, T. F.; Nørskov, J. K. Materials for Solar Fuels and Chemicals. *Nat. Mater.* **2017**, *16* (1), 70–81. https://doi.org/10.1038/nmat4778.

(23) Ciamician, G. The Photochemistry of the Future. *Science* **1912**, *36* (926), 385–394. https://doi.org/10.1126/science.36.926.385.

(24) Bassham, J. A. Photosynthesis. *Britannica*; Encyclopedia Britannica, 1998.

(25) Romero, E.; Novoderezhkin, V. I.; Van Grondelle, R. Quantum Design of Photosynthesis for Bio-Inspired Solar-Energy Conversion. *Nature* **2017**, *543* (7645), 355–365. https://doi.org/10.1038/nature22012.

(26) Wraight, C. A.; Clayton, R. K. The Absolute Quantum Efficiency of Bacteriochlorophyll Photooxidation in Reaction Centres of Rhodopseudomonas Spheroides. *Biochim. Biophys. Acta - Bioenerg.* **1974**, *333* (2), 246–260. https://doi.org/10.1016/0005-2728(74)90009-7.

(27) Nocera, D. G. The Artificial Leaf. *Acc. Chem. Res.* **2012**, *45* (5), 767–776. https://doi.org/10.1021/ar2003013.

(28) Umena, Y.; Kawakami, K.; Shen, J. R.; Kamiya, N. Crystal Structure of Oxygen-Evolving Photosystem II at a Resolution of 1.9Å. *Nature* **2011**, *473* (7345), 55–60. https://doi.org/10.1038/nature09913.

(29) Romero, E.; Augulis, R.; Novoderezhkin, V. I.; Ferretti, M.; Thieme, J.; Zigmantas, D.; Van Grondelle, R. Quantum Coherence in Photosynthesis for Efficient Solar-Energy Conversion. *Nat.*

Phys. **2014**, *10* (9), 676–682. https://doi.org/10.1038/NPHYS3017.

(30) Cox, N.; Pantazis, D. A.; Neese, F.; Lubitz, W. Biological Water Oxidation. *Acc. Chem. Res.* **2013**, *46* (7), 1588–1596. https://doi.org/10.1021/ar3003249.

(31) Charles Dismukes, G.; Brimblecombe, R.; Felton, G. A. N.; Pryadun, R. S.; Sheats, J. E.; Spiccia, L.; Swiegers, G. F. Development of Bioinspired Mn4O4-Cubane Water Oxidation Catalysts: Lessons from Photosynthesis. *Acc. Chem. Res.* **2009**, *42* (12), 1935–1943. https://doi.org/10.1021/ar900249x.

(32) Volpato, G. A.; Bonetto, A.; Marcomini, A.; Mialane, P.; Bonchio, M.; Natali, M.; Sartorel, A. Proton Coupled Electron Transfer from Co3O4 Nanoparticles to Photogenerated Ru(bpy)3 3+ : Base Catalysis and Buffer Effect. *Sustain. Energy Fuels* **2018**, *2* (9), 1951–1956. https://doi.org/10.1039/C8SE00275D.

(33) Aro, E.-M.; Virgin, I.; Andersson, B. Photoinhibition of Photosystem II. Inactivation, Protein Damage and Turnover. *Biochim. Biophys. Acta - Bioenerg.* **1993**, *1143* (2), 113–134. https://doi.org/10.1016/0005-2728(93)90134-2.

(34) Nocera, D. G. Solar Fuels and Solar Chemicals Industry. *Acc. Chem. Res.* **2017**, *50* (3), 616–619. https://doi.org/10.1021/acs.accounts.6b00615.

(35) Bard, A. J.; Fox, M. A. Artificial Photosynthesis: Solar Splitting of Water to Hydrogen and Oxygen. *Acc. Chem. Res.* **1995**, *28* (3), 141–145. https://doi.org/10.1021/ar00051a007.

(36) Björn L.O. The Nature of Light and Its Interaction with Matter. In *Photobiology*; Springer, New York, NY, 2008. https://doi.org/https://doi.org/10.1007/978-0-387-72655-7_1.

(37) Sze, S. M.; Ng, K. K. *Physics of Semiconductor Devices*; John Wiley & Sons, Inc., 2007.

(38) Youngblood, W. J.; Lee, S. A.; Kobayashi, Y.; Hernandez-Pagan, E. A.; Hoertz, P. G.; Moore, T. A.; Moore, A. L.; Gust, D.; Mallouk, T. E. Photoassisted Overall Water Splitting in a Visible Light-Absorbing Dye-Sensitized Photoelectrochemical Cell. *J. Am. Chem. Soc.* **2009**, *131* (3), 926–927. https://doi.org/10.1021/ja809108y.

(39) Fujishima, A.; Honda, K. Electrochemical Photolysis of Water at a Semiconductor Electrode. *Nature* **1972**, *238* (5358), 37–38. https://doi.org/10.1038/238037a0.

(40) Wang, Y.; Silveri, F.; Bayazit, M. K.; Ruan, Q.; Li, Y.; Xie, J.; Catlow, C. R. A.; Tang, J. Bandgap Engineering of Organic Semiconductors for Highly Efficient Photocatalytic Water Splitting. *Adv. Energy Mater.* **2018**, *8* (24), 1801084. https://doi.org/10.1002/aenm.201801084.

(41) Wang, X.; Maeda, K.; Thomas, A.; Takanabe, K.; Xin, G.; Carlsson, J. M.; Domen, K.; Antonietti, M. A Metal-Free Polymeric Photocatalyst for Hydrogen Production from Water under Visible Light. *Nat. Mater.* **2009**, *8* (1), 76–80. https://doi.org/10.1038/nmat2317.

(42) Kosco, J.; Moruzzi, F.; Willner, B.; McCulloch, I. Photocatalysts Based on Organic Semiconductors with Tunable Energy Levels for Solar Fuel Applications. *Adv. Energy Mater.* **2020**, *10* (39). https://doi.org/10.1002/aenm.202001935.

(43) Brütting, W. Introduction to the Physics of Organic Semiconductors. In *Physics of Organic Semiconductors*; John Wiley & Sons, Ltd, 2005; pp 1–14. https://doi.org/https://doi.org/10.1002/3527606637.ch.

(44) Lee, J.; Lee, S. M.; Chen, S.; Kumari, T.; Kang, S. H.; Cho, Y.; Yang, C. Organic Photovoltaics with Multiple Donor–Acceptor Pairs. *Adv. Mater.* **2019**, *31* (20), 1–17. https://doi.org/10.1002/adma.201804762.

(45) Lu, L.; Lv, Z.; Si, Y.; Liu, M.; Zhang, S. Recent Progress on Band and Surface Engineering of Graphitic Carbon Nitride for Artificial Photosynthesis. *Appl. Surf. Sci.* **2018**, *462*, 693–712. https://doi.org/10.1016/j.apsusc.2018.08.131.

(46) Liras, M.; Barawi, M.; de la Peña O'Shea, V. A. Hybrid Materials Based on Conjugated Polymers and Inorganic Semiconductors as Photocatalysts: From Environmental to Energy Applications. *Chem. Soc. Rev.* **2019**, *48* (22), 5454–5487. https://doi.org/10.1039/C9CS00377K.

(47) Schlesinger, R.; Bianchi, F.; Blumstengel, S.; Christodoulou, C.; Ovsyannikov, R.; Kobin, B.; Moudgil, K.; Barlow, S.; Hecht, S.; Marder, S. R.; Henneberger, F.; Koch, N. Efficient Light Emission from Inorganic and Organic Semiconductor Hybrid Structures by Energy-Level Tuning. *Nat. Commun.* **2015**, *6*, 1–7. https://doi.org/10.1038/ncomms7754.

(48) Guo, X.; Burda, C. Coordination Engineering toward High Performance Organic – Inorganic Hybrid Perovskites. *Coord. Chem. Rev.* **2016**, *320-321*, 53–65. https://doi.org/10.1016/j.ccr.2016.03.013.

(49) Brenner, T. M.; Egger, D. A.; Kronik, L.; Hodes, G.; Cahen, D. Hybrid Organic—inorganic Perovskites: Low-Cost Semiconductors with Intriguing Charge-Transport Properties. *Nat. Rev. Mater.* **2016**, *1* (1), 15007. https://doi.org/10.1038/natrevmats.2015.7.

(50) Mir, S. H.; Nagahara, L. A.; Thundat, T.; Mokarian-Tabari, P.; Furukawa, H.; Khosla, A. Review—Organic-Inorganic Hybrid Functional Materials: An Integrated Platform for Applied Technologies. *J. Electrochem. Soc.* **2018**, *165* (8), B3137–B3156. https://doi.org/10.1149/2.0191808jes.

(51) Zuehlsdorff, T. J.; Isborn, C. M. Modeling Absorption Spectra of Molecules in Solution. *Int. J. Quantum Chem.* **2019**, *119* (1), 1–18. https://doi.org/10.1002/qua.25719.

(52) Zhu, Y.; Wang, D.; Huang, Q.; Du, J.; Sun, L.; Li, F.; Meyer, T. J. Stabilization of a Molecular Water Oxidation Catalyst on a Dye−sensitized Photoanode by a Pyridyl Anchor. *Nat. Commun.* **2020**, *11* (1), 1–8. https://doi.org/10.1038/s41467-020-18417-5.

(53) Limburg, B.; Bouwman, E.; Bonnet, S. Rate and Stability of Photocatalytic Water Oxidation Using [Ru(bpy)3]2+ as Photosensitizer. *ACS Catal.* **2016**, *6* (8), 5273–5284. https://doi.org/10.1021/acscatal.6b00107.

(54) Nayak, A.; Roy, S.; Sherman, B. D.; Alibabaei, L.; Lapides, A. M.; Brennaman, M. K.; Wee, K. R.; Meyer, T. J. Phosphonate-Derivatized Porphyrins for Photoelectrochemical Applications. *ACS Appl. Mater. Interfaces* **2016**, *8* (6), 3853–3860. https://doi.org/10.1021/acsami.5b10587.

(55) Ashford, D. L.; Gish, M. K.; Vannucci, A. K.; Brennaman, M. K.; Templeton, J. L.; Papanikolas, J. M.; Meyer, T. J. Molecular Chromophore–Catalyst Assemblies for Solar Fuel Applications. *Chem. Rev.* **2015**, *115* (23), 13006–13049. https://doi.org/10.1021/acs.chemrev.5b00229.

(56) McCormick, T. M.; Han, Z.; Weinberg, D. J.; Brennessel, W. W.; Holland, P. L.; Eisenberg, R. Impact of Ligand Exchange in Hydrogen Production from Cobaloxime-Containing Photocatalytic Systems. *Inorg. Chem.* **2011**, *50* (21), 10660–10666. https://doi.org/10.1021/ic2010166.

(57) Mou, Z.; Dong, Y.; Li, S.; Du, Y.; Wang, X.; Yang, P.; Wang, S. Eosin Y Functionalized Graphene for Photocatalytic Hydrogen Production from Water. *Int. J. Hydrogen Energy* **2011**, *36* (15), 8885–8893. https://doi.org/10.1016/j.ijhydene.2011.05.003.

(58) McCormick, T. M.; Calitree, B. D.; Orchard, A.; Kraut, N. D.; Bright, F. V.; Detty, M. R.; Eisenberg, R. Reductive Side of Water Splitting in Artificial Photosynthesis: New Homogeneous Photosystems of Great Activity and Mechanistic Insight. *J. Am. Chem. Soc.* **2010**, *132* (44), 15480–15483. https://doi.org/10.1021/ja1057357.

(59) Brennaman, M. K.; Dillon, R. J.; Alibabaei, L.; Gish, M. K.; Dares, C. J.; Ashford, D. L.; House, R. L.; Meyer, G. J.; Papanikolas, J. M.; Meyer, T. J. Finding the Way to Solar Fuels with Dye-Sensitized Photoelectrosynthesis Cells. *J. Am. Chem. Soc.* **2016**, *138* (40), 13085–13102. https://doi.org/10.1021/jacs.6b06466.

(60) Gueret, R.; Poulard, L.; Oshinowo, M.; Chauvin, J.; Dahmane, M.; Dupeyre, G.; Lainé, P. P.; Fortage, J.; Collomb, M. N. Challenging the [Ru(bpy)3]2+ Photosensitizer with a Triazatriangulenium Robust Organic Dye for Visible-Light-Driven Hydrogen Production in Water. *ACS Catal.* **2018**, *8* (5), 3792–3802. https://doi.org/10.1021/acscatal.7b04000.

(61) Vagnini, M. T.; Smeigh, A. L.; Blakemore, J. D.; Eaton, S. W.; Schley, N. D.; D'Souza, F.; Crabtree, R. H.; Brudvig, G. W.; Co, D. T.; Wasielewski, M. R. Ultrafast Photodriven Intramolecular Electron Transfer from an Iridium-Based Water-Oxidation Catalyst to Perylene Diimide Derivatives. *Proc. Natl. Acad. Sci. U. S. A.* **2012**, *109* (39), 15651–15656. https://doi.org/10.1073/pnas.1202075109.

(62) Alibabaei, L.; Brennaman, M. K.; Meyer, T. J. Light-Driven Water Splitting in the Dye-Sensitized Photoelectrosynthesis Cell. In *Molecular Devices for Solar Energy Conversion and Storage*; Tian, H., Boschloo, G., Hagfeldt, A., Eds.; Springer, Singapore, 2018; pp 229–257. https://doi.org/10.1007/978-981-10-5924-7_6.

(63) Wu, L.; Nayak, A.; Shao, J.; Meyer, T. J. Crossing the Bridge from Molecular Catalysis to a Heterogenous Electrode in Electrocatalytic Water Oxidation. *Proc. Natl. Acad. Sci. U. S. A.* **2019**, *166* (23), 11153–11158. https://doi.org/10.1073/pnas.1902455116.

(64) Schneider, J.; Matsuoka, M.; Takeuchi, M.; Zhang, J.; Horiuchi, Y.; Anpo, M.; Bahnemann, D. W. Understanding TiO2 Photocatalysis: Mechanisms and Materials. *Chem. Rev.* **2014**, *114* (19), 9919–9986. https://doi.org/10.1021/cr5001892.

(65) Liang, Y.; Tsubota, T.; Mooij, L. P. A.; Van De Krol, R. Highly Improved Quantum Efficiencies for Thin Film BiVO4 Photoanodes. *J. Phys. Chem. C* **2011**, *115* (35), 17594–17598. https://doi.org/10.1021/jp203004v.

(66) Hong, S. J.; Lee, S.; Jang, J. S.; Lee, J. S. Heterojunction BiVO4/WO3 Electrodes for Enhanced Photoactivity of Water Oxidation. *Energy Environ. Sci.* **2011**, *4* (5), 1781–1787. https://doi.org/10.1039/c0ee00743a.

(67) Li, X.-B.; Tung, C.-H.; Wu, L.-Z. Semiconducting Quantum Dots for Artificial Photosynthesis. *Nat. Rev. Chem.* **2018**, *2* (8), 160–173. https://doi.org/10.1038/s41570-018-0024-8.

(68) Yang, L.; Zhou, H.; Fan, T.; Zhang, D. Semiconductor Photocatalysts for Water Oxidation: Current Status and Challenges. *Phys. Chem. Chem. Phys.* **2014**, *16* (15), 6810–6826. https://doi.org/10.1039/c4cp00246f.

(69) Maeda, K.; Wang, X.; Nishihara, Y.; Lu, D.; Antonietti, M.; Domen, K. Photocatalytic Activities of Graphitic Carbon Nitride Powder for Water Reduction and Oxidation under Visible Light. *J. Phys. Chem. C* **2009**, *113* (12), 4940–4947. https://doi.org/10.1021/jp809119m.

(70) Zhang, G.; Huang, C.; Wang, X. Dispersing Molecular Cobalt in Graphitic Carbon Nitride Frameworks for Photocatalytic Water Oxidation. *Small* **2015**, *11* (9-10), 1215–1221. https://doi.org/10.1002/smll.201402636.

(71) Lee, R.-L.; Tran, P. D.; Pramana, S. S.; Chiam, S. Y.; Ren, Y.; Meng, S.; Wong, L. H.; Barber, J. Assembling Graphitic-Carbon-Nitride with Cobalt-Oxide-Phosphate to Construct an Efficient Hybrid Photocatalyst for Water Splitting Application. *Catal. Sci. Technol.* **2013**, *3* (7), 1694. https://doi.org/10.1039/c3cy00054k.

(72) Pan, Z.; Zheng, Y.; Guo, F.; Niu, P.; Wang, X. Decorating CoP and Pt Nanoparticles on Graphitic Carbon Nitride Nanosheets to Promote Overall Water Splitting by Conjugated Polymers. *ChemSusChem.* **2017**, *10* (1), 87–90. https://doi.org/10.1002/cssc.201600850.

(73) Wang, L.; Wan, Y.; Ding, Y.; Niu, Y.; Xiong, Y.; Wu, X.; Xu, H. Photocatalytic Oxygen Evolution from Low-Bandgap Conjugated Microporous Polymer Nanosheets: A Combined First-Principles Calculation and Experimental Study. *Nanoscale* **2017**, *9* (12), 4090–4096. https://doi.org/10.1039/c7nr00534b.

(74) Stahel, W. R. The Circular Economy. *Nature* **2016**, *531* (7595), 435–438. https://doi.org/10.1038/531435a.

(75) Levie, R. de. The Electrolysis of Water. *J. Electroanal. Chem.* **1999**, *476*, 92–93. https://doi.org/10.1007/s11124-008-2002-x.

(76) Garrido-Barros, P.; Gimbert-Suriñach, C.; Matheu, R.; Sala, X.; Llobet, A. How to Make an Efficient and Robust Molecular Catalyst for Water Oxidation. *Chem. Soc. Rev.* **2017**, *46* (20), 6088–6098. https://doi.org/10.1039/c7cs00248c.

(77) Kibsgaard, J.; Chorkendorff, I. Considerations for the Scaling-up of Water Splitting Catalysts. *Nat. Energy* **2019**, *4* (6), 430–433. https://doi.org/10.1038/s41560-019-0407-1.

(78) McCrory, C. C. L.; Jung, S.; Ferrer, I. M.; Chatman, S. M.; Peters, J. C.; Jaramillo, T. F. Benchmarking Hydrogen Evolving Reaction and Oxygen Evolving Reaction Electrocatalysts for Solar Water Splitting Devices. *J. Am. Chem. Soc.* **2015**, *137* (13), 4347–4357. https://doi.org/10.1021/ja510442p.

(79) Gersten, S. W.; Samuels, G. J.; Meyer, T. J. Catalytic Oxidation of Water by an Oxo-Bridged Ruthenium Dimer. *J. Am. Chem. Soc.* **1982**, *104* (14), 4029–4030. https://doi.org/10.1021/ja00378a053.

(80) Sens, C.; Romero, I.; Rodríguez, M.; Llobet, A.; Parella, T.; Benet-Buchholz, J. A New Ru Complex Capable of Catalytically Oxidizing Water to Molecular Dioxygen. *J. Am. Chem. Soc.* **2004**, *126* (25), 7798–7799. https://doi.org/10.1021/ja0486824.

(81) Zong, R.; Thummel, R. P. A New Family of Ru Complexes for Water Oxidation. *J. Am. Chem. Soc.* **2005**, *127* (37), 12802–12803. https://doi.org/10.1021/ja054791m.

(82) Concepcion, J. J.; Jurss, J. W.; Templeton, J. L.; Meyer, T. J. One Site Is Enough. Catalytic Water Oxidation by [Ru(tpy)(bpm)(OH2)]2+ and [Ru(tpy)(bpz)(OH2)]2+. *J. Am. Chem. Soc.* **2008**, *130* (49), 16462–16463. https://doi.org/10.1021/ja8059649.

(83) Duan, L.; Fischer, A.; Xu, Y.; Sun, L. Isolated Seven-Coordinate Ru(IV) Dimer Complex with [HOHOH]− Bridging Ligand as an Intermediate for Catalytic Water Oxidation. *J. Am. Chem. Soc.* **2009**, *131* (30), 10397–10399. https://doi.org/10.1021/ja9034686.

(84) Duan, L.; Bozoglian, F.; Mandal, S.; Stewart, B.; Privalov, T.; Llobet, A.; Sun, L. A Molecular Ruthenium Catalyst with Water-Oxidation Activity Comparable to that of Photosystem II. *Nat. Chem.* **2012**, *4* (5), 418–423. https://doi.org/10.1038/nchem.1301.

(85) Duan, L.; Wang, L.; Inge, A. K.; Fischer, A.; Zou, X.; Sun, L. Insights into Ru-Based Molecular Water Oxidation Catalysts: Electronic and Noncovalent-Interaction Effects on Their Catalytic Activities. *Inorg. Chem.* **2013**, *52* (14), 7844–7852. https://doi.org/10.1021/ic302687d.

(86) Matheu, R.; Ertem, M. Z.; Gimbert-Suriñach, C.; Sala, X.; Llobet, A. Seven Coordinated Molecular Ruthenium–Water Oxidation Catalysts: A Coordination Chemistry Journey. *Chem. Rev.* **2019**, *119* (6), 3453–3471. https://doi.org/10.1021/acs.chemrev.8b00537.

(87) Matheu, R.; Ertem, M. Z.; Benet-Buchholz, J.; Coronado, E.; Batista, V. S.; Sala, X.; Llobet, A.

Intramolecular Proton Transfer Boosts Water Oxidation Catalyzed by a Ru Complex. *J. Am. Chem. Soc.* **2015**, *137* (33), 10786–10795. https://doi.org/10.1021/jacs.5b06541.

(88) Garrido-Barros, P.; Matheu, R.; Gimbert-Suriñach, C.; Llobet, A. Electronic, Mechanistic, and Structural Factors That Influence the Performance of Molecular Water Oxidation Catalysts Anchored on Electrode Surfaces. *Curr. Opin. Electrochem.* **2019**, *15*, 140–147. https://doi.org/10.1016/j.coelec.2019.04.027.

(89) Vereshchuk, N.; Matheu, R.; Benet-Buchholz, J.; Pipelier, M.; Lebreton, J.; Dubreuil, D.; Tessier, A.; Gimbert-Suriñach, C.; Z. Ertem, M.; Llobet, A. Second Coordination Sphere Effects in an Evolved Ru Complex Based on a Highly Adaptable Ligand Results in Rapid Water Oxidation Catalysis. *J. Am. Chem. Soc.* **2020**, *142* (11), 5068–5077. https://doi.org/10.1021/jacs.9b11935.

(90) Matheu, R.; Garrido, P.; Gil-Sepulcre, M.; Sala, X.; Gimbert-Suriñach, C.; Llobet, A. The Development of Molecular Water Oxidation Catalysts. *Nat. Rev. Chem.* **2019**, *2* (3), 331–341. https://doi.org/10.1038/s41570-019-0096-0.

(91) Najafpour, M. M.; Feizi, H. Water Oxidation Catalyzed by Two Cobalt Complexes: New Challenges and Questions. *Catal. Sci. Technol.* **2018**, *8* (7), 1840–1848. https://doi.org/10.1039/c7cy02602a.

(92) Pattanayak, S.; Chowdhury, D. R.; Garai, B.; Singh, K. K.; Paul, A.; Dhar, B. B.; Gupta, S. Sen. Electrochemical Formation of FeV(O) and Mechanism of Its Reaction with Water During O−O Bond Formation. *Chem. - A Eur. J.* **2017**, *23* (14), 3414–3424. https://doi.org/10.1002/chem.201605061.

(93) Hong, D.; Mandal, S.; Yamada, Y.; Lee, Y.-M.; Nam, W.; Llobet, A.; Fukuzumi, S. Water Oxidation Catalysis with Nonheme Iron Complexes under Acidic and Basic Conditions: Homogeneous or Heterogeneous? *Inorg. Chem.* **2013**, *52* (16), 9522–9531. https://doi.org/10.1021/ic401180r.

(94) Najafpour, M. M.; Moghaddam, A. N.; Dau, H.; Zaharieva, I. Fragments of Layered Manganese Oxide Are the Real Water Oxidation Catalyst after Transformation of Molecular Precursor on Clay. *J. Am. Chem. Soc.* **2014**, *136* (20), 7245–7248. https://doi.org/10.1021/ja5028716.

(95) Pelosin, P.; Gil-Sepulcre, M.; Garrido-Barros, P.; Moonshiram, D.; Benet-Buchholz, J.; Gimbert-Suriñach, C.; Llobet, A. Analysis of the Active Species Responsible for Water Oxidation Using a Pentanuclear Fe Complex. *iScience* **2020**, *23* (8). https://doi.org/10.1016/j.isci.2020.101378.

(96) Solomon, E. I.; Heppner, D. E.; Johnston, E. M.; Ginsbach, J. W.; Cirera, J.; Qayyum, M.; Kieber-Emmons, M. T.; Kjaergaard, C. H.; Hadt, R. G.; Tian, L. Copper Active Sites in Biology. *Chem. Rev.* **2014**, *114* (7), 3659–3853. https://doi.org/10.1021/cr400327t.

(97) Barnett, S. M.; Goldberg, K. I.; Mayer, J. M. A Soluble Copper-Bipyridine Water-Oxidation Electrocatalyst. *Nat. Chem.* **2012**, *4* (6), 498–502. https://doi.org/10.1038/nchem.1350.

(98) Zhang, M. T.; Chen, Z.; Kang, P.; Meyer, T. J. Electrocatalytic Water Oxidation with a copper(II) Polypeptide Complex. *J. Am. Chem. Soc.* **2013**, *135* (6), 2048–2051. https://doi.org/10.1021/ja3097515.

(99) Zhang, T.; Wang, C.; Liu, S.; Wang, J. L.; Lin, W. A Biomimetic Copper Water Oxidation Catalyst with Low Overpotential. *J. Am. Chem. Soc.* **2014**, *136* (1), 273–281. https://doi.org/10.1021/ja409267p.

(100) Garrido-Barros, P.; Funez-Ardoiz, I.; Drouet, S.; Benet-Bucholz, J.; Maseras, F.; Llobet, A. Redox Non-Innocent Ligand Controls Water Oxidation Overpotential in a New Family of Mononuclear Cu-Based E Ffi Cient Catalysts. *J. Am. Chem. Soc.* **2015**, *137*. https://doi.org/10.1021/jacs.5b03977.

(101) Garrido-Barros, P.; Gimbert-Surinifach, C.; Moonshiram, D.; Picón, A.; Monge, P.; Batista, V. S.; Llobet, A. Electronic I-Delocalization Boosts Catalytic Water Oxidation by Cu(II) Molecular Catalysts Heterogenized on Graphene Sheets. *J. Am. Chem. Soc.* **2017**, *139* (37), 12907–12910. https://doi.org/10.1021/jacs.7b06828.

(102) Weinberg, D. R.; Gagliardi, C. J.; Hull, J. F.; Murphy, C. F.; Kent, C. A.; Westlake, B. C.; Paul, A.; Ess, D. H.; McCafferty, D. G.; Meyer, T. J. Proton-Coupled Electron Transfer. *Chem. Rev.* **2012**, *112* (7), 4016–4093. https://doi.org/10.1021/cr200177j.

(103) Savéant, J. M. Electrochemical Approach to Proton-Coupled Electron Transfers: Recent Advances. *Energy Environ. Sci.* **2012**, *5* (7), 7718–7731. https://doi.org/10.1039/c2ee03241d.

(104) Gagliardi, C. J.; Vannucci, A. K.; Concepcion, J. J.; Chen, Z.; Meyer, T. J. The Role of Proton Coupled Electron Transfer in Water Oxidation. *Energy Environ. Sci.* **2012**, *5* (7), 7704–7717. https://doi.org/10.1039/c2ee03311a.

(105) Elgrishi, N.; Rountree, K. J.; McCarthy, B. D.; Rountree, E. S.; Eisenhart, T. T.; Dempsey, J. L. A Practical Beginner's Guide to Cyclic Voltammetry. *J. Chem. Educ.* **2018**, *95* (2), 197–206. https://doi.org/10.1021/acs.jchemed.7b00361.

(106) Matheu, R.; Ertem, M. Z.; Gimbert-Suriñach, C.; Benet-Buchholz, J.; Sala, X.; Llobet, A. Hydrogen Bonding Rescues Overpotential in Seven-Coordinated Ru Water Oxidation Catalysts. *ACS Catal.*

2017, *7* (10), 6525–6532. https://doi.org/10.1021/acscatal.7b01860.

(107) Roduner, E. Size Matters: Why Nanomaterials Are Different. *Chem. Soc. Rev.* **2006**, *35* (7), 583–592. https://doi.org/10.1039/b502142c.

(108) Zahran, Z. N.; Tsubonouchi, Y.; Mohamed, E. A.; Yagi, M. Recent Advances in the Development of Molecular Catalyst-Based Anodes for Water Oxidation toward Artificial Photosynthesis. *ChemSusChem.* **2019**, *12*, 1775–1793. https://doi.org/10.1002/cssc.201802795.

(109) Zhang, B.; Sun, L. Artificial Photosynthesis : Opportunities and Challenges of Molecular Catalysts. *Chem. Soc. Rev.* **2019**, *48*, 2216–2264. https://doi.org/10.1039/c8cs00897c.

(110) Dumortier, M.; Tembhurne, S.; Haussener, S. Holistic Design Guidelines for Solar Hydrogen Production by Photo-Electrochemical Routes. *Energy Environ. Sci.* **2015**, *8* (12), 3614–3628. https://doi.org/10.1039/c5ee01821h.

(111) Jia, J.; Seitz, L. C.; Benck, J. D.; Huo, Y.; Chen, Y.; Ng, J. W. D.; Bilir, T.; Harris, J. S.; Jaramillo, T. F. Solar Water Splitting by Photovoltaic-Electrolysis with a Solar-to-Hydrogen Efficiency over 30%. *Nat. Commun.* **2016**, *7* (1), 13237. https://doi.org/10.1038/ncomms13237.

(112) Pinaud, B. A.; Benck, J. D.; Seitz, L. C.; Forman, A. J.; Chen, Z.; Deutsch, T. G.; James, B. D.; Baum, K. N.; Baum, G. N.; Ardo, S.; Wang, H.; Miller, E.; Jaramillo, T. F. Technical and Economic Feasibility of Centralized Facilities for Solar Hydrogen Production via Photocatalysis and Photoelectrochemistry. *Energy Environ. Sci.* **2013**, *6* (7), 1983–2002. https://doi.org/10.1039/c3ee40831k.

(113) Carmo, M.; Fritz, D. L.; Mergel, J.; Stolten, D. A Comprehensive Review on PEM Water Electrolysis. *Int. J. Hydrogen Energy* **2013**, *38* (12), 4901–4934. https://doi.org/10.1016/j.ijhydene.2013.01.151.

(114) Miller, H. A.; Bouzek, K.; Hnat, J.; Loos, S.; Bernäcker, C. I.; Weißgärber, T.; Röntzsch, L.; Meier-Haack, J. Green Hydrogen from Anion Exchange Membrane Water Electrolysis: A Review of Recent Developments in Critical Materials and Operating Conditions. *Sustain. Energy Fuels* **2020**, *4* (5), 2114–2133. https://doi.org/10.1039/c9se01240k.

(115) Xu, J.; Murphy, S.; Xiong, D.; Cai, R.; Wei, X. K.; Heggen, M.; Barborini, E.; Vinati, S.; Dunin-Borkowski, R. E.; Palmer, R. E.; Liu, L. Cluster Beam Deposition of Ultrafine Cobalt and Ruthenium Clusters for Efficient and Stable Oxygen Evolution Reaction. *ACS Appl. Energy Mater.* **2018**, *1* (7), 3013–3018. https://doi.org/10.1021/acsaem.8b00111.

(116) Dalle, K. E.; Warnan, J.; Leung, J. J.; Reuillard, B.; Karmel, I. S.; Reisner, E. Electro- and Solar-Driven Fuel Synthesis with First Row Transition Metal Complexes. *Chem. Rev.* **2019**, *119* (4), 2752–2875. https://doi.org/10.1021/acs.chemrev.8b00392.

(117) Materna, K. L.; Crabtree, R. H.; Brudvig, G. W. Anchoring Groups for Photocatalytic Water Oxidation on Metal Oxide Surfaces. *Chem. Soc. Rev.* **2017**, *46* (20), 6099–6110. https://doi.org/10.1039/c7cs00314e.

(118) Harris, T. G. A. A.; Götz, R.; Wrzolek, P.; Davis, V.; Knapp, C. E.; Ly, K.; Hildebrandt, P.; Schwalbe, M.; Weidinger, I.; Zebger, I.; Fischer, A. Robust Electrografted Interfaces on Metal Oxides for Electrocatalysis – an *in Situ* Spectroelectrochemical Study. *J. Mater. Chem. A* **2018**. https://doi.org/10.1039/C8TA02983K.

(119) Niu, F.; Wang, D.; Li, F.; Liu, Y.; Shen, S.; Meyer, T. J. Hybrid Photoelectrochemical Water Splitting Systems: From Interface Design to System Assembly. *Adv. Energy Mater.* **2020**, *10* (11), 1–24. https://doi.org/10.1002/aenm.201900399.

(120) Dalle, K. E.; Warnan, J.; Leung, J. J.; Reuillard, B.; Karmel, I. S.; Reisner, E. Electro- and Solar-Driven Fuel Synthesis with First Row Transition Metal Complexes. *Chem. Rev.* **2019**, *119*, 2752–2875. https://doi.org/10.1021/acs.chemrev.8b00392.

(121) Wang, Y.; Li, F.; Li, H.; Bai, L.; Sun, L. Photocatalytic Water Oxidation via Combination of BiVO4-RGO and Molecular Cobalt Catalysts. *Chem. Commun.* **2016**, *52* (14), 3050–3053. https://doi.org/10.1039/c5cc09588c.

(122) Jackson, M. N.; Oh, S.; Kaminsky, C. J.; Chu, S. B.; Zhang, G.; Miller, J. T.; Surendranath, Y. Strong Electronic Coupling of Molecular Sites to Graphitic Electrodes via Pyrazine Conjugation. *J. Am. Chem. Soc.* **2018**, *140* (3), 1004–1010. https://doi.org/10.1021/jacs.7b10723.

(123) Georgakilas, V.; Kordatos, K.; Prato, M.; Guldi, D. M.; Holzinger, M.; Hirsch, A. Organic Functionalization of Carbon Nanotubes. *J. Am. Chem. Soc.* **2002**, *124* (5), 760–761. https://doi.org/10.1021/ja016954m.

(124) Toma, F. M.; Sartorel, A.; Carraro, M.; Bonchio, M.; Prato, M. Dendron-Functionalized Multiwalled Carbon Nanotubes Incorporating Polyoxometalates for Water-Splitting Catalysis. *Pure Appl.*

Chem. **2011**, *83* (8), 1529–1542. https://doi.org/10.1351/PAC-CON-10-11-12.

(125) Zhang, L.; Chen, J.; Fan, T.; Shen, K.; Jiang, M.; Li, Y. A High-Valent Di-μ-Oxo Dimanganese Complex Covalently Anchored in a Metal-Organic Framework as a Highly Efficient and Recoverable Water Oxidation Catalyst. *Chem. Commun.* **2018**, *54* (33), 4188–4191. https://doi.org/10.1039/c8cc00258d.

(126) Devadoss, A.; Chidsey, C. E. D. Azide-Modified Graphitic Surfaces for Covalent Attachment of Alkyne-Terminated Molecules By "click" chemistry. *J. Am. Chem. Soc.* **2007**, *129* (17), 5370–5371. https://doi.org/10.1021/ja071291f.

(127) Bullock, R. M.; Das, A. K.; Appel, A. M. Surface Immobilization of Molecular Electrocatalysts for Energy Conversion. *Chem. - A Eur. J.* **2017**, *23* (32), 7626–7641. https://doi.org/10.1002/chem.201605066.

(128) Brennan, B. J.; Llansola Portolés, M. J.; Liddell, P. A.; Moore, T. A.; Moore, A. L.; Gust, D. Comparison of Silatrane, Phosphonic Acid, and Carboxylic Acid Functional Groups for Attachment of Porphyrin Sensitizers to TiO2 in Photoelectrochemical Cells. *Phys. Chem. Chem. Phys.* **2013**, *15* (39), 16605–16614. https://doi.org/10.1039/c3cp52156g.

(129) Bae, E.; Choi, W.; Park, J.; Shin, H. S.; Kim, S. Bin; Lee, J. S. Effects of Surface Anchoring Groups (Carboxylate vs Phosphonate) in Ruthenium-Complex-Sensitized TiO 2 on Visible Light Reactivity in Aqueous Suspensions. *J. Phys. Chem. B* **2004**, *108* (37), 14093–14101. https://doi.org/10.1021/jp047777p.

(130) Creus, J.; Matheu, R.; Peñafiel, I.; Moonshiram, D.; Blondeau, P.; Benet-Buchholz, J.; García-Antón, J.; Sala, X.; Godard, C.; Llobet, A. A Million Turnover Molecular Anode for Catalytic Water Oxidation. *Angew. Chemie Int. Ed.* **2016**, *55* (49), 15382–15386. https://doi.org/10.1002/anie.201609167.

(131) Hoque, M. A.; Gil-Sepulcre, M.; de Aguirre, A.; Elemans, J. A. A. W.; Moonshiram, D.; Matheu, R.; Shi, Y.; Benet-Buchholz, J.; Sala, X.; Malfois, M.; Solano, E.; Lim, J.; Garzón-Manjón, A.; Scheu, C.; Lanza, M.; Maseras, F.; Gimbert-Suriñach, C.; Llobet, A. Water Oxidation Electrocatalysis Using Ruthenium Coordination Oligomers Adsorbed on Multiwalled Carbon Nanotubes. *Nat. Chem.* **2020**, *12* (11), 1060–1066. https://doi.org/10.1038/s41557-020-0548-7.

(132) Wadsworth, B. L.; Beiler, A. M.; Khusnutdinova, D.; Jacob, S. I.; Moore, G. F. Electrocatalytic and Optical Properties of Cobaloxime Catalysts Immobilized at a Surface-Grafted Polymer Interface. *ACS Catal.* **2016**, *6* (12), 8048–8057. https://doi.org/10.1021/acscatal.6b02194.

(133) Mola, J.; Mas-Marza, E.; Sala, X.; Romero, I.; Rodríguez, M.; Viñas, C.; Parella, T.; Llobet, A. Ru-Hbpp-Based Water-Oxidation Catalysts Anchored on Conducting Solid Supports. *Angew. Chem. Int. Ed.* **2008**, *47* (31), 5830–5832. https://doi.org/10.1002/anie.200704912.

(134) Wang, L.; Fan, K.; Daniel, Q.; Duan, L.; Li, F.; Philippe, B.; Rensmo, H.; Chen, H.; Sun, J.; Sun, L. Electrochemical Driven Water Oxidation by Molecular Catalysts in Situ Polymerized on the Surface of Graphite Carbon Electrode. *Chem. Commun.* **2015**, *51* (37), 7883–7886. https://doi.org/10.1039/c5cc00242g.

(135) Wang, L.; Fan, K.; Chen, H.; Daniel, Q.; Philippe, B.; Rensmo, H.; Sun, L. Towards Efficient and Robust Anodes for Water Splitting: Immobilization of Ru Catalysts on Carbon Electrode and Hematite by in Situ Polymerization. *Catal. Today* **2017**, *290*, 73–77. https://doi.org/10.1016/j.cattod.2016.07.011.

(136) Kaloni, T. P.; Giesbrecht, P. K.; Schreckenbach, G.; Freund, M. S. Polythiophene: From Fundamental Perspectives to Applications. *Chem. Mater.* **2017**, *29* (24), 10248–10283. https://doi.org/10.1021/acs.chemmater.7b03035.

(137) Blanchard, P.; Cravino, A.; Levillain, E. *Electrochemistry of Oligothiophenes and Polythiophenes*; 2009. https://doi.org/10.1002/9780470745533.ch9.

(138) Le, T.-H.; Kim, Y.; Yoon, H. Electrical and Electrochemical Properties of Conducting Polymers. *Polymers (Basel).* **2017**, *9* (12), 150. https://doi.org/10.3390/polym9040150.

(139) Matheu, R.; Francàs, L.; Chernev, P.; Ertem, M. Z.; Batista, V.; Haumann, M.; Sala, X.; Llobet, A. Behavior of the Ru-Bda Water Oxidation Catalyst Covalently Anchored on Glassy Carbon Electrodes. *ACS Catal.* **2015**, *5* (6), 3422–3429. https://doi.org/10.1021/acscatal.5b00132.

(140) Hyde, J. T.; Hanson, K.; Vannucci, A. K.; Lapides, A. M.; Alibabaei, L.; Norris, M. R.; Meyer, T. J.; Harrison, D. P. Electrochemical Instability of Phosphonate-Derivatized, ruthenium(III) Polypyridyl Complexes on Metal Oxide Surfaces. *ACS Appl. Mater. Interfaces* **2015**, *7* (18), 9554–9562. https://doi.org/10.1021/acsami.5b01000.

(141) Schindler, D.; Gil-Sepulcre, M.; Lindner, J. O.; Stepanenko, V.; Moonshiram, D.; Llobet, A.;

Würthner, F. Efficient Electrochemical Water Oxidation by a Trinuclear Ru(bda) Macrocycle Immobilized on Multi-Walled Carbon Nanotube Electrodes. *Adv. Energy Mater.* **2020**, *10* (43), 1–7. https://doi.org/10.1002/aenm.202002329.

(142) Creus, J.; Matheu, R.; Peñafiel, I.; Moonshiram, D.; Blondeau, P.; Benet-Buchholz, J.; García-Antón, J.; Sala, X.; Godard, C.; Llobet, A. Supporting Information: A Million Turnover Molecular Anode for Catalytic Water Oxidation. *Angew. Chem. Int. Ed.* **2016**, *55* (49), 15382–15386. https://doi.org/10.1002/anie.201609167.

(143) Wang, D.; Wang, L.; Brady, M. D.; Dares, C. J.; Meyer, G. J.; Meyer, T. J.; Concepcion, J. J. Self-Assembled Chromophore-Catalyst Bilayer for Water Oxidation in a Dye-Sensitized Photoelectrosynthesis Cell. *J. Phys. Chem. C* **2019**, *123* (50), 30039–30045. https://doi.org/10.1021/acs.jpcc.9b07125.

(144) Chen, Z.; Concepcion, J. J.; Jurss, J. W.; Meyer, T. J. Single-Site, Catalytic Water Oxidation on Oxide Surfaces. *J. Am. Chem. Soc.* **2009**, *131* (43), 15580–15581. https://doi.org/10.1021/ja906391w.

(145) Kirner, J. T.; Finke, R. G. Water-Oxidation Photoanodes Using Organic Light-Harvesting Materials: A Review. *J. Mater. Chem. A* **2017**, *5* (37), 19560–19592. https://doi.org/10.1039/c7ta05709a.

(146) Wang, Q.; Domen, K. Particulate Photocatalysts for Light-Driven Water Splitting: Mechanisms, Challenges, and Design Strategies. *Chem. Rev.* **2020**, *120* (2), 919–985. https://doi.org/10.1021/acs.chemrev.9b00201.

(147) O'Regan, B.; Grätzel, M. A Low-Cost, High-Efficiency Solar Cell Based on Dye-Sensitized Colloidal TiO2 Films. *Nature* **1991**, *353* (6346), 737–740. https://doi.org/10.1038/353737a0.

(148) Alibabaei, L.; Luo, H.; House, R. L.; Hoertz, P. G.; Lopez, R.; Meyer, T. J. Applications of Metal Oxide Materials in Dye Sensitized Photoelectrosynthesis Cells for Making Solar Fuels: Let the Molecules Do the Work. *J. Mater. Chem. A* **2013**, *1* (13), 4133. https://doi.org/10.1039/c2ta00935h.

(149) Treadway, J. A.; Moss, J. A.; Meyer, T. J. Visible Region Photooxidation on TiO 2 with a Chromophore−Catalyst Molecular Assembly. *Inorg. Chem.* **1999**, *38* (20), 4386–4387. https://doi.org/10.1021/ic990466m.

(150) Sathre, R.; Scown, C. D.; Morrow, W. R.; Stevens, J. C.; Sharp, I. D.; Ager, J. W.; Walczak, K.; Houle, F. A.; Greenblatt, J. B. Life-Cycle Net Energy Assessment of Large-Scale Hydrogen Production via Photoelectrochemical Water Splitting. *Energy Environ. Sci.* **2014**, *7* (10), 3264–3278. https://doi.org/10.1039/c4ee01019a.

(151) Wang, D.; Marquard, S. L.; Troian-Gautier, L.; Sheridan, M. V.; Sherman, B. D.; Wang, Y.; Eberhart, M. S.; Farnum, B. H.; Dares, C. J.; Meyer, T. J. Interfacial Deposition of Ru(II) Bipyridine-Dicarboxylate Complexes by Ligand Substitution for Applications in Water Oxidation Catalysis. *J. Am. Chem. Soc.* **2018**, *140* (2), 719–726. https://doi.org/10.1021/jacs.7b10809.

(152) Wang, D.; Sheridan, M. V.; Shan, B.; Farnum, B. H.; Marquard, S. L.; Sherman, B. D.; Eberhart, M. S.; Nayak, A.; Dares, C. J.; Das, A. K.; Bullock, R. M.; Meyer, T. J. Layer-by-Layer Molecular Assemblies for Dye-Sensitized Photoelectrosynthesis Cells Prepared by Atomic Layer Deposition. *J. Am. Chem. Soc.* **2017**, *139* (41), 14518–14525. https://doi.org/10.1021/jacs.7b07216.

(153) Sherman, B. D.; Xie, Y.; Sheridan, M. V.; Wang, D.; Shaffer, D. W.; Meyer, T. J.; Concepcion, J. J. Light-Driven Water Splitting by a Covalently Linked Ruthenium-Based Chromophore–Catalyst Assembly. *ACS Energy Lett.* **2017**, *2* (1), 124–128. https://doi.org/10.1021/acsenergylett.6b00661.

(154) Eberhart, M. S.; Wang, D.; Sampaio, R. N.; Marquard, S. L.; Shan, B.; Brennaman, M. K.; Meyer, G. J.; Dares, C.; Meyer, T. J. Water Photo-Oxidation Initiated by Surface-Bound Organic Chromophores. *J. Am. Chem. Soc.* **2017**, *139* (45), 16248–16255. https://doi.org/10.1021/jacs.7b08317.

(155) Moore, G. F.; Blakemore, J. D.; Milot, R. L.; Hull, J. F.; Song, H. E.; Cai, L.; Schmuttenmaer, C. A.; Crabtree, R. H.; Brudvig, G. W. A Visible Light Water-Splitting Cell with a Photoanode Formed by Codeposition of a High-Potential Porphyrin and an Iridium Water-Oxidation Catalyst. *Energy Environ. Sci.* **2011**, *4* (7), 2389–2392. https://doi.org/10.1039/c1ee01037a.

(156) Zhao, Y.; Swierk, J. R.; Megiatto, J. D.; Sherman, B.; Youngblood, W. J.; Qin, D.; Lentz, D. M.; Moore, A. L.; Moore, T. A.; Gust, D.; Mallouk, T. E. Improving the Efficiency of Water Splitting in Dye-Sensitized Solar Cells by Using a Biomimetic Electron Transfer Mediator. *Proc. Natl. Acad. Sci. U. S. A.* **2012**, *109* (39), 15612–15616. https://doi.org/10.1073/pnas.1118339109.

(157) Sheridan, M. V.; Sherman, B. D.; Coppo, R. L.; Wang, D.; Marquard, S. L.; Wee, K. R.; Murakami Iha, N. Y.; Meyer, T. J. Evaluation of Chromophore and Assembly Design in Light-Driven Water Splitting with a Molecular Water Oxidation Catalyst. *ACS Energy Lett.* **2016**, *1* (1), 231–236. https://doi.org/10.1021/acsenergylett.6b00142.

(158) Hisatomi, T.; Domen, K. Reaction Systems for Solar Hydrogen Production via Water Splitting with Particulate Semiconductor Photocatalysts. *Nat. Catal.* **2019**, *2* (5), 387–399. https://doi.org/10.1038/s41929-019-0242-6.

(159) Wang, Z.; Li, C.; Domen, K. Recent Developments in Heterogeneous Photocatalysts for Solar-Driven Overall Water Splitting. *Chem. Soc. Rev.* **2019**, *48* (7), 2109–2125. https://doi.org/10.1039/C8CS00542G.

(160) Wolff, C. M.; Frischmann, P. D.; Schulze, M.; Bohn, B. J.; Wein, R.; Livadas, P.; Carlson, M. T.; Jäckel, F.; Feldmann, J.; Würthner, F.; Stolarczyk, J. K. All-in-One Visible-Light-Driven Water Splitting by Combining Nanoparticulate and Molecular Co-Catalysts on CdS Nanorods. *Nat. Energy* **2018**, *3* (10), 862–869. https://doi.org/10.1038/s41560-018-0229-6.

(161) Ye, S.; Chen, R.; Xu, Y.; Fan, F.; Du, P.; Zhang, F.; Zong, X.; Chen, T.; Qi, Y.; Chen, P.; Chen, Z.; Li, C. An Artificial Photosynthetic System Containing an Inorganic Semiconductor and a Molecular Catalyst for Photocatalytic Water Oxidation. **2016**, *338*, 168–173. https://doi.org/10.1016/j.jcat.2016.02.024.

(162) Niu, F.; Shen, S.; Wang, J.; Guo, L. Engineering Interfacial Energetics : A Novel Hybrid System of Metal Oxide Quantum Dots and Cobalt Complex for Photocatalytic Water Oxidation. *Electrochim. Acta* **2016**, *212*, 905–911. https://doi.org/10.1016/j.electacta.2016.07.091.

Chapter 2

Objectives

Chapter 2.

II

In face of the consequences of human activity on the Earth system, Chapter 1 introduced a variety of scientific and technical solutions for the sunlight-driven transformation of water and CO_2 into chemical fuels. Indeed, natural photosynthesis is a great inspiration for scientists because all mechanisms of light absorption, charge transfer, and final catalysis have been combined efficiently. As discussed, the tremendous progress in the field of molecular catalysts for water oxidation has led researchers to take the next step. Yet, their integration with light-absorbers on practical supports, all stable under such oxidation conditions, is of a holistic challenge. For that reason, the final goal of this thesis is to study and analyze a wide range of systems that combine different light-absorbing materials, such as dyes, inorganic and organic semiconductors, with highly active molecular water oxidation catalysts. The aim is to add progress in the field and to analyze the *pros*- and *cons*- of each system in order to define a line of future research.

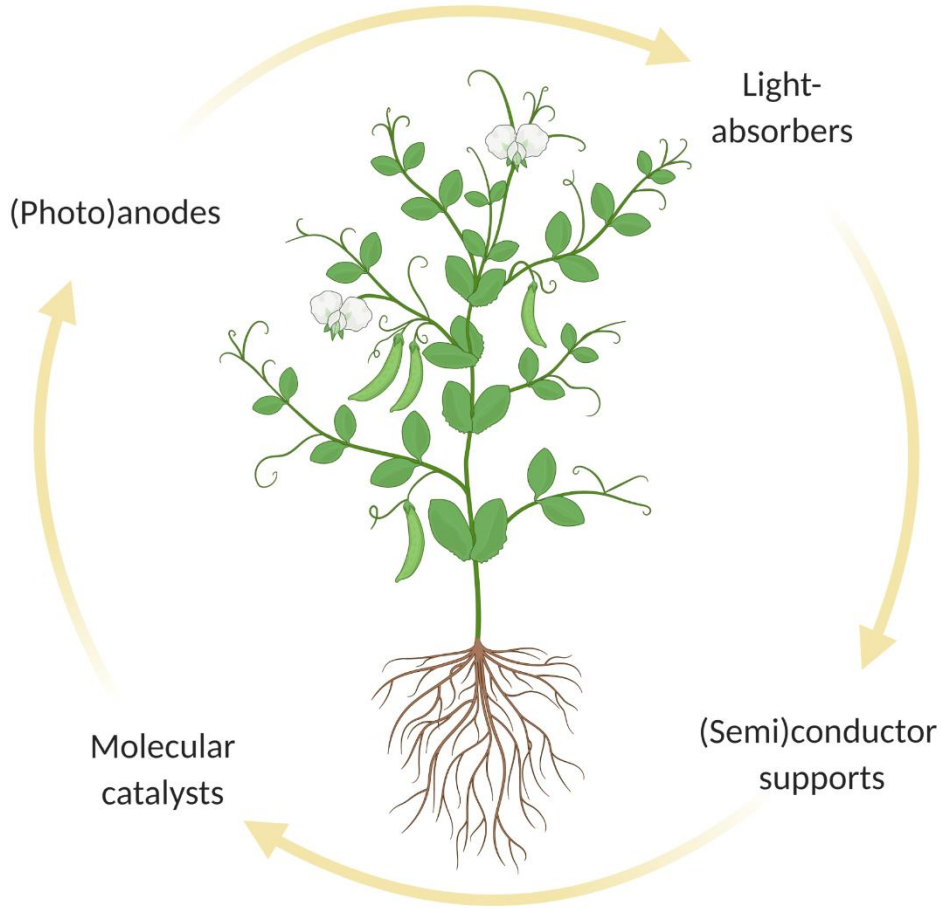

II

Objective 1

To functionalize a highly active Ru-based complex for water oxidation with a thiophene group for later electropolymerization on graphitic materials. The aim is to generate a Ru-modified polythiophene polymeric layer as illustrated in Figure 1. Heterogenization of molecular catalysts is essential for their incorporation in useful (photo)electrochemical cells. This anchoring is of particular interest because of the good conductivity and high resistance to oxidation of polythiophene polymers.

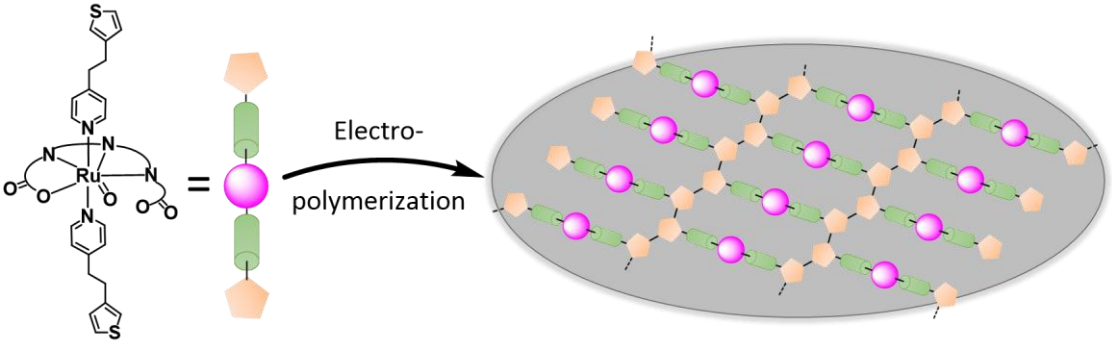

Figure 1. Schematic drawing of the functionalized Ru-based complex (left) and the polythiophene material derived from its electropolymerization (right) on a graphitic material.

Objective 2

To combine the state-of-the-art in water oxidation molecular catalysts with organic dyes as the first step towards homogeneous light-driven water oxidation catalysis. This strategy aims for efficient visible light absorption and electron transfer, together with high catalytic activity to overcome the kinetic barrier of the reaction. Organic dyes of the family of 4,4-Difluoro-4-bora-3a,4a-diaza-*s*-indacene (BODIPY, Figure 2) can be stable under harsh oxidative conditions and are promising candidates to bring the Ru-based molecular catalyst to its active high oxidation states, which trigger the catalysis. Thus, two BODIPY dyes will be tested in combination with Ru-based molecular catalysts, in the presence and the absence of a sacrificial agent, for homogeneous water oxidation to dioxygen.

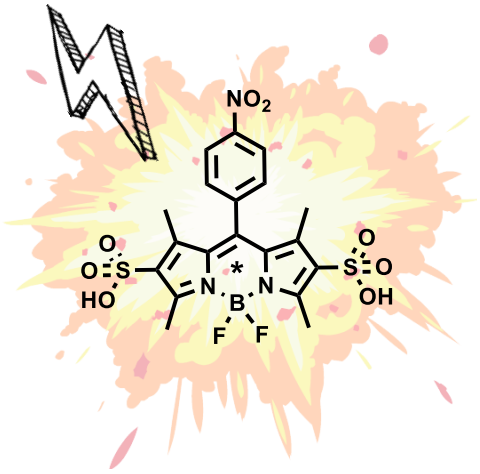

Figure 2. Example of BODIPY dye employed in this work.

II

Objective 3

To build a photoanode using widely available and earth-abundant materials for its ultimate incorporation into Dye-Sensitized Photoelectrochemical Cells (DSPECs). We aim to incorporate an organic dye of the perylenediimide family (purple in Figure 3) with a first-row macrocyclic Cu-complex (orange in Figure 3) on semiconductor nanoparticles of Antimony doped Tin Oxide (ATO, blue nanoparticles in Figure 3) at the top of a transparent conductive oxide substrate. The structural and electronic interaction of the molecular catalyst/dye/support is the target of study along with the photocatalytic performance.

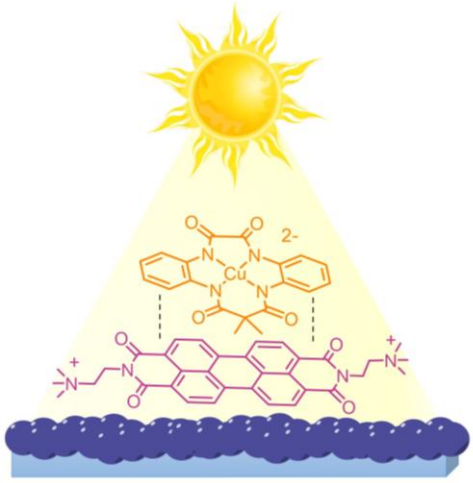

Figure 3. Photoanode made of a molecular water oxidation catalyst (orange), an organic dye (purple) on semiconductor nanoparticles at a transparent conductive substrate (blue).

Objective 4

To synthesize and characterize a new library of Covalent Triazine Frameworks (CTFs, Figure 4), expanding the narrow scope of conjugated polymers as colloidal photocatalysts for water oxidation. Stability issues and band alignment with the catalyst required for the reaction are the main constraints in this field. We aim at tackling these issues by selecting monomers that allow: (i) engineering of the valence band position; (ii) anchoring of highly active molecular catalysts that through the extraction of oxidative charges can perform the oxidation of water and hinder decomposition.

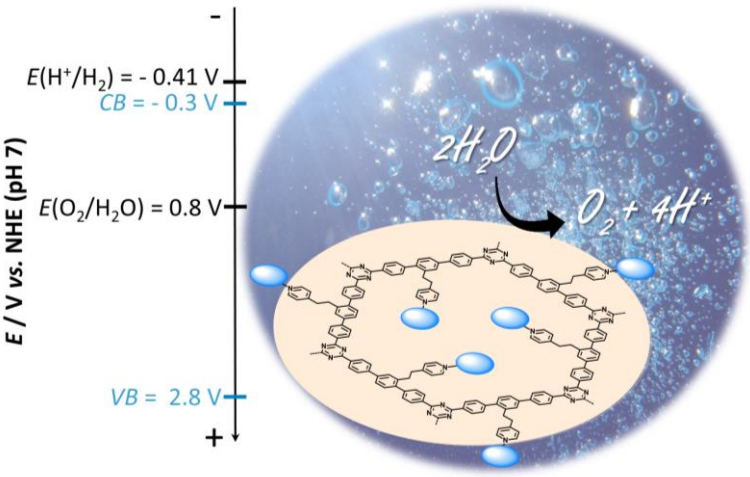

Figure 4. CTF's basic structure with a covalently attached molecular catalyst (blue balls) for the water oxidation reaction. On the left, energy levels for conduction band (CB), valence band (VB), and thermodynamic potential for water oxidation and proton reduction.

II

Objective 5

To build a hybrid colloidal photocatalyst in the shape of a modular platform. The design consists of three main components: (i) robust light-absorbing inorganic nanocrystals; (ii) a highly efficient molecular water oxidation catalyst; (iii) carbon nanotubes as conductive support to anchor and connect both (Figure 5). This design provides versatility and rational adjustments of each component independently.

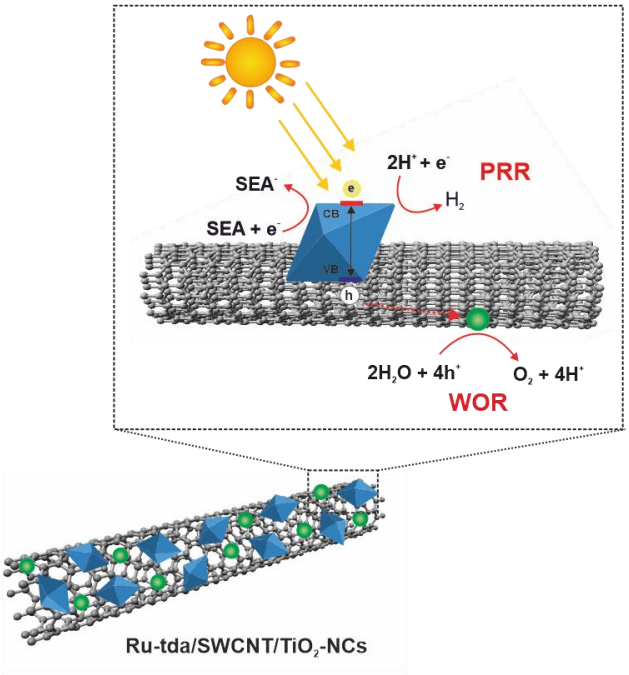

Figure 5. Design for a hybrid colloidal photocatalyst composed of light-absorbing inorganic nanocrystals (octahedrons in blue), water oxidation catalysts (green spheres), on conductive support (carbon nanotube in grey).

Chapter 3

An anode based on a molecular Ru water oxidation catalyst covalently bonded to polythiophene

Chapter 3.

III

An anode based on a molecular Ru water oxidation catalyst covalently bonded to polythiophene

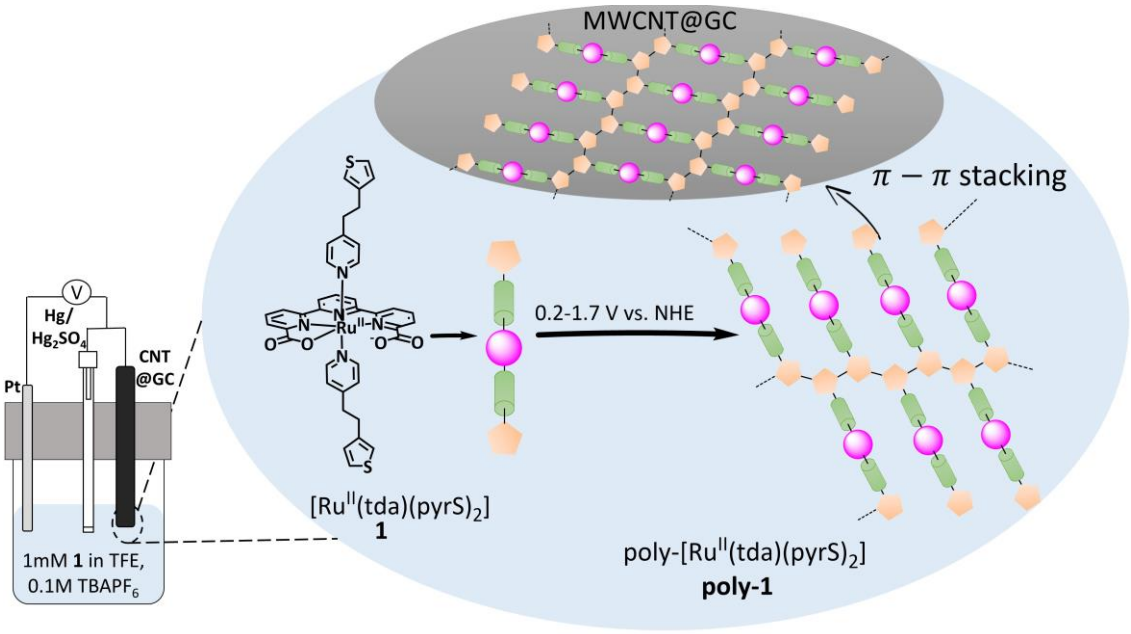

Abstract

The current challenge in the field of homogeneous water oxidation is to incorporate the catalysts into technologically useful devices such as electrolyzers and/or Photoelectrochemical Cells (PEC). Towards this goal, we present a derivative of the family of Ru-tda complexes containing pyridyl axial ligands functionalized with a thiophene group, [Ru(tda)(pyrS)], **1** (tda^{2-} is [2,2':6',2''-terpyridine]-6,6''-dicarboxylate, and pyrS is 4-[2-(thiophen-3-yl)ethyl]pyridine). Exposed to sufficiently anodic potentials, the thiophene group polymerizes at the surface of graphitic electrodes, generating the corresponding polythiophene material, **poly-1**@CNT@GC, and **poly-1**@CFP (CNT is Carbon Nanotubes, GC is Glassy Carbon Electrode, CFP is Carbon Fiber Paper). The active species, **poly-1-OH**@CNT@GC and **poly-1-OH**@CFP, are generated after an activation step consisting of E_{app} = 1.25 V (V *vs.* NHE, pH 7) for 500 s in basic solution. These Ru-tda functionalized polythiophenes can achieve current densities of 90 $mA \cdot cm^{-2}$ at 1.45 V (V vs. NHE) and Turnover Numbers (TONs) over 20,000 in 4 hours, which ranks among the best molecular anodes described up to now.

Contributions:

Marta Ventosa synthesized the molecular complex and performed its electropolymerization on CNT@GC. The resulting molecular anodes were studied by electrochemistry and oxygen detection experiments.

3.1 Introduction

The present rate of consumption of fossil fuels from our society is the main responsible for the increase of CO_2 concentration in the atmosphere,[1] leading to global warming and its catastrophic consequences.[2] To fix this situation, the generation of clean and renewable fuels is urgently needed. A potential option is the generation of solar fuels based on water oxidation coupled to either proton or CO_2 reduction using sunlight as the only external energy input.[3–5] To achieve this goal, one of the key challenges to be controlled and mastered is the oxidation of water to molecular oxygen. Therefore, robust and efficient Water Oxidation Catalysts (WOCs) are needed so to be coupled with light-absorbing molecules or materials.[6–8]

From a molecular perspective, the best WOCs described up to now are based on Ru complexes coordinated to Flexible Adaptative Multidentate Equatorial (FAME) ligands, including the family of Ru-tda and Ru-bda coordination complexes (tda^{2-} is [2,2':6',2''-terpyridine]-6,6''-dicarboxylate and bda^{2-} is [2,2'-bipyridine]-6,6'-dicarboxylate), mainly developed under homogeneous catalytic conditions.[9–11] The current challenge in the field is to incorporate these catalysts into technologically useful devices based on electrolyzers and/or photoelectrochemical cells (PEC).[6,12] Towards this goal WOCs must be anchored on conductive and/or semiconductive surfaces so that efficient molecular (photo)anodes can be created. The anchoring is important because it simplifies the construction engineering as opposed to using homogeneous phase catalysts in factual devices.[13,14,15] Several strategies have been developed for the anchoring of WOCs into surfaces including covalent bonding,[16–19] polymerization into insoluble but conductive polymers such as polythiophenes (poly-S)[20] or polypyrroles (poly-P),[21,22] and supramolecular interactions such as CH-π,[23] π-π[24] or aliphatic interactions by the use of bilayers.[25]

Here on we present our results using Ru-tda and poly-S. The latter has a wide range of applications in the field of organic electronic devices, such as transistors, light-emitting diodes, solar cells, sensors, and capacitors.[26] Polythiophenes are of particular interest in the field of water oxidation because of their good conductivity and high resistance to oxidation.[27] This fact is contrary to the previously reported non-oxidatively robust

materials,[13] that decompose under the harsh reaction conditions. Further, poly-S are promising materials in the emerging field of semiconducting polymers.[27,28] The semiconductive nature of some would allow generating a copolymer with a WOC monomer resulting in a solid-state dyad.

III

3.2 Results

3.2.1 Synthesis and structure of the monomeric complex 1

The synthetic strategy followed to prepare the monomer [Ru^{II}(tda)(pyrS)$_2$], **1**, (pyrS is 4-[2-(thiophen-3-yl)ethyl]pyridine) is outlined in Scheme 1 and uses [Ru(tda)(dmso)(H_2O)], (dmso is dimethyl sulfoxide), as a synthetic intermediate.[29]

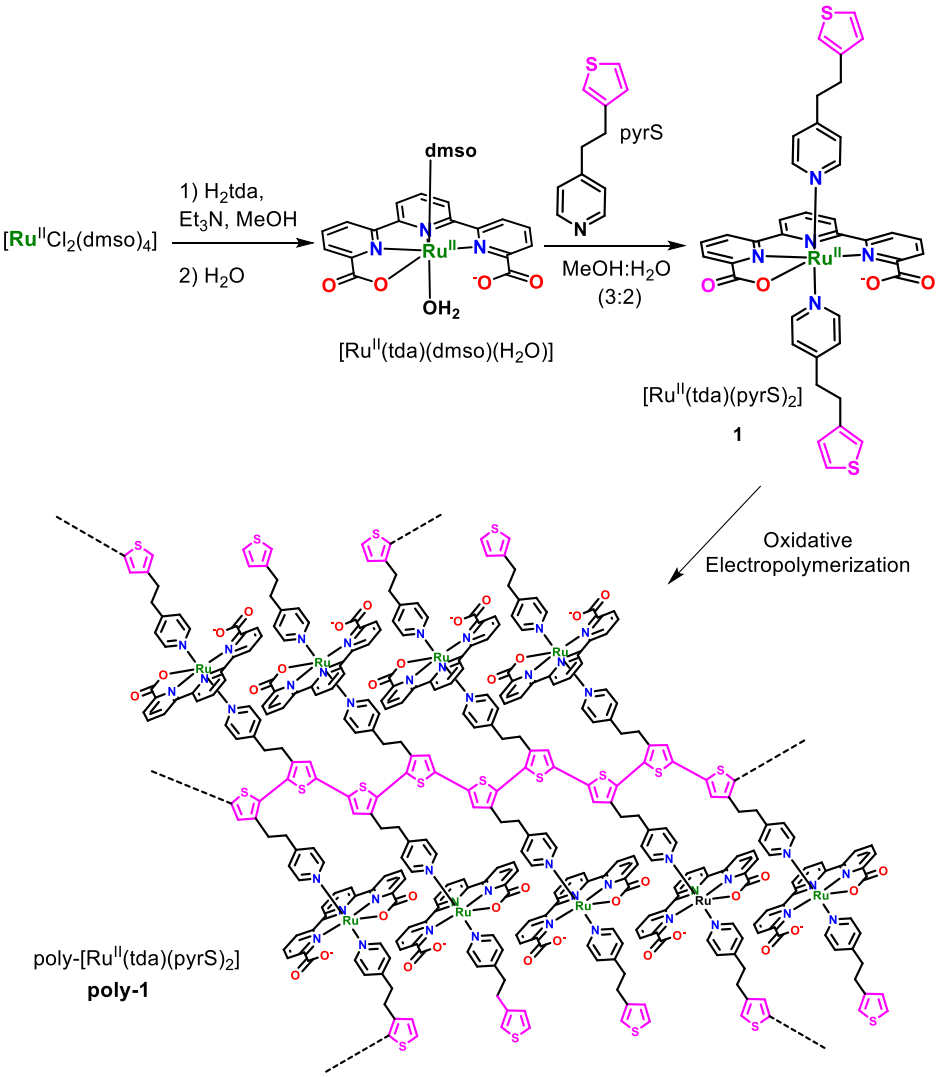

Scheme 1. Synthetic strategy with labelling scheme. Abbreviations are as follows: tda^{2-} is [2,2':6',2"-terpyridine]-6,6"-dicarboxylate; pyrS is 4-[2-(thiophen-3-yl)ethyl]pyridine); dmso is dimethyl sulfoxide.

Addition of pyrS to [Ru(tda)(dmso)(H_2O)] in MeOH:H_2O (3:2) produces the substitution of the axial ligands leading to **1** in 56 % overall yield. Sufficiently good crystals of **1** for X-ray diffraction analysis were grown by slow diffusion of ether to a methanol solution of **1** (0.2 mM). Figure 1 shows the ORTEP plot of **1** drawn at 50% probability where the metal center adopts a pseudo-octahedral geometry as expected for a Ru(II) low spin d^6 ion with the tda^{2-} ligand bonding in a k-N^3O fashion, and thus leaving one of the carboxylates groups non bonded to Ru. The rest of the positions are occupied by the pyrS ligand coordinated through the pyridyl groups.

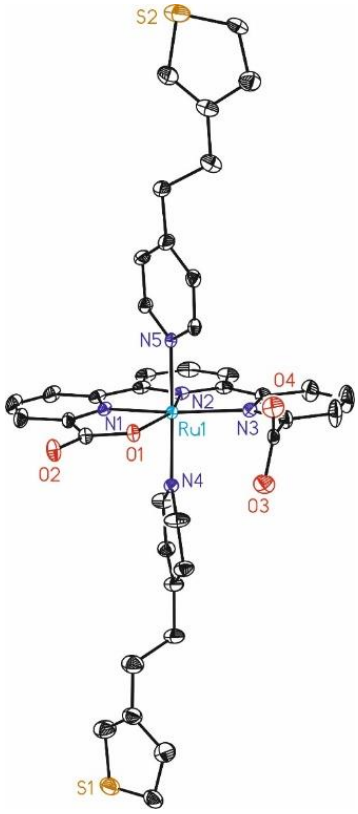

*Figure 1. ORTEP drawing (thermal ellipsoids 50 %) showing the structure of [Ru(tda-k-N^3O)($pyrS)_2$], **1**. Solvent molecules and hydrogen atoms have been omitted for the sake of clarity.*

In solution, complex **1** was characterized by UV-vis and Nuclear Magnetic Resonance spectroscopy (NMR) as shown in Figure 2 and the Supporting Information (SI). The NMR spectroscopy displays a set of resonances that are assigned based on their chemical shift, integration, multiplicity, and the 2D COSY spectra (Figure S6). As can be observed in Figure 2, the resonances that appear in the ^{1}H-NMR spectrum are consistent with a C_{2v} geometry for **1**. This is due to the dynamic behavior of this molecule in MeOH where the tda^{2-} carboxylate groups synchronically coordinate and de-coordinate very fast from

the metal center. A similar phenomenon has also been observed for the related complex $[Ru^{II}(tda)(py)_2]$, **2**, (py is pyridine).[29,30]

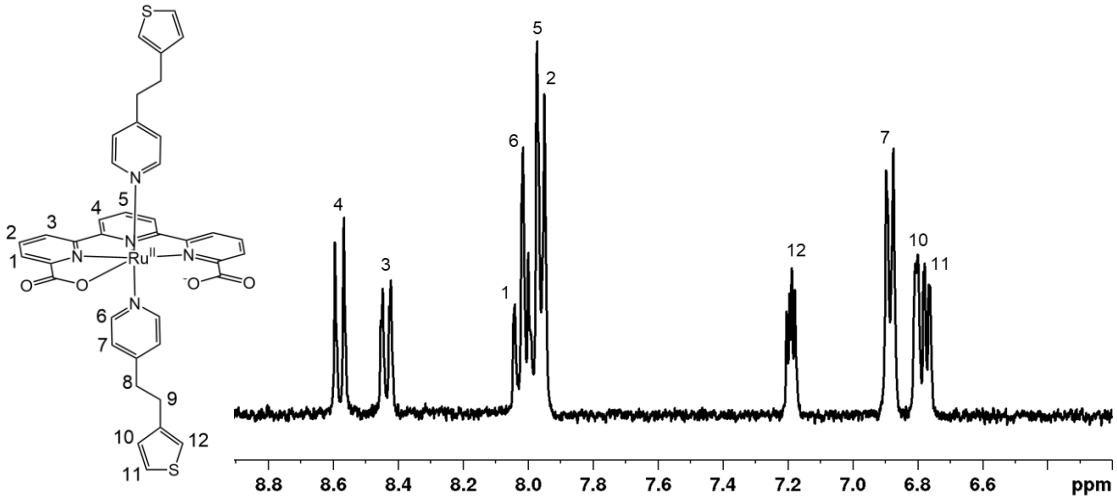

Figure 2. Aromatic region of the ^{1}H NMR spectrum of $[Ru(tda)(pyrS)_2]$ in $[d_4]$-methanol at 298 K.

3.2.2 Electrochemical properties and electropolymerization

The redox properties of **1** were investigated by electrochemical techniques including Cyclic Voltammetry (CV), Differential Pulse Voltammetry (DPV), Linear Sweep Voltammetry (LSV), Bulk Electrolysis (BE), and Chronocoulometry (CC). The latter was studied using a Rotating Ring Disk Electrode (RRDE). The electrochemical experiments were performed using a Glassy Carbon Electrode (GC) or a Carbon Fiber Paper (CFP) electrode (280 ± 30 µm thickness), as Working Electrodes (WE), a Pt mesh as a Counter Electrode (CE), and Hg/Hg_2SO_4 as a Reference Electrode (RE). All redox potentials in this work are reported *vs.* NHE by adding 0.6 V to the measured potential.

To increase the loading of functionalized polythiophene on the GC working electrode, multiwall Carbon Nanotubes (CNTs, see SI for details) were deposited on top of the GC by drop-casting generating CNT@GC. Carbon fiber paper was also used in this direction, allowing comparison of stability between graphitic substrates.

The CV of **1** in Trifluoroethanol (TFE) at CNT@GC is displayed in Figure 3. The first cycle shows the presence of two waves associated with the Ru(III)/Ru(II) and Ru(IV)/Ru(III) redox couples at 0.58 V ($E_{p,a}$ = 0.66 V; $E_{p,c}$ = 0.50 V) and 1.13 V ($E_{p,a}$ = 1.23 V; $E_{p,c}$ = 1.03 V) respectively, analogous to the previously described for $[Ru^{II}(tda)(py)_2]$, **2**, at pH 7.[30]

However, upon repetitive cycling in the range of 0.245-1.745 V (50 cycles), the intensity of these waves progressively increases consistent with the anodic electropolymerization of the thiophene group and thus, generating a polymeric material **poly-1** on the surface of the electrode, from now on regarded as **poly-1**@CNT@GC (Scheme 1).

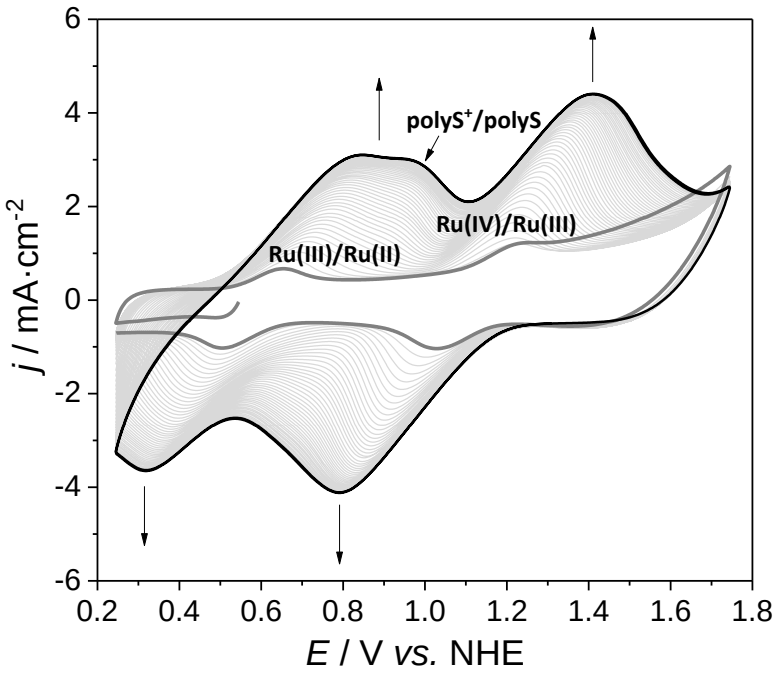

*Figure 3. Electropolymerization of 1.0 mM [Ru(tda)(pyrS)$_2$], **1**, in TFE (0.1M TBAPF$_6$ as supporting electrolyte) consisting of 50 consecutive CV cycles (from 0.245 to 1.745 V, starting at open circuit potential E_i = 0.52 V and scanning cathodically at 50 mV·s^{-1}). Three-electrode set-up was employed with CNT@GC as WE, Pt as CE and Hg/Hg$_2$SO$_4$ as RE.*

Typical oxidative electropolymerization of thiophene derivatives is described in the literature in the range of 0.7-2.9 V depending on the monomer's substituent groups.[27,31,32] As shown in Figure 3, a new wave associated with the electroactivity of the polythiophene film in **poly-1**@CNT@GC, is observed approximately at $E_{p,a}$ = 0.8 V that overlaps with the anodic peak of the Ru(III)/Ru(II) and the cathodic peak of the Ru(VI)/Ru(III) waves. This wave, which is clearly detected in TFE, is not observed in H_2O due to the widening of the redox couples in water or the slow electron transfer of the latter.[27,31,32]

The red trace in Figure 4 shows the electrochemical behavior of the **poly-1**@CNT@GC electrode transferred to a clean pH 7 phosphate buffer (phbf) solution. As it can be observed, IV/III and III/II waves of the ruthenium centers are very well defined even under the restricted translational mobility of the anchored catalyst within the

polythiophene network. Based on the charge under the Ru(III)/Ru(II) reductive wave, a surface loading of Γ = 43.5 nmols·cm^{-2} is obtained based on the Ru complex (Equation S3). Similarly, the same experiments were carried out with the CFP electrode generating **poly-1**@CFP, as can be observed in Figure S1 in the SI.

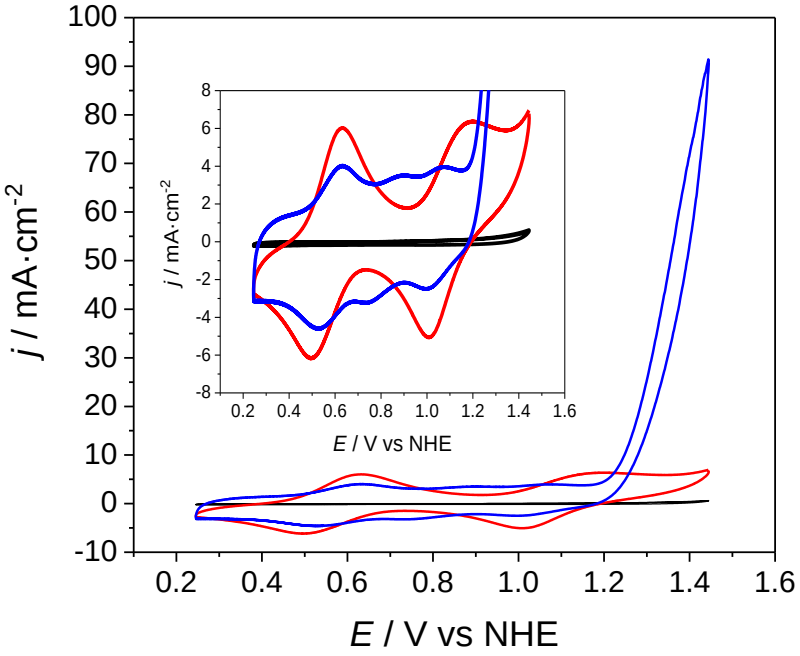

*Figure 4. Cyclic voltammetry experiments (v = 100 mV·s^{-1}) in a pH 7 phbf solution using **poly-1**@CNT@GC (Γ = 43.5 nmols·cm^{-2}; red line), **poly-1-OH**@CNT@GC (Γ = 3.8 nmols·cm^{-2}; blue line) and for the blank CNT@GC (black line) as working electrodes (Pt as CE and Hg/Hg$_2$SO$_4$ as RE). All the CVs were under the same conditions except for **poly-1-OH**@CNT@GC that a 90% iR compensation was applied.*

3.2.3 Performance as a molecular electroanode for water oxidation

The **poly-1**@CNT@GC described in the previous section contains a catalyst precursor that needs to be activated to generate the species responsible for water oxidation catalysis. This activation involves the coordination of a hydroxido ligand to the Ru metal center generating a Ru(IV)-OH group that is in equilibrium with its precursor as indicated in the equation below,

$$\text{Ru(IV)} + \text{OH} \leftrightarrow \text{Ru(IV)-OH} \qquad \text{(Equation 1)}$$

This process is favored under basic pH and turnover conditions. For this purpose, the electrode containing **poly-1**, that is, **poly-1**@CNT@GC is placed in a pH 11.6 solution under an applied potential of 1.25 V for 500 s. This generates **poly-1-OH**@CNT@GC that is then rinsed with a copious amount of water. The electroactivity of this new electrode

poly-1-OH@CNT@GC is studied in a fresh pH 7 phbf solution and the results are reported in Figure 4 (blue trace).

As it can be observed during the activation process two new redox couples appear with $E_{1/2}$ values at approximately 0.60 V (overlapped with the catalyst precursor) and at 0.80 together with a catalytic wave in the range of 1.2-1.4 V for **poly-1-OH**@CNT@GC. The initial precursor is partially converted into the active species as evidenced by the partial disappearance of its Ru(IV/III) redox couple at $E_{1/2}$ = 1.10 V. The molar loss that has occurred during this process can also be observed in the new waves. Assuming that the new waves correspond to a one-electron process, it gives a loading of Γ = 3.8 nmols·cm^{-2} for **poly-1-OH**@CNT@GC. It is interesting to note here that in the activation process approximately 90% of the Ru complex deposited at the electrode is lost whereas the same process for the CFP is reduced to only 30% (Figure S1). It thus points out that the main mass loss is associated with the CNTs detaching from the GC surface under these harsh conditions.

However, even with the partial loss of the initial Ru content the water oxidation catalytic activity for the new **poly-1-OH**@CNT@GC is remarkable with a current density reaching 90 mA·cm^{-2} at 1.45 V. To further kinetically characterize this catalytic process, a Foot Of the Wave Analysis (FOWA)[33,34] was carried out giving a TOF_{max} of 8,800 s^{-1} (Figure S3) in line with related Ru-tda complexes and electrodes.[23,30]

The **poly-1-OH** was also prepared at a Glassy Carbon plate electrode (GC_{plate}, 1 cm^2 active area), which was previously modified by drop-casting CNT. As a result, the anode **poly-1-OH**@CNT@GC_{plate} (Γ = 1 nmol·cm^{-2}) was generated. A Bulk Electrolysis (BE) experiment using an H cell was performed with the new anode **poly-1-OH**@CNT@GC_{plate} as working electrode at an applied potential E_{app} = 1.345 V for 1 h (Pt grid as CE, Hg/Hg_2SO_4 as RE). At the headspace of the working compartment, a Clark electrode was placed, so that oxygen concentration could be measured during the experiment. Figure 5 left, shows the *j vs*. t (red) and *Q vs*. t (blue) traces recorded, whereas Figure 5 right displays the oxygen evolution profile obtained during the BE. During this experiment, a total charge of 3.3 C was passed that corresponds to 34.2 µmols of electrons and thus, 8.6 µmols of O_2 assuming 100% Faradaic Efficiency (Figure 5 left). The oxygen measured in this experiment is 7.1 µmols, which implies a Faradaic Efficiency of 83% (FE, Figure 5 right).

Similar values were also obtained using an RRDE electrode by LSV as shown in the SI (Figure S10). Based on the oxygen generated together with the mols of catalyst used (Γ = 1 nmol·cm^{-2}) Turnover Numbers (TONs) of 7,100 cycles are obtained during the first hour.

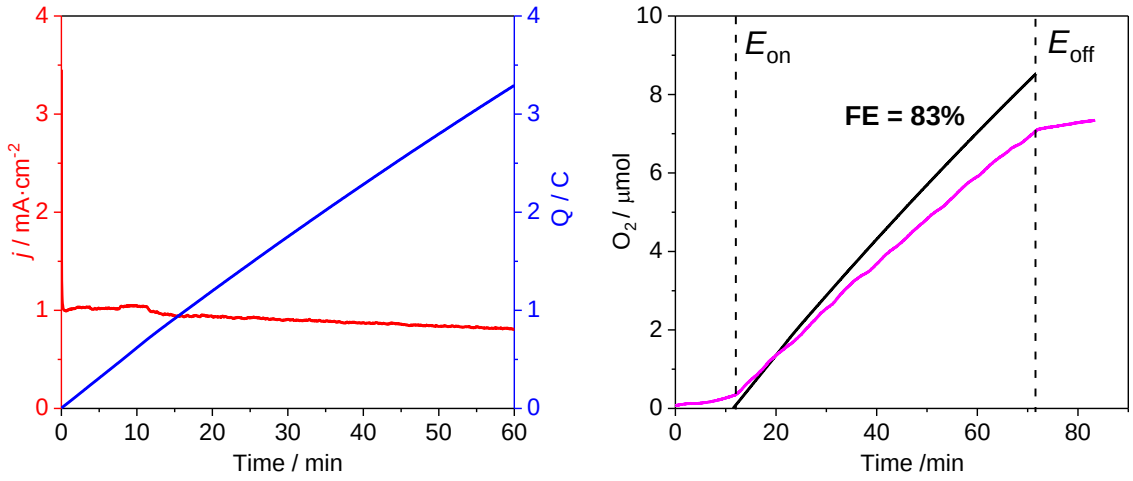

*Figure 5. Left, j vs. t (red line) and Q vs. t (blue line) curves obtained in the bulk electrolysis experiment carried out for **poly-1-OH**@CNT@GCplate (Γ = 1 nmol·cm^{-2}, S(C_{plate}) = 1 cm^2) at E_{app} = 1.345 V for 1 h, immersed in a 15 mL pH 7 phbf solution (CE, Pt mesh; RE, Hg/Hg_2SO_4) in an H cell with a glass frit separating the two compartments (gas phase V = 10 mL in the WE compartment). Right, oxygen was detected from the BE using a Clark electrode in the headspace of the working compartment (pink trace) together with the expected oxygen based on the charge passed of 3.26 C assuming 100% Faradaic efficiency (black trace). At minute 80 the Faradaic efficiency reached a value of 83%.*

BE was also performed on **poly-1-OH**@CNT@GC (Γ = 3.71 nmol·cm^{-2}, Figure S11), under the same conditions as in the previous experiment. During the 4 h BE at 1.345 V, a total charge of 9.1 C was passed, and by assuming an 83% FE (from BE and RRDE experiments), that corresponds to a remarkable 20,591 TONs.

The stability of the functionalized electrodes is highly dependent on the conductive support. While certain degradation is observed in the case of the CNT@GC electrodes leading to FE of approximately 83 %, this is not the case of the CFP electrodes, which give FE of 100 % (Figure S9). Thus, these results suggest that the main factor accounting for the loss of efficiency is the oxidation of the CNT@GC electrode and not the degradation of the **poly-1** material. They also highlight the robustness of the polythiophene scaffold and the Carbon Fiber Paper, which might play promising roles in the development of future anodes and photoanodes for water oxidation. Importantly, CV analysis before and after catalysis shows that the ruthenium species is unaltered

(Figure S11). Although the loss of the intensity of the Ru(III/II) and Ru(IV/III) waves and the catalysis is observed, no new species that could be associated with catalyst degradation are formed. The loss of intensity is most likely due to CNT detachment from the GC surface, a phenomenon that has already been observed before for other CNT@GC electrodes functionalized with ruthenium water oxidation catalysts.

3.3 Discussion

From a technological perspective, the use of solid-state anodes containing the corresponding catalyst attached to their surface significantly simplifies PEC engineering as opposed to using these catalysts in the homogeneous phase. [13,14,15] It is thus important to design strategies to anchor catalysts onto solid supports that provide robust and long-lasting performance. In the present work a Ru water oxidation catalyst was anchored through the electropolymerization of a thiophene-based monomer on CNTs and CFPs generating **poly-1-OH**@CNT@GC and **poly-1-OH**@CFP respectively. Table 1 provides valuable data regarding the performance of **poly-1-OH** as a molecular anode, together with related data for other relevant molecular anodes using different monomers and anchoring strategies. These include covalent bonding,[16–19] polymerization into insoluble but conductive polymers such as polythiophenes (poly-S)[20] or polypyrroles (poly-P),[21,22] and supramolecular interactions such as CH-π,[23] π-π[24] or self-assembled aliphatic bilayers.[25]

The main parameters describing the performance of the Ru-tda catalyst anchored via three different strategies are gathered in entries 1, 2, and 3 of Table 1. If we focus on the catalyst's loading (Γ column), the CH-π anchoring gives the largest values (Γ = 16 ± 1.5 nmols·cm^{-2}) whereas the π-π stacking gives the lowest (Γ = 0.55 nmols·cm^{-2}). The CH-π and π- π interactions generate a monolayer at the surfaces of the graphitic material contrary to the conductive polymers based on poly-S and poly-P. The polymer's morphology depends on the polymerization conditions such as type of substrate, monomer concentration, potential applied, and time of applied potential. As a consequence, the molar deposition obtained for poly-S in entries 1 and 1' differ by more than an order of magnitude. For the Ru-bda analogs based on poly-S and poly-P, entries 4 and 5, display a loading deposition of 0.90 and 0.40 nmols·cm^{-2} respectively. For the

dinuclear complex $[Ru_2(\mu\text{-bpp})(\mu\text{-OAc})(t\text{-trpy})_2]^{2+}$ based on poly-P (entry 9, where bpp is bis[pyridine]pyrazolate and trpy is 2,2':6',2''-terpyridine), a remarkable value of 4.6 nmols·cm^{-2} is achieved. Finally, the covalent phosphonate bonding in $[Ru(Mebimpy)(4,4'\text{-}((HO)_2\text{-}OPCH_2)_2\text{-}bpy)(OH_2)]^{2+}$ (entry 8, where Mebimpy is 2,6-bis[1-methylbenzimidazol-2-yl]pyridine and bpy is 2,2'-bipyridine) gives the lowest values of only 0.12 nmols·cm^{-2}, about two orders of magnitude lower than in the CH-π case. However, by using a highly porous electrode, such as n-TiO_2/n-SnO_2/FTO, the deposition increases up to 21 nmols·cm^{-2} (entry 6).

Another interesting parameter described in Table 1 is the current densities (*j* in mA·cm^2) achieved by the catalysts at the top of their electrocatalytic wave that range from 240 to 0.015 mA·cm^{-2}. However, given the porosity of the electrodes, this value is a composite of at least three factors: the loading deposition capacity, the intrinsic water oxidation electrocatalytic activity of each catalyst, and the water diffusion into the active center. To obtain the intrinsic activity of the catalyst, current densities are normalized by the molar deposition and are presented in the *J* column in units of mA·nmol^{-1}. For the Ru-tda derivatives, the *J* values oscillate between 16.7-19.6 mA·nmol^{-1} (entries 1, 2, and 3 in Table 1) where the highest value is for **poly-1-OH**@CNT@GC (entry 1). This can be potentially associated with the higher hydrophilicity of the material that embeds the catalytically active Ru center. This data suggests that in all the Ru-tda anodes reported (except for the CFP), the main factor influencing performance is their intrinsic activity and to a lesser extent their hydrophilicity that can favor water diffusion into the porous material. Indeed, for the CFP, whose loading is much lower (entry 1', in Table 1), a value of 50 mA·nmol^{-1} is obtained, which reflects the higher degree of access of water molecules at the Ru active site. Similar conclusions can be derived from the Ru-bda case, with values of 2.8 and 6.6 mA·nmol^{-1} (entries 4, 5). Interestingly, the trimer $[Ru(bda)(bpb)]_3$ (entry 7) has a value of 20 mA·nmol^{-1}, that is about 3-7 times higher than for their related monomers (entries 4, 5). Presumably, this is because in the solid surface it evolves to a new active species, $[Ru(H_2O)_2(bda\text{-}\kappa\text{-}NO)(bpb)]_3$, with two aquo ligands coordinated to the Ru center, showing higher intrinsic activity compared to the typical Ru-bda precursor with only one aquo ligand. In sharp contrast, for [Ru(Mebimpy)(4,4'-

$((HO)_2\text{-}OPCH_2)_2\text{-}bpy)(OH_2)]^{2+}$ (entry 8) the value obtained is 0.13 $mA{\cdot}nmol^{-1}$, which is about two orders of magnitude less active than the Ru-tda catalysts

Another important factor to take into consideration when building an anode is the long-term stability under turnover conditions, which can be roughly estimated from the TONs reported for each system. As observed for Ru-tda complexes (entries 1, 2, and 3), the π-π, the CH-π, and the poly-S give a million, 200,000, and 20,591 cycles respectively. Finally, the catalyst anchored via the PO_3^{2-} moiety (entry 8) achieves a remarkable TON of 11,000 cycles for 8 h of experiment. Here the stability of the molecular anode is compromised by the presence of the unavoidable supporting electrolyte buffer in aqueous solutions that competes for the same surface anchoring site as the catalyst, as previously reported in the literature.[13,35]Unfortunately, the activity of the Ru-bda family of catalyst anchored via the bilayer approach (entry 6, Table 1) cannot be properly compared because no detailed results of their electrocatalytic activity have been reported so far.[36]

Entry[ref]	Catalyst or Catalyst precursor[b]	Anchoring group[c]	Electrode[d]	pH	Γ / nmol·cm^{-2}	j (mA·cm^{-2}) @ E_{cat} (V)[e]	J / $mA{\cdot}nmol^{-1}$	E vs RHE	TOFs[j] /s^{-1}	TONsx10^{-3}
1[tw,a]	poly-[Ru(OH)(tda)(pyrS)$_2$]	Poly-S	CNT@GC	7.0	3.8	90 (1.40)	23.7 (19.6)[f]	1.86	8.8x10^3	20.6 (4h)
1',[tw]	poly-[Ru(OH)(tda)(pyrS)$_2$]	Poly-S	CFP	7.0	0.3	15 (1.40)	50	1.86	7.0x10^3	50.8 (0.5h)
2[23]	{[Ru(tda)(4,4'-bpy)]$_{15}$(4,4'-bpy)}	Ar-CH	CNT@GC	7.0	16.0	240 (1.40)	16.5	1.86	8.1x10^3	200 (12h)
3[24]	[Ru(tda)(OH)(pypA)$_2$]	Pyrene	CNT@GC	7.0	0.55	10.5 (1.40)	19.1	1.86	8.9x10^3	1000 (12h)
4[20]	poly-[Ru(bda)(F-Isoq)(pyrS)]	Poly-S	BPG	7.2	0.96	2.0 (1.20)	2.8[g]	1.65	3.98	5.2 (7h)
5[21]	poly-[Ru(bda)(py-pyr)$_2$]	Poly-P	BPG	7.2	0.42	2.8 (1.30)	6.6[g]	1.6	10.47	31.6 (1h)
6[36]	[Ru(bda)(4-(C_5H_{11})-py)$_2$]/[Ru(4,4'-(C_7H_{15})$_2$-bpy)(4,4'-(PO_3H_2)$_2$-bpy)$_2$]$^{2+}$	R-PO_3^{2-}	n-TiO_2/n-SnO_2/FTO	4.6	21.0	1.8 (1.40)[h]	0.1	1.3	5x10^{-5},[i]	0.53 (3h)[i]
7[37]	[($Ru(H_2O)_2$(bda-κ-NO)(bpb)]$_3$	π–π & CH–π	CNT@GC	7.0	8.4	168 (1.40)	20	1.86	3.2x10^3	1800 (6h)
8[38]	[Ru(Mebimpy)(4,4'-(($HO)_2$-$OPCH_2$)$_2$-bpy)(OH_2)]$^{2+}$	R-PO_3^{2-}	n-ITO/FTO	5.0	0.12	0.015 (1.85)	0.13	2.15	0.36	11 (8h)
9[22]	[Ru_2(μ-bpp)(μ-OAc)(t-trpy)$_2$]$^{2+}$	Poly-P	VCS	1.0	4.6	--	--	--	--	0.041

Table 1. Catalytic performance of poly-1-OH@CNT@GC and poly-1-OH@CFP compared to other selected Ru WOCs anchored on conductive surfaces.a) tw means this work. b) bbpy, 2,2'-bipyridine; pypA, 4-(pyren-1-yl)-N-(pyridin-4-ylmethyl)butanamide; bpy-$CH_2PO_3H_2$, ([2,2'-bipyridine]-4,4'-diylbis(methylene))bis(phosphonic acid); bda, 2,2'-bipyridine–6,6'–dicarboxylate; F-Isoq, 6-fluroisoquinoline; pyrS, 4-(2-(thiophen-3-yl)ethyl)pyridine; py-pyr is 4-(pyren-1-yl)pyridine; py, pyridine; 4,4'-PO_3H_2-bpy, 4,4'-diphosphonate- 2,2'-bipyridine; bpb, 1,2-bis(pyridine-2-carboxamido)benzenate; Mebimpy, 2,6-bis(1-methylbenzimidazol-2-yl)pyridine; bpp, 3,5-bis(2-pyridyl)pyrazolato; μ-OAc, acetato bridging ligand; t-tpy, 4'-(p-pyrrolylmethylphenyl)-2,2':6',2''-terpyridine. c) Poly-P, polypyrrole. d) CNT, Multi Walled Carbon Nanotubes; CFP, carbon fiber paper; GC, glassy carbon; BPG, basal-plane pyrolytic graphite; n-TiO2, nano-TiO2; FTO, fluorinated tin oxide; n-ITO, nano-Indium Tin Oxide; VCS, vitreous carbon sponge. e) Taken from the top of the electrocatalytic wave (E vs. NHE, pH 7). f) FE corrected. g) Orientative only, because key data is not available or reliable. h) Corrected value removing the intensity associated with $[Ru(bpy)_3]^{2+}$ moiety in Figure S6a. i) TOFs and TONs based on photocatalytic experiments. j) Measured using FOWA for entries 1-4 and 7, and other methodologies for the rest.

3.4 Conclusions

In this work, we have described the preparation and characterization of a new member of the family of Ru-tda complexes containing pyridyl axial ligands functionalized with a thiophene group, [Ru(tda)(pyrS)], **1**. This complex exposed to sufficiently anodic potentials polymerizes at the surface of graphitic materials generating electrodes **poly-1**@CNT@GC and, **poly-1**@CFP, with a polythiophene material functionalized with the Ru water oxidation catalyst precursor on the top of its surface. Exposing this material at E_{app} = 1.25 V for 500 s in basic solution generates the active species, **poly-1-OH**@CNT@GC, and **poly-1-OH**@CFP, that behave as efficient and robust molecular water oxidation anodes. When compared to the main reported molecular anodes in the literature, **poly-1-OH**@CNT@GC shows the highest intrinsic activity of the catalyst (*J* in units of $mA \cdot nmol^{-1}$). Besides, this new material can achieve maximum current densities of 90 $mA \cdot cm^{-2}$ at 1.45 V and TONs over 20,000 in just 4 h. However, the attachment of CNT on carbon electrodes is one of the main constraints for long-term stability. Therefore, other graphitic substrates such as CFP should be further studied for practical applications. Moreover, the resulting functionalized polymer is a promising candidate to be coupled with semiconductors in a PEC, taking advantage of the (semi)conductive nature of some polythiophenes.

3.5 References

(1) Steffen, W.; Rockström, J.; Richardson, K.; Lenton, T. M.; Folke, C.; Liverman, D.; Summerhayes, C. P.; Barnosky, A. D.; Cornell, S. E.; Crucifix, M.; Donges, J. F.; Fetzer, I.; Lade, S. J.; Scheffer, M.; Winkelmann, R.; Schellnhuber, H. J. Trajectories of the Earth System in the Anthropocene. *Proc. Natl. Acad. Sci. U. S. A.* **2018**, *115* (33), 8252–8259. https://doi.org/10.1073/pnas.1810141115.

(2) IPCC, 2018: Global Warming of 1.5°C. An IPCC Special Report on the impacts of global warming of 1.5°C above pre-industrial levels and related global greenhouse gas emission pathways, in the context of strengthening the global response to the threat of climate change, sustainable development, and efforts to eradicate poverty [Masson-Delmotte, V., P. Zhai, H.-O. Pörtner, D. Roberts, J. Skea, P.R. Shukla, A. Pirani, W. Moufouma-Okia, C. Péan, R. Pidcock, S. Connors, J.B.R. Matthews, Y. Chen, X. Zhou, M.I. Gomis, E. Lonnoy, T. Maycock, M. Tignor, and T. Waterfield (eds.)]. In Press.

(3) Berardi, S.; Drouet, S.; Francàs, L.; Gimbert-Suriñach, C.; Guttentag, M.; Richmond, C.; Stoll, T.; Llobet, A. Molecular Artificial Photosynthesis. *Chem. Soc. Rev.* **2014**, *43* (22), 7501–7519. https://doi.org/10.1039/C3CS60405E.

(4) Nocera, D. G. Solar Fuels and Solar Chemicals Industry. *Acc. Chem. Res.* **2017**, *50* (3), 616–619. https://doi.org/10.1021/acs.accounts.6b00615.

(5) De Luna, P.; Hahn, C.; Higgins, D.; Jaffer, S. A.; Jaramillo, T. F.; Sargent, E. H. What Would It Take for Renewably Powered Electrosynthesis to Displace Petrochemical Processes? *Science* **2019**, *364* (6438). https://doi.org/10.1126/science.aav3506.

(6) Niu, F.; Wang, D.; Li, F.; Liu, Y.; Shen, S.; Meyer, T. J. Hybrid Photoelectrochemical Water Splitting Systems: From Interface Design to System Assembly. *Adv. Energy Mater.* **2020**, *10* (11), 1–24. https://doi.org/10.1002/aenm.201900399.

(7) Sun, K.; Moreno-Hernandez, I. A.; Schmidt, W. C.; Zhou, X.; Crompton, J. C.; Liu, R.; Saadi, F. H.; Chen, Y.; Papadantonakis, K. M.; Lewis, N. S. A Comparison of the Chemical, Optical and Electrocatalytic Properties of Water-Oxidation Catalysts for Use in Integrated Solar-Fuel Generators. *Energy Environ. Sci.* **2017**, *10* (4), 987–1002. https://doi.org/10.1039/C6EE03563A.

(8) Zahran, Z. N.; Tsubonouchi, Y.; Mohamed, E. A.; Yagi, M. Recent Advances in the Development of Molecular Catalyst-Based Anodes for Water Oxidation toward Artificial Photosynthesis. *ChemSusChem.* **2019**, *12*, 1775–1793. https://doi.org/10.1002/cssc.201802795.

(9) Matheu, R.; Ertem, M. Z.; Gimbert-Suriñach, C.; Sala, X.; Llobet, A. Seven Coordinated Molecular Ruthenium–Water Oxidation Catalysts: A Coordination Chemistry Journey. *Chem. Rev.* **2019**, *119* (6), 3453–3471. https://doi.org/10.1021/acs.chemrev.8b00537.

(10) Vereshchuk, N.; Matheu, R.; Benet-Buchholz, J.; Pipelier, M.; Lebreton, J.; Dubreuil, D.; Tessier, A.; Gimbert-Suriñach, C.; Z. Ertem, M.; Llobet, A. Second Coordination Sphere Effects in an Evolved Ru Complex Based on a Highly Adaptable Ligand Results in Rapid Water Oxidation Catalysis. *J. Am. Chem. Soc.* **2020**, *142* (11), 5068–5077. https://doi.org/10.1021/jacs.9b11935.

(11) Matheu, R.; Garrido, P.; Gil-Sepulcre, M.; Sala, X.; Gimbert-Suriñach, C.; Llobet, A. The Development of Molecular Water Oxidation Catalysts. *Nat. Rev. Chem.* **2019**, *2* (3), 331–341. https://doi.org/10.1038/s41570-019-0096-0.

(12) Duan, L.; Tong, L.; Xu, Y.; Sun, L. Visible Light-Driven Water Oxidation - From Molecular Catalysts to Photoelectrochemical Cells. *Energy Environ. Sci.* **2011**, *4* (9), 3296–3313. https://doi.org/10.1039/c1ee01276b.

(13) Materna, K. L.; Crabtree, R. H.; Brudvig, G. W. Anchoring Groups for Photocatalytic Water Oxidation on Metal Oxide Surfaces. *Chem. Soc. Rev.* **2017**, *46* (20), 6099–6110. https://doi.org/10.1039/c7cs00314e.

(14) Bullock, R. M.; Das, A. K.; Appel, A. M. Surface Immobilization of Molecular Electrocatalysts for Energy Conversion. *Chem. - A Eur. J.* **2017**, *23* (32), 7626–7641. https://doi.org/10.1002/chem.201605066.

(15) Garrido-Barros, P.; Matheu, R.; Gimbert-Suriñach, C.; Llobet, A. Electronic, Mechanistic, and Structural Factors That Influence the Performance of Molecular Water Oxidation Catalysts Anchored on Electrode Surfaces. *Curr. Opin. Electrochem.* **2019**, *15*, 140–147. https://doi.org/10.1016/j.coelec.2019.04.027.

(16) Ernstorfer, R.; Gundlach, L.; Felber, S.; Storck, W.; Eichberger, R.; Willig, F. Role of Molecular Anchor Groups in Molecule-to-Semiconductor Electron Transfer. *J. Phys. Chem. B* **2006**, *110* (50), 25383–25391. https://doi.org/10.1021/jp064436y.

(17) Bangle, R.; Sampaio, R. N.; Troian-Gautier, L.; Meyer, G. J. Surface Grafting of Ru(II) Diazonium-Based Sensitizers on Metal Oxides Enhances Alkaline Stability for Solar Energy Conversion. *ACS Appl. Mater. Interfaces* **2018**, *10* (3), 3121–3132. https://doi.org/10.1021/acsami.7b16641.

(18) Bae, E.; Choi, W.; Park, J.; Shin, H. S.; Kim, S. Bin; Lee, J. S. Effects of Surface Anchoring Groups (Carboxylate vs Phosphonate) in Ruthenium-Complex-Sensitized TiO 2 on Visible Light Reactivity in Aqueous Suspensions. *J. Phys. Chem. B* **2004**, *108* (37), 14093–14101. https://doi.org/10.1021/jp047777p.

(19) Brennan, B. J.; Llansola Portolés, M. J.; Liddell, P. A.; Moore, T. A.; Moore, A. L.; Gust, D. Comparison of Silatrane, Phosphonic Acid, and Carboxylic Acid Functional Groups for Attachment of Porphyrin Sensitizers to TiO2 in Photoelectrochemical Cells. *Phys. Chem. Chem. Phys.* **2013**, *15* (39), 16605. https://doi.org/10.1039/c3cp52156g.

(20) Wang, L.; Fan, K.; Chen, H.; Daniel, Q.; Philippe, B.; Rensmo, H.; Sun, L. Towards Efficient and Robust Anodes for Water Splitting: Immobilization of Ru Catalysts on Carbon Electrode and Hematite by in Situ Polymerization. *Catal. Today* **2017**, *290*, 73–77. https://doi.org/10.1016/j.cattod.2016.07.011.

(21) Wang, L.; Fan, K.; Daniel, Q.; Duan, L.; Li, F.; Philippe, B.; Rensmo, H.; Chen, H.; Sun, J.; Sun, L. Electrochemical Driven Water Oxidation by Molecular Catalysts in Situ Polymerized on the Surface of Graphite Carbon Electrode. *Chem. Commun.* **2015**, *51* (37), 7883–7886. https://doi.org/10.1039/c5cc00242g.

(22) Mola, J.; Mas-Marza, E.; Sala, X.; Romero, I.; Rodríguez, M.; Viñas, C.; Parella, T.; Llobet, A. Ru-Hbpp-Based Water-Oxidation Catalysts Anchored on Conducting Solid Supports. *Angew. Chem.*

Int. Ed. **2008**, *47* (31), 5830–5832. https://doi.org/10.1002/anie.200704912.

(23) Hoque, M. A.; Gil-Sepulcre, M.; de Aguirre, A.; Elemans, J. A. A. W.; Moonshiram, D.; Matheu, R.; Shi, Y.; Benet-Buchholz, J.; Sala, X.; Malfois, M.; Solano, E.; Lim, J.; Garzón-Manjón, A.; Scheu, C.; Lanza, M.; Maseras, F.; Gimbert-Suriñach, C.; Llobet, A. Water Oxidation Electrocatalysis Using Ruthenium Coordination Oligomers Adsorbed on Multiwalled Carbon Nanotubes. *Nat. Chem.* **2020**, *12* (11), 1060–1066. https://doi.org/10.1038/s41557-020-0548-7.

(24) Creus, J.; Matheu, R.; Peñafiel, I.; Moonshiram, D.; Blondeau, P.; Benet-Buchholz, J.; García-Antón, J.; Sala, X.; Godard, C.; Llobet, A. A Million Turnover Molecular Anode for Catalytic Water Oxidation. *Angew. Chem. Int. Ed.* **2016**, *55* (49), 15382–15386. https://doi.org/10.1002/anie.201609167.

(25) Wang, L.; Polyansky, D. E.; Concepcion, J. J. Self-Assembled Bilayers as an Anchoring Strategy: Catalysts, Chromophores, and Chromophore-Catalyst Assemblies. *J. Am. Chem. Soc.* **2019**, *141* (L), 8020–8024. https://doi.org/10.1021/jacs.9b01044.

(26) Kaloni, T. P.; Giesbrecht, P. K.; Schreckenbach, G.; Freund, M. S. Polythiophene: From Fundamental Perspectives to Applications. *Chem. Mater.* **2017**, *29* (24), 10248–10283. https://doi.org/10.1021/acs.chemmater.7b03035.

(27) Blanchard, P.; Cravino, A.; Levillain, E. *Electrochemistry of Oligothiophenes and Polythiophenes*; 2009. https://doi.org/10.1002/9780470745533.ch9.

(28) Le, T. H.; Kim, Y.; Yoon, H. Electrical and Electrochemical Properties of Conducting Polymers. *Polymers.* **2017**, *9* (4). https://doi.org/10.3390/polym9040150.

(29) Matheu, R.; Benet-Buchholz, J.; Sala, X.; Llobet, A. Synthesis, Structure, and Redox Properties of a Trans -Diaqua Ru Complex That Reaches Seven-Coordination at High Oxidation States. *Inorg. Chem.* **2018**, *57*, 1757–1765. https://doi.org/10.1021/acs.inorgchem.7b02375.

(30) Matheu, R.; Ertem, M. Z.; Benet-Buchholz, J.; Coronado, E.; Batista, V. S.; Sala, X.; Llobet, A. Intramolecular Proton Transfer Boosts Water Oxidation Catalyzed by a Ru Complex. *J. Am. Chem. Soc.* **2015**, *137* (33), 10786–10795. https://doi.org/10.1021/jacs.5b06541.

(31) Kang, J. F.; Perry, J. D.; Tian, P.; Kilbey, S. M. Growth and Morphology of Polythiophene on Thiophene-Capped Monolayers: 1. Single Component Monolayers. *Langmuir* **2002**, *18* (26), 10196–10201. https://doi.org/10.1021/la020397f.

(32) Heinze, J.; Frontana-Uribe, B. A.; Ludwigs, S. Electrochemistry of Conducting Polymers - Persistent Models and New Concepts. *Chem. Rev.* **2010**, *110*, 4724–4771. https://doi.org/10.1021/cr900226k.

(33) Costentin, C.; Drouet, S.; Robert, M.; Savéant, J. M. Turnover Numbers, Turnover Frequencies, and Overpotential in Molecular Catalysis of Electrochemical Reactions. Cyclic Voltammetry and Preparative-Scale Electrolysis. *J. Am. Chem. Soc.* **2012**, *134* (27), 11235–11242. https://doi.org/10.1021/ja303560c.

(34) Matheu, R.; Neudeck, S.; Meyer, F.; Sala, X.; Llobet, A. Foot of the Wave Analysis for Mechanistic Elucidation and Benchmarking Applications in Molecular Water Oxidation Catalysis. *ChemSusChem.* **2016**, *9* (23), 3361–3369. https://doi.org/10.1002/cssc.201601286.

(35) Hyde, J. T.; Hanson, K.; Vannucci, A. K.; Lapides, A. M.; Alibabaei, L.; Norris, M. R.; Meyer, T. J.; Harrison, D. P. Electrochemical Instability of Phosphonate-Derivatized, ruthenium(III) Polypyridyl Complexes on Metal Oxide Surfaces. *ACS Appl. Mater. Interfaces* **2015**, *7* (18), 9554–9562. https://doi.org/10.1021/acsami.5b01000.

(36) Wang, D.; Wang, L.; Brady, M. D.; Dares, C. J.; Meyer, G. J.; Meyer, T. J.; Concepcion, J. J. Self-Assembled Chromophore-Catalyst Bilayer for Water Oxidation in a Dye-Sensitized Photoelectrosynthesis Cell. *J. Phys. Chem. C* **2019**, *123* (50), 30039–30045. https://doi.org/10.1021/acs.jpcc.9b07125.

(37) Schindler, D.; Gil-Sepulcre, M.; Lindner, J. O.; Stepanenko, V.; Moonshiram, D.; Llobet, A.; Würthner, F. Efficient Electrochemical Water Oxidation by a Trinuclear Ru(bda) Macrocycle Immobilized on Multi-Walled Carbon Nanotube Electrodes. *Adv. Energy Mater.* **2020**, *10* (43), 1–7. https://doi.org/10.1002/aenm.202002329.

(38) Chen, Z.; Concepcion, J. J.; Jurss, J. W.; Meyer, T. J. Single-Site, Catalytic Water Oxidation on Oxide Surfaces. *J. Am. Chem. Soc.* **2009**, *131* (43), 15580–15581. https://doi.org/10.1021/ja906391w.

3.6 Supporting Information

3.6.1 Materials and Methods

General considerations

All the materials were provided by Sigma-Aldrich unless for 4-[2-(thiophen-3-yl)ethyl]pyridine that was purchased from Chemspace and they have been used without further purification. [2,2':6',2''-terpyridine]-6,6''-dicarboxylic acid (H_2tda) and $RuCl_2DMSO_4$ were synthesized and purified according to the literature.[1] Multi-Walled Carbon Nanotubes (CNTs) were purchased from HeJi, Inc. (China) with > 95% purity, length ~10 μm and OD > 50 nm. The solvents were selected to be HPLC grade and high-purity water was acquired by passing distilled water through a nanopure Milli-Q water purification system. All the synthetic procedure was performed under N_2 atmosphere using vacuum-line techniques.

Preparation of phosphate buffer solutions:

The pH of all solutions was measured by a pHmeter.

pH = 7.0 buffered solution (1 M ionic strength): powders of NaH_2PO_4 (4.62 g, 0.038 M) and Na_2HPO_4 (7.54 g, 0.052 M) were dissolved with Mili-Q water up to 1 L solution.

pH = 12.0 buffered solution (0.1M ionic strength): powders of Na_2HPO_4 (10.293 g, 0.0073 M) and Na_3PO_4 (2.06 g, 0.0126 M) were dissolved with Mili-Q water up to 1 L solution.

General instrumentation

NMR Spectroscopy: A Bruker Avance 400 MHz or a Bruker 500 MHz were employed for recording ^{1}H NMR and ^{13}C NMR spectra. Chemical shifts (δ) are reported in ppm.

High-resolution mass spectrometry (HRMS): A ThermoFinnigan MAT95XL spectrometer was used for Chemical Ionization and a ThermoFisher Scientific LTQ-Orbitrap spectrometer for Electrospray ionization.

pH determination: A pH meter (Mettler Toledo, SevenCompact™ pH/Ion) was employed. Prior to determination, calibration with standard solutions of pH 4.01, 7.00, and 9.21 was performed.

Single Crystal XRD Methods:

- *Crystal preparation:* Crystals of **1** were grown by slow diffusion of diethyl ether into a methanol solution (0.2 mM). The crystal used for structure determination was selected employing a Zeiss stereomicroscope using polarized light and prepared under inert conditions immersed in perfluoropolyether as protecting oil for manipulation.
- *Data collection:* Crystal structure determination for **1** was carried out using an Apex DUO Kappa 4-axis goniometer equipped with an APPEX 2 4K CCD area detector,[2] a Microfocus Source E025 IuS using MoK_α radiation, Quazar MX multilayer Optics as monochromator, and an Oxford Cryosystems low-temperature device Cryostream 700 plus (T = -173 °C). Full-sphere data collection was used with ω and φ scans. Programs used: Data collection APEX-2,[2] data reduction Bruker Saint[3] V/.60A and absorption correction SADABS.[4]
- *Structure solution and refinement:* Crystal structure solution was achieved using the computer program SHELXT.[5] Visualization was performed with the program SHELXle.[6] Missing atoms were subsequently located from different Fourier syntheses and added to the atom list. Least-squares refinement on F2 using all measured intensities was carried out using the program SHELXL 2015.[5] All non-hydrogen atoms were refined including anisotropic displacement parameters.
- *Comments to the structure*: The asymmetric unit contains one molecule of the metalorganic compound and some molecules of toluene. In the main molecule, the thiophene-containing ligands are disordered in different orientations with ratios of (S1): 59:41 and (S2): 77:17:6. One of the carboxylate groups is disordered in two orientations with a ratio (60:40). In the two carboxylate groups contained in the main molecule, no hydrogen atoms could be localized, so that it was assumed that both are not protonated. The distances in the carboxylate group with the atoms C1, O1, O2 confirms that it is not protonated C1-O1: 1.29 Å (coordinated to the Ruthenium atom) and C1-O1: 1.22 Å. For the second group with the atoms C17 O3 O4, the distances cannot be considered due to the disorder observed. In the asymmetric unit, one of the toluene molecules has an occupancy of 0.5 and is disordered in two orientations shared through Ci-

symmetry with the neighboring asymmetric unit. A second position containing toluene could not be refined properly. In order to avoid this highly disordered solvent molecule, the program SQUEEZE was applied to remove it from the electron density.[7]

III

Electrochemical methods

All electrochemical experiments were conducted with a Cambria HI-730 bipotentiostat. All redox potentials herein reported are *versus* NHE (pH 7). $E_{1/2}$ values are an average of the oxidative and reductive peak (Equation S1) from Cyclic Voltammograms (CV).

$$E_{1/2} = \frac{(E_{p,c}+E_{p,a})}{2} \qquad \text{(Equation S1)}$$

Cyclic Voltammograms: Technique used for electropolymerization purposes, from **1** to **poly-1**. Afterward, CV was useful for redox potentials' determination and catalyst's activity (phosphate buffer in pH 7). A three-electrode set-up was used, consisting of: Hg/Hg_2SO_4 as the Reference Electrode (RE, K_2SO_4 saturated), platinum disk as the Counter Electrode (CE), and two types of Working Electrodes (WE): (i) a Carbon Fiber Paper, CFP (S = 5.9 cm^2), alike Gas Diffusion Layers (GDL), and (ii) a modified Glassy Carbon disk, GC_{disk} (ϕ = 0.3 cm, S = 0.07 cm^2). The latter was first polished with 0.05 µm alumina paste and rinsed with water and acetone. Afterward, 80 µmL of 1 $mg \cdot mL^{-1}$ CNT were drop-cast on the GC as reported[8] (CNT@GC). The majority of the CVs were *i*R compensated in all the measurements unless stated. CVs were recorded at 100 $mV \cdot s^{-1}$ for all the experiments, except for electropolymerization, which was done at 50 $mV \cdot s^{-1}$. For CVs, 20 mL vials were employed as electrochemical cell, which was sealed with a Teflon cap with holes for the 3 electrodes and the gas supply. For CVs in aqueous media, phosphate buffer solutions were employed of pH 7 (I = 1M) and pH 11.6 (I = 0.1 M). For electropolymerization, trifluoroethanol was used as a solvent with tetrabutylammonium hexafluorophosphate ($TBAPF_6$) as the supporting electrolyte (0.1M).

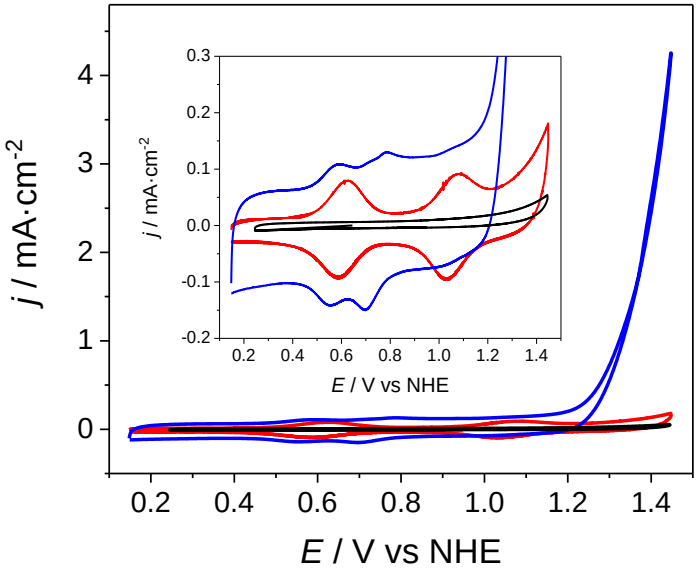

*Figure S1. Cyclic voltammetry experiments (v = 100 mV·s^{-1}) in a pH 7 phbf solution for **poly-1**@CFP (Γ = 0.49 nmols·cm^{-2}; red line), **poly-1-OH**@CFP (Γ = 0.37 nmols·cm^{-2}; blue line) and for the blank CFP (black line) as working electrodes (WE, CNT@GC; CE, Pt; RE, Hg/Hg$_2$SO$_4$), all under the same conditions.*

Bulk Electrolysis (BE): Electrochemical method employed to activate the precursor to form catalyst's aqua species (in phosphate buffer pH 11.6). Besides, BE combined with a Clark electrode for O_2 detection was employed to determine Faradaic Efficiency (FE) of **poly-1-OH**@CNT@GC and **poly-1-OH**@CFP by comparing theoretical and detected O_2 production (in pH 7 phosphate buffer). A two-compartment cell (25 mL per unit) was employed with a frit separating both compartments. A three-electrode set-up was employed: Hg/Hg_2SO_4 as the Reference Electrode (RE, K_2SO_4 saturated), platinum grid as the Counter Electrode (CE), and two types of Working Electrode (WE): (i) a Carbon Fiber Paper, CFP (S = 5.2 cm^2), and (ii) a modified Glassy Carbon plate, GC_{plate}, as working electrode (S = 1 cm^2). The latter was prepared by drop-casting 150 µmL of 1 mg·mL^{-1} CNT on one side of the GC_{plate} as previously done in[8] ($CNT@GC_{plate}$). No *i*R compensation was employed. Yet, the solution was continually stirred at 500 rpm.

Rotating Ring Disk Electrode (RRDE): This technique was used to detect FE of **poly-1-OH**@CNT@GC by Linear Sweep Voltammetry (LSV). Moreover, Chronocoulometry (CC) experiments using RRDE were employed for evaluating the stability of **poly-1-OH**@CNT@GC over time (Figure S12). A RRDE-3A from IJ-Cambria was employed with an electrode composed of a GC disk (WE1) and a Pt ring (WE2) electrodes and the following diameters: 7 mm outer, 5 mm middle, and 4 mm inner. Aside Pt mesh was

used as CE and Hg/Hg_2SO_4 as RE (K_2SO_4 saturated). The electrochemical set-up consists of a one-compartment cell with a Teflon top that closes hermetically with a specific hole for RRDE, two smaller ones for the CE and RE, and two thinner ones for the nitrogen flow tubes. All of them fitted tightly so that nitrogen atmosphere was maintained over the experiments with prior solution purged with nitrogen for 20 min. The electrodes were connected to an IJ-Cambria CHI-660 potentiostat for electrochemical measurements. The collection efficiency of the RRDE, N, was previously determined by using the redox couple $Fe(CN)_6^{4-}/Fe(CN)_6^{3-}$ as a one-electron transfer process (Figure S2).

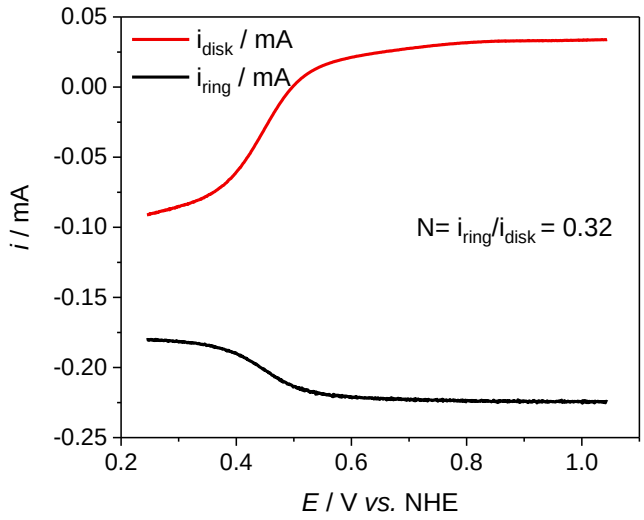

Figure S2. Experimental calculation of the RRDE's collection efficiency, N, by using the well behaved one-electron transfer process of $Fe(CN)_6^{4-}/Fe(CN)_6^{3-}$.

Foot of the wave analysis (FOWA): It was applied according to the *procedure* of Savéant *et al.* in the literature.[9] For heterogeneous water oxidation, Equation S2 was deduced for a mechanism consisting of a single chemical step coupled to a fast single electron transfer, both being responsible for the rate of the reaction.[8]

$$\frac{i}{Q_R} = \frac{k_{WNA}}{1+\exp(\frac{F(E°-E)}{RT})} \qquad \text{(Equation S2)}$$

Where R is the gas constant, T is the temperature, k_{WNA} is a pseudo constant, E° is the apparent potential for the Ru(V)/Ru(IV) redox couple, E is the applied potential, F is the faraday constant, i is the current intensity associated to $Ru(III)OH/Ru(II)OH_2$ redox couple, and Q_{Ru} is the charge under the charge of the cathodic wave of the $Ru(III)OH/Ru(II)OH_2$ redox couple. k_{WNA} is equivalent to TOF_{MAX} (s^{-1}), which is the

maximum turnover frequency that a molecule of catalyst can catalyze water oxidation when *E* tends to infinite potential.[9] It can be extracted from the plot of i/Q_R vs. 1/(1+exp[(F/RT)(E°-E)]) (Figure S3). This is valid for our electrocatalytic scheme, i.e. for a Water Nucleophilic Attack (WNA) mechanism in the heterogeneous phase.

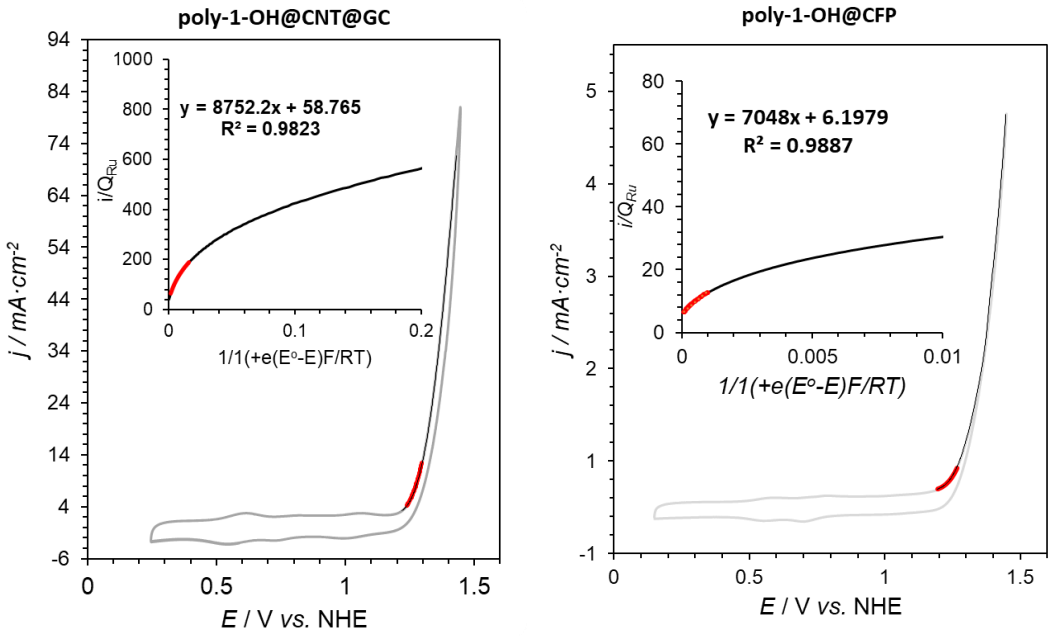

*Figure S3. CVs of **poly-1-OH**@CNT@GC (left) and **poly-1-OH**@CFP (right) in grey at pH 7 phosphate buffer (Pt as CE, Hg/Hg_2SO_4 as RE, 100 mV·s^{-1}). The data points used for analysis are from the foot of the wave of the catalysis,[8] which is represented in the inset graph assuming WNA mechanism (black line). The fitting points are represented by a red line in the inset, from where the rate constants are extracted, leading to a TOF_{max} = 8,752 s^{-1} for **poly-1-OH**@CNT@GC (left), and TOF_{max} = 7,048 s^{-1} for **poly-1-OH**@CFP (right).*

Surface coverage determination: The surface coverage (*Γ*) of **poly-1-OH**@CNT@GC and **poly-1-OH**@CFP was estimated by applying Equation S3:

$$\Gamma\ (mol \cdot g^{-1}) = \frac{Q}{n \cdot m \cdot F} \qquad \text{(Equation S3)}$$

Q is the charge under the reductive peak of the reversible, one-electron wave obtained by integration of the CV (Ru(III)/Ru(II)); *n* is the number of electrons involved in that reduction process, which is 1; *m* is the hybrid catalyst mass on the electrode and *F* is the Faradaic constant (96,485 C·mol^{-1}).

3.6.2 Synthetic procedures

Synthesis of [Ru(tda)(pyrS)$_2$], **1***:* The complex was synthesized following a modified reported procedure.[1] As described in Scheme S1, [Ru(II)Cl$_2$(DMSO)$_4$] is used as a

precursor, which was refluxed for 4h with a mixture of H_2tda and Et_3N in MeOH under N_2 atmosphere (step I). The intermediate brown solid was filtered and refluxed for three days in the presence of an excess of commercial ligand 4-[2-(thiophen-3-yl)ethyl]pyridine in a mixture of MeOH:H_2O under N_2 atmosphere (3:2) (step II). A dark purple precipitate was obtained and purified by column chromatography on silica gel using a mixture of MeOH:Et3N:TFE:DCM (5:3:10:100) as eluents (55.7% yield). ^{1}H-NMR (500Hz, [d_4] Methanol) δ: 2.78 (s, 8H), 6.78 (d, 2H), 6.8 (s, 2H), 6.89 (d, 4H), 7.19 (m, 2H), 7.98 (br, 9H), 8.49 (d, 2H), 8.59 (d, 2H). ^{13}C-NMR (500Hz, [d_4] Methanol) δ: 30.3, 35.5, 121.2, 122, 125.2, 125.4, 126.1, 128.1, 128.8, 133.8, 137.5, 142.0, 152.3, 153.5, 158.4, 159.6, 163.3, 172.9. ESI$^+$-HRMS m/z: calc. for [Ru(tda)(pyrS)$_2$] ($C_{39}H_{31}N_5O_4RuS_2^+$): 800, found m/z: 800.0933 (0.7 ppm). ESI$^+$-HRMS m/z: calc. for [Ru(tda)(pyrS)$_2$]-Na^+($C_{39}H_{31}N_5NaO_4RuS_2^+$): 822, found m/z: 822.0753 (0.7 ppm). *Anal.* Calc. *for [Ru(tda)(pyrS)$_2$]·0.5H2O·TFE*: C, 53.76%; H, 3.85 %; N, 7.65 %; S, 7.01%. Found: C, 54.07 %; H, 3.82 %; N, 7.69%; S, 7.37.

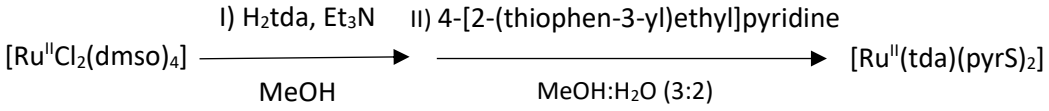

*Scheme S1. Synthetic proceadure for [Ru(tda)(pyrS)$_2$], **1**.*

Synthesis of [Ru(tda)(pyrS)$_2$]$_n$, **poly-1**: The polymer was obtained by electropolymerization of **1** on the working electrode following a modified procedure.[2] The electropolymerization was conducted using a typical three-electrode electrochemistry cell with Hg/Hg_2SO_4 as the reference electrode (RE), platinum as the counter electrode (CE), and a modified glassy carbon, GC_{disk}, or a modified carbon paper, CFP, as working electrode (WE). 80 µmL of 1 mg·mL^{-1} CNT were drop-cast on the GC as reported,[3] CNT@GC. The latter was 50 times cycled at scan rates of 50 mV·s^{-1} from -0.25 to 1.7 V (*vs.* NHE) in trifluoroethanol solution of 1mM **1** to form **poly-1**@CNT@GC (Figure 3 in the main text). Cyclic voltammograms, CVs, in Na_2HPO_4 buffer pH7 1M before and after modification of WE were performed to check if the Ru complex was anchored (Figure 4 in the main text). Two catalytic peaks appear on the WE after electropolymerization, corresponding to the redox waves of Ru^{II}/Ru^{III} ($E_{1/2}$ = 0.54 V) and Ru^{III}/Ru^{IV} ($E_{1/2}$ = 1.1 V *vs.* NHE) respectively.

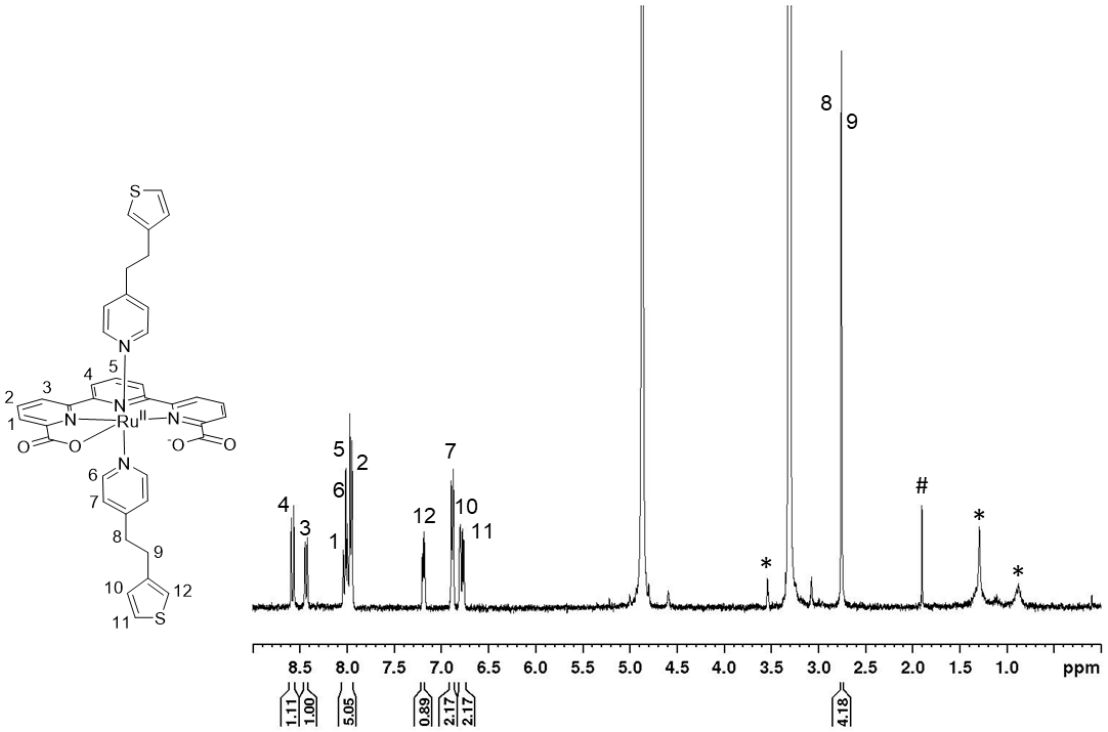

*Figure S4. [1]H NMR of **1** in [d4]-methanol, T = 298 K (# acetone, * Ethylene glycol).*

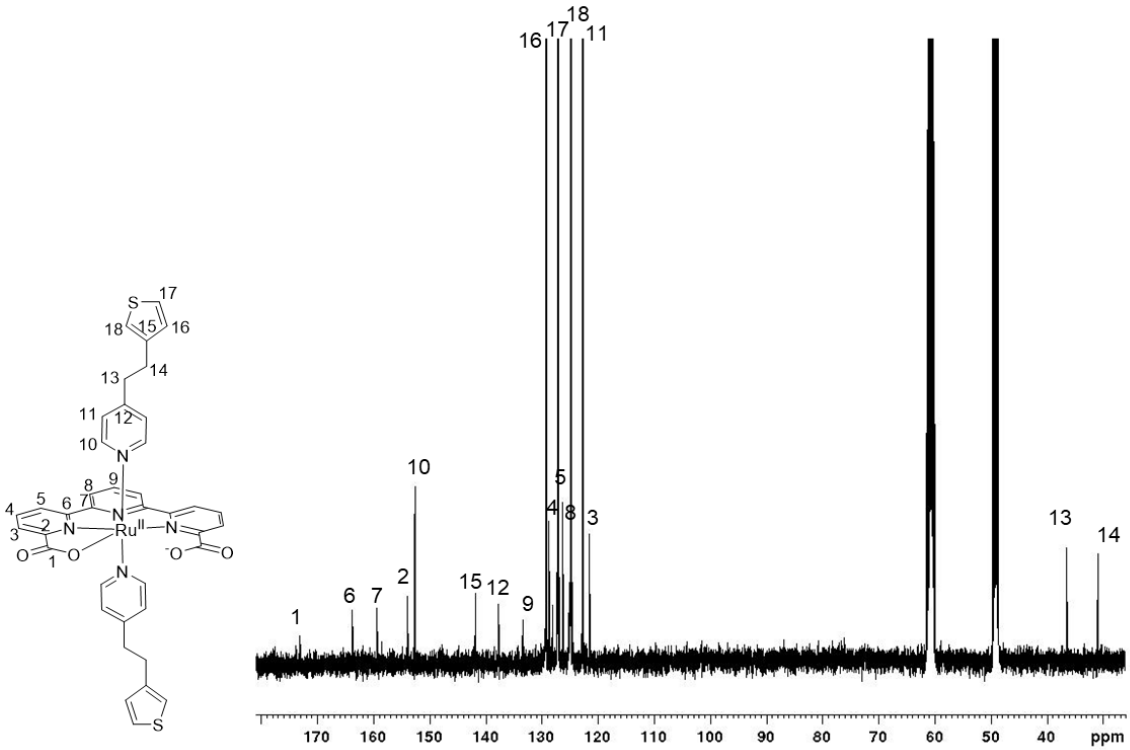

*Figure S5. [13]C-{H}-NMR (DEPT45) of **1** in [d4]-methanol, T = 298 K.*

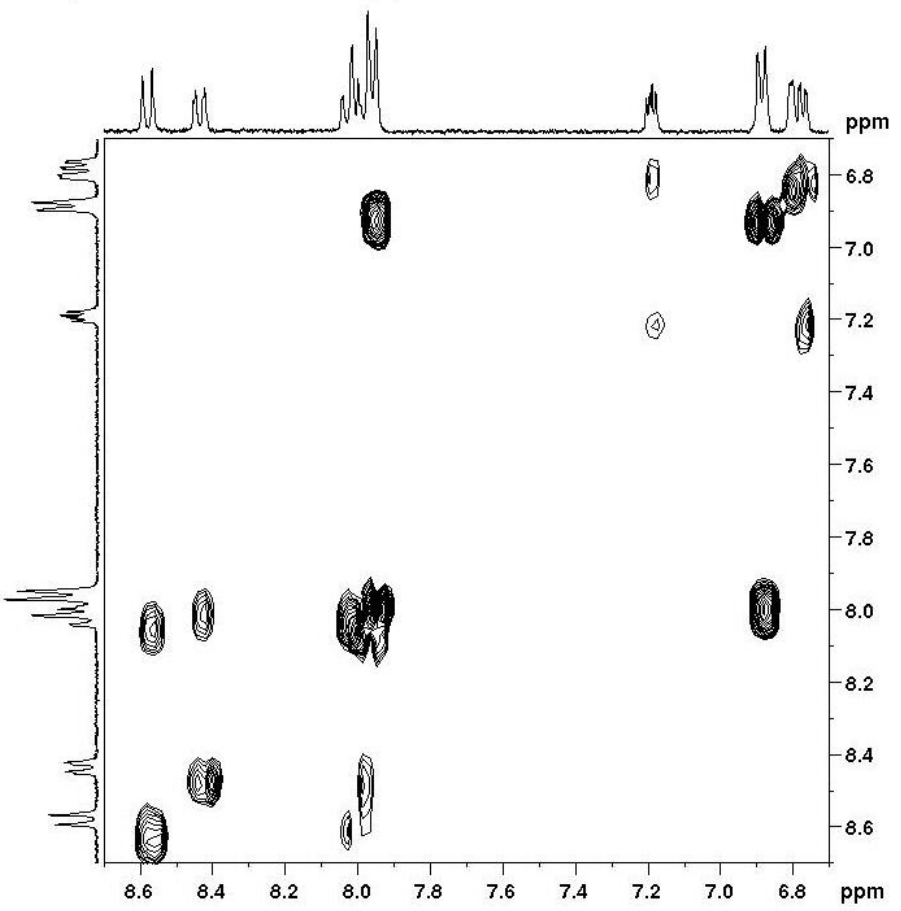

*Figure S6. ^{1}H-^{1}H-COSY NMR of **1** in [d_4]-methanol, T = 298 K.*

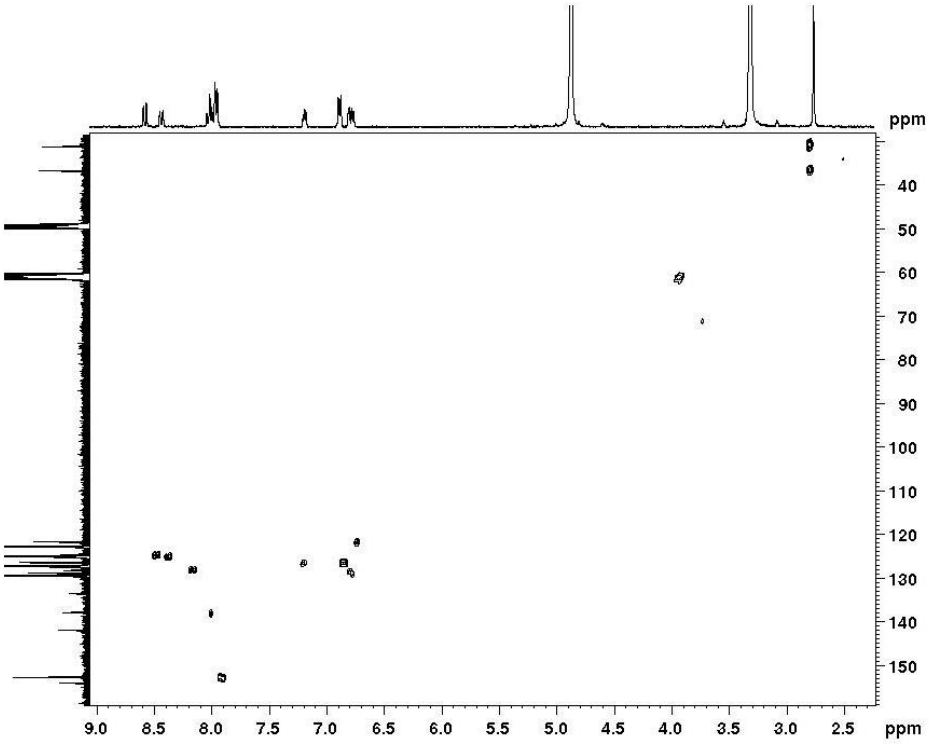

*Figure S7. ^{1}H-^{13}C-HMQC NMR of **1** in [d_4]-methanol, T = 298 K.*

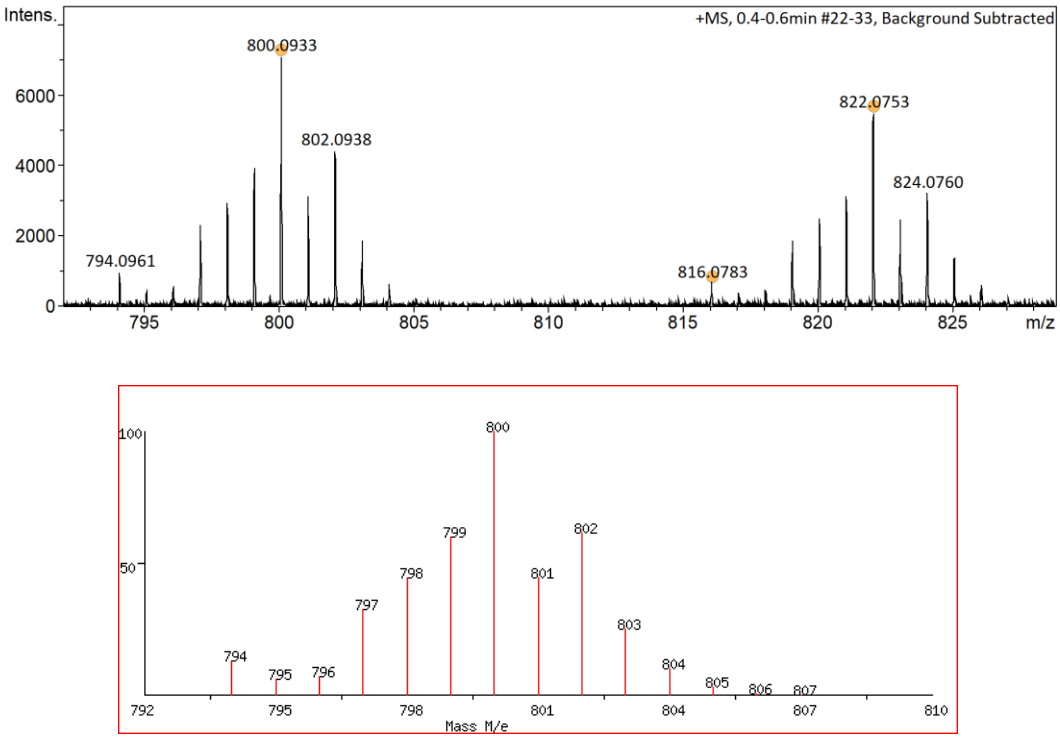

*Figure S8. High resolution MS (ESI⁺) of **1** (m/z 800) (top) and simulated MS (bottom). MS (ESI⁺) of **1** + Na⁺ on the right (m/z 822).*

3.6.3 Oxygen evolution and Faradaic efficiency experiments

All electrocatalytic experiments were performed in phosphate buffer pH 7 (I = 1 M) unless mentioned. Prior to experiments, complex **1** was electropolymerized on CNT@GC_{plate} or CFP to form **poly-1**@CNT@GC_{plate} or **poly-1**@CFP, following the procedure explained previously. Afterward, the anodes were activated by BE at 1.45 V *vs.* NHE for 500s at pH 11.6 to form its active catalytic species. Subsequently, the same anode was placed in a fresh solution of pH 7 phosphate buffer to study the catalytic performance towards water oxidation (Figure 5 and Figure S9).

Oxygen evolution was monitored by an OXNP Clark electrode (Unisense, Denmark) during bulk electrolysis in a 2 compartment cell. The Clark electrode was located through a septum in the gas phase of the anodic compartment, which was bubbled for 20 min in N_2 before use. The other electrodes in this compartment were **poly-1-OH**@CNT@GC_{plate} or **poly-1-OH**@CFP and the RE, immersed in pH 7 buffer solution. In the other compartment, which was separated by a frit, a Pt mesh was located and gas-tight by a septum. After the N_2 purge, the oxygen sensor was stable and low in signal. Then, 1 h bulk electrolysis (for **poly-1-OH**@CNT@ GC_{plate}) and 33 min (for **poly-1-OH**@CFP) was

performed under vigorous magnetic stirring. Calibration of the Clark electrode was carried out after each experiment by adding a known amount of air into the cell using a gas-tight Hamilton syringe. The Faradaic efficiency was determined according to the total charge passed during the BE (blue line in Figure 5) and the total amount of generated oxygen through $4e^-$ water oxidation reaction (pink line in Figure 5). As a result, 83% of FE is comparable to the one obtained by RRDE experiments explained below. The same experiment performed on **poly-1-OH**@CFP showed a FE of 100% (Figure S9).

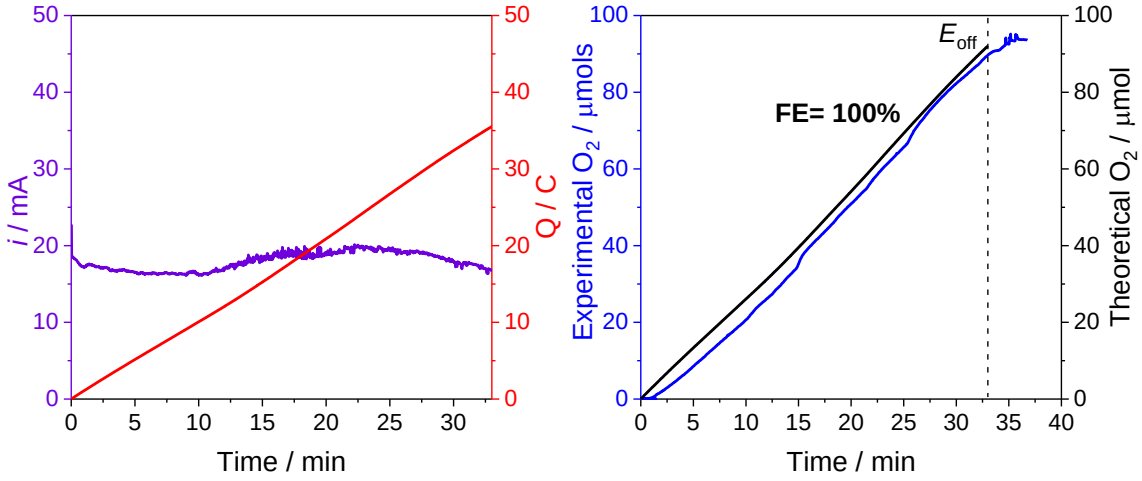

*Figure S9. Left, j vs. t (purple line) and Q vs. t (red line) curves obtained in the bulk electrolysis experiment carried out for **poly-1-OH**@CFP (Γ = 0.37 nmol·cm^{-2}, S(CFP) = 5.2 cm^2) at E_{app} = 1.345 V for 33 min, immersed in a 15 mL pH 7 phbf solution (CE, Pt mesh; RE, Hg/Hg_2SO_4) in an H cell with a glass frit separating the two compartments (gas phase V = 10 mL in the WE compartment). Right, oxygen evolution was detected in the very same experiment using a Clark electrode in the working compartment (pink trace) together with the expected O_2 based on the charge passed of 35.3 C assuming 100% Faradaic efficiency (black trace). At minute 37 the Faradaic efficiency reached a value of 100%.*

In addition to the BE-Clark electrode experiment, a Rotating Ring Disk Electrode (RRDE) was used to determine the FE, similarly to Jaramillo *et al.* for heterogeneous catalysts.[10] 80 µmL of 1 mg·mL^{-1} CNT were loaded on the surface of the glassy carbon disk electrode. Afterward, the molecular catalyst **1** was electropolymerized on the WE, in the same manner as explained above. To evaluate the catalytic activity, the disk electrode was subjected to a linear sweep voltammetry experiment in pH 7 (1 M) at a slow scan rate (10 mV·s^{-1}) in the potential range from 0.2 V to 1.5 V *vs.* NHE, while the whole RRDE was rotating at a constant rate of 1600 rpm under nitrogen atmosphere. The oxygen produced in this electrode moves to the surrounding Pt ring electrode due to the centrifugal force generated by the rotation. In this ring electrode, the oxygen is

electrochemically detected (dark blue, bottom of Figure S10) by its reduction applying a constant potential of -0.155 V vs NHE (light blue, bottom in Figure S10).

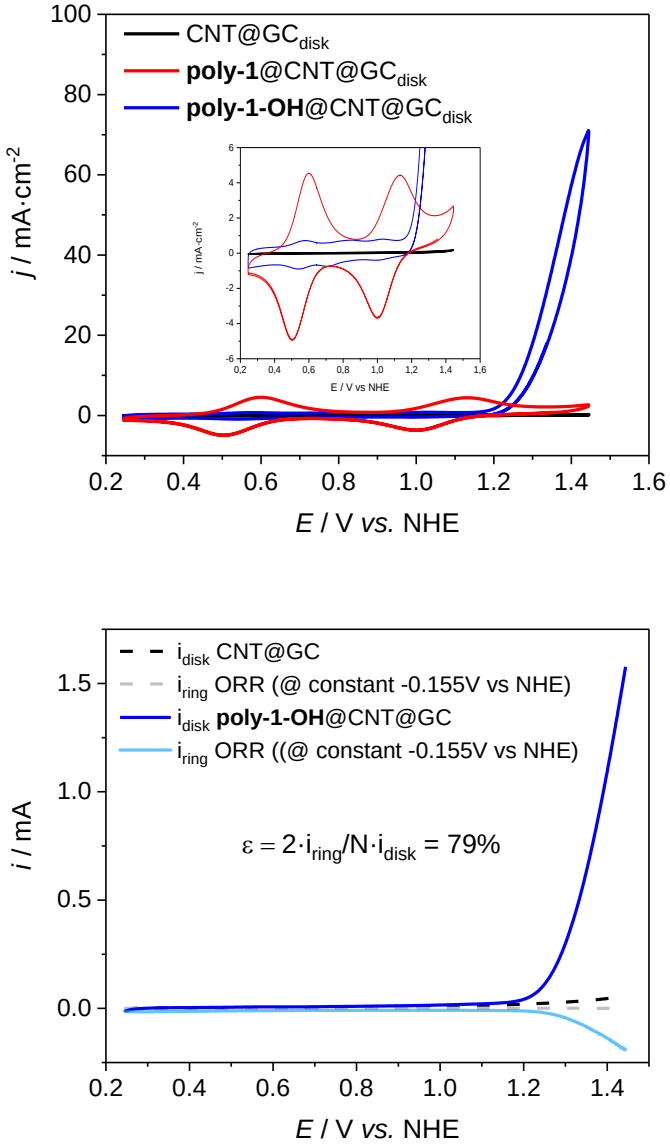

*Figure S10. RRDE experiments to calculate the Faradaic Efficiency (FE) of activated **poly-1**. Top, CV of the RRDE's GC$_{disk}$ (WE) after electropolymerization (red) and activation (blue). Bottom, LSV at 10 mV·s^{-1} and 1600 rpm of **poly-1-OH**@CNT@GC$_{disk}$ (dark blue) while the Pt ring is held at -0.155V vs. NHE to detect the ORR (light blue) in pH7 1 M. Blank CNT@GC$_{disk}$ in dashed lines. A final 79% Faradaic efficiency was calculated.*

3.6.4 Stability tests

For practical applications, the anode poly-1-OH@CNT@GC must be stable over time. To determine its stability, two different experiments have been performed: (a) BE in a two-compartment electrochemical cell, and (b) BE in an RRDE set-up.

Bulk Electrolysis and Cyclic Voltammetry: Both techniques were employed to detect the stability of the catalyst under long periods of water oxidation. To prevent parasite reactions and separate gas generations, a two-compartment electrochemical cell was used with a glass frit as a separator. On one compartment, oxygen was evolved on **poly-1-OH**@CNT@GC, and on the other hydrogen was produced by the Pt grid AE. A potential of 1.45 V *vs.* NHE was applied for 4 h, with a stop each hour to perform CV and follow the catalyst leach and/or degradation (Figure S11).

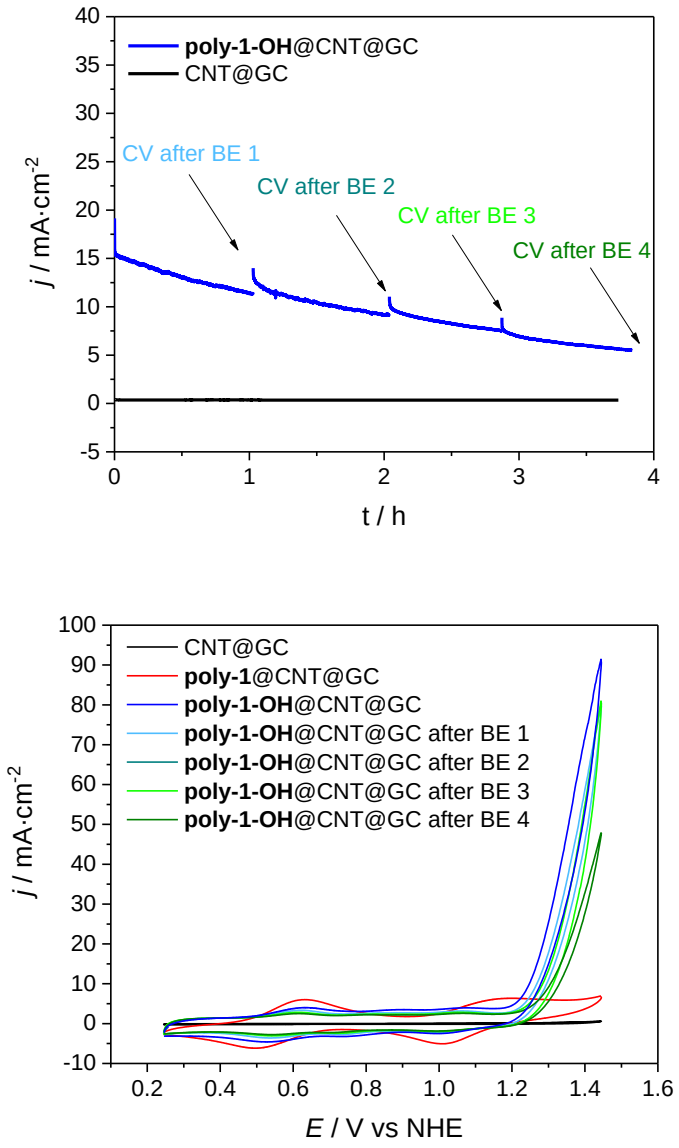

*Figure S11. Stability tests in a two-compartment electrochemical cell. The upper graph shows a BE at 1.345V vs. NHE in pH 7 (1 M) of **poly-1-OH**@CNT@GC overtime under stirring (500 rpm). WE: **poly-1-OH**@CNT@GC; CE: Pt grid; RE: Hg/Hg_2SO_4. On the lower graph, CVs were performed at 100 $mV \cdot s^{-1}$ every hour during BE experiment and in the same set-up. After 4 h, a total charge of 9.1 C was passed that assuming an 83% FE, which corresponds to 20,591 TONs.*

Chronocoulometry (CC): To further characterize the stability, a CC with an RRDE was performed. The same electrochemical set-up was used as explained in the previous section. In Figure S12, **poly-1-OH**@CNT (red) leached from the surface of the electrode over time water oxidation conditions. During the CC, ORR was followed by holding the Pt ring at -0.155V *vs.* NHE. The ORR follows the same trend as the OER, giving evidence that O_2 is evolved.

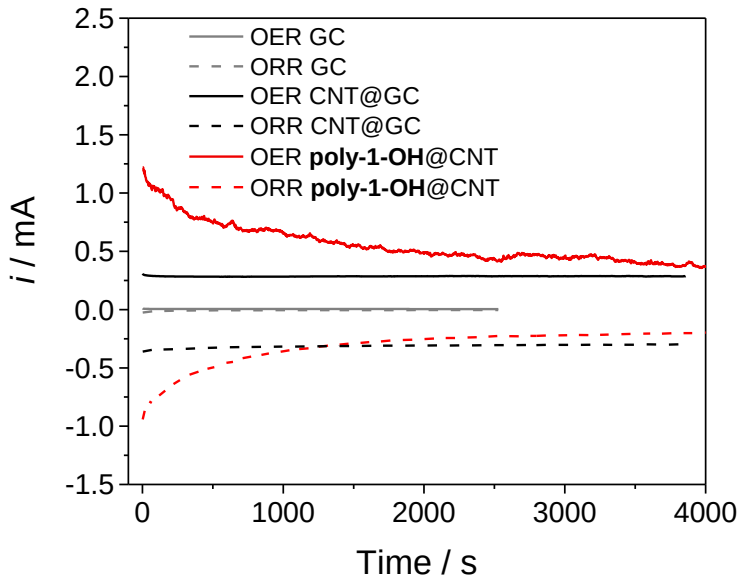

Figure S12. Stability performance in pH 7 (1 M) through a chronocoulometry (CC) with a RRDE set-up. WE1: ***poly-1-OH****@CNT@Gcdisk at 1.345 V; WE2 - Pt ring at -0.155 V; 16000 rpm.*

3.6.5 References

(1) Matheu, R.; Ertem, M. Z.; Benet-Buchholz, J.; Coronado, E.; Batista, V. S.; Sala, X.; Llobet, A. Intramolecular Proton Transfer Boosts Water Oxidation Catalyzed by a Ru Complex. *J. Am. Chem. Soc.* **2015**, *137* (33), 10786–10795. https://doi.org/10.1021/jacs.5b06541.

(2) Bruker. APEX II. Bruker AXS Inc.: Madison, Wisconsin, USA 2007.

(3) Bruker. SAINT. Bruker AXS Inc.: Madison, Wisconsin, USA 2007.

(4) Bruker. SADABS. Bruker AXS, Inc.: Madison, Wisconsin, USA 2007.

(5) Sheldrick, G. M. SHELXT - Integrated Space-Group and Crystal-Structure Determination. *Acta Crystallogr. Sect. A Found. Crystallogr.* **2015**, *71* (1), 3–8. https://doi.org/10.1107/S2053273314026370.

(6) Hübschle, C. B.; Sheldrick, G. M.; Dittrich, B. ShelXle: A Qt Graphical User Interface for SHELXL. *J. Appl. Crystallogr.* **2011**, *44* (6), 1281–1284. https://doi.org/10.1107/S0021889811043202.

(7) Spek, A. L. PLATON SQUEEZE: A Tool for the Calculation of the Disordered Solvent Contribution to the Calculated Structure Factors. *Acta Crystallogr. Sect. C Struct. Chem.* **2015**, *71*, 9–18. https://doi.org/10.1107/S2053229614024929.

(8) Matheu, R.; Neudeck, S.; Meyer, F.; Sala, X.; Llobet, A. Foot of the Wave Analysis for Mechanistic Elucidation and Benchmarking Applications in Molecular Water Oxidation Catalysis. *ChemSusChem.* **2016**, *9* (23), 3361–3369. https://doi.org/10.1002/cssc.201601286.

Chapter 3.

III

Chapter 4

Visible-light oxygen evolution at neutral pH by an organic dye/molecular catalyst homogeneous system

Chapter 4.

IV

IV

Visible-light oxygen evolution at neutral pH by an organic dye/molecular catalyst homogeneous system

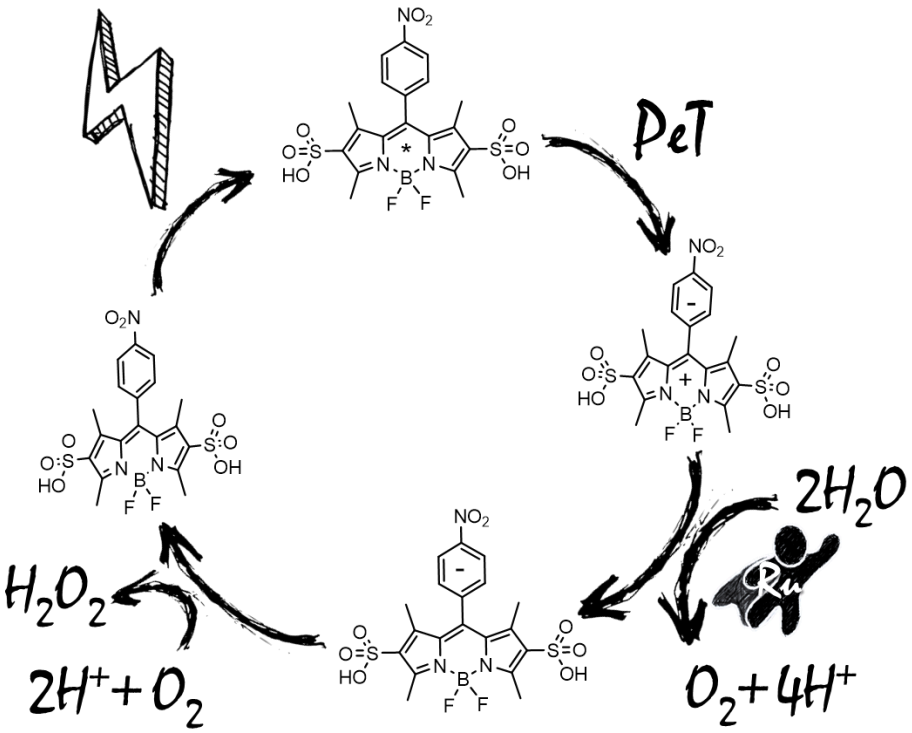

Abstract

Dye-Sensitized Photoelectrochemical Cells (DSPECs) are devices that convert solar energy into chemical fuels for the future free-carbon energy scheme. One of their key components is the water oxidation photoanode, which is constituted by a rationally designed molecular dye/catalyst system. This strategy aims at efficient visible light absorption and electron transfer, together with high catalytic activities in order to overcome the kinetic barrier of water oxidation. In this direction, herein we study the homogeneous photocatalytic performance of two organic dyes 4,4-Difluoro-4-bora-3a,4a-diaza-*s*-indacene (BODIPY) derivatives with a previously reported Ru-based Water Oxidation Catalyst (WOC). Right substitution of BODIPY's aryl moiety leads to an organic dye stable under harsh oxidative conditions and capable of bringing Ru-WOC to its active higher oxidation states. Moreover, the dye itself performs the reduction half-reaction by reducing oxygen to hydrogen peroxide. In dark conditions, this hydrogen peroxide is converted to water and oxygen by the Ru-based complex. The system shows a singular mechanism that leads to oxygen evolution and overcomes the instability of the well-studied ruthenium(II) tris(bipyridine), $[Ru(bpy)_3]^{2+}$, and other organic dyes.

Contributions:

Marta Ventosa performed the electrochemistry and oxygen evolution experiments with concomitant characterization by spectroscopy before and after photocatalysis.

4.1 Introduction

The current epoch, called Anthropocene, is characterized by the impact of human activities on Earth.[1] As a consequence, human actions can lead to the transgression of the planetary boundaries[2] and irreversibly break the environmental stability of the Holocene. The current energy system based on fossil fuels has been one of the major contributors to the climate crisis.[3] To overcome this matter, the field of artificial photosynthesis[4,5] is one of the strategies to obtain clean and renewable fuels. Similar to natural photosynthesis, it relies on the catalytic oxidation of water to dioxygen, and the reduction of protons or CO_2 to obtain fuels such as H_2 or hydrocarbons as energy vectors.[4,6,7]

Within the field of artificial photosynthesis, Dye-Sensitized Photoelectrochemical Cells (DSPECs)[8] are devices that convert solar energy into chemical fuels. The main components[9] of these devices are: (i) catalysts for water oxidation and proton or CO_2 reduction, (ii) light-harvesters, (iii) semiconductors for electron-hole transport, and (iv) a membrane. Finding efficient catalysts for the Water Oxidation Reaction (WOR) is one of the determining issues to develop DSPEC, owing to the reaction's thermodynamic requirements and kinetic barriers involving four electrons and four protons.[6] Over the past decades, several molecular Water Oxidation Catalysts (WOC) have been developed with activities even higher than those of the Oxygen-Evolving Complex in Photosystem II (OEC-PSII).[6,10] However, these results seldom progress towards photoactivated water oxidation. One of the main reasons is the lack of photosensitizers (PS) with high enough oxidation and that are stable in aqueous media.[11,12] Besides that, the reported ones rarely digress from the well-known ruthenium(II) tris(bipyridine) ($[Ru(bpy)_3]^{2+}$) and zinc porphyrin derivatives,[13–15] which suffer from stability issues, fast charge recombination and they are composed of scarce metals. Alternatively, various organic dyes were successfully employed for the complementary proton reduction reaction, such as fluorescein,[16] eosin,[17] and rhodamine dyes,[18] triarylamines derivatives,[8] triazatriangulenium dyes,[19] and perylene derivatives.[20] An important milestone occurred in 2017 when Meyer and co-workers[21] reported the first dye-sensitized photoanode using organic photosensitizers consisting of triarylamines on TiO_2. Despite this achievement, O_2 evolution was limited to ~1 h with a maximum IPCE of 0.3%.

4,4-Difluoro-4-bora-3a,4a-diaza-*s*-indacene (BODIPY) compounds[22,23] are particularly interesting due to their exceptional optical properties and low photodegradation and chemical robustness in organic and aqueous solvents.[24] BODIPY organic dyes have proven to even outperform well-known $[Ru(bpy)_3]^{2+}$ under similar reaction conditions.[25] Their redox and photophysical signatures can be easily tuned by rational design giving rise to a library of dyes with several applications.[26] Additionally, these organic dyes are metal-free and easy to synthesize and purify. In this regard, they are suitable candidates to meet the criteria for the water oxidation reaction. Moreover, there are several examples of water-soluble BODIPY dyes[27] with well documented (photo)stability under harsh reaction conditions.[28]

In this chapter, we report a homogenous set-up combining BODIPY dyes **BDP1** and **BDP2** with highly active molecular catalysts for light-induced water oxidation (Figure 1). Dyes **BDP1** and **BDP2** have been previously studied as possible fluorescence sensors in biological environments,[26,27] with high enough oxidation potentials and very good water solubility.[27,29] On the other hand, the recently published Ru-based complex[30] with formula $[Ru^{II}(HtPa\text{-}\kappa\text{-}N^3O)(py)_2]^+$ or **Ru-tPa** (tPa^{4-} is [2,2':6',2''-terpyridine]-6,6''-diphosphonate, Figure 1), has an advantage over its predecessor $[Ru^{II}(tda)(py)_2]$ or **Ru-tda**[31] (tda^{2-} is [2,2':6',2''-terpyridine]-6,6''-dicarboxylate) because it can be converted stoichiometrically into its active WOC form and isolated by applying certain potential. Interestingly, under oxidative conditions, one of the pyridyl phosphonate arms of the tPa^{4-} ligand gets uncoordinated, rotates, and oxidizes to a pyridoxo group that coordinates to the Ru center.[30] The new complex $[Ru^{III}(tPaO\text{-}\kappa\text{-}N^2O_PO_C)(py)_2]^{2-}$ ($tPaO^{5-}$ is 3-[hydroxo-(2,2':6',2''-terpyridine)-6,6''-diyl]bisphosphonate), herein labeled as **Ru(O)-tPa** (Figure 1), emerges to be an exceptional WOC at neutral pH by achieving record high TOF_{max} of 16,000 s^{-1} with an overpotential of 530 mV (*vs.* NHE, pH 7).[30] Recent studies in our group[32] show further oxidative decay of **Ru(O)-tPa** by applying potential or adding an excess of H_2O_2, leading to the generation of the molecular WOC $[Ru^{II}(Hbpc)(py)_2]$ ($Hbpc^{2-}$ is 2,2'-bipyridine-6-phosphonic acid-6'-carboxylate) which is a new example of a family of complexes previously reported by Concepción and co-workers.[33] The latter is labeled herein as **Ru(O)-bPa** (Figure 1) and has an overpotential as low as 330 mV at pH 7.[33] **Ru(O)-bPa** has a characteristic reversible redox wave at $E_{1/2}$ = 0.55 V (*vs.* NHE pH 7)

while **Ru(O)-tPa** presents it $E_{1/2}$ = 0.36 V (*vs.* NHE pH 7). Therefore, the WOC employed in this work is the result of activation of Ru-tPa by applied potential, which leads to the formation mostly of **Ru(O)-tPa** but also **Ru(O)-bPa.**[32]

Initially, the photophysical and electrochemical characterization of BODIPY dyes **BDP1** and **BDP2** is described in detail and helps in understanding the feasibility of using both dyes in aqueous media under high oxidizing conditions. Later, we examine both PS in combination with the WOC derived from **Ru-tPa** to develop the first fully homogeneous photocatalytic system for water oxidation based on an organic dye that lacks the need for any sacrificial agent.

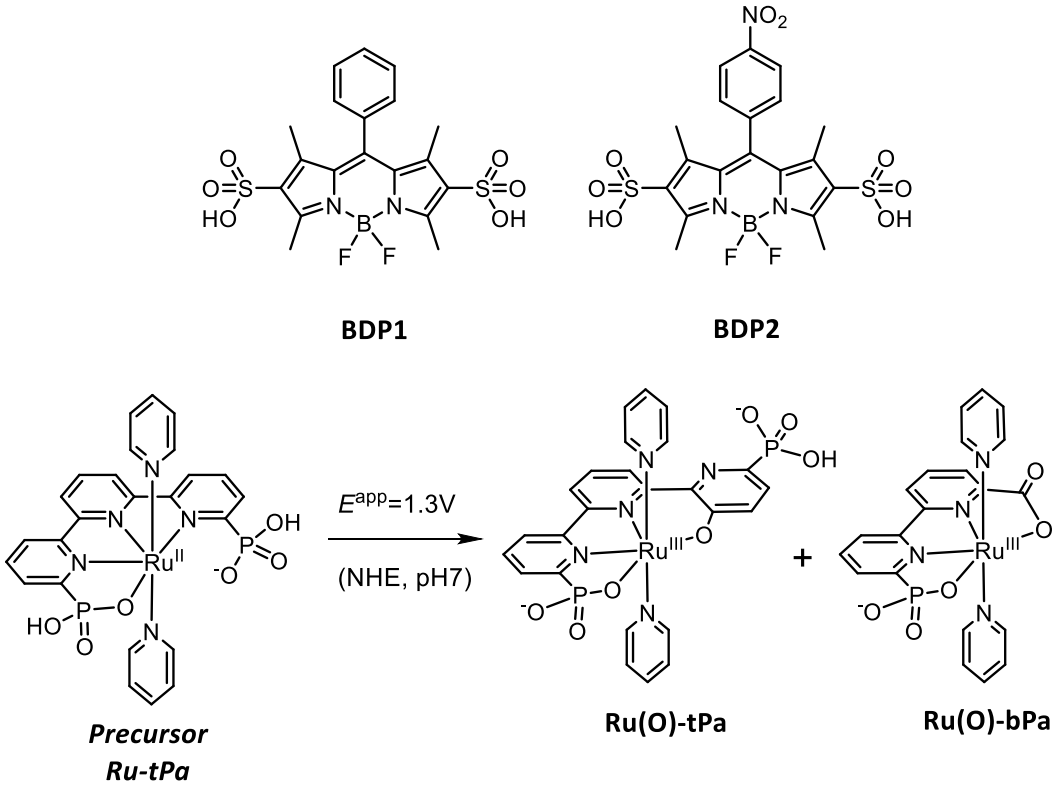

Figure 1. Top, photosensitizers used in this work based on BODIPY dyes: ***BDP1*** *and* ***BDP2****. Bottom, water oxidation catalysts employed,* ***Ru(O)-tPa*** *and* ***Ru(O)-bPa.***

4.2 Results and Discussion

4.2.1 Synthesis, spectroscopic and photophysical properties of BDP1 and BDP2

BDP1 and **BDP2** were synthesized in two steps following previously published procedures[26,27] (Figure S1) and confirmed by Nuclear Magnetic Resonance (NMR) spectroscopy. UV-Vis spectra of the dyes in the water at pH 7 were dominated by the $S_0 \rightarrow S_1$ transition at λ = 516 nm for **BDP1** and at λ = 519 nm for **BDP2** (Figure 2 left) which closely corresponded to previously reported values.[27,29] Extinction coefficients in water were determined as 49,000 $L \cdot mol^{-1} \cdot cm^{-1}$ for **BDP1** (λ = 516 nm), and 62,000 $L \cdot mol^{-1} \cdot cm^{-1}$ for **BDP2** (λ = 519 nm). Emission of both in pH 7 phosphate buffer (phbf) proved to be very low, with quantum yields of virtually 0. However, fluorescence lifetimes in pH 7 could be determined as 3.98 ns (**BDP1**) and 4.02 ns (**BDP2**) as shown in Figure 2, right. Upon changing the solvent to acetonitrile, fluorescence was slightly improved due to the lower polarity of the solvent (Figure S3). Furthermore, emission maximum in acetonitrile was observed at 507 nm (**BDP1**) and 525 nm (**BDP2**) with quantum yields of 0.03% (**BDP1**) and 0.81% (**BDP2**) (Figure S4). Those values deviate slightly from previously reported data,[26,27] excepting the quantum yield of **BDP1**, which was reported as 0.2% in MeOH. This could be explained by solvent polarity, which has a profound effect on the quantum yield of low emitting BODIPY dyes, such as **BDP1** and **BDP2**. As Nagano and coworkers[29] demonstrated, a change from MeCN (polarity index 5.8) to MeOH (polarity index 5.1) can result in a 3-fold increase of the fluorescence quantum yield for some BODIPY dyes. A complete list of relevant photophysical data can be found in Table S1. On the other hand, **Ru(O)-tPa** does not show any emission or fluorescence. Its absorption is characterized by weak-broad bands in the 400-600 nm range due to Metal to Ligand Charge Transfers (MLCTs) and more intense and sharper bands in the UV region due to π- π^* ligand-based transitions (green line in Figure 2).

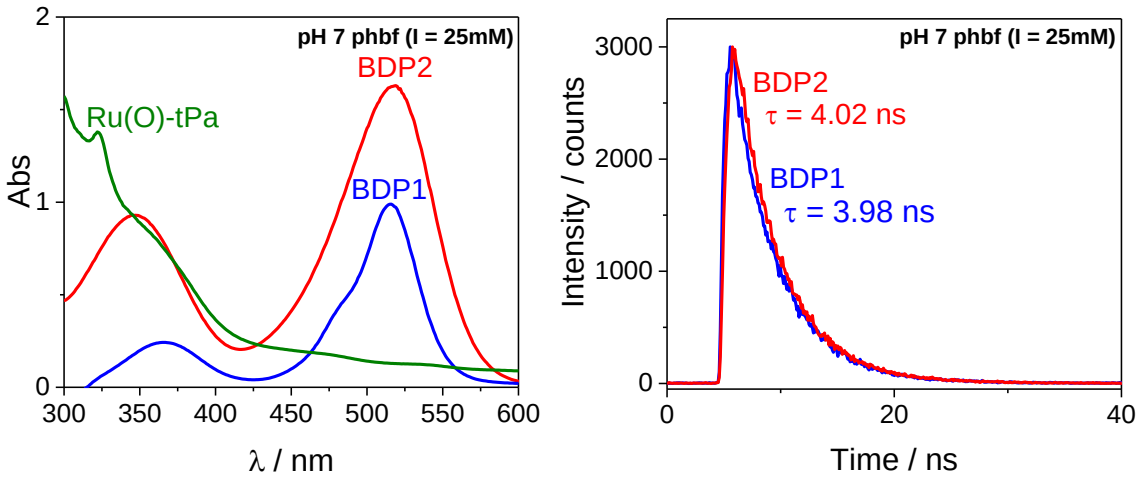

*Figure 2. Spectroscopic data of **BDP1** (15 μM), **BDP2** (20 μM) and **Ru(O)-tPa** (200 μM) in pH 7 phosphate buffer (I = 25mM): UV-Vis spectra (left); fluorescence lifetime spectra at λ_{em} = 540 nm for **BDP1** and **BDP2** (right).*

Quantum yields, as well as lifetimes, remained virtually unchanged when measured under an inert atmosphere or under air indicating that quenching by O_2 can be neglected as the cause of the low quantum yields. Therefore, the most plausible process is an intramolecular quenching as described previously by Nagano and co-workers.[29] This process consists of an intramolecular electron transfer of the excited electron, called Photo-electron Transfer (PeT). As depicted by Scheme 1, this results in a zwitterionic state, in which the core donates an electron to the aryl moiety. This feature can be considered an example of a charge separation, which could enhance the electron transfer of **BDP1** and **BDP2** to the molecular water oxidation catalyst. Additionally, the presence of an electron-withdrawing group in **BDP2** further enhances the stabilization of this zwitterionic state.[34] Further photophysical experiments and theoretical calculations are required to prove that this is the mechanism for **BDP1** and **BDP2** in water under the conditions used in this work.

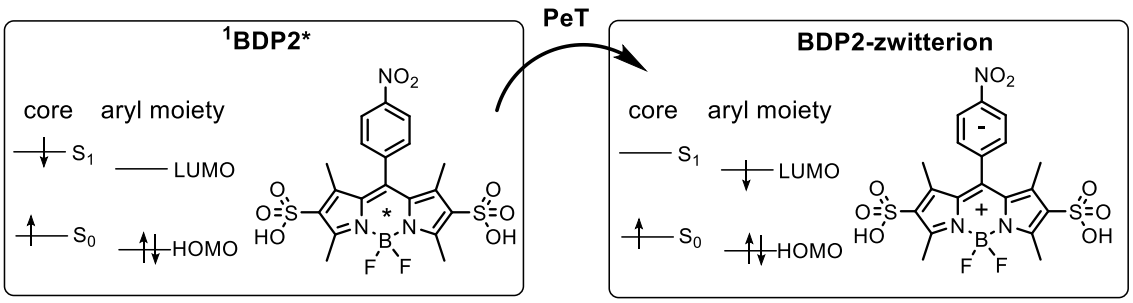

Scheme 1. Proposed mechanism for BDP2 to BDP2-zwitterion through a Photo-electron Transfer from its core to the electron-withdrawing aryl moiety.*

4.2.2 Electrochemical characterization and analysis of BDP1 and BDP2

Electrochemical characterization of **BDP1** and **BDP2** was studied by Cyclic Voltammetry (CV). The set-up consisted of a three-electrode configuration in pH 7 (phbf, 0.1 M) or in acetonitrile containing 0.1M tetrabutylammonium hexafluorophosphate ($TBAPF_6$) as supporting electrolyte (Figure 3 and supporting information). All the redox potentials herein presented are reported versus NHE at pH = 7.0.

IV

BDP1 and **BDP2** show an irreversible oxidation wave in aqueous phbf at pH 7 and under N_2 atmosphere, (Figure 3 left). The oxidation peaks are at $E_{p,a}$ = 1.16 V for **BDP1** (blue), and $E_{p,a}$ = 1.10 V for **BDP2** (red). Although these results do not provide a reliable value for the **$BDP^{+/0}$** couple, they are useful to estimate the oxidative power of the BDP^+ species. Thus, we expect that the excited dyes will provide sufficient driving force to the molecular catalyst for water oxidation, which shows a catalytic onset at $E_{cat,onset}$ = 1.13 V (green trace in Figure 3). The electrochemical characterization of the WOC corresponds to the literature,[30,33] showing a reversible redox wave at $E_{1/2}$ = 0.36 V for **$Ru^{III/II}$(O)-tPa**. Besides, traces of **Ru(O)-bPa** are present due to the less intensive wave at $E_{1/2}$ = 0.55 V. The right graph of Figure 3 shows CV experiments in acetonitrile, which were performed to avoid the competition of dye reduction with proton reduction present in aqueous solution. Additionally, a gold disk was used as a working electrode to circumvent the dye adsorption. CV of **BDP1** in acetonitrile under inert conditions (blue trace) showed one quasi-reversible reduction wave with reduction peak potential of $E_{p,c}$ = -0.78 V. In the case of **BDP2** (red), two quasi-reversible reduction potentials appear in acetonitrile under N_2, with a first one at $E_{1/2}$ = -0.57 V (**$BDP2^{0/-}$**) and a second one at $E_{1/2}$ = -0.75 V (**$BDP2^{-/2-}$**). It is noteworthy that CVs under air (inset on the right graph of Figure 3 or Figure S5) reveals the capacity of both dyes to reduce oxygen as reported in previous work.[35] In the presence of oxygen, **BDP1,** and **BDP2** show a significant irreversible reduction wave at $E_{p,c}$ = -1.12 V and $E_{p,c}$ = -0.99 V respectively. These waves are related to the reduction of oxygen by comparing the response of the bare gold electrode under air or N_2.

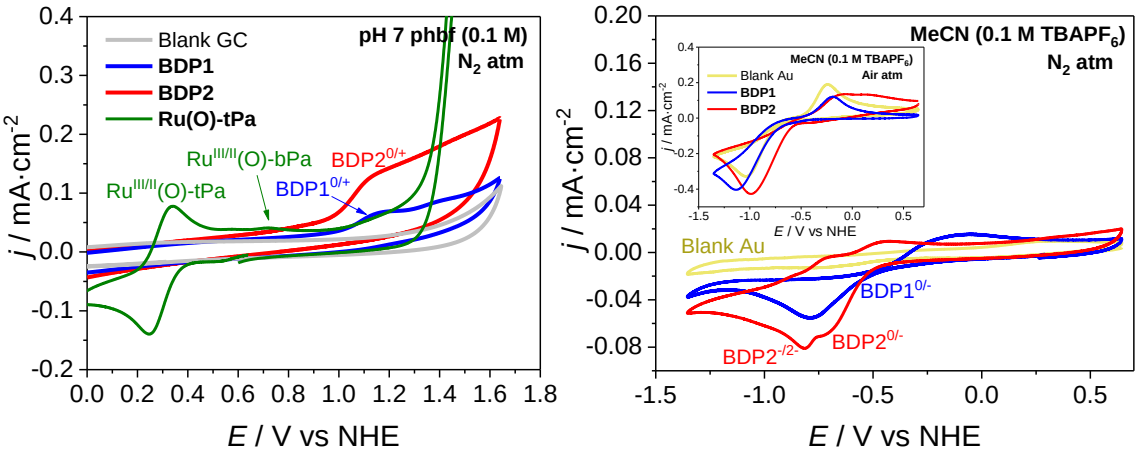

*Figure 3. On the left, CV of **BDP1** (blue), BDP2 (red) and **Ru(O)-tPa** (green) in pH 7 phosphate buffer (phbf 0.1 M) under N_2 atm. CVs at v = 50 mV·s^{-1} using a three-electrode set-up: Glassy Carbon disk (GC) as Working Electrode (WE), Pt disk as the Counter Electrode (CE), and Hg/Hg_2SO_4 as theRreference Electrode (RE). On the right, CV of **BDP1** (blue) and **BDP2** (red) in acetonitrile (MeCN) with 0.1 M of tetrabutylammonium hexafluorophosphate ($TBAPF_6$) as supporting electrolyte and under N_2 atm. CVs were scanned at v = 100 mV·s^{-1} using 3-electrode set-up: gold disk (Au) as the WE, Pt disk as the CE, and Hg/Hg_2SO_4 as the RE. A gold disk was used as working electrode to circumvent the dye adsorption. The inset graph shows the same set-up under air atm.*

4.2.3 O_2 evolution experiments and the effect of the sacrificial agent

BDP1 and **BDP2** were combined with the active molecular catalyst derived from **Ru(O)-tPa** to assess their ability to act as photosensitizers in photochemical water oxidation. The experiments were conducted in 25 mM phbf at pH 7 containing a ratio of 13:1 Ru(O)-tPa/BDP. All the experiments were conducted in a single compartment thermostated cell at 25 ˚C and with a Clark sensor to monitor oxygen in the gas phase (V_T = 2 mL). The system was purged for 20 min with N_2 and a stable baseline was recorded before illumination. All the samples were irradiated with visible light (1.1 suns, AM 1.5 G) from a Xe lamp (150 W) equipped with a 400 nm cut-off filter. The main experimental details and results are reported in Table 1, Figure 4 and 5, and the SI.

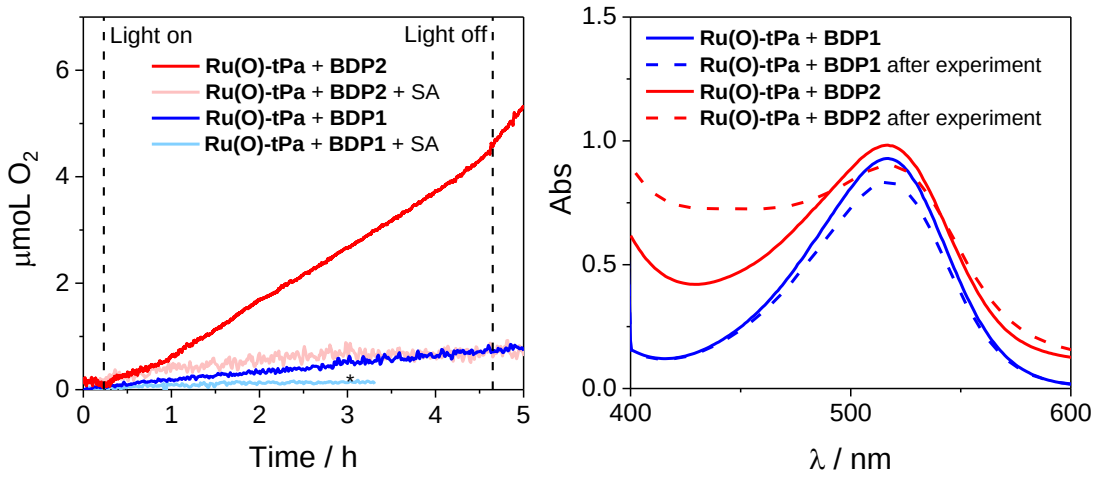

Figure 4. Left, photo-evolution of oxygen by using a Clark electrode in the gas phase (V_T = 2 mL) upon irradiation of the different samples in a one-compartment cell at 1.1 suns (400 nm cut-off filter) and 25˚C. In solution: ***Ru(O)-tPa*** *+* ***BDP1*** *(dark blue),* ***Ru(O)-tPa + BDP2*** *(dark red),* ***Ru(O)-tPa*** *+* ***BDP1*** *+ $Na_2S_2O_8$ (light blue),* ***Ru(O)-tPa*** *+* ***BDP1*** *+ $Na_2S_2O_8$ (light red). The blanks of only catalyst, only* ***BDP1,*** *and only* ***BDP2*** *can be found in Figure S6. (*) The light was stopped before other samples. Right, UV-Vis spectra of the samples before (solid line) and after (dashed line) WO experiments:* ***Ru(O)-tPa*** *with* ***BDP1*** *(blue) and* ***BDP2*** *(red).*

The left graph in Figure 4 shows the results of representative experiments in the presence and the absence of 10 mM of $Na_2S_2O_8$ as an electron acceptor Sacrificial Agent (SA) for the half-reduction reaction. To our surprise, the best catalytic mixture was that containing **BDP2** and the catalyst without the sacrificial agent, which generated noteworthy amounts of O_2 with initial rates of 0.751 µmol·h^{-1} and 163 turnover numbers *versus* dye concentration (TON_{BDP}) in 4.5 h (red line above, entry 1 in Table 1 below). The use of sacrificial agents in photochemical water oxidation enhances the kinetics of half reduction reaction, which increases the lifetime of charge pairs and thus improves reaction with the counter oxidation catalyst.[36] However, in this case, the presence of $Na_2S_2O_8$ evokes only slight O_2 evolution for **BDP2 + Ru(O)-tPa**, with an initial slope of 0.138 µmol·h^{-1} and no O_2 generation after 2.5h of irradiation (pink trace in Figure 4 left, entry 2 in Table 1). For the **BDP1** case, the mixture without the SA also generates a significant amount of oxygen at a lower yet steady rate of 0.197 mmol·h^{-1} and 26 TON_{BDP} in 4.5 h (blue trace in Figure 4 left, entry 3 in Table 1). However, in the presence of SA virtually no oxygen was detected (cyan trace in Figure 4 left, entry 4 in Table 1). One possible explanation for the latter result is the interaction of $Na_2S_2O_8$ with the excited state of the dyes (Dye*). Previous literature reports have demonstrated this interaction with other dyes, resulting in the oxidative quenching of Dye* to generate Dye^{+}.[12] The latter species needs to have sufficient potential to oxidize the molecular catalyst to Ru^{V}=O (E > 1.13 V, green trace in Figure 3). We hypothesize that the oxidation potential

of **BDP1**$^{+}$ compared to **BDP2**$^{+}$ (Figure 3) is not enough to oxidize the **Ru^{III}(O)-tPa** to the higher oxidation states needed for the catalytic cycle, or due to enhanced kinetics of the process for **BDP2**.

Indeed, electrochemical studies on libraries of BODIPY derivatives have demonstrated that the oxidation potential of the dyes is mainly influenced by the oxidation potential of the aryl moiety.[37] In this study, the effect of the electron-withdrawing nitrobenzyl group could enhance the higher oxidation potential of **BDP2** and the longer fluorescence lifetimes (Figure 2), expecting longer-lived zwitterion species of **BDP2** compared to **BDP1**. However, the irreversibility of the oxidation waves of the dyes observed in the CV experiments (Figure 3) hinders the calculations of the real thermodynamic $E_{1/2}$ values of the **BDP$^{0/+}$** couples and we currently can not prove this hypothesis. Thus, further steady-state and transient photophysical experiments are needed to confirm this hypothesis.

The right graph in Figure 4 shows UV-Vis spectra of both WO systems in the absence of sacrificial agent before (solid line) and after (dashed line) 4.5 h irradiation. It is noteworthy the robustness of the catalytic mixture, which experiences a 20-30% decrease in dye concentration after photocatalysis. Moreover, **BDP2** did not experience a significant decrease in concentration even in the presence of a highly oxidizing sacrificial agent (Figure S2). To verify that all the components of the system are necessary to produce O_2, systems omitting either **BDP** or **Ru(O)-tPa** were tested. As expected, schemes missing either the catalyst or the photosensitizer proved inactive (Figure S6). In view of these results, further research was done for the best-performing sample, which is **BDP2** + **Ru(O)-tPa** without SA. The aim was to determine the undergoing mechanism that produces O_2 and what is the corresponding product of the half reduction reaction.

Entry	Experiment	BDP1 μM	BDP2 μM	WOC μM	Ru:PS	SA mM	V_t (pH) mL	O_2 (@t/h) μmol	TON_{Ru}	TON_{BDP}
1	Fig. 4 red		18	200	13:1	--	2 (7)	5.9 (4.5)	14	163
2	Fig. 4 pink	--	18	200	13:1	10	2 (7)	0.46 (4.5)	4	15
3	Fig. 4 dark blue	20	--	200	13:1	--	2 (7)	1.04 (4.5)	10	26
4	Fig. 4 light blue	20	--	200	13:1	10	2 (7)	--	--	--
5	Fig. 5 red (1st cycle)	--	15	200	13:1	--	2 (7)	25 (18)	62.5	833.3
6	Fig. 5 blue (2nd cycle)	--	10	200	20:1	--	2 (7)	29 (24.5)	72.5	1450

*Table 1. Comparison of dye concentration, ratio Ru:PS, and O_2 evolved. All dye's amounts were calculated from absorption spectra of 2 mL samples before and after irradiation using extinction coefficients of 49,000 L·mol^{-1}·cm^{-1} (**BDP1**) and 62,000 L·mol^{-1}·cm^{-1} (**BDP2**). O_2 was detected by employing a Clark electrode in the gas phase (V_T = 2 mL).*

4.2.4 Study of the O_2 evolution using Ru-tPa + BDP2 system

Interestingly, the combination of **BDP2** and the molecular WOC generated significant amounts of O_2 without any sacrificial agent. After 4.5 h of irradiation (Figure 4), the system performed activity of 15 TONs versus catalyst and 163 TONs versus **BDP2**. This activity is among the best performing light-induced water oxidation dye-WOC systems.[12,38]

On the other hand, the reduction half-reaction with the absence of a SA can only be explained by Proton or Oxygen Reduction Reactions (PRR Equation 1, ORR Equation 2).

$$2H^+ + 2e^- \rightarrow H_2 \qquad E = -0.41 \text{ V vs. NHE pH 7} \quad \text{(Equation 1)}$$

$$O_2 + 2H^+ + 2e^- \rightarrow H_2O_2 \qquad E = 0.36 \text{ V } \textit{vs.} \text{ NHE pH 7} \quad \text{(Equation 2)}$$

Two experiments were designed to detect either hydrogen or hydrogen peroxide, as products of proposed reduction reactions. The experimental conditions were the same as in the previous section, in which a sample of **BDP2** and WOC in pH 7 at 25˚C was irradiated with 1.1 suns using a 400 nm cut-off filter for 4 h. A Clark electrode for H_2 was employed but no signal was detected (Figure S7). Additionally, repetitive manual

injections of 50 µL of headspace to a gas chromatograph equipped with a thermal conductivity detector resulted in no H_2 detection. Thus, proton reduction was discarded.

In the absence of hydrogen, we focused our attention on the possibility of an Oxygen Reduction Reaction. Past literature[35] has shown the potential of BODIPYs for ORR through a $2e^-$ pathway to produce H_2O_2. As shown in Figure 5A, a fresh sample was irradiated for 4 h and kept under dark conditions for an additional 15.5 h while O_2 production was monitored. Before photocatalysis, a 30 min stable baseline was recorded to ensure no O_2 leak. After 4 h of photocatalysis, the light was switched off and the cell was covered by aluminum foil, avoiding any light contamination. Despite all the measures, the O_2 production continued for 13 h after irradiation although with a slightly lower slope (from 1.78 µmols $O_2 \cdot h^{-1}$ under irradiation to 1.26 µmols $O_2 \cdot h^{-1}$ in dark). This tendency was also detected in previous experiments. As reported by other members of our group and explained in the introduction, **Ru(O)-tPa** can further suffer from an oxidative decay by H_2O_2 oxidation to **Ru(O)-bPa** and O_2 without the need for any potential/light bias.[32] A UV-Vis spectra at the end of the experiment (Figure 5B) displays a new shoulder at λ = 355 nm, confirming the presence of **Ru(O)-bPa**, generated by the interaction of H_2O_2 with Ru(O)-tPa (Scheme 1).

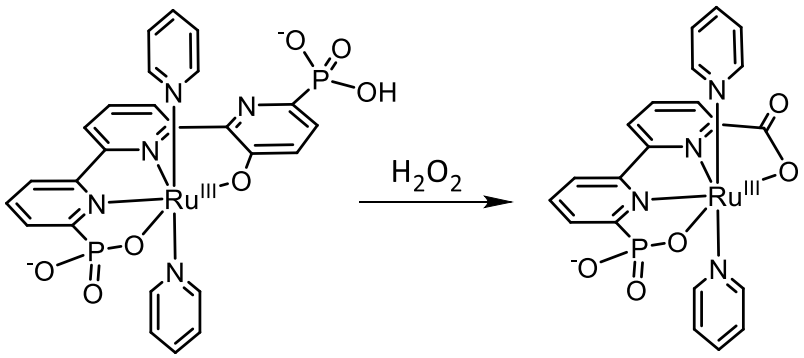

Scheme 1. Oxidative decay of Ru(O)-tPa to Ru(O)-bPa in the presence of H_2O_2, as reported in.[32]

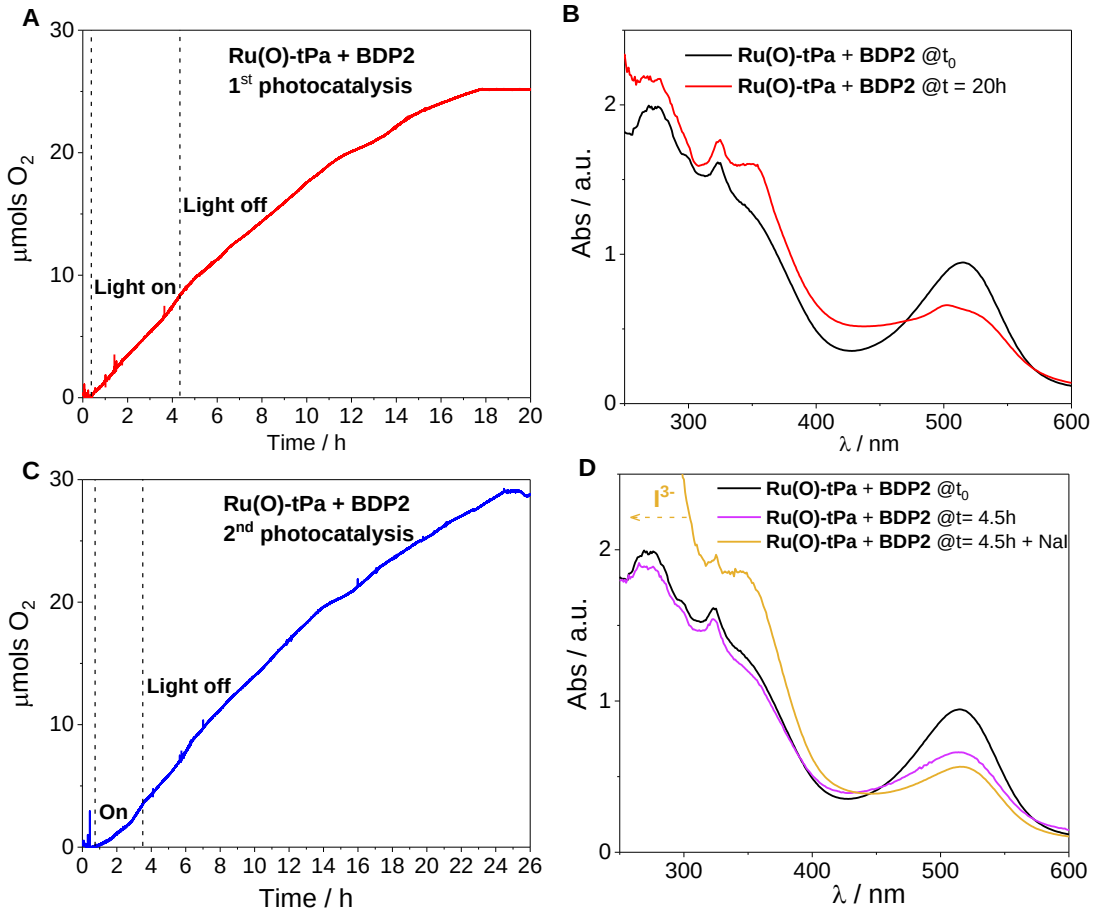

*Figure 5. (A) Long-term oxygen detection experiment of sample **Ru(O)-tPa** + **BDP2** with and without light. (B) UV-Vis spectra of **Ru(O)-tPa** + **BDP2** before (black line) and after (red line) experiment in (A), which shows a new shoulder at 361 nm corresponding to **Ru(O)-bPa**. (C) Oxygen evolution during a second photocatalytic experiment on the same sample from (A). (D) UV-Vis spectra of an analogous sample before (black) and after 4.5 h photocatalysis (purple); at the end of 4.5 h of irradiation, an excess of NaI was added (gold line) for H_2O_2 detection.*

To fully prove the hypothesis of ORR to H_2O_2 and further oxidation in dark conditions, H_2O_2 produced was detected by the iodometric titration method.[39] An analogous experiment was performed under the same conditions for 4.5 h under 1.1 suns irradiation and the final mixture was treated with an excess amount of sodium iodide (NaI). The I^{3-} produced was detected by its characteristic absorption at $\lambda < 361$ nm (yellow line in Figure 5D). Excess of NaI was also added to a non-irradiated sample as a blank experiment with the result of no increase in absorption intensity (Figure S8). Therefore, the experiments in Figure 5 demonstrate that the ORR reaction is indeed responsible for taking the electrons from **BDP2**$^-$ generating H_2O_2 (Figure 5D), which accumulates and produces oxygen in the headspace in dark conditions (Figure 5A). Finally, after photocatalysis and subsequent dark reactions a solid plateau was reached, as a consequence of full H_2O_2 consumption (Figure 5A).

After spectroscopic characterization, the same sample was inserted in the photocatalytic reactor for a 2nd cycle of 3.5 h of irradiation (Figure 5C). The robustness and reproducibility of the system were proved by the high rate of oxygen evolution. Although, the initial slope (1.06 µmols $O_2 \cdot h^{-1}$ under light conditions) was slightly lower than in the 1st cycle (1.78 µmols $O_2 \cdot h^{-1}$), the overall O_2 produced in the 2nd cycle was higher. Besides, it took longer times to finally disproportionate all the H_2O_2 (20 h compared to the 13 h of the 1st cycle). The reasoning behind these results can be multiple. For example, the changing ratio **Ru(O)-tPa:Ru(O)-bPa** (Scheme 1) might have a role in the final O_2 concentration.

It is noteworthy the performance of both dye and catalyst, which is summarized in Table 1. At the end of the 1st cycle (18 h), the system achieves 25 µmol O_2 with TON_{Ru}= 62.5 and TON_{BDP}= 833.3 (entry 5 in Table 1). Moreover, the same sample gives remarkable performances after a 2nd cycle (24.5 h) with TON_{Ru}= 72.5 and TON_{BDP}= 1450 (entry 6 in Table 1). To the best of our knowledge, this is the best homogenous system dye-catalyst in terms of activity and stability.[8,12,16–20,38]

4.2.5 Proposed mechanism

With these results, we can conclude that the photocatalytic system composed of **BDP2** and WOC derived from **Ru-tPa** shows significant WOR and proven ORR. With the photophysical and electrochemical characterization of both dyes and the O_2 detection experiments, we propose the mechanism in Figure 6 as the most plausible scheme for this particular system.

Firstly, **BDP2** is photoexcited to its singlet excited state and by Photo-electron Transfer (PeT) it gets converted to its zwitterionic state with subsequent activation of the catalyst. This is contrary to previously reported photoactivation mechanisms, which assume an oxidative quenching of the excited photosensitizer to generate the oxidized PS by the sacrificial agent or oxygen, usually a $[(Ru(bpy)_3]^{2+}$ derivative going from Ru(II) to Ru(III).[12,40] Hitherto, the presence of O_2 does not quench the dyes and the lack of SA makes only possible the reductive quenching to **BDP2**$^-$ by the WOC. Despite this fact, further photophysical experiments are required to fully confirm this hypothesis.

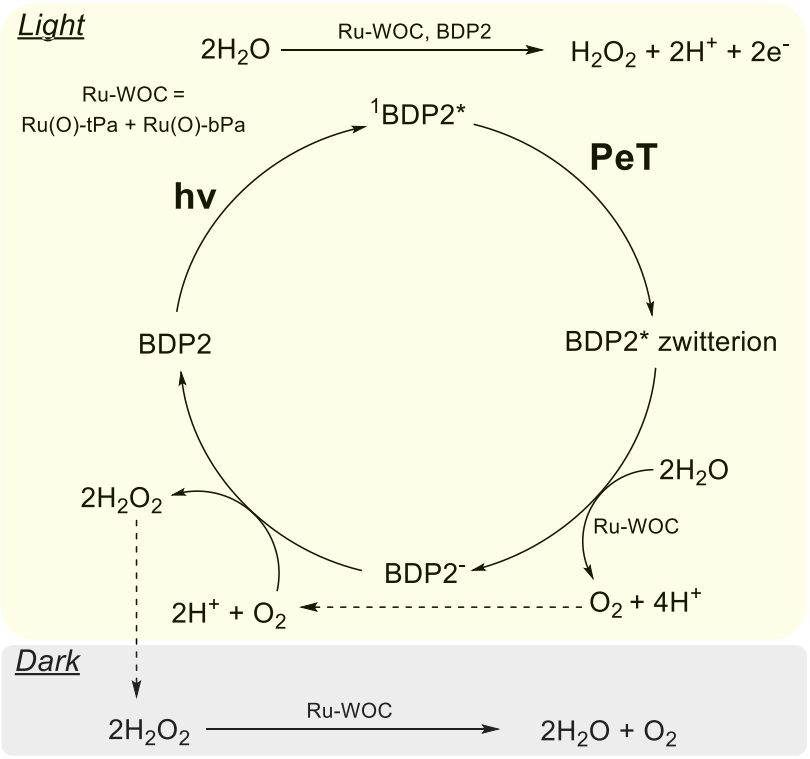

*Figure 6. Scheme of the proposed mechanisms for the oxygen evolution of the photochemical system **BDP2** and **Ru(O)-tPa**. Excitation of **BDP2** under light gets followed by a Photo-electron Transfer process (PeT) that generates the zwitterion. Afterward, water oxidation catalyzed by **Ru(O)-tPa** + **Ru(O)-bPa** (**Ru-WOC**) forms the reductive dye (**BDP2**$^-$). Finally, oxygen reduction to H_2O_2 will bring the dye to the ground state. In dark conditions, the H_2O_2 produced will disproportionate to O_2. The detected O_2 is the difference between the generated (WO by **Ru-WOC** and the disproportion of H_2O_2) and the consumed (ORR by **BDP2**$^-$).*

In the reductive quenching scheme, PeT generates a charge separation or zwitterionic state, schematically represented in Figure 6 (see also Scheme 1). Therefore, we propose the direct electron transfer from **Ru(O)-tPa** and/or **Ru(O)-bPa** to **BDP2-zwitterion**, a key step to produce its reduced species or **BDP2**$^-$. The **BDP2**$^-$ dye can further reduce the O_2 present in the solution to H_2O_2 (Equation 2). Regarding the catalyst, we assume the conversion of **Ru(O)-tPa** to **Ru(O)-bPa** in the presence of H_2O_2 (Scheme 1), which will disproportionate to O_2. Subsequently, the generated **Ru(O)-bPa** will act as WOC upon oxidation by **BDP2-zwitterion**. The overall reaction is the difference between the water oxidation ($4e^-$ process) and the oxygen reduction ($2e^-$ process). Further work is still needed to identify the fate of the two protons and two electrons not involved in the formation of hydrogen peroxide neither in its disproportion reaction.

4.3 Conclusions

In summary, we present two organic dyes that can support photoactivated oxygen evolution in a fully homogeneous system without a Sacrificial Agent (SA). In the absence of $Na_2S_2O_8$, dye's performance achieve TON_{BDP} of 15 (**BDP1**) and 163 (**BDP2**) within 4.5 h of irradiation. After further analysis of the spectroscopic data collected before and after the experiment, we concluded that the system is fully catalytic. No stoichiometric decrease of dye concentration with the amount of produced O_2 was observed, although **BDP1** and **BDP2** suffered some degradation. The electron-withdrawing effect of the nitrobenzyl moiety of **BDP2** presumably influences the oxidation potential of **BDP2-zwitterion**, thermodynamically favoring the reaction or enhancing the kinetics of the reaction. Besides, **BDP2**$^-$ is responsible for ORR to H_2O_2 through a $2e^-$ process. Subsequently, hydrogen peroxide converts **Ru(O)-tPa** to **Ru(O)-bPa** with concomitant O_2 production without any light/potential bias. Moreover, **Ru(O)-bPa** is an efficient water oxidation catalyst with lower overpotential compared to **Ru(O)-tPa**. All in all, herein we present a homogeneous photocatalytic system that generates significant amounts of O_2 under light and dark conditions with considerable TONs and remarkable stabilities. Further research is needed to fully confirm our mechanistic hypothesis through photophysical experiments.

4.4 References

(1) Waters, C. N.; Zalasiewicz, J.; Summerhayes, C.; Barnosky, A. D.; Poirier, C.; Galuszka, A.; Cearreta, A.; Edgeworth, M.; Ellis, E. C.; Ellis, M.; Jeandel, C.; Leinfelder, R.; McNeill, J. R.; Richter, D. d.; Steffen, W.; Syvitski, J.; Vidas, D.; Wagreich, M.; Williams, M.; Zhisheng, A.; Grinevald, J.; Odada, E.; Oreskes, N.; Wolfe, A. P. The Anthropocene Is Functionally and Stratigraphically Distinct from the Holocene. *Science* **2016**, *351* (6269), aad2622–aad2622. https://doi.org/10.1126/science.aad2622.

(2) Rockström, J.; Steffen, W.; Noone, K.; Persson, Å.; Chapin, F. S.; Lambin, E. F.; Lenton, T. M.; Scheffer, M.; Folke, C.; Schellnhuber, H. J.; Nykvist, B.; de Wit, C. A.; Hughes, T.; van der Leeuw, S.; Rodhe, H.; Sörlin, S.; Snyder, P. K.; Costanza, R.; Svedin, U.; Falkenmark, M.; Karlberg, L.; Corell, R. W.; Fabry, V. J.; Hansen, J.; Walker, B.; Liverman, D.; Richardson, K.; Crutzen, P.; Foley, J. A. A Safe Operating Space for Humanity. *Nature* **2009**, *461* (7263), 472–475. https://doi.org/10.1038/461472a.

(3) Nocera, D. G. Solar Fuels and Solar Chemicals Industry. *Acc. Chem. Res.* **2017**, *50* (3), 616–619. https://doi.org/10.1021/acs.accounts.6b00615.

(4) Tachibana, Y.; Vayssieres, L.; Durrant, J. R. Artificial Photosynthesis for Solar Water-Splitting. *Nat. Photonics* **2012**, *6* (8), 511–518. https://doi.org/10.1038/nphoton.2012.175.

(5) Gratzel, M. Artificial Photosynthesis: Water Cleavage into Hydrogen and Oxygen by Visible Light. *Acc. Chem. Res.* **1981**, *14* (12), 376–384. https://doi.org/10.1021/ar00072a003.

(6) Berardi, S.; Drouet, S.; Francàs, L.; Gimbert-Suriñach, C.; Guttentag, M.; Richmond, C.; Stoll, T.;

Llobet, A. Molecular Artificial Photosynthesis. *Chem. Soc. Rev.* **2014**, *43* (22), 7501–7519. https://doi.org/10.1039/C3CS60405E.

(7) Concepcion, J. J.; House, R. L.; Papanikolas, J. M.; Meyer, T. J. Chemical Approaches to Artificial Photosynthesis. *Proc. Natl. Acad. Sci.* **2012**, *109* (39), 15560–15564. https://doi.org/10.1073/pnas.1212254109.

(8) Brennaman, M. K.; Dillon, R. J.; Alibabaei, L.; Gish, M. K.; Dares, C. J.; Ashford, D. L.; House, R. L.; Meyer, G. J.; Papanikolas, J. M.; Meyer, T. J. Finding the Way to Solar Fuels with Dye-Sensitized Photoelectrosynthesis Cells. *J. Am. Chem. Soc.* **2016**, *138* (40), 13085–13102. https://doi.org/10.1021/jacs.6b06466.

(9) Alibabaei, L.; Brennaman, M. K.; Meyer, T. J. Light-Driven Water Splitting in the Dye-Sensitized Photoelectrosynthesis Cell. In *Molecular Devices for Solar Energy Conversion and Storage*; Tian, H., Boschloo, G., Hagfeldt, A., Eds.; Springer, Singapore, 2018; pp 229–257. https://doi.org/10.1007/978-981-10-5924-7_6.

IV

(10) Blakemore, J. D.; Crabtree, R. H.; Brudvig, G. W. Molecular Catalysts for Water Oxidation. **2015**. https://doi.org/10.1021/acs.chemrev.5b00122.

(11) Zhu, Y.; Wang, D.; Huang, Q.; Du, J.; Sun, L.; Li, F.; Meyer, T. J. Stabilization of a Molecular Water Oxidation Catalyst on a Dye−sensitized Photoanode by a Pyridyl Anchor. *Nat. Commun.* **2020**, *11* (1), 1–8. https://doi.org/10.1038/s41467-020-18417-5.

(12) Francàs, L.; Matheu, R.; Pastor, E.; Reynal, A.; Berardi, S.; Sala, X.; Llobet, A.; Durrant, J. R. Kinetic Analysis of an Efficient Molecular Light-Driven Water Oxidation System. *ACS Catal.* **2017**, *7* (8), 5142–5150. https://doi.org/10.1021/acscatal.7b01357.

(13) Limburg, B.; Bouwman, E.; Bonnet, S. Rate and Stability of Photocatalytic Water Oxidation Using [Ru(bpy)3]2+ as Photosensitizer. *ACS Catal.* **2016**, *6* (8), 5273–5284. https://doi.org/10.1021/acscatal.6b00107.

(14) Nayak, A.; Roy, S.; Sherman, B. D.; Alibabaei, L.; Lapides, A. M.; Brennaman, M. K.; Wee, K. R.; Meyer, T. J. Phosphonate-Derivatized Porphyrins for Photoelectrochemical Applications. *ACS Appl. Mater. Interfaces* **2016**, *8* (6), 3853–3860. https://doi.org/10.1021/acsami.5b10587.

(15) Ashford, D. L.; Gish, M. K.; Vannucci, A. K.; Brennaman, M. K.; Templeton, J. L.; Papanikolas, J. M.; Meyer, T. J. Molecular Chromophore–Catalyst Assemblies for Solar Fuel Applications. *Chem. Rev.* **2015**, *115* (23), 13006–13049. https://doi.org/10.1021/acs.chemrev.5b00229.

(16) McCormick, T. M.; Han, Z.; Weinberg, D. J.; Brennessel, W. W.; Holland, P. L.; Eisenberg, R. Impact of Ligand Exchange in Hydrogen Production from Cobaloxime-Containing Photocatalytic Systems. *Inorg. Chem.* **2011**, *50* (21), 10660–10666. https://doi.org/10.1021/ic2010166.

(17) Mou, Z.; Dong, Y.; Li, S.; Du, Y.; Wang, X.; Yang, P.; Wang, S. Eosin Y Functionalized Graphene for Photocatalytic Hydrogen Production from Water. *Int. J. Hydrogen Energy* **2011**, *36* (15), 8885–8893. https://doi.org/10.1016/j.ijhydene.2011.05.003.

(18) McCormick, T. M.; Calitree, B. D.; Orchard, A.; Kraut, N. D.; Bright, F. V.; Detty, M. R.; Eisenberg, R. Reductive Side of Water Splitting in Artificial Photosynthesis: New Homogeneous Photosystems of Great Activity and Mechanistic Insight. *J. Am. Chem. Soc.* **2010**, *132* (44), 15480–15483. https://doi.org/10.1021/ja1057357.

(19) Gueret, R.; Poulard, L.; Oshinowo, M.; Chauvin, J.; Dahmane, M.; Dupeyre, G.; Lainé, P. P.; Fortage, J.; Collomb, M. N. Challenging the [Ru(bpy)3]2+ Photosensitizer with a Triazatriangulenium Robust Organic Dye for Visible-Light-Driven Hydrogen Production in Water. *ACS Catal.* **2018**, *8* (5), 3792–3802. https://doi.org/10.1021/acscatal.7b04000.

(20) Vagnini, M. T.; Smeigh, A. L.; Blakemore, J. D.; Eaton, S. W.; Schley, N. D.; D'Souza, F.; Crabtree, R. H.; Brudvig, G. W.; Co, D. T.; Wasielewski, M. R. Ultrafast Photodriven Intramolecular Electron Transfer from an Iridium-Based Water-Oxidation Catalyst to Perylene Diimide Derivatives. *Proc. Natl. Acad. Sci. U. S. A.* **2012**, *109* (39), 15651–15656. https://doi.org/10.1073/pnas.1202075109.

(21) Eberhart, M. S.; Wang, D.; Sampaio, R. N.; Marquard, S. L.; Shan, B.; Brennaman, M. K.; Meyer, G. J.; Dares, C.; Meyer, T. J. Water Photo-Oxidation Initiated by Surface-Bound Organic Chromophores. *J. Am. Chem. Soc.* **2017**, *139* (45), 16248–16255. https://doi.org/10.1021/jacs.7b08317.

(22) Sabatini, R. P.; McCormick, T. M.; Lazarides, T.; Wilson, K. C.; Eisenberg, R.; McCamant, D. W. Intersystem Crossing in Halogenated Bodipy Chromophores Used for Solar Hydrogen Production. *J. Phys. Chem. Lett.* **2011**, *2* (3), 223–227. https://doi.org/10.1021/jz101697y.

(23) Bartelmess, J.; Francis, A. J.; El Roz, K. A.; Castellano, F. N.; Weare, W. W.; Sommer, R. D. Light-Driven Hydrogen Evolution by Bodipy-Sensitized Cobaloxime Catalysts. *Inorg. Chem.* **2014**, *53* (9),

4527–4534. https://doi.org/10.1021/ic500218q.

(24) Bañuelos, J. BODIPY Dye, the Most Versatile Fluorophore Ever? *Chem. Rec.* **2016**, *16* (1), 335–348. https://doi.org/10.1002/tcr.201500238.

(25) Dura, L.; Wächtler, M.; Kupfer, S.; Kübel, J.; Ahrens, J.; Höfler, S.; Bröring, M.; Dietzek, B.; Beweries, T. Photophysics of BODIPY Dyes as Readily-Designable Photosensitisers in Light-Driven Proton Reduction. *Inorganics* **2017**, *5* (2), 1–17. https://doi.org/10.3390/inorganics5020021.

(26) Banfi, S.; Nasini, G.; Zaza, S.; Caruso, E. Synthesis and Photo-Physical Properties of a Series of BODIPY Dyes. *Tetrahedron* **2013**, *69* (24), 4845–4856. https://doi.org/10.1016/j.tet.2013.04.064.

(27) Li, L.; Han, J.; Nguyen, B.; Burgess, K. Syntheses and Spectral Properties of Functionalized, Water-Soluble BODIPY Derivatives. *J. Org. Chem.* **2008**, *73* (5), 1963–1970. https://doi.org/10.1021/jo702463f.

(28) Loudet, A.; Burgess, K. BODIPY Dyes and Their Derivatives: Syntheses and Spectroscopic Properties. *Chem. Rev.* **2007**, *107* (11), 4891–4932. https://doi.org/10.1021/cr078381n.

(29) Komatsu, T.; Oushiki, D.; Takeda, A.; Miyamura, M.; Ueno, T.; Terai, T.; Hanaoka, K.; Urano, Y.; Mineno, T.; Nagano, T. Rational Design of Boron Dipyrromethene (BODIPY)-Based Photobleaching- Resistant Fluorophores Applicable to a Protein Dynamics Study. *Chem. Commun.* **2011**, *47* (36), 10055–10057. https://doi.org/10.1039/c1cc13367e.

(30) Vereshchuk, N.; Matheu, R.; Benet-Buchholz, J.; Pipelier, M.; Lebreton, J.; Dubreuil, D.; Tessier, A.; Gimbert-Suriñach, C.; Z. Ertem, M.; Llobet, A. Second Coordination Sphere Effects in an Evolved Ru Complex Based on a Highly Adaptable Ligand Results in Rapid Water Oxidation Catalysis. *J. Am. Chem. Soc.* **2020**, *142* (11), 5068–5077. https://doi.org/10.1021/jacs.9b11935.

(31) Matheu, R.; Ertem, M. Z.; Gimbert-Suriñach, C.; Sala, X.; Llobet, A. Seven Coordinated Molecular Ruthenium–Water Oxidation Catalysts: A Coordination Chemistry Journey. *Chem. Rev.* **2019**, *119* (6), 3453–3471. https://doi.org/10.1021/acs.chemrev.8b00537.

(32) Vereshchuk, N. Ph.D. Thesis: Rational Design of the Molecular Ru-Based Water Oxidation Catalysts, Universitat Rovira i Virgili, 2021.

(33) Shaffer, D. W.; Xie, Y.; Szalda, D. J.; Concepcion, J. J. Lability and Basicity of Bipyridine-Carboxylate-Phosphonate Ligand Accelerate Single-Site Water Oxidation by Ruthenium-Based Molecular Catalysts. *J. Am. Chem. Soc.* **2017**, *139* (43), 15347–15355. https://doi.org/10.1021/jacs.7b06096.

(34) Filatov, M. A. Heavy-Atom-Free BODIPY Photosensitizers with Intersystem Crossing Mediated by Intramolecular Photoinduced Electron Transfer. *Org. Biomol. Chem.* **2019**, *18* (1), 10–27. https://doi.org/10.1039/c9ob02170a.

(35) Guo, X.; Li, X.; Liu, X. C.; Li, P.; Yao, Z.; Li, J.; Zhang, W.; Zhang, J. P.; Xue, D.; Cao, R. Selective Visible-Light-Driven Oxygen Reduction to Hydrogen Peroxide Using BODIPY Photosensitizers. *Chem. Commun.* **2018**, *54* (7), 845–848. https://doi.org/10.1039/c7cc09383g.

(36) Berardi, S.; Francàs, L.; Neudeck, S.; Maji, S.; Benet-Buchholz, J.; Meyer, F.; Llobet, A. Efficient Light-Driven Water Oxidation Catalysis by Dinuclear Ruthenium Complexes. *ChemSusChem.* **2015**, *8* (21), 3688–3696. https://doi.org/10.1002/cssc.201500798.

(37) Ulrich, G.; Ziessel, R.; Harriman, A. The Chemistry of Fluorescent Bodipy Dyes: Versatility Unsurpassed. *Angew. Chem. Int. Ed.* **2008**, *47* (7), 1184–1201. https://doi.org/10.1002/anie.200702070.

(38) Andreiadis, E. S.; Chavarot-Kerlidou, M.; Fontecave, M.; Artero, V. Artificial Photosynthesis: From Molecular Catalysts for Light-Driven Water Splitting to Photoelectrochemical Cells. *Photochem. Photobiol.* **2011**, *87* (5), 946–964. https://doi.org/10.1111/j.1751-1097.2011.00966.x.

(39) Honda, T.; Kojima, T.; Fukuzumi, S. Proton-Coupled Electron-Transfer Reduction of Dioxygen Catalyzed by a Saddle-Distorted Cobalt Phthalocyanine. *J. Am. Chem. Soc.* **2012**, *134* (9), 4196–4206. https://doi.org/10.1021/ja209978q.

(40) Kaledin, A. L.; Huang, Z.; Geletii, Y. V.; Lian, T.; Hill, C. L.; Musaev, D. G. Insights into Photoinduced Electron Transfer between [Ru(bpy) 3]2+ and [S2O8]2- in Water: Computational and Experimental Studies. *J. Phys. Chem. A* **2010**, *114* (1), 73–80. https://doi.org/10.1021/jp908409n.

4.5 Supporting Information

4.5.1 Experimental

Anhydrous dichloromethane (DCM) was purchased from Sigma Aldrich. 2,3-dichloro-5,6-dicyano-benzoquinone (DDQ), Trifloroboron Etherate ($BF_3{\cdot}OEt_2$), and 2,4-dimethylpyrrole were purchased from TCI Chemicals. All other reagents were purchased from Sigma Aldrich. All liquid reagents and solvents were degassed prior to use by bubbling with argon or nitrogen for at least 10 min. Chlorosulphonic acid for the sulphonation step was purchased from Sigma Aldrich. A fresh solution was used for every sulphonation reaction. Na_2HPO_4 and NaH_2PO_4 for buffer solutions were purchased from Sigma Aldrich. Buffer solutions were prepared in 25 mL batches and the pH was checked using a Seven Compact pH meter from Mettler Toledo before every 5th experiment. Tetrabutylammonium hexafluorophosphate ($TBAPF_6$) and anhydrous acetonitrile (MeCN) for the electrochemical experiments as well as $Na_2S_2O_8$ for the oxygen evolution experiments were purchased from Sigma Aldrich and used without further purification. Acetonitrile for the photophysical experiments was purchased from Chem Lab as HPLC grade solvent.

Synthesis

Dyes **BDP1** and **BDP2** were synthesized from benzaldehyde and *p*-nitrobenzaldehyde respectively in 2 steps following procedures reported by Caruso and coworkers[1] and Burgess and coworkers[2] (see Figure S1). Both dyes were isolated as free acids in high purity and used for the subsequent experiments without further purification.

8-phenyl-1,3,5,7-tetramethyl-2,6-sulphonate-4,4-difluoro-4-bora-3a,4a-diaza-s-indacene (**BDP1**) was synthesised in 2 steps from benzaldehyde and 2,4-dimethylpyrrole. For the first step benzaldehyde (1.0 eq) and 2,4-dimethylpyrrole (2.1 eq) were dissolved in DCM. The other reagents were added at room temperature (RT) step by step when the characteristic color change (yellow-orange – deep red – dark violet) indicated the completion of the previous reaction. The crude unsulphonated BODIPY dye (**1'**) was isolated by filtrating the reaction solution through a plug of silica. The solid was carefully washed with DCM to increase the yield. Subsequently, the

solvent was removed from the combined filtrates. The crude product was further purified by preparative TLC on a silica plate with a 1:2 mixture of DCM and pentane as mobile phase yielding **1'** (24%) as a dark green, glittering powder.

R_f = 0.44 (DCM:pentane 1:2)

^{1}H-NMR: (300 MHz, CD_2Cl_2) d 7.49 (m_c, 3H, CH_{arom}), 7.30 (m_c, 2H, CH_{arom}), 6.01 (s, 2H, 2-CH, 6-CH), 2.51 (s, 6H, 3-CH_3, 5-CH_3), 1.39 (s, 6H, 1-CH_3, 7-CH_3)

For the second step **BDP1'** (1.0 eq) was dissolved in DCM under inert conditions. Chlorosulphonic acid (2.1 eq) was added as a 0.38 M solution in DCM at -40 °C. A color change from yellow to orange indicated the completion of the reaction. After warming to RT the reaction solution was extracted with water until the water remained colorless upon extraction. Removal of the solvent from the combined aqueous phases yielded **BDP1** (56%) as free acid in high purity.

R_f = 0.40 (methanol)

^{1}H-NMR: (400 MHz , D_2O) d 7.81 (mc, 1H, CH_{para}), 7.68 (mc, 2H, CH_{ortho}), 7.54 (mc, 2H, CH_{meta}), 2.41 (s, 6H, *3*-CH_3, *5*-CH_3), 1.75 (s, 6H, *1*-CH_3, *7*-CH_3)

8-(p-nitrophenyl)-1,3,5,7-tetramethyl-2,6-sulphonate-4,4-difluoro-4-bora-3a,4a-diaza-s-indacene (**BDP2**) was synthesised in two steps from *p*-nitrobenzaldehyde and 2,4-dimethylpyrrole. For the first step benzaldehyde (1.0 eq) and 2,4-dimethylpyrrole (2.1 eq) were dissolved in DCM. The other reagents were added step by step when the characteristic color change (yellow – red-brown – dark blue) indicated the completion of the previous reaction. The crude unsulphonated BODIPY dye (**2'**) was isolated by filtrating the reaction solution through a plug of silica. The solid was carefully washed with DCM to increase the yield. Subsequently, the solvent was removed from the combined filtrates. The crude product was further purified by preparative TLC on a silica plate with a 1:1 mixture of DCM and pentane as mobile phase yielding **2'** (12%) as an orange powder.

R_f = 0.48 (DCM:pentane 1:1)

^{1}H-NMR: (300 MHz, CD_2Cl_2) d 8.38 (d, 2H, arom-CH), 7.54 (d, 2H, arom-CH), 6.02 (s, 2H, 2-CH, 6-CH), 2.57 (s, 6H, 3-CH_3, 5-CH_3), 1.36 (s, 6H, 1-CH_3, 7-CH_3).

For the second step **BDP2'** (1.0 eq) was dissolved in DCM under inert conditions. Chlorosulphonic acid (2.1 eq) was added as a 0.38 M solution in DCM at -40 °C. A color change from yellow to red indicated the completion of the reaction. After warming to RT the reaction solution was extracted with water until the water remained colorless upon extraction. Removal of the solvent from the combined aqueous phases yielded **BDP2** (56%) as free acid in high purity.

IV

Rf = 0.54 (methanol)

^{1}H-NMR (400 MHz , D_2O) d 8.34 (mc, 2H, CH_{meta}), 7.54 (m_c, 2H, CH_{ortho}), 2.68 (s, 6H, *3*-CH_3, *5*-CH_3), 1.71 (s, 6H, *1*-CH_3 *7*-CH_3)

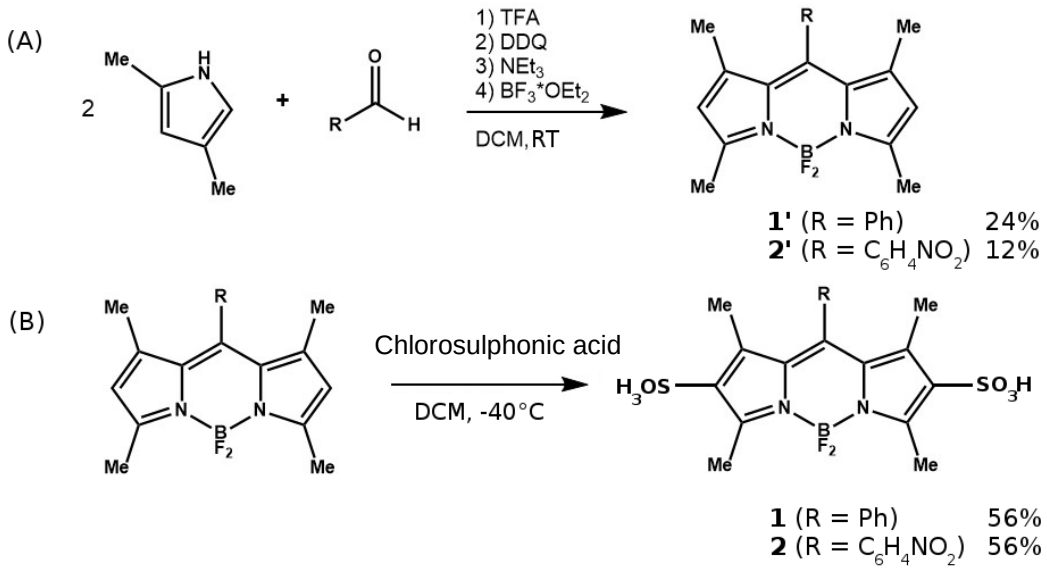

*Figure S1. Synthesis of dyes **BDP1** and **BDP2**. Step (A) was performed following a procedure by Caruso and coworkers[2] as a one-pot synthesis subsequently adding all four reagents. The step (B) was performed in a cooling bath from dry ice and MeCN at -40°C under inert atmosphere according to a procedure by Burgess and coworkers.*[2]

Ruthenium-based water oxidation catalyst

The WOC was prepared in two steps following a procedure described by Llobet and coworkers[3] and activated by bulk electrolysis to yield the desired **Ru(O)-tPa** (Figure 1).

4.5.2 Spectroscopy

All spectra were measured in 10x10 mm quartz cuvettes under ambient conditions unless stated otherwise. All analytics of reaction solutions were done in 2 mL samples. Photophysical characterization was done with optical densities as befit the method.

UV-Vis: Extinction coefficients and maximum absorptions in aqueous phosphate buffer (25 mM, pH7) were determined with a UV-2401PC spectrometer by Shimadzu measuring at least 4 solutions at different concentrations one of them 0 for the extinction coefficients. All spectra were measured from 300–600 nm in steps of 0.5 nm with the pure solvent as a reference and the entrance slit fixed at 2 nm.

Degradation experiments and analysis of the reaction solutions were conducted with a Cary 50 Bio Spectrometer by Varian starting with solutions of the dyes with an optical density of ~1. All spectra were measured from 300–600 nm in steps of 1 nm with the pure solvent as a reference and a speed of 4800 nm/s. Amounts of dye before and after oxygen-evolving experiments were calculated based on the absorbance at 516 nm (**BDP1**) and 519 nm (**BDP2**) using Lambert Beer´s Law with l = 1 cm and extinction coefficients as determined previously. The volume of each sample was 2 mL.

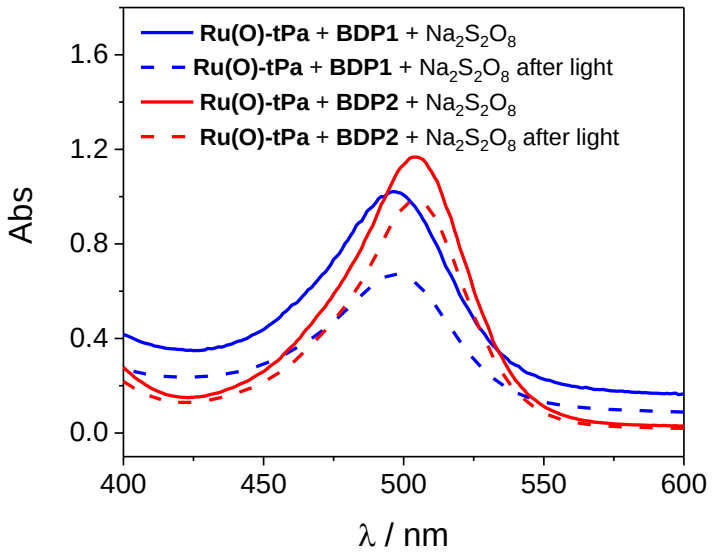

Figure S2. UV-Vis spectra of BDP1 (blue) and BDP2 (red) showing the decrease in dye concentration due to the presence of sacrificial agent before (solid lines) and after (dashed lines) photocatalysis.

IV

Fluorescence spectroscopy: All spectra were measured with a fluorolog spectrometer by Horiba Jobin Yvon in a 90° geometry using a 150 W Xe-lamp for excitation and a R928P PMT detector. As solvents either an aqueous phosphate buffer (25 mM, pH7.3) or acetonitrile were used with the pure solvent as a reference. Emission data were collected between 480–650 nm in steps of 1 nm, exciting at 470 nm. The entrance slit was fixed at 5 nm and the exit slit at 2 nm and for better signal to noise ratio 5 averaged spectra were collected.

For quantum yield measurements, a slightly different setup was used to befit the properties of the calibration sample. Both exit and entrance slit were fixed at 2 nm and only one spectrum per sample was measured. For each dye and solvent combination, multiple data sets at different optical densities were collected. All data analysis was done in origin, calculating the quantum yields of **BDP1** and **BDP2** using previously reported data on fluorescein in NaOH (0.1 M) for calibration (F = 85%).[3]

Time-resolved fluorescence: Fluorescence lifetimes were measured with a Life Spec II Spectrometer from Edinburgh Instruments. Samples were excited at 470 nm by a ps-pulsed diode laser EPL-470 by Edinburgh Instruments with an average maximum output of 5 mW set at a time window of 100 ns. Emission decay was detected at 540 nm using a High Speed Red PMT detector with a slit setting of 86 and an iris setting of 100%. Fluorescence lifetimes were determined from a single exponential decay fit done in Origin.

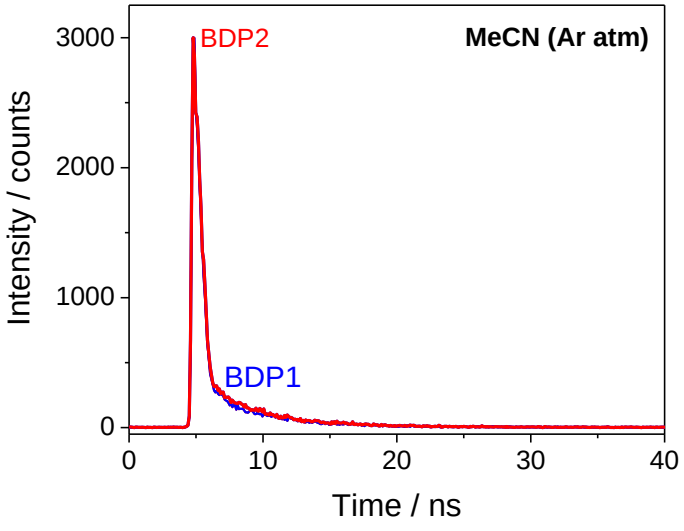

*Figure S3. Fluorescence decay (λ_{em} = 540 nm) of **BDP1** (blue) and **BDP2** (red) measured in MeCN.*

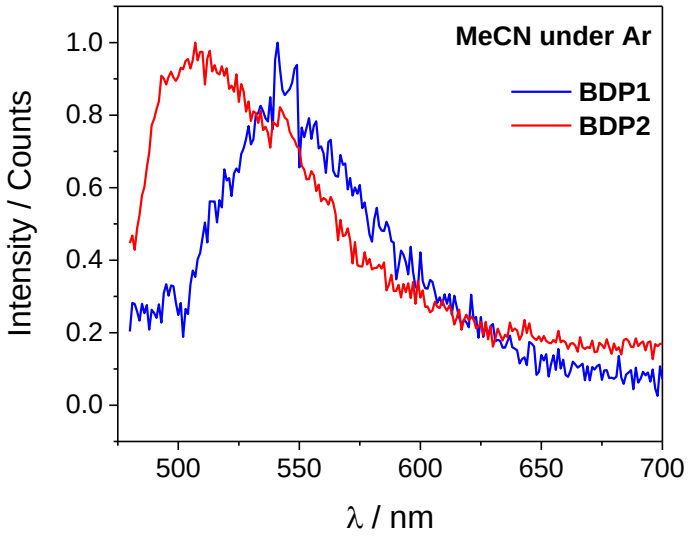

*Figure S4. Emission spectra of **BDP1** (blue) and **BDP2** (red) were measured in MeCN. Samples of appropriate optical density were excited with a 150 W Xenon Lamp at 470 nm and the signal was detected in a 90° geometry.*

	Measured data				***Literature data***	
dye	**BDP1**		**BDP2**		**BDP1**[4]	**BDP2**[5]
solvent	MeCN	pH 7	MeCN	pH 7	MeOH	Water
λ_{abs} (nm)	-/-	516	-/-	519	501	503
e (L/mol cm)	61000	49000	67000	62000	No data	No data
λ_{em} (nm)	507	-/-	525	-/-	508	511
Φ on air	0.03%	-/-	0.81%	-/-	0.2%	0.1%
t on air (ns)	5.40	3.98	5.13	4.02	No data	No data
t under Ar (ns)	5.64	4.00	5.14	3.95	No data	No data

*Table S1. Photophysical data of dyes **BDP1** and **BDP2** as well as relevant literature data.*[4,5] *Extinction coefficients and quantum yields were measured from at least four samples of suitable optical densities. Measurements in water were done in a 25 mM phosphate buffer at pH7. All measurements were done under ambient conditions unless stated otherwise.*

4.5.3 Electrochemistry

Cyclic Voltammetry (CV) was performed by using a CHI66D potentiostat. All the experiments were conducted in MeCN and aqueous phosphate buffer (100 mM) and under air or inert (N_2) conditions. In the latter, a continuous N_2 flow was left in the gas phase. Before the measurements, all solutions were degassed by bubbling nitrogen for

at least 15 min. A classical three electrodes set-up was used. For pH 7 phosphate buffer, the 3-electrode set-up consisted of a glassy carbon electrode as a working electrode (WE), a platinum counter electrode (CE), and an Hg/Hg_2SO_4 (sat. K_2SO_4) as a reference electrode (RE). All redox potentials in this work are reported vs NHE by adding 0.6 V to the measured potential.

To reproduce phytochemical's reaction conditions as much as possible an aqueous phosphate buffer at pH7 (100 mM) was used as a solvent. Higher concentrations of buffer were used because 25 mM resulted in very low signals due to conductivity issues. Each sample was degassed by bubbling a N_2 for at least 15 min prior to the experiment.

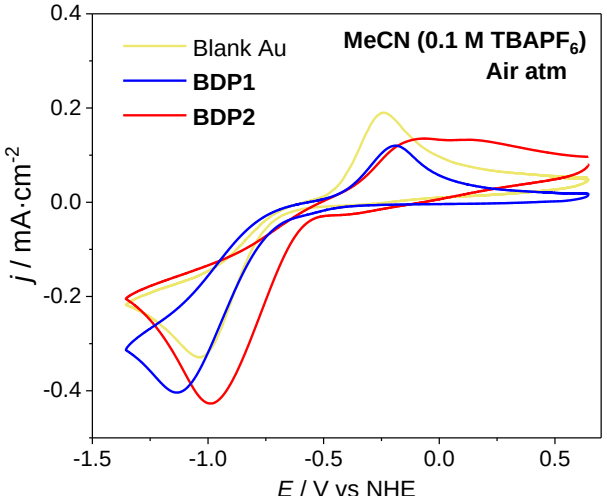

*Figure S5. CV of **BDP1** and **BDP2** in acetonitrile 0.1 M $TBAPF_6$ at 100 $mV \cdot s^{-1}$ under air atmosphere. Three-electrode set-up: Au as WE, Pt as CE and Hg/Hg_2SO_4 as RE.*

	BDP1		***BDP2***		***Ru(O)-tPa***
Solvent	MeCN	pH 7 pb	MeCN	pH 7 pb	pH 7 pb
E^{ox} (V vs NHE)	-/-	+1.16 ($PS^{0/1+}$)	-/-	+1.1 ($PS^{0/1+}$)	+1.4 ($Ru^{IV/III}$ & $Ru^{V/IV}$)
1st E^{red} (V vs NHE)	-0.78 ($PS^{1-/0}$)	-/- ($PS^{1-/0}$)	-0.57 ($PS^{1-/0}$)	-/- ($PS^{1-/0}$)	+0.36 ($Ru^{III/II}$)
2nd E^{red} (V vs NHE)	-/- ($PS^{2-/1-}$)	-/- ($PS^{2-/1-}$)	-0.75 ($PS^{2-/1-}$)	-/- ($PS^{2-/1-}$)	-/-

*Table S2. Electrochemical data of **BDP1**, **BDP2,** and **Ru(O)-tPa** measured by CV. All values are denoted vs. NHE (pH 7). Measurements in MeCN were done using $TBAPF_6$ as supporting electrolyte and Au as WE. Experiments in water were done in a 0.1 M phbf at pH 7 with a glassy carbon as WE. All samples were saturated with N_2 previous to the measurements.*

4.5.4 Oxygen Evolution Experiments

Oxygen evolution experiments were conducted in an aqueous phosphate buffer (25 mM) at pH7 in a 2 mL cell closed with a septum and equipped with a mantle for temperature control. Irradiation of 1.1 suns was provided by a Xe-lamp by Abet Technologies (150 W) equipped with a 400 nm cut-off filter. The temperature was kept at 25 °C by a PolyScience temperature controller using water as cooling agent. Oxygen evolution was measured in the gas phase using an NPOX709552 Clark electrode by Unisense. For a typical experiment, the reaction solution was assembled in the dark, the cell closed with a septum and the solution was stirred and degassed by bubbling nitrogen for at least 30 min. Subsequently, the Clark electrode was introduced and the temperature control started. After equilibration of the system irradiation was started. After 4.5 h the irradiation (average time across the experiments) was stopped and the Clark electrode calibrated. Calibration consisted of several injections of O_2 in the cell headspace. Calibrations were analyzed assuming the validity of ideal gas law. Initial slopes of the oxygen evolution were determined by a linear fit of the data measured during the first 1 h of irradiation. Initial turnover numbers (TONs) were calculated as the quotient of the total amount of O_2 produced in 4.5 h and the amount of WOC at the start of the irradiation.

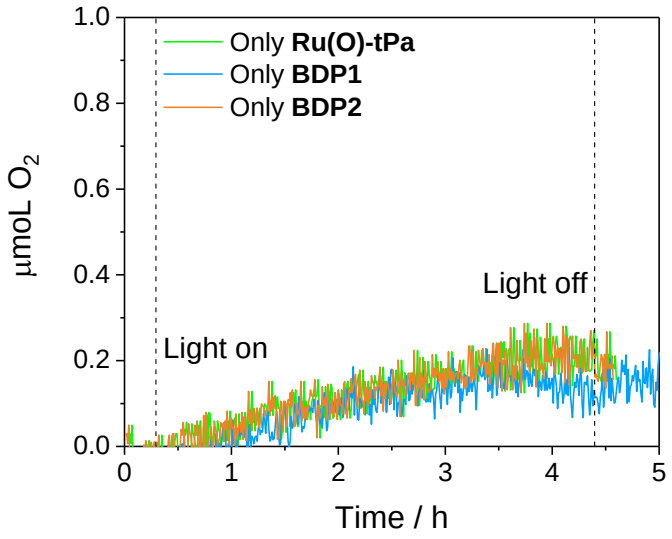

Figure S6. Blank photochemical experiments using only the dyes (approx. 20 µM) or the catalyst (200 µM) under the same conditions as in Figure 4 (1.1 sun irradiation by a Xe-lamp 150W with 400nm cut-off filter), 2 mL samples with the same concentrations.

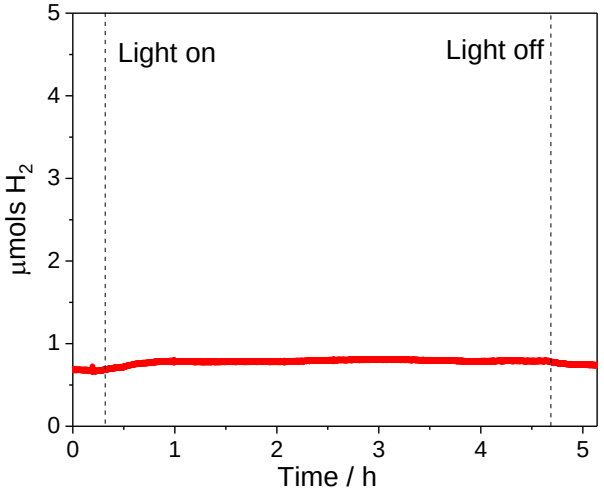

Figure S7. Hydrogen evolution experiment using the same set-up as WO experiments but with a selective Clark electrode for H_2.

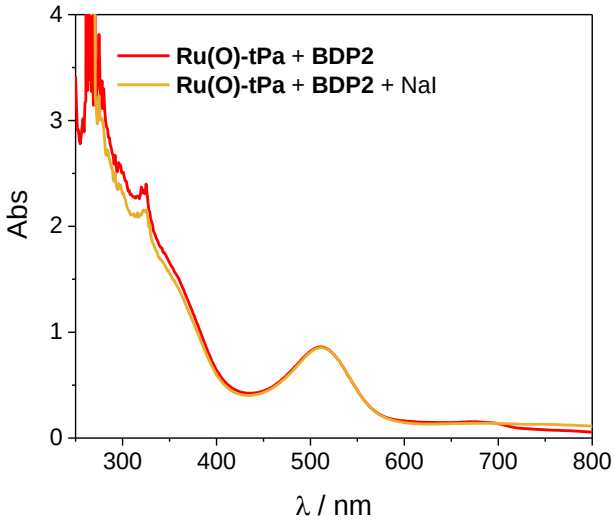

Figure S8. UV-Vis spectra showing the absence of I^{3-}, and thus of H_2O_2, in non-photoactivated samples.

4.5.5 References

(1) Banfi, S.; Nasini, G.; Zaza, S.; Caruso, E. Synthesis and Photo-Physical Properties of a Series of BODIPY Dyes. *Tetrahedron* **2013**, *69* (24), 4845–4856. https://doi.org/10.1016/j.tet.2013.04.064.

(2) Li, L.; Han, J.; Nguyen, B.; Burgess, K. Syntheses and Spectral Properties of Functionalized, Water-Soluble BODIPY Derivatives. *J. Org. Chem.* **2008**, *73* (5), 1963–1970. https://doi.org/10.1021/jo702463f.

(3) Vereshchuk, N.; Matheu, R.; Benet-Buchholz, J.; Pipelier, M.; Lebreton, J.; Dubreuil, D.; Tessier, A.; Gimbert-Suriñach, C.; Z. Ertem, M.; Llobet, A. Second Coordination Sphere Effects in an Evolved Ru Complex Based on a Highly Adaptable Ligand Results in Rapid Water Oxidation Catalysis. *J. Am. Chem. Soc.* **2020**, *142* (11), 5068–5077. https://doi.org/10.1021/jacs.9b11935.

(4) Gabe, Y.; Ueno, T.; Urano, Y.; Kojima, H.; Nagano, T. Tunable Design Strategy for Fluorescence Probes Based on 4-Substituted BODIPY Chromophore: Improvement of Highly Sensitive Fluorescence Probe for Nitric Oxide. *Anal. Bioanal. Chem.* **2006**, *386* (3), 621–626. https://doi.org/10.1007/s00216-006-0587-y.

(5) Komatsu, T.; Oushiki, D.; Takeda, A.; Miyamura, M.; Ueno, T.; Terai, T.; Hanaoka, K.; Urano, Y.; Mineno, T.; Nagano, T. Rational Design of Boron Dipyrromethene (BODIPY)-Based Photobleaching- Resistant Fluorophores Applicable to a Protein Dynamics Study. *Chem. Commun.* **2011**, *47* (36), 10055–10057. https://doi.org/10.1039/c1cc13367e.

Chapter 5

Noble-metal-free organic dye-sensitized photoanode with a molecular Cu water oxidation catalyst

Chapter 5.

Noble-metal-free organic dye-sensitized photoanode with a Cu water oxidation catalyst

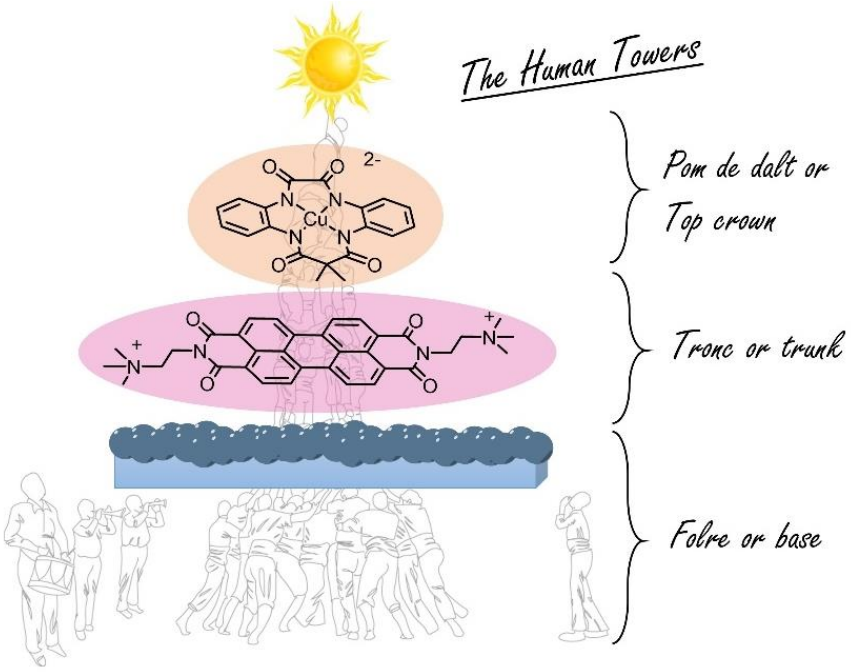

Abstract

We are witnessing a change in paradigm in the way we live, communicate, and transport. Our fossil fuel-based energy system is the main contributor to greenhouse gas emissions and thus, the rise in global average temperature and sea level with terrible consequences for the biosphere, the climate, and our society. For these reasons, the scientific community, inspired by Nature, has focused the attention on the design of artificial photosynthetic devices. Dye-Sensitized Photoelectrochemical Cells (DSPECs) are among all the proposed technologies. Their key components are (i) light-harvesting dye, (ii) n-type semiconductor materials to absorb light and/or promote electron-hole separation and transfer; (iii) catalysts for water oxidation and reduction of protons or carbon dioxide to useful chemicals or fuels. The present work is a preliminary attempt to rationally design a photoanode for water oxidation using widely available and earth-abundant materials. For this study we have employed a molecular dye from the perylene diimide family (namely N,N'-bis(2-(trimethylammonium)-ethylene)-perylene-3,4,9,10-tetracarboxylic acid bis-imide)]$(PF_6)_2$, and abbreviated as PDI) on Antimony doped Tin

Oxide (ATO, Sb:SnO_2). A copper complex with a macrocyclic tetraamidate ligand (N1,N1'-(1,2-phenylene)bis(N2-methyloxalamide)), labeled as Cu-MAC, is used as water oxidation catalyst. The resulting photoanode shows electronic communication through π-π and coloumbic interactions between catalyst/dye/support, becoming the first step towards a noble-metal-free water oxidation photoanode for DSPECs.

Contributions:

Marta Ventosa prepared the electrodes and performed photoelectrochemical and oxygen detection experiments.

5.1 Introduction

Globalization is the new paradigm in the 21st century.[1] The technological revolution has led to hyperconnectivity in communication and transportation. As a consequence, we are experiencing global economic growth with a concomitant increase in the human population,[2] and therefore, a proportional energy demand. Currently, our energy system is based on fossil fuels that contribute to the increase in atmospheric greenhouse gas concentration. As a result, higher global average temperatures and sea-level rise can push the Earth System beyond a planetary safe threshold with terrible consequences for the biosphere, the climate, and our society.[3] Therefore, it is utterly necessary to change and diversify our energy system. Nowadays, commercialized renewable energies, such as photovoltaics or wind turbines, are based on intermittent production of electricity, which can only be used on-site and does not achieve the demand.[2]

To overcome these limitations, researchers are focusing on technologies that can convert the energy of the sun into chemical bonds, i.e. solar fuels, which can be stored and transported regardless of the intermittency of the sun.[4–6] One of these envisioned technologies is Dye-Sensitized Photoelectrochemical Cells (DSPECs),[7,8] which fundamental mechanisms are based on artificial photosynthesis.[9,10] These devices are photoelectrochemical cells that use the sunlight energy to perform the oxidation of water (Equation 1) as a source of protons and electrons to reduce protons (Equation 2) or carbon dioxide (Equation 3 for a representative of the many reaction possibilities) to produce hydrogen or reduced carbon products as solar fuels, respectively.

Oxidation half-reaction: $2H_2O \rightarrow O_2 + 4H^+ + 4e^-$ $E°$= 1.23 V *vs.* NHE, pH 0 (Eq. 1)

Reduction half-reaction: $4H^+ + 4e^- \rightarrow 2H_2$ $E°$= 0 V *vs.* NHE, pH 0 (Eq. 2)

$CO_2 + 6H^+ + 6e^- \rightarrow CH_3OH + H_2O$ $E°$= 0.03 V *vs.* NHE, pH 0 (Eq. 3)

The main components of DSPECs[7] that promote these reactions are (a) dyes that act as light-harvesting antennas biomimicking protein complexes in Nature; (b) n- and p-type semiconductor materials that promote electron-hole separation and transfer to the reaction center; (c) highly active catalysts for the half-oxidation and half-reduction reactions, and (d) a membrane to keep the products separate. As seen in equations 1 to

3, water oxidation is key because it provides the necessary electrons and protons for solar fuel production. However, the oxidative conditions and high kinetic barriers are challenging to overcome, as shown by the lack of published photoanodes.[11] Moreover, most of the examples for dyes and water oxidation catalysts (WOCs) are based on noble metal complexes, which are scarce and expensive.[12] In this line, Meyer and coworkers[11] recently reported a TiO_2 photoanode with anchored phosphonate-derivatized Ru(II)bpy-based chromophores (bpy is 2,2'-bipyridine) and a phosphonate-derivative of Ru-bda family of WOCs (bda is 2,2'-bipyridine-6,6'-dicarboxylate).[13] Benchmarking Incident Photon to Current Efficiency (IPCE) of 25% was achieved, but O_2 evolution was limited to ~1 h at pH 5.8.

The present work is a preliminary attempt to build a photoanode for water oxidation, free of noble metal complexes. The abovementioned components are present in the studied photoanode, consisting of an organic dye, a wide-bandgap n-type semiconductor, and a first-row transition metal water oxidation catalyst. Figure 1 depicts the different units all together with their respective redox potentials, essential for band engineering, electronic communication, and successful photocatalysis. Firstly, the light-harvesting materials that have been selected for this project are a specific molecular dye from the perylene diimide family (namely N,N'-bis(2-(trimethylammonium)-ethylene)-perylene-3,4,9,10-tetracarboxylic acid bis-imide)]$(PF_6)_2$, and abbreviated as PDI) deposited on top of Antimony doped Tin Oxide (ATO, Sb:SnO_2). The adsorption of PDI onto ATO's surface is based on hydrophobic/π-stacking interactions giving rise to a hydrophobic layer that is stable in water.[14] This photoelectrode has been successfully used in the past for the splitting of hydrohalic acids (HX) to the corresponding halogen (X_2) and hydrogen (H_2).[14] The energy of the lowest unoccupied molecular orbital (LUMO) of the dye, PDI, is more negative than that of the ATO's conduction band (CB), enabling electron injection from $LUMO_{PDI}$ to CB_{ATO} as shown schematically in Figure 1. Besides, the highest occupied molecular orbital (HOMO) of the PDI, is high enough to promote hole transfer to the solution or the selected WOC. For this study, we have employed a copper complex with a cyclic tetraamidate ligand (N1,N1'-(1,2-phenylene)bis(N2-methyloxalamide)), labeled as Cu-MAC (Figure 1).[15] The selected WOC belongs to the family of first-row transition metal

complexes, which are earth-abundant and less toxic for the environment. Nonetheless, first-row transition metal complexes generally suffer from ligand lability that produces substitution and decomposition reactions leading to their corresponding oxides. Hence, most of the published examples are wrongly described as molecular catalysts.[16–20] In the case of Cu-MAC, the ligand scaffold promotes a "macrocyclic effect" that enhances the stability of the complex on a pH range from neutral to basic. Furthermore, the macrocycle surrounding the metal center acts as a non-innocent ligand, stabilizing high oxidation states by cooperating during water oxidation catalysis. Also, Cu-MAC is negatively charged which can enhance the coulombic interactions with the positively charged PDI (Figure 1). Moreover, it does not need an additional activation step to perform water oxidation as it happens for other benchmarking Ru-based catalysts.[21]

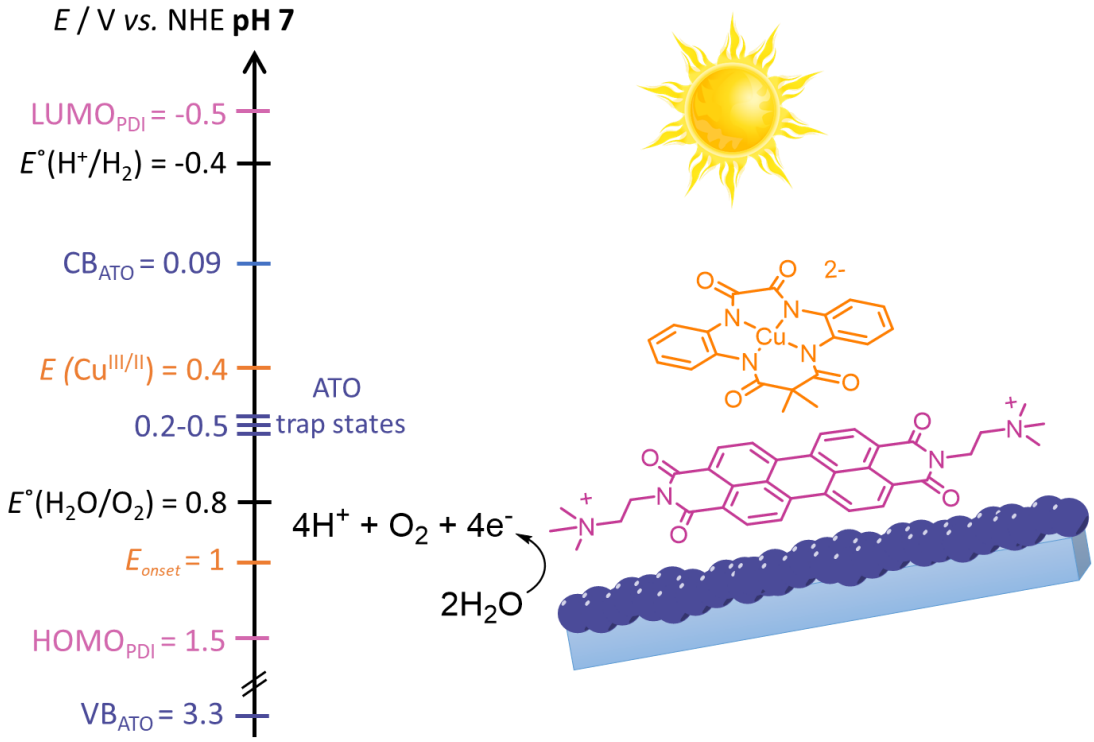

Figure 1. Band diagram of the studied photoanode. On the left axis, the potentials for water oxidation and proton reduction (black); PDI's HOMO-LUMO energy states (pink); ATO's energy bands (dark blue); $Cu^{III/II}$ redox potential of Cu-MAC (orange), and the onset of the catalysis (E_{onset}, orange). As seen, the studied bandgap engineering is suitable for the photon absorption by the PDI@ATO, the hole transfer to the Cu-MAC, and the oxidation of water.

5.2 Results and Discussion

5.2.1 Photoanode preparation and characterization

The procedure used to build the photoanode consisted of three main steps (Scheme 1). Firstly, a wide bandgap semiconductor ink was prepared by ultrasonicating Sb:SnO_2 nanoparticles (10 wt%) in ethanol:acetic acid solution. Then, the colloidal solution was spin-coat on a Fluorine Tin Oxide (FTO) to form ATO@FTO. Once the photoelectrode was dried and annealed in a muffle, ATO@FTO was modified by anchoring the dye and the catalyst via an optimized soaking methodology. The soaking solution consisted of a 1:1 mixture of PDI (1 mM in acetonitrile) and Cu-MAC (1 mM in isopropanol) and left to air dry. Two types of interactions play a role in the formation of the macromolecule Cu-MAC/PDI: π- π stacking between the perylene and the macrocycle ligand, and coulombic interactions between the negatively charged Cu-MAC and positively charged PDI. Nuclear Magnetic Resonance (NMR) spectroscopy supports this hypothesis by showing a small shift in the Cu-MAC's aromatic peaks once it interacts with PDI (Figure S2). In addition, the final aggregate interacts with the negatively charged ATO layer through π-stacking and coulombic contacts, as previously studied PDI-ATO interfaces.[14] Thus, the result is a new photoanode herein labeled as Cu-MAC/PDI@ATO@FTO. Besides, photoelectrodes without Cu-catalyst were prepared as blanks for the experiments. A similar synthetic procedure was followed but the ATO@FTO was soaked in a solution containing only the PDI (1 mM in acetonitrile), leading to PDI@ATO@FTO (Figure S1).

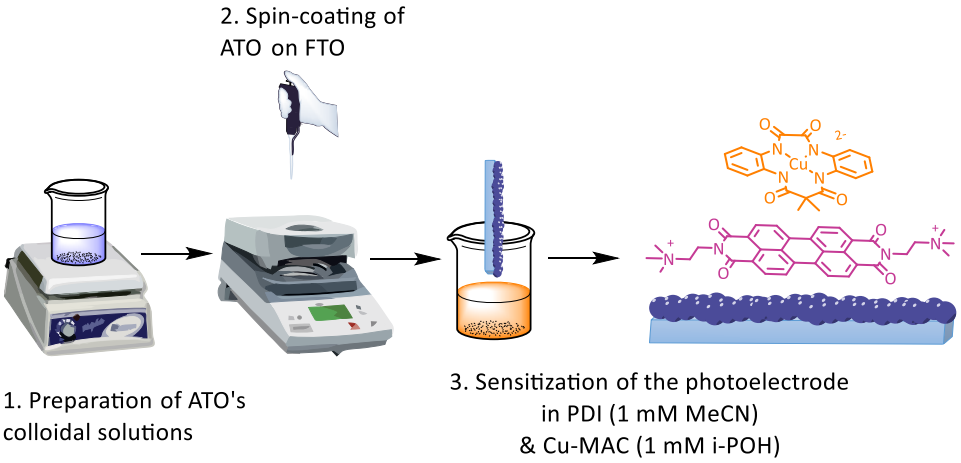

Scheme 1. Preparation of the photoelectrode Cu-MAC/PDI@ATO@FTO : 1) preparation of the colloidal solution of ATO by ultrasonication; 2) spin-coating of the ATO solution on FTO slides; 3) soaking of the fresh photoelectrodes in a solution of PDI (1 mM acetonitrile) and Cu-MAC (1 mM isopropanol) and leaving it to air dry.

By naked eye, the colors of the end photoelectrodes are grey-blue for ATO@FTO, purple-red for PDI@ATO@FTO, and orange-red for Cu-MAC/PDI@ATO@FTO. To verify sensitization, UV-Vis, and Linear Sweep Voltammetry (LSV) were performed (Figures 2 and 3). Figure 2 presents the data for PDI@ATO@FTO. On the left, the absorption spectra of the photoelectrode indicate the presence of PDI with the same fingerprint as reported previously characterized by a strong absorption band at λ_{max} = 488 nm with a shoulder at λ = 523-552 nm.[22] On the right, sequential chopped light LSVs performed to provide information of the (photo)current as a function of applied bias at a scan rate of 10 $mV \cdot s^{-1}$. The LSVs were performed in a home-made cell with a three-electrode set-up (the studied photoelectrodes as working electrodes, a Pt coil as the counter electrode, and Hg/Hg_2SO_4 as the reference electrode) in phosphate buffer pH = 7.0 (I = 0.1 M) and with chopped light illumination (1 sun, AM 1.5 G, see Supporting Information for details). All potentials were measured using a Hg/Hg_2SO_4 (K_2SO_4 sat.) as the reference electrode and converted to V *vs.* NHE (pH = 7.0) by adding 0.65 V to the measured potential. The outcome *J-V* curves are recorded under transient dark/light conditions, indicating dark-currents, photocurrents, electron-hole recombination, and stability. As shown in the *J-V* curves of Figure 2, the n-type PDI@ATO@FTO shows high photocurrents up to 0.4 $mA \cdot cm^{-2}$ in the first scan (red line) that decrease dramatically in the second LSV (orange line). Upon repetitive LSVs scans (grey lines), the decrease rate lowers down until a plateau in photocurrent is reached in the 13^{th}-15^{th} sweeps (0.089 $mA \cdot cm^{-2}$ at 0.845 V). These experiments suggest that the PDI, which is responsible for light absorption and charge transfer leading to the observed photocurrent, is lost during electrochemical experiments. Besides, charge recombination is only noticeable on the 15^{th} LSV (highlighted with a black circle), which takes the form of overshooting or spike during the transient dark/light conditions. As well, short-circuit or dark-currents are only significant in the first scans and at higher potentials (E > 0.6 V, see red and orange). To confirm that the decrease in photocurrent is related to the decrease in PDI's concentration on the surface of the ATO@FTO electrode, UV-Vis spectra were recorded after each sweep. As seen on the left graph in Figure 2, the dye's concentration decreases approximately 33% until a plateau is reached (blue-green lines in UV-Vis) coinciding with the last LSVs. Averagely, across samples, the plateau was reached at an Abs = 0.4-0.5 at λ_{max} = 488 nm, which implied around 13-15 LSVs. Therefore, stability

issues have to be taken into consideration before testing such photoanodes in catalytic assays. Thus, a new step was added to the preparation protocol previous to water oxidation experiments: fresh photoanodes were swept in the potential range of 0.2 V to 1.0 V *vs*. NHE under 1 sun illumination until stable values in PDI's concentration and photoactivity were reached.

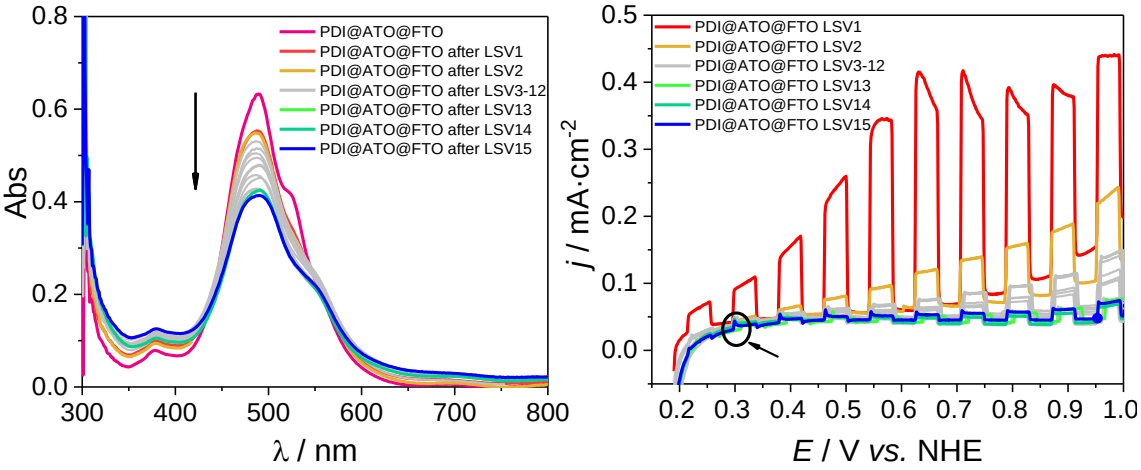

Figure 2. Left, UV-Vis spectra of PDI@ATO@FTO freshly prepared (red) and after undergoing several LSVs (grey) until a stable value in absorption and concentration (after 13-15 LSVs, green-blue lines). Right, a photoelectrode PDI@ATO@FTO in pH 7 phosphate buffer and under 1 sun (AM 1.5 G) was swept in potential under dark/light conditions (chopped light LSVs at 10 mV·s^{-1}, see SI for electrochemical set-up). The result is sequential J-V curves indicating low recombination and dark-currents but presenting a high decrease in photoactivity over 13 scans until photocurrent stabilization is achieved (from LSV1 in red to LSV13-15 in green-blue).

The same type of analysis was performed with Cu-MAC/PDI@ATO@FTO photoanodes (Figure 3). In this case, the sensitization process is characterized by the dye-catalyst solution abovementioned. As shown by the UV-Vis spectra on the left graph of Figure 3, the loading of PDI is significantly lower than for the PDI@ATO@FTO fresh sample (with maximum absorbances of approximately 0.4 and 0.6 for the fresh samples, respectively, at λ_{max} = 488 nm). However, Cu-MAC/PDI@ATO@FTO UV-Vis spectrum coincides with the one of PDI@ATO@FTO after 15 LSVs (Figure 2), suggesting that the loading of PDI reaching absorbances of ~0.4 provides optimum stability in this photoelectrode configuration. For this PDI concentration, photocurrents *ca.* 30 μA·cm^{-2} at 0.8 V with no recombination are recorded after consecutive chopped light LSVs (Figure 3, right). Furthermore, the LSVs show an oxidative wave at E_a ≈ 0.38-0.42 V that corresponds to the $Cu^{III/II}$ wave of the Cu-MAC complex, which matches the reported value (see also Figure S5).[15] Moreover, similar absorption spectra before and after LSVs (Figure 3, left) can be observed, indicative of the stability of the dye on the surface. Interestingly, a

slight shift of the maximum absorption peak and its shoulder between the two types of electrodes is observed (λ_{max} = 492 and λ = 526 nm for Cu-MAC/PDI@ATO@FTO and λ_{max} = 487-490 nm and λ = 523-552 nm for PDI@ATO@FTO, see also Figure 4). We attribute this phenomenon to the interaction of the π-system of the PDI with that of the copper complex mentioned above. Noteworthy is the dark currents for Cu-MAC/PDI@ATO@FTO photoanodes. For PDI@ATO@FTO photoanodes, the hydrophobic layer of PDI protects ATO@FTO from the electrolyte and thus, from short-circuits. Yet in the case of Cu-MAC/PDI, unlike thin layer photoelectrodes, dye-catalyst systems are not forming differentiated layers, which means that some Cu-MAC molecules will be in direct contact with ATO@FTO favoring short-circuit currents. However, the dark current is not significant compared to the photocurrents achieved.

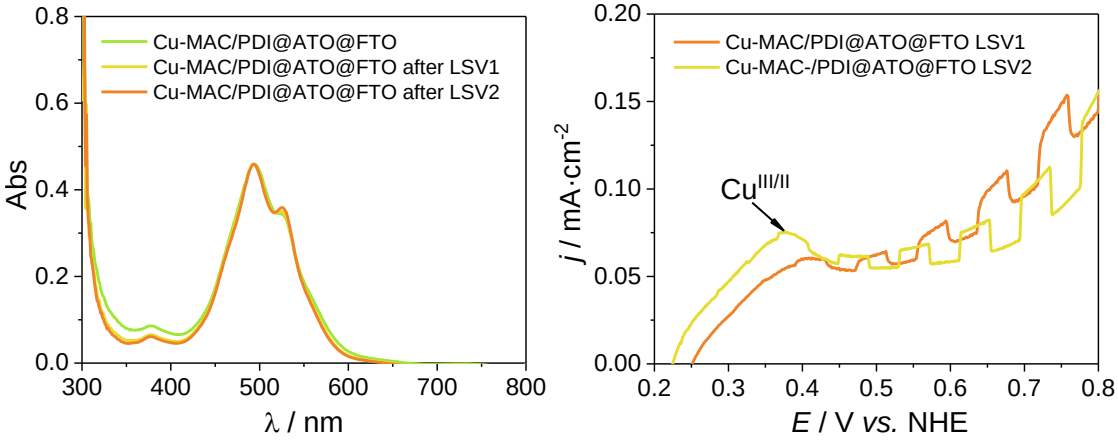

Figure 3. Left, UV-Vis spectra of Cu-MAC/PDI@ATO@FTO (in green) and the same sample after two LSVs (yellow and orange). The spectra show similar absorption values, i.e. stable concentration after LSVs. Right, a photoelectrode Cu-MAC/PDI@ATO@FTO in pH 7 phosphate buffer and under 1 sun (AM 1.5 G) was swept in potential under dark/light conditions (chopped light LSVs at 10 mV·s^{-1}, see SI for electrochemical set-up).

5.2.2 Photoelectrochemical water oxidation

Comparative photoelectrochemical experiments Cu-MAC/PDI@ATO@FTO *vs.* PDI@ATO@FTO were carried out to examine its performance for photocatalytic water oxidation. Figure 4 left, shows the UV-Vis spectra of both electrodes with the same maximum absorption of 0.4 (λ_{max} = 488 nm), i.e. dye concentration. The broadness of the bands confirms the aggregation of the dye onto the surface, which is confirmed by previous evidence[14] and by comparison with the absorption of the PDI in solution (Figure S3). In fact, the PDI in homogeneous phase has two well-defined peaks, typical vibronic structures for non-aggregated chromophores. PDI@ATO@FTO has a more broadened

shoulder than Cu-MAC/PDI@ATO@FTO, presumably as a result of the interaction with Cu-MAC that translates into more pronounced peaks. Such interaction has been proposed above from NMR experiments (Figure S2) and will be further discussed below based on X-ray Absorption Spectroscopy (XAS) characterization.

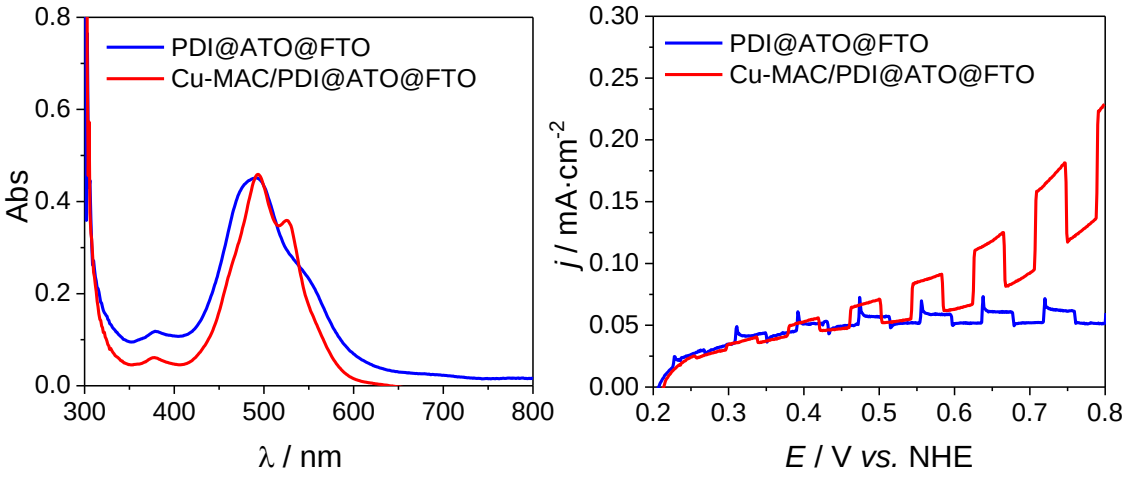

Figure 4. Left, UV-Vis spectra of PDI@ATO@FTO (blue) and Cu-MAC/PDI@ATO@FTO (red) photoelectrodes. Both show similar absorption values and thus, in dye concentration. Right, photoelectrodes Cu-MAC/PDI@ATO@FTO (red) and the blank PDI@ATO@FTO (blue) were swept in potential under dark/light conditions (chopped light LSVs at 10 mV·s^{-1}, 1 sun AM 1.5 G) in pH 7 phosphate buffer (see SI for details of the electrochemical set-up).

The right graph in Figure 4 shows comparative LSVs with (red) and without (blue) the water oxidation catalyst Cu-MAC on the surface, corresponding to almost superimposable λ_{max} (UV-Vis spectra, left graph). It is clear that the presence of catalyst increases the overall photocurrent in the potential range $E \approx 0.45$-0.8 V. For example, at $E = 0.65$ V the photocurrents of Cu-MAC/PDI@FTO are ~56 μA·cm^{-2} compared to the photocurrents of 10 μA·cm^{-2} registered by PDI@ATO@FTO. These results confirm the successful electronic interaction between Cu-MAC/PDI and the Cu-MAC activity towards oxidation. Besides, another obvious consequence of the presence of the catalyst is that efficient hole extraction eliminates the recombination spikes shown by PDI@ATO@FTO (blue line). However, the latter has much lower photocurrents maybe due to the hydrophobic layer formed by stacked PDI and/or the absence of harsh water oxidation conditions. Analogous results were obtained with the samples prepared at the University of Ferrara (Figure S6), showing high reproducibility and proving the influence of the catalyst in enhancing the electrode photocurrent. With these promising results, experiments for O_2 detection were conducted to confirm that the observed photocurrent is indeed due to the water oxidation reaction.

5.2.3 O_2 evolution experiments

Collector-Generator experiments[23] provide O_2 quantification when working with photocurrents in the range of $\mu A \cdot cm^{-2}$. This method is fully explained in the Supporting Information and represents a useful alternative to O_2 liquid-phase detection. Briefly, two interfaced electrodes with minimum separation between them (Figure S7) are immersed in solution (phosphate buffer at pH 7) and connected to a bipotentiostat, which allows the use of two Working Electrodes (WE) with controlled potential or current. The WEs are: the studied photoanode (WE1 or Generator) and a bare FTO electrode (WE2, Collector). In our case, WE1 is held at the thermodynamic potential for the water oxidation to dioxygen reaction (bulk electrolysis at 0.845 V *vs.* NHE pH 7) with net production of O_2 only when the sample is back-illuminated. It is then when the generated O_2 diffuses to the FTO-Collector, where its reduction takes place. The ratio between the charge passed in the WE1-Generator (Oxygen Evolution Reaction, OER) and the WE2-Collector (Oxygen Reduction Reaction, ORR) depends on the rate of diffusion of the O_2 and the Faradaic Efficiency (FE) of the process. Before testing the samples, a calibration of the set-up is required to determine the gas diffusion rate between a generator with known FE of 100% and the collector, as explained in the SI (Figure S8).

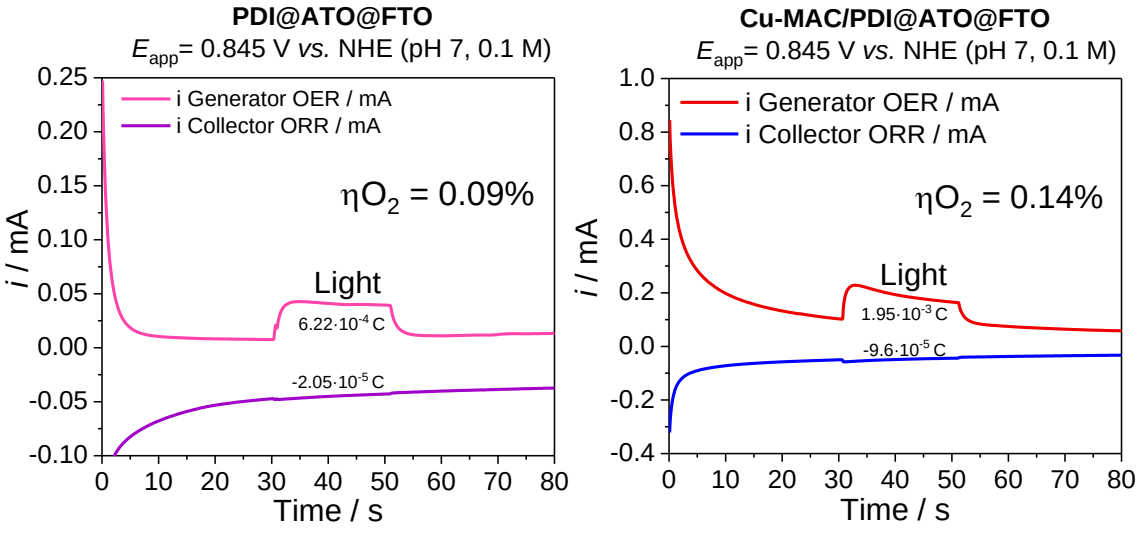

Figure 5. Collector-Generator experiments for O_2 detection. G-C set-up: left, PDI@ATO@FTO as generator (pink); right, Cu-MAC/PDI@ATO@FTO as generator (red). Both photoelectrodes are interfaced to an FTO electrode that collects the diffused oxygen and reduces it.

Figure 5 depicts C-G experiments for PDI@ATO@FTO (left) and Cu-MAC/PDI@ATO@FTO (right) acting as generator photoelectrodes, both interfaced to different bare FTO collectors. During the experiment, samples were held at the

thermodynamic water oxidation potential, acting as a baseline for the integration of the photocurrent to determine the charge (*Q)*. After a 30 s baseline, 20 s illumination gave rise to the expected photocurrent in the generator electrodes (in pink for PDI, left, and in red for Cu-MAC/PDI, right). Despite the increase in photocurrent, low amounts of charge passed through the FTO collectors leading to FE lower than 1% (purple for PDI and blue for Cu-MAC/PDI). The reason for the low efficiencies is still unknown and currently under study. Three main hypotheses are (i) ATO's trap states could hindrance catalysis by trapping holes; (ii) dye degradation consuming electrons; (iii) instability of the pair Cu-MAC/PDI, whose contact by coulombic forces could get affected during the redox reactions. Moreover, the G-C set-up could enhance mechanical de-attachment of the dye as seen by the naked eye. Figure S9 compares the UV-Vis spectra before and after G-C experiment. Further research is being carried out to determine if the low reduction in absorption intensity is enough to explain all the observed photocurrent in Figure 5. Importantly, the photocurrent generated by Cu-MAC/PDI@ATO@FTO (right) is higher than the blank (left) as well as the charge generated by ORR (FTO collector). Therefore, the oxygen detection efficiency (ηO_2) for Cu-MAC/PDI@ATO@FTO is 0.14%, which is slightly higher than that of the catalyst-free PDI@ATO@FTO photoelectrode (ηO_2 = 0.09%), highlighting the potential beneficial role of the copper catalyst on the surface of the electrode, enhancing the water oxidation reaction. Although these values are far from those reported for benchmarking water oxidation photoanodes based on purely inorganic n-type semiconductors such as bismuth vanadate or tungsten oxide,[24,25] they are strong evidence of the successful interaction of the different parts of the complex multicomponent system.

5.2.4 X-ray Absorption Spectroscopy (XAS)

X-ray Absorption Near-Edge (XANES) and Extended X-ray Absorption Fine Structure (EXAFS) spectroscopies were performed to further characterize the electronic and structural interactions between Cu-MAC/PDI and its stability after photocatalysis. The experiments were done in CLAESS beamline at ALBA synchrotron in collaboration with Dr. D. Moonshiram (IMDEA Materiales, Madrid).

Figure 6 depicts XANES and EXAFS spectra of Cu-MAC, Cu-MAC/PDI in solution, and the photoanode Cu-MAC/PDI@ATO@FTO before and after photocatalysis. The Cu(II) K-edge of square planar and tetrahedral complexes are generally characterized by the main peak along the rising edge from 8980 to 9000 eV identified as the 1s → ($4p_z$ + shakedown) contributions, with concurrent Ligand to Metal Charge Transfer (LMCT) transition induced by X-rays.[26] In our study, Cu-MAC in aqueous solution shows a 1s → (4 p_z + shakedown) transition at 8987 eV and a main 1s → 4p peak at 8999 eV (black, Figure 6A). In contrast, a solution of Cu-MAC containing PDI shows a broader 1s → ($4p_z$ + shakedown) transition and small variations in the XANES features (compare black and red traces in Figure 6A). The rising edge at 8980 to 9020 eV corresponds to small changes in the local coordination sphere and local symmetry of Cu-MAC upon homogenous dissolution with PDI, suggesting close contact of the copper complex with the PDI either by coulombic or π-π stacking interactions, as suggested before by NMR spectroscopy. On the other hand, the spectra of Cu-MAC/PDI@ATO@FTO before and after photocatalysis display a missing 1s → ($4p_z$+shakedown) transition, typically observed for transformation from four-to-five or six-coordinate geometry (pink and green in Figure 6 top).[27,28] A change in the coordination geometry of the Cu center leads to a greater delocalization of the metal 4p orbitals, resulting in a broader and smoother 1s → $4p_z$ transition feature.[29] The intensity of the 8999 eV peak is also higher upon deposition on ATO@FTO, suggesting a higher coordination number due to the proportionality of the oscillation amplitude with the coordination number. [27,28] All these results indicate the potential interaction (probably a contact) of the Cu center with either H_2O or OH^- ligands or even of the Cu metal center with the aromatic cloud of the PDI and/or the oxide surface.[30]

A prominent peak at ca. 1.92-1.98 Å is observed in the EXAFS spectra of the Cu complex in solution and on the surface of the electrode, corresponding to the averaged contribution of the Cu-N bond distances and weaker peaks at longer Cu-C distances ca. 2.64-3.79 Å (Figure 6C and Table S1). Analysis of Cu-MAC-PDI@ATO@FTO before and after photocatalysis shows a clear reduction in the Cu-C distances in the 2nd and 3rd coordination spheres in comparison to the Cu-MAC complex in solution or with PDI

(Figure 6), again highlighting the strong influence of the electrode deposition on the copper catalyst structure.

Importantly, the XAS analysis of the photoelectrodes before and after catalysis rules out the possibility of copper oxide formation during photooxidation and shows no significant change of the original copper complex on the surface (pink and green in Figure 6C and D). The lack of copper oxide is indicated by the absence of the characteristic peak at 8986 eV in the XANES and EXAFS spectra (brown in Figure 6B and D).

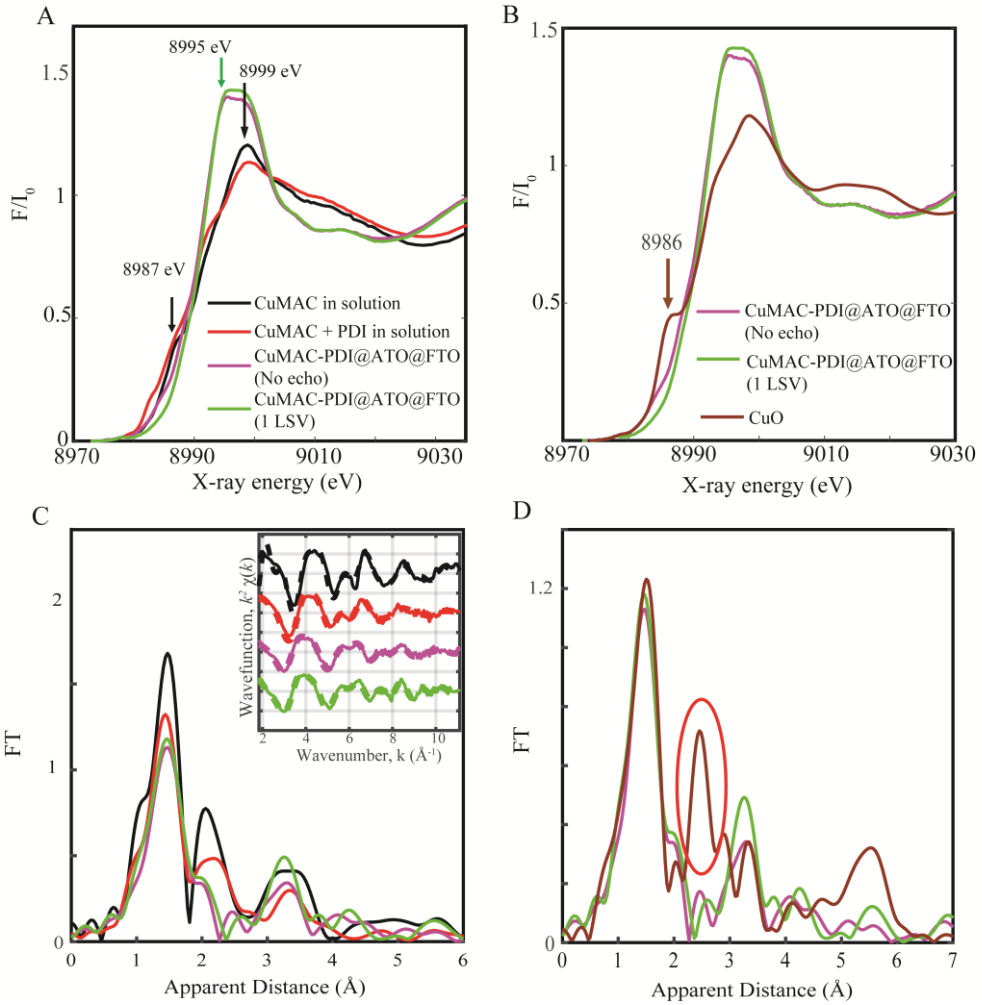

Figure 6. A) Cu K-edge XANES of Cu-MAC in aqueous solution (black), Cu-MAC + PDI in solution (red), Cu-MAC/PDI on ATO@FTO after directly soaking (pink), and Cu-MAC/PDI@ATO@FTO after electrochemistry (echo). For this experiment, echo consists of 1 LSV, 10 mV·s^{-1} from 0.2-0.8 V (green). B) Normalized Cu K-edge XANES of fresh Cu-MAC/PDI@ATO@FTO (pink) and after 1 LSV, 10 mV/s from 0.2-0.8 V (green) in comparison with CuO (red). The typical XANES feature at 8986 eV present in CuO is absent in the Cu-MAC/PDI@ATO@FTO, both before and after photocatalysis. C) Experimental Fourier transforms of k2-weighted Cu EXAFS of Cu-MAC in solution (black), Cu-MAC with PDI in solution (red), a fresh Cu-MAC/PDI@ATO@FTO (pink) and Cu-MAC/PDI@ATO@FTO after 1 LSV from 0.2-0.8 V (green); inset, back Fourier transformed experimental (solid lines) and fitted (dashed lines) k2[χ(k)] of the analyzed samples. Experimental spectra were calculated for k values of 1.839-11.1 Å-1. D) Experimental Fourier transforms of k2-weighted Cu EXAFS of a fresh Cu-MAC/PDI@ATO@FTO (pink) and Cu-MAC/PDI@ATO@FTO after 1 LSV from 0.2-0.8 V (green); together with CuO (brown). The EXAFS features of CuO are clearly absent from the Cu-MAC complexes anchored on ATO@FTO surfaces before and after photocatalysis.

5.3 Conclusions

We have presented a rationally designed modular DSPEC photoanode based on noble-metal-free components, suitable for the envisioned circular economy and material scarcity. This work combines a first-row transition metal water oxidation catalyst, Cu-MAC, with a PDI@ATO@FTO photoanode both working at neutral pH conditions. In addition, the selected WOC displays complementary charge to that of the PDI favoring coulombic interactions as well as π- π interactions between the aromatic regions. These interactions are proposed based on NMR, UV-Vis, and XAS spectroscopy. The final Cu-MAC/PDI@ATO@FTO photoanodes were characterized by UV-Vis and LSV, demonstrating higher photocurrents than the bare PDI@ATO@FTO electrodes, proving the interaction of the different components and the beneficial role of the copper catalyst on the surface. However, Faradaic efficiencies are still too low for device implementation. Despite this fact, Cu-MAC/PDI@ATO@FTO photoelectrode is the first example of a noble-metal-free DSPEC-photoanode reported to date and is the proof-of-concept of a broad field of research with high potential to achieve low-cost water oxidation photoelectrocatalysis. These results also highlight important challenges in the field which are i) increasing Faradaic efficiency by studying charge transfer dynamics; ii) improving the stability of the dye/catalyst supramolecular complex on the surface of the electrode which is paramount for long term operation. However, it is important to highlight that XAS analysis demonstrated the presence of molecular Cu-MAC after light-driven water oxidation.

5.5 References

(1) United Nations General Assembly. *Fulfilling the Promise of Globalization: Advancing Sustainable Development in an Interconnected World: Report of the Secretary-General*; 2017; Vol. 13609.
(2) Lewis, N. S.; Nocera, D. G. Powering the Planet: Chemical Challenges in Solar Energy Utilization. *Proc. Natl. Acad. Sci.* **2006**, *103* (43), 15729–15735. https://doi.org/10.1073/pnas.0603395103.
(3) Steffen, W.; Rockström, J.; Richardson, K.; Lenton, T. M.; Folke, C.; Liverman, D.; Summerhayes, C. P.; Barnosky, A. D.; Cornell, S. E.; Crucifix, M.; Donges, J. F.; Fetzer, I.; Lade, S. J.; Scheffer, M.; Winkelmann, R.; Schellnhuber, H. J. Trajectories of the Earth System in the Anthropocene. *Proc. Natl. Acad. Sci. U. S. A.* **2018**, *115* (33), 8252–8259. https://doi.org/10.1073/pnas.1810141115.
(4) Nocera, D. G. Solar Fuels and Solar Chemicals Industry. *Acc. Chem. Res.* **2017**, *50* (3), 616–619. https://doi.org/10.1021/acs.accounts.6b00615.
(5) Office of Basic Energy Sciences. *Report of the Basic Energy Sciences Roundtable on Liquid Solar*

Fuels; Rockville, 2019. https://doi.org/10.2172/1615599.

(6) Lewis, N. S. Research Opportunities to Advance Solar Energy Utilization. *Science* **2016**, *351* (6271). https://doi.org/10.1126/science.aad1920.

(7) Brennaman, M. K.; Dillon, R. J.; Alibabaei, L.; Gish, M. K.; Dares, C. J.; Ashford, D. L.; House, R. L.; Meyer, G. J.; Papanikolas, J. M.; Meyer, T. J. Finding the Way to Solar Fuels with Dye-Sensitized Photoelectrosynthesis Cells. *J. Am. Chem. Soc.* **2016**, *138* (40), 13085–13102. https://doi.org/10.1021/jacs.6b06466.

(8) Alibabaei, L.; Brennaman, M. K.; Meyer, T. J. Light-Driven Water Splitting in the Dye-Sensitized Photoelectrosynthesis Cell. In *Molecular Devices for Solar Energy Conversion and Storage*; Tian, H., Boschloo, G., Hagfeldt, A., Eds.; Springer, Singapore, 2018; pp 229–257. https://doi.org/10.1007/978-981-10-5924-7_6.

(9) Tachibana, Y.; Vayssieres, L.; Durrant, J. R. Artificial Photosynthesis for Solar Water-Splitting. *Nat. Photonics* **2012**, *6* (8), 511–518. https://doi.org/10.1038/nphoton.2012.175.

(10) Berardi, S.; Drouet, S.; Francàs, L.; Gimbert-Suriñach, C.; Guttentag, M.; Richmond, C.; Stoll, T.; Llobet, A. Molecular Artificial Photosynthesis. *Chem. Soc. Rev.* **2014**, *43* (22), 7501–7519. https://doi.org/10.1039/C3CS60405E.

(11) Zhu, Y.; Wang, D.; Huang, Q.; Du, J.; Sun, L.; Li, F.; Meyer, T. J. Stabilization of a Molecular Water Oxidation Catalyst on a Dye−sensitized Photoanode by a Pyridyl Anchor. *Nat. Commun.* **2020**, *11* (1), 1–8. https://doi.org/10.1038/s41467-020-18417-5.

(12) Vesborg, P. C. K.; Jaramillo, T. F. Addressing the Terawatt Challenge: Scalability in the Supply of Chemical Elements for Renewable Energy. *RSC Adv.* **2012**, *2* (21), 7933–7947. https://doi.org/10.1039/c2ra20839c.

(13) Eberhart, M. S.; Wang, D.; Sampaio, R. N.; Marquard, S. L.; Shan, B.; Brennaman, M. K.; Meyer, G. J.; Dares, C.; Meyer, T. J. Water Photo-Oxidation Initiated by Surface-Bound Organic Chromophores. *J. Am. Chem. Soc.* **2017**, *139* (45), 16248–16255. https://doi.org/10.1021/jacs.7b08317.

(14) Berardi, S.; Cristino, V.; Canton, M.; Boaretto, R.; Argazzi, R.; Benazzi, E.; Ganzer, L.; Cerullo, G.; Syrgiannis, Z.; Bignozzi, C. A.; Caramori, S.; Rigodanza, F.; Prato, M. Perylene Diimide Aggregates on Sb-Doped SnO 2 : Charge Transfer Dynamics Relevant to Solar Fuel Generation. *J. Phys. Chem. C* **2017**, *121*, 17737–17745. https://doi.org/10.1021/acs.jpcc.7b05928.

(15) Garrido-Barros, P.; Moonshiram, D.; Gil-Sepulcre, M.; Pelosin, P.; Gimbert-Suriñach, C.; Benet-Buchholz, J.; Llobet, A. Redox Metal-Ligand Cooperativity Enables Robust and Efficient Water Oxidation Catalysis at Neutral pH with Macrocyclic Copper Complexes. *J. Am. Chem. Soc.* **2020**, *142* (41), 17434–17446. https://doi.org/10.1021/jacs.0c06515.

(16) Najafpour, M. M.; Feizi, H. Water Oxidation Catalyzed by Two Cobalt Complexes: New Challenges and Questions. *Catal. Sci. Technol.* **2018**, *8* (7), 1840–1848. https://doi.org/10.1039/c7cy02602a.

(17) Pattanayak, S.; Chowdhury, D. R.; Garai, B.; Singh, K. K.; Paul, A.; Dhar, B. B.; Gupta, S. Sen. Electrochemical Formation of FeV(O) and Mechanism of Its Reaction with Water During O−O Bond Formation. *Chem. - A Eur. J.* **2017**, *23* (14), 3414–3424. https://doi.org/10.1002/chem.201605061.

(18) Hong, D.; Mandal, S.; Yamada, Y.; Lee, Y.-M.; Nam, W.; Llobet, A.; Fukuzumi, S. Water Oxidation Catalysis with Nonheme Iron Complexes under Acidic and Basic Conditions: Homogeneous or Heterogeneous? *Inorg. Chem.* **2013**, *52* (16), 9522–9531. https://doi.org/10.1021/ic401180r.

(19) Najafpour, M. M.; Moghaddam, A. N.; Dau, H.; Zaharieva, I. Fragments of Layered Manganese Oxide Are the Real Water Oxidation Catalyst after Transformation of Molecular Precursor on Clay. *J. Am. Chem. Soc.* **2014**, *136* (20), 7245–7248. https://doi.org/10.1021/ja5028716.

(20) Pelosin, P.; Gil-Sepulcre, M.; Garrido-Barros, P.; Moonshiram, D.; Benet-Buchholz, J.; Gimbert-Suriñach, C.; Llobet, A. Analysis of the Active Species Responsible for Water Oxidation Using a Pentanuclear Fe Complex. *iScience* **2020**, *23* (8). https://doi.org/10.1016/j.isci.2020.101378.

(21) Matheu, R.; Ertem, M. Z.; Benet-Buchholz, J.; Coronado, E.; Batista, V. S.; Sala, X.; Llobet, A. Intramolecular Proton Transfer Boosts Water Oxidation Catalyzed by a Ru Complex. *J. Am. Chem. Soc.* **2015**, *137* (33), 10786–10795. https://doi.org/10.1021/jacs.5b06541.

(22) Ronconi, F.; Syrgiannis, Z.; Bonasera, A.; Prato, M.; Argazzi, R.; Caramori, S.; Cristino, V.; Bignozzi, C. A. Modi Fi Cation of Nanocrystalline WO 3 with a Dicationic Perylene Bisimide: Applications to Molecular Level Solar Water Splitting. **2015**, 16–19. https://doi.org/10.1021/jacs.5b01519.

(23) Grau, S.; Berardi, S.; Moya, A.; Matheu, R.; Cristino, V.; Vilatela, J. J.; Bignozzi, C. A.; Caramori, S.; Gimbert-Suriñach, C.; Llobet, A. A Hybrid Molecular Photoanode for Efficient Light-Induced Water Oxidation. *Sustain. Energy Fuels* **2018**, *2* (9), 1979–1985. https://doi.org/10.1039/C8SE00146D.

(24) Liang, Y.; Tsubota, T.; Mooij, L. P. A.; Van De Krol, R. Highly Improved Quantum Efficiencies for Thin Film BiVO4 Photoanodes. *J. Phys. Chem. C* **2011**, *115* (35), 17594–17598. https://doi.org/10.1021/jp203004v.
(25) Hong, S. J.; Lee, S.; Jang, J. S.; Lee, J. S. Heterojunction BiVO4/WO3 Electrodes for Enhanced Photoactivity of Water Oxidation. *Energy Environ. Sci.* **2011**, *4* (5), 1781–1787. https://doi.org/10.1039/c0ee00743a.
(26) Sarangi, R. X-Ray Absorption near-Edge Spectroscopy in Bioinorganic Chemistry: Application to M-O 2 Systems. *Coord. Chem. Rev.* **2013**, *257* (2), 459–472. https://doi.org/10.1016/j.ccr.2012.06.024.
(27) Lockard, J. V.; Kabehie, S.; Zink, J. I.; Smolentsev, G.; Soldatov, A.; Chen, L. X. Influence of Ligand Substitution on Excited State Structural Dynamics in Cu(I) Bisphenanthroline Complexes. *J. Phys. Chem. B* **2010**, *114* (45), 14521–14527. https://doi.org/10.1021/jp102278u.
(28) Chen, L. X.; Jennings, G.; Liu, T.; Gosztola, D. J.; Hessler, J. P.; Scaltrito, D. V.; Meyer, G. J. Rapid Excited-State Structural Reorganization Captured by Pulsed X-Rays. *J. Am. Chem. Soc.* **2002**, *124* (36), 10861–10867. https://doi.org/10.1021/ja017214g.
(29) Baker, M. L.; Mara, M. W.; Yan, J. J.; Hodgson, K. O.; Hedman, B.; Solomon, E. I. K- and L-Edge X-Ray Absorption Spectroscopy (XAS) and Resonant Inelastic X-Ray Scattering (RIXS) Determination of Differential Orbital Covalency (DOC) of Transition Metal Sites. *Coord. Chem. Rev.* **2017**, *345*, 182–208. https://doi.org/10.1016/j.ccr.2017.02.004.
(30) Garrido-Barros, P.; Gimbert-Surinifach, C.; Moonshiram, D.; Picón, A.; Monge, P.; Batista, V. S.; Llobet, A. Electronic I-Delocalization Boosts Catalytic Water Oxidation by Cu(II) Molecular Catalysts Heterogenized on Graphene Sheets. *J. Am. Chem. Soc.* **2017**, *139* (37), 12907–12910. https://doi.org/10.1021/jacs.7b06828.

5.6 Supporting Information

5.6.1 Experimental

Na_2HPO_4, NaH_2PO_4, polyethylene glycol 600 (PEG600), and liquid reagents were purchased from Sigma-Aldrich and Sb:SnO_2 from Alfa Aesar (Sb_2O_5:SnO_2 15:85 wt%, 13-22 nm particles). FTO substrates were purchased from Pilkington (FTO TEC 8, 8 $\Omega \cdot sq^{-1}$). Buffer solutions were prepared in 25 mL batches and the pH was checked using a Seven Compact pH meter from Mettler Toledo before every 5th experiment. The dye PDI was obtained from the laboratory of Prof. Caramori at the University of Ferrara, and the water oxidation catalyst Cu-MAC was previously synthesized in our group following the reported procedure.

pH = 7.0 buffered solution (0.1 M ionic strength) was prepared by dissolving NaH_2PO_4 (2.3 g, 0.017 M) and Na_2HPO_4 (3.75 g, 0.026 M) were dissolved with Mili-Q water up to 1 L solution. The pH was measured by a pHmeter.

5.6.2 Preparation of photoelectrodes

ATO@FTO: FTO slides were cleaned by 10 min ultrasonication in different solutions: (1) detergent solution (Hellmanex); (2) Milli-Q water; (3) ethanol. Afterward, they were dried with a *Kimtech*™ paper and in the muffle at 495°C. Meanwhile, 10 wt% ATO colloidal solution was prepared by 20 min ultrasonication of Sb:SnO_2 commercial powder in a mixture of acetic acid and ethanol solution (1.5 g:5 mL). Then, PEG600 was added up to 2 wt% and sonicated for 20 more minutes. Subsequently, the colloidal grey-blue solution was spin-coated (6 seconds at 600 rpm, then 20 seconds at 2000 rpm) and annealed at 550 °C for 15-20 minutes in the muffle. The spin-coating and annealing procedure was repeated 3 times. Finally, the photoelectrodes were cut into pieces with an active area of 1 cm^2 and some bare FTO for electric contact with cupper-tape.

PDI@ATO@FTO: ATO@FTO was sensitized with dye following a reported procedure.[1] Fresh photoelectrodes ATO@FTO were soaked overnight in a solution of PDI (1 mM in acetonitrile, $PF6^-$ as counterion). Then, they were rinsed with clean acetonitrile and left to air dry. Figure S1 depicts the resulting photoanode.

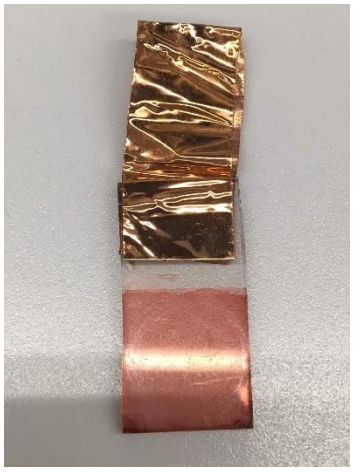

Figure S1. Photography of PDI@ATO@FTO after preparation.

Cu-MAC/PDI@ATO@FTO: Fresh photoelectrodes ATO@FTO were soaked overnight in a 1:1 solution of PDI (1 mM in acetonitrile, $PF6^-$ as counterion) and Cu-MAC (1mM in isopropanol). Both molecules form an ionic pair in solution with concomitant counterions precipitation possibly as Me_4NPF_6. Then, they were rinsed with clean acetonitrile and left to air dry. Find Scheme 1 in the main text as a support to understand the procedure employed.

5.6.3 Spectroscopy

^{1}H-NMR: A Bruker Avance 400 MHz or a Bruker 500 MHz were employed for recording ^{1}H NMR. Chemical shifts (δ) are reported in ppm.

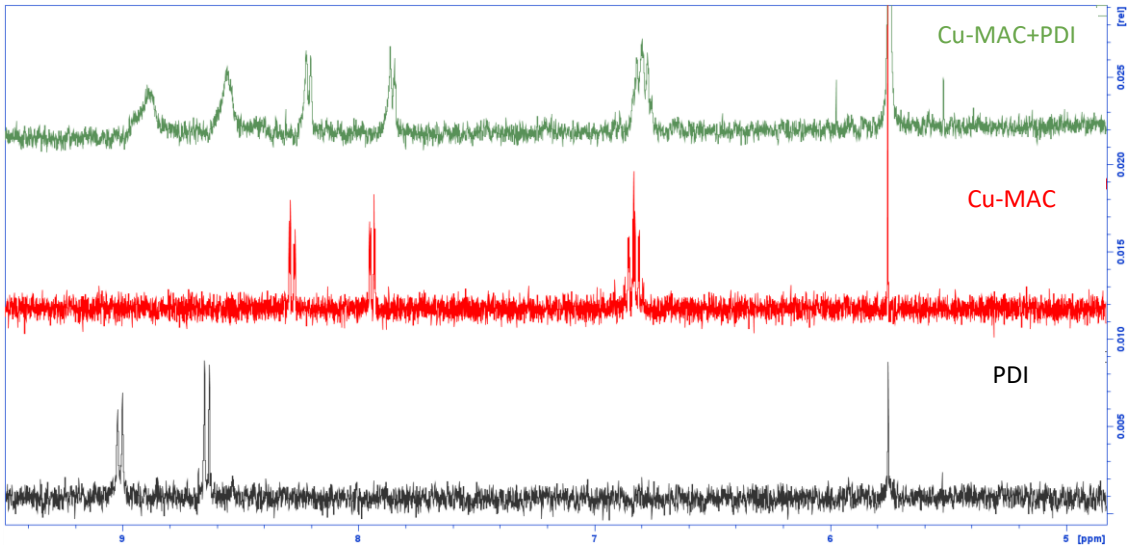

Figure S2. ^{1}H-NMR of Cu-MAC (red), PDI (black), and C-uMAC+PDI (green) in DMSO-d. The latter has a displacement of the aromatic peaks towards to lower ppm compared to only Cu-MAC and only PDI solutions.

*UV-Vis: M*aximum absorptions were recorded with a Cary 50 Bio Spectrometer (Varian) directly on the photoelectrodes from 300–800 nm (steps of 1 nm and a speed of 4800 nm·s^{-1}).

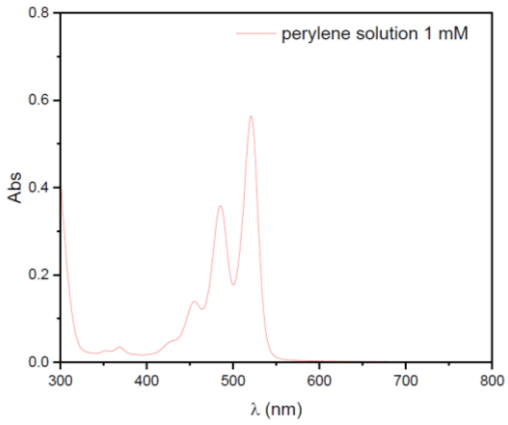

Figure S3. UV-Vis spectra of a 1 mM PDI in acetonitrile (adapted from[2]).

5.6.4 Electrochemistry

Two different (photo)electrochemical techniques were used to determine the performance of the photoelectrodes. Both were performed in a three-electrode configuration, being the photoanode the Working Electrode (WE), a Pt coil as the Counter Electrode (CE), and a Hg/Hg_2SO_4 the Reference Electrode (RE). The photoanode

was mounted as the window of a custom-made Teflon cell for back illumination (Figure S4). Thus, a 0.5 cm^2 area of the photoanode was in contact with the electrolyte. The CE and the RE were immersed from the top directly in the solution. Unless stated, pH 7 phosphate buffer solution (I = 0.1M) was used as an electrolyte. As well, the light source was a Xenon Lamp (Abet LS150) with a solar simulator filter (AM 1.5 G) unless otherwise stated. 1 sun illumination was calibrated using a silicon photodiode providing total light of 100 $mW \cdot cm^2$ to the photoelectrode.

Figure S4. Photography of the custom-made Teflon cell used for the (photo)electrochemical experiments (adapted from[3]).

Linear sweep voltammetry (LSV) and bulk electrolysis (BE) were measured using a CHI660D potentiostat or CHI660D bipotentiostat. For the LSV, the photoanode was swept with a scan rate of 10 $mV \cdot s^{-1}$. For the BE, photoanodes were held at 0.845 V *vs.* NHE (pH 7). For both, chopped illumination was provided by a shutter with a speed of 4 s pulse. All the potentials reported in this work converted to the Normal Hydrogen Electrode (NHE) at pH 7.

In Figure S5 additional electrochemical data is provided so the reader has an understanding of the electrochemical behavior of Cu-MAC.[4]

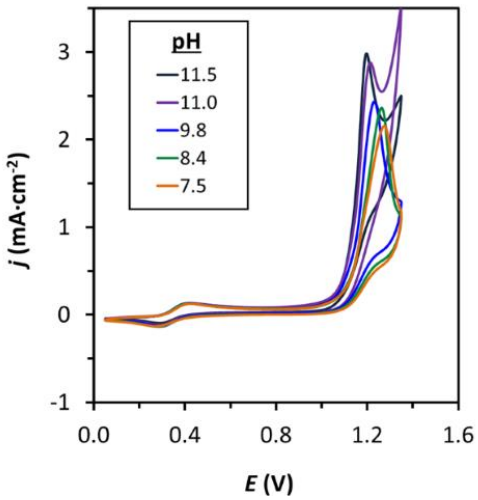

Figure S5. Cyclic voltammetry of Cu-MAC at different pH complex (adapted from[4]). In pH 7.5 the redox wave $Cu^{III/II}$ is at 0.4 V vs. NHE (pH 7).

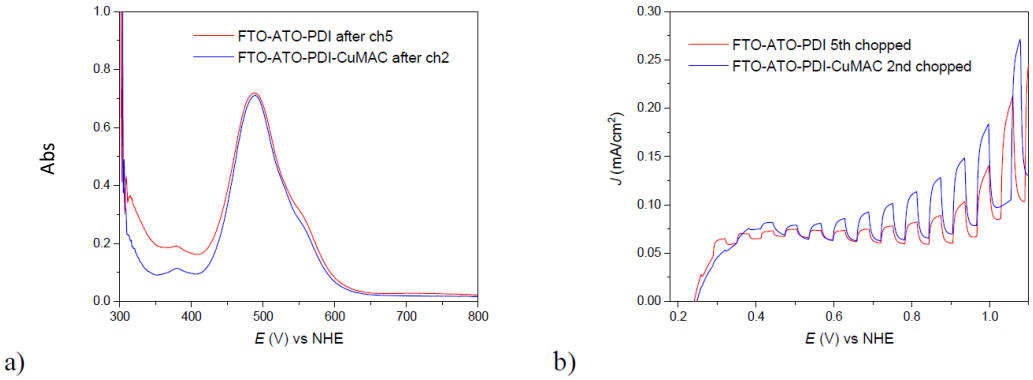

Figure S6. UV-Vis (left) and chopped light LSV (right) of Cu-MAC@PDI@ATO@FTO and PDI@ATO@FTO reproduced in other work.[2]

V

5.6.5 Collector-Generator experiments for oxygen detection

Oxygen quantification was carried out by using the Collector-Generator method previously reported for related systems,[3] with photocurrents in the range of $\mu A \cdot cm^{-2}$. Thus, it allows the quantification of oxygen gas *in situ* and to determine the Faradaic efficiency of the photoelectrodes. The set-up consists of two interfaced electrodes with minimal separation between them and connected to a bipotentiostat, which allows the use of 2 working electrodes (WE). The working electrodes are: the studied photoanode (WE1 or Generator) and a bare FTO electrode (WE2, Collector). Two small pieces of coverslip (Menzel-Gläser, 130-140µm of thickness) are used to keep a constant distance between them and covered with parafilm leaving lateral apertures in both sides to allow the solution to fill the inner space (Figure S7). In our case, WE1 is held at the thermodynamic potential for water oxidation (bulk electrolysis at 0.845 V vs. NHE pH 7) with net production of O_2 only when the sample is back-illuminated. It is then when the generated O_2 diffuses to the FTO-Collector where its reduction takes place. The ratio between the charge Q passed in WE1-Generator (Water Oxidation Reaction, WOR) and WE2-Collector (Oxygen Reduction Reaction, ORR) is proportional to the Faradaic Efficiency (FE) of the process. The oxygen collection efficiency $\eta(O_2)$ is calculated as in Equation S1. Before testing the samples, the ORR potential was determined by cyclic voltammetry of an FTO photoelectrode in pH 7 (0.1 M) under air/N_2 atmosphere (Figure S8). As well, a calibration of the set-up is required to determine the gas diffusion rate between a generator with 100% (FE) and the collector. For that, a modified FTO with cobalt oxide was prepared using a reported methodology (Figure S8).[5]

$$\eta(O_2) = \frac{-Q(WE2)}{Q(WE1)x\ \eta(calibration)} \quad \text{(Equation S1)}$$

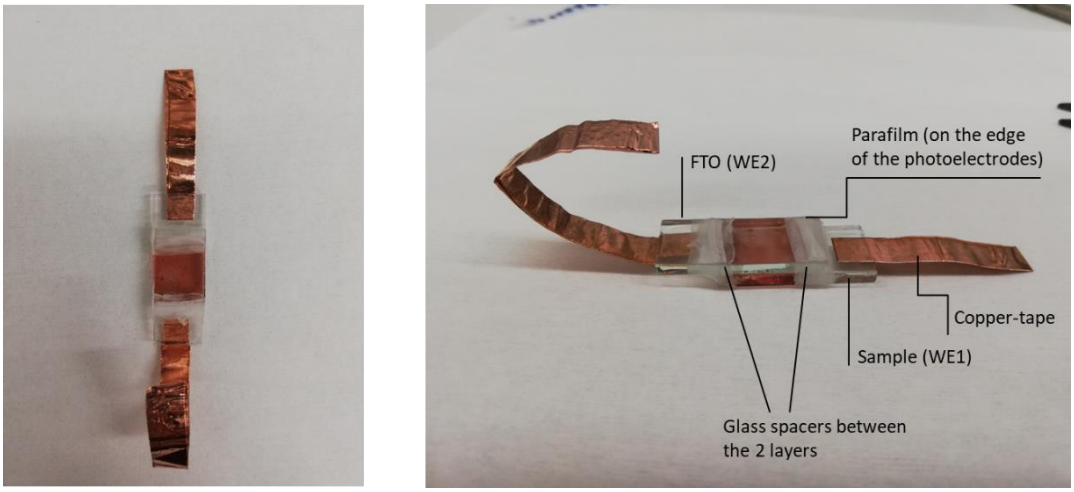

Figure S7. Photographies of the C-G set-up employed in this work with their parts labeled for reader's comprehension.

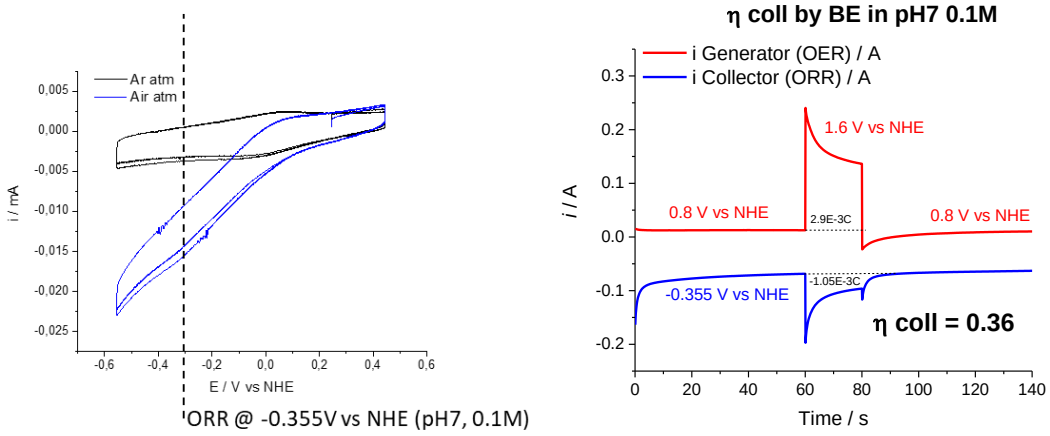

Figure S8. Left, cyclic voltammetry of an FTO electrode under argon (black) and air (blue) atmosphere to determine ORR potential (0.1 M pH 7 solution, Pt coil as CE and Hg/Hg_2SO_4 as RE). Right, bulk electrolysis at 0.845 V vs. NHE pH 7 under dark/light/dark steps to calculate the oxygen collection efficiency $\eta(O_2)$ (Equation S1). For that, WE1-Generator with 100% FE was employed, consisting of a modified FTO with cobalt oxide.

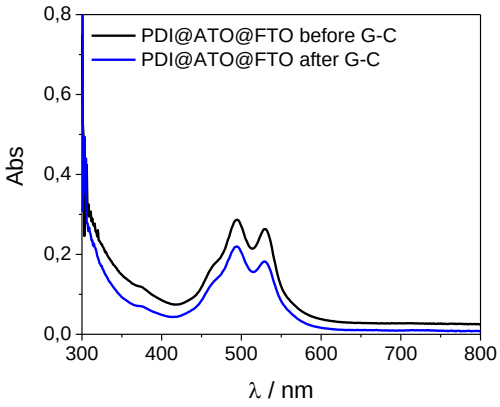

Figure S9. UV-Vis spectra before (black) and after (blue) collector-generator bulk electrolysis of the sample PDI@ATO@FTO.

5.6.6 X-ray Absorption Spectroscopy (XAS) Methods

X-ray absorption spectra were collected at the Advanced Photon Source (APS) at Argonne National Laboratory on bending magnet beamline 20 at electron energy 9.0 KeV and an average current of 100 mA and at the CLAESS beamline at ALBA synchrotron light source. The radiation at APS was monochromatized by a Si(110) crystal monochromator. The intensity of the X-rays was monitored by three ion chambers (I_0, I_1, and I_2) filled with 80% nitrogen and 20% helium and placed before the sample (I_0) and after the sample (I_1 and I_2). Cu metal was placed between ion chambers I_1 and I_2 and its absorption was recorded with each scan for energy calibration. The samples were kept at 20 K in a He atmosphere at ambient pressure. Hybrid materials on glassy carbon surfaces were recorded as fluorescence excitation spectra using a 13-element energy-resolving detector. All samples were measured in a continuous helium flow cryostat in fluorescence mode with a 13-element Germanium detector. Around 15-20 XAS spectra were collected for each solution sample. No more than 5 scans were taken at each sample position at any condition. Two glassy carbon sheets with sub-monolayer coverage of the hybrid materials were on the other hand stacked on top of each other and wrapped in Kapton tape. Around 30 XAS spectra of each hybrid sample were collected. Care was again taken to measure at several sample positions on each sample and no more than 5 scans were taken at each sample position. In order to reduce the risk of sample damage by x-ray radiation, 80% flux was used in the defocused mode (beam size 5500 µm(Horizontal) x 600 µm(Vertical)) and no damage was observed scan after scan to any samples. All samples were also protected from the x-ray beam during spectrometer movements by a shutter synchronized with the scan program. Cu XAS energy was calibrated by the first maxima in the second derivative of the copper metal X-ray Absorption Near-Edge Structure (XANES) spectrum. The CuO reference compound diluted with Boron Nitride (BN) and the Cu complexes in solution and upon deposition electrode surfaces were additionally measured on the CLAESS wiggler beamline at the ALBA synchrotron light source whereby the radiation was monochromatized using a pair of Si(111) crystals. Similarly, two glassy carbon sheets wrapped in Kapton tape were mounted between PEEK sample holders and measured with a circular beam spot size of around 15 µm using a liquid nitrogen cryostat cooled down to 77 K. Fluorescence

absorption measurements were carried out on hybrid materials at ALBA with an Amptek silicon drift solid-state detector (XR-100 SDD)[6] placed at 90 degrees to the incoming beam. The silicon drift detector was placed on a motorized stage allowing the sample-detector distance to be easily changed between 30-110 mm. Solid CuO diluted with BN powder, was pressed between polypropylene and mylar tape, and measured in the cryostat in transmission mode. Around 3 scans were collected on CuO and around 20-25 scans were collected on the solution samples and hybrid materials. Care was once again taken to measure at both solution and hybrid samples to minimize radiation damage. No more than 2 scans were taken in this instance on each spot on the solution samples.

Extended X-ray Absorption Fine Structure (EXAFS) Analysis: Athena software[7] was used for data processing. The energy scale for each scan was normalized using copper metal standard. Data in energy space were pre-edge corrected, normalized, and background corrected. The processed data were next converted to the photoelectron wave vector (k) space and weighted by k^2. The electron wave number is defined as $k = [2m(E - E_0)/\hbar^2]^{1/2}$, E_0 is the energy origin or the threshold energy. K-space data were truncated near the zero crossings k = 1.839 to 11.1 $Å^{-1}$ for the solution and the hybrid materials, in Cu EXAFS before Fourier transformation. The k-space data were transferred into the Artemis Software for curve fitting. In order to fit the data, the Fourier peaks were isolated separately, grouped, or the entire (unfiltered) spectrum was used. The individual Fourier peaks were isolated by applying a Hanning window to the first and last 15% of the chosen range, leaving the middle 70% untouched. Curve fitting was performed using *ab initio*-calculated phases and amplitudes from the FEFF8 program[7] from the University of Washington. *Ab initio*-calculated phases and amplitudes were used in the EXAFS equation

$$\chi(k) = S_0^2 \sum_j \frac{N_j}{kR_j^2} f_{eff_j}(\pi, k, R_j) e^{-2\sigma_j^2 k^2} e^{\frac{-2R_j}{\lambda_j(k)}} \sin(2kR_j + \phi_{ij}(k)) \qquad \text{(Equation S2)}$$

where N_j is the number of atoms in the j^{th} shell; R_j the mean distance between the absorbing atom and the atoms in the j^{th} shell; f_{eff_j} (π,*k*, R_j) is the *ab initio* amplitude function for shell *j*, and the Debye-Waller term $e^{-2\sigma_j^2 k^2}$ accounts for damping due to static and thermal disorder in absorber-backscatterer distances. The mean free path term $e^{\frac{-2R_j}{\lambda_j(k)}}$

reflects losses due to inelastic scattering, where $\lambda_j(k)$, is the electron mean free path. The oscillations in the EXAFS spectrum are reflected in the sinusoidal term $\sin(2kR_j + \phi_{ij}(k))$, where $\phi_{ij}(k)$ is the *ab initio* phase function for shell *j*. This sinusoidal term shows the direct relation between the frequency of the EXAFS oscillations in the k-space and the absorber-backscatterer distance. S_0^2 is an amplitude reduction factor.

The EXAFS equation[8] (Equation S2) was used to fit the experimental Fourier isolated data (q-space) as well as unfiltered data (k-space) and Fourier transformed data (R-space) using *N*, S_0^2, E_0, *R*, and σ^2 as variable parameters (Table S1). *N* refers to the number of coordination atoms surrounding Cu for each shell. The quality of fit was evaluated by R-factor and the reduced Chi^2 value. The deviation in E_0 ought to be less than or equal to 10 eV. R-factor less than 2% denotes that the fit is good enough whereas R-factor between 2 and 5% denotes that the fit is correct within a consistently broad model. The reduced Chi^2 value is used to compare fits as more absorber-backscatter shells are included to fit the data. A smaller reduced Chi^2 value implies a better fit. Similar results were obtained from fits done in k, q, and R-spaces.

XANES Simulations analysis: TD-DFT Calculations for the XAS spectrum of the Cu pre-edge were performed using ORCA, B3LYP[9,10] as functional, the Zeroth Order Regular Approximation (ZORA) as previously reported[11] with def2-TZVP triple-zeta basis sets[12], and the atom-pairwise Grimme dispersion correction with the Becke-Johnson damping scheme[13] (D3BJ) and the fully decontracted def2-TZVP/J[12] auxiliary basis set. The pre-edge absorption spectra from the TD-DFT calculations were shifted in energy by -4 eV relative to the experimental data and a broadening of 1.0 eV was applied to all calculated spectra. The donor orbitals for XAS calculations were chosen as Cu 1s and all virtual orbitals were selected as acceptor orbitals. Up to 150 roots were calculated. The calculated pre-edge spectrum contains contributions from electric quadrupole, electric dipole, and magnetic dipole transitions.

Complex	Fit	Peak	Shell,N	R, Å	E_0	ss.^{2} (10^{-3})	R-factor	Reduced Chi-square
Cu(II)-MAC in H_2O	1	1	Cu-N,4	1.93	6.6	3.9	0.0012	1428
	2	I,II	Cu-N,4 Cu-C,8	1.92 2.75	2.4	3.2 18.8	0.0261	5535
	3	I,II,III	Cu-N,4 Cu-C,8 Cu-C,17	1.92 2.79 3.41	3.5	3.3 13.2 38.1	0.0115	5220
	4	All	Cu-N,4 Cu-C,8 Cu-C,17 Cu-C,13 Cu-N,8	1.92 2.80 3.29 3.66 3.82	3.1	3.6 10.8 26.6 26.3 5.5	0.0130	2087
Solution of 1mM Cu(II)-MAC and PDI in isopropanol:acetonitrile (1:1)	5	I	Cu-N,4	1.94	0.2	7.8	0.0034	47
	6	I,II	Cu-N,4 Cu-C,8	1.91 2.75	-4.9	7.6 23.5	0.0213	253
	7	I,II,III	Cu-N,4 Cu-C,8 Cu-C,17	1.92 2.79 3.39	-3.1	7.9 18.8 76.0	0.0187	164
	8	All	Cu-N,4 Cu-C,8 Cu-C,17 Cu-C,13 Cu-N,8	1.92 2.82 3.37 3.79 4.35	-2.3	8.0 17.3 34.7 20.8 31.1	0.0084	60
Cu-MAC/PDI@ ATO@FTO (no electrochemistry performed)	9	I	Cu-N,4	2.01	-1.4	8.6	0.0057	134
	10	I,II	Cu-N,4 Cu-C,8	1.97 2.71	-9.0	7.7 32.2	0.0054	33
	11	I,II	Cu-N,4 Cu-C,9	1.95 2.66	-12.2	7.7 26.9	0.0059	35
	12	I,II,III	Cu-N,4 Cu-C,8 Cu-C,17	1.96 2.64 2.92	-11.2	8.0 26.2 86.1	0.0096	63
	13	I,II,III	Cu-N,4 Cu-C,9	1.96 2.64	-11.1	8.0 28.7	0.0097	64

			Cu-C,17	2.94		85.4		
	14	All	Cu-N,4 Cu-C,8 Cu-C,17 Cu-C,13 Cu-N,8	1.98 2.68 3.06 3.44 3.78	-6.9 -6.9	8.4 20.2 35.2 18.1 9.5	0.0046	20
	15	All	Cu-N,4 Cu-C,9 Cu-C,17 Cu-C,13 Cu-N,8	1.98 2.69 3.06 3.44 3.78	-7.0	8.3 22.4 34.0 17.8 9.5	0.0048	21.2
Cu-MAC/PDI@ ATO@FTO after photocatalysis (1 LSV 10 $mV \cdot s^{-1}$ from 0.2-0.8 V *vs*. NHE pH7)	16	I	Cu-N,4	2.01	-1.1	8.6	0.0044	57
	17	I,II	Cu-N,4 Cu-C,8	1.95 2.71	-10.6	8.1 23.8	0.0037	29
	18	I,II	Cu-N,4 Cu-C,9	1.95 2.70	-11.1	8.1 26.0	0.0037	30
	19	I,II,III	Cu-N,4 Cu-C,8 Cu-C,17	1.97 2.71 3.10	-7.9	8.4 26.7 87.7	0.0203	241
	20	I,II,III	Cu-N,4 Cu-C,9 Cu-C,17	1.98 2.73 3.14	-7.4	8.4 30.4 83.9	0.0205	242
	21	All	Cu-N,4 Cu-C,8 Cu-C,17 Cu-C,13 Cu-N,8	1.98 2.73 3.11 3.47 3.78	-6.4	8.8 16.7 30.6 12.0 4.1	0.0031	19
	22	All	Cu-N,4 Cu-C,9 Cu-C,17 Cu-C,13 Cu-N,8	1.98 2.73 3.12 3.47 3.78	-6.5	8.8 18.7 29.2 11.8 4.1	0.0031	19

*Table S1. EXAFS Fits parameters. * Peak I refers to the EXAFS region between 1.05 to 2 Å, peaks, I and II to 1.05- 2.7 Å, peaks I,II,III to 1.05-3.1 Å, and all to 1.05 to 4 Å.*

5.6.7 References

(1) Berardi, S.; Cristino, V.; Canton, M.; Boaretto, R.; Argazzi, R.; Benazzi, E.; Ganzer, L.; Cerullo, G.; Syrgiannis, Z.; Bignozzi, C. A.; Caramori, S.; Rigodanza, F.; Prato, M. Perylene Diimide Aggregates on Sb-Doped SnO 2 : Charge Transfer Dynamics Relevant to Solar Fuel Generation. *J. Phys. Chem. C* **2017**, *121*, 17737–17745. https://doi.org/10.1021/acs.jpcc.7b05928.

(2) Salati, M. M.Sc. Thesis: Functionalization of Dye-Sensitized Photoelectrodes with Ru- and Cu-Based Catalysts for Water Oxidation Reaction, 2020.

(3) Grau, S.; Berardi, S.; Moya, A.; Matheu, R.; Cristino, V.; Vilatela, J. J.; Bignozzi, C. A.; Caramori, S.; Gimbert-Suriñach, C.; Llobet, A. A Hybrid Molecular Photoanode for Efficient Light-Induced Water Oxidation. *Sustain. Energy Fuels* **2018**, *2* (9), 1979–1985. https://doi.org/10.1039/C8SE00146D.

(4) Garrido-Barros, P.; Moonshiram, D.; Gil-Sepulcre, M.; Pelosin, P.; Gimbert-Suriñach, C.; Benet-Buchholz, J.; Llobet, A. Redox Metal-Ligand Cooperativity Enables Robust and Efficient Water Oxidation Catalysis at Neutral pH with Macrocyclic Copper Complexes. *J. Am. Chem. Soc.* **2020**, *142* (41), 17434–17446. https://doi.org/10.1021/jacs.0c06515.

(5) Kanan, M. W.; Nocera, D. G. In Situ Formation of an Oxygen-Evolving Catalyst in Neutral Water Containing Phosphate and Co2+. *Science* **2008**, *321* (5892), 1072–1075. https://doi.org/10.1126/science.1162018.

(6) Nohara, I.; Prescimone, A.; Housecroft, C.; Constable, E. Softening the Donor-Set: From [Cu(P^P)(N^N)][PF6] to [Cu(P^P)(N^S)][PF6]. *Inorganics* **2019**, *7* (1), 11. https://doi.org/10.3390/inorganics7010011.

(7) Ravel, B.; Newville, M. ATHENA, ARTEMIS, HEPHAESTUS: Data Analysis for X-Ray Absorption Spectroscopy Using IFEFFIT. *J. Synchrotron Radiat.* **2005**, *12* (4), 537–541. https://doi.org/10.1107/S0909049505012719.

(8) Koningsberger, D. C.; Prins, R. *X Ray Absorption: Principles, Applications, Techniques of EXAFS, SEXAFS and XANES*; John Wiley & Sons, 1998.

(9) Becke, A. D. Density-functional Thermochemistry. III. The Role of Exact Exchange. *J. Chem. Phys.* **1993**, *98* (7), 5648–5652. https://doi.org/10.1063/1.464913.

(10) Stephens, P. J.; Devlin, F. J.; Chabalowski, C. F.; Frisch, M. J. Ab Initio Calculation of Vibrational Absorption and Circular Dichroism Spectra Using Density Functional Force Fields. *J. Phys. Chem.* **1994**, *98* (45), 11623–11627. https://doi.org/10.1021/j100096a001.

(11) Novozhilova, I. V.; Volkov, A. V.; Coppens, P. On the Nature of the Lowest Triplet Excited State of the [Rh 2(1,3-diisocyanopropane)4]2+ Ion. *Inorg. Chem.* **2004**, *43* (7), 2299–2307. https://doi.org/10.1021/ic035243h.

(12) Weigend, F.; Ahlrichs, R. Balanced Basis Sets of Split Valence, Triple Zeta Valence and Quadruple Zeta Valence Quality for H to Rn: Design and Assessment of Accuracy. *Phys. Chem. Chem. Phys.* **2005**, *7* (18), 3297–3305. https://doi.org/10.1039/b508541a.

(13) Grimme, S.; Antony, J.; Ehrlich, S.; Krieg, H. A Consistent and Accurate *Ab Initio* Parametrization of Density Functional Dispersion Correction (DFT-D) for the 94 Elements H-Pu. *J. Chem. Phys.* **2010**, *132* (15), 154104. https://doi.org/10.1063/1.3382344.

Chapter 6

Functionalized covalent triazine frameworks for water oxidation photocatalysis

Chapter 6.

VI

Functionalized covalent triazine frameworks for water oxidation photocatalysis

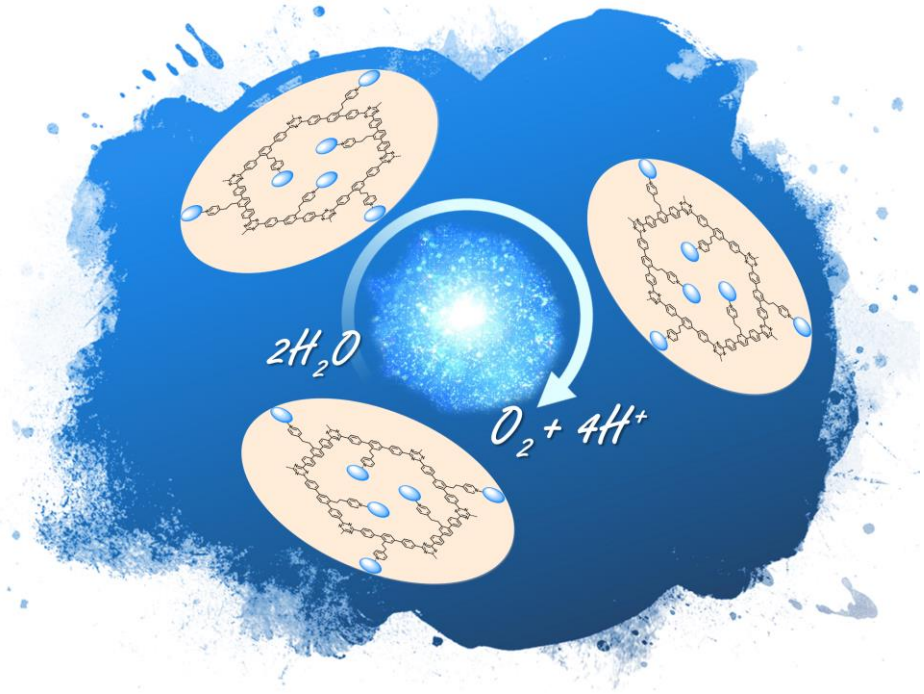

Abstract

In the field of artificial photosynthesis, organic photocatalysts are emerging materials due to synthetic versatility, earth-abundancy, and low-toxicity. Nevertheless, there is a lack of reported examples for the water oxidation reaction because of its high thermodynamic and kinetic requirements. Covalent Triazine Frameworks (CTFs) have proved to be good candidates in thermodynamic terms. Herein we present, a library of four novel CTFs (CTF-COOH, CTF-$CONH_2$, CTF-F, and CTF-py) with different functionalities in the aromatic ring (carboxylic acid, amide, fluoro, and pyridyl) with the aim to (i) modulate band positions, (ii) incorporate molecular catalysts that surpass the kinetic barrier for water oxidation. CTF-COOH, CTF-$CONH_2$, and CTF-F have been deposited on robust photoelectrodes with remarkable photocurrents between 24-30 $\mu A \cdot cm^{-2}$ over 60 min at the thermodynamic potential for water oxidation (0.8 V *vs.* NHE pH 7). On the other hand, [Ru(tda)(dmso)py] (tda^{2-} is [2,2′:6′,2″-terpyridine]-6,6″-dicarboxylate) has been covalently attached to the dangling pyridines of CTF-py. CTF-py-Ru(tda) proves to be active towards water oxidation with remarkable turnover numbers (TONs) of 54 and with just 0.7 at% of Ru, which contributes to the lack of published organic photocatalysts for light-driven water oxidation.

Contributions:

Marta Ventosa synthesized CTF-1, CTF-COOH, CTF-F, CTF-$CONH_2$, and [Ru(tda)(dmso)py], as well as performed all characterization of the materials and photochemical experiments of CTF-py-Ru(tda).

6.1 Introduction

Globalized human activities have had an impact on terrestrial ecosystems.[1] For example, the stratigraphic signature of sediments with halogenated polyaromatic hydrocarbons, pesticide residues, and Pb from leaded gasoline, among others.[2] Another consequence is the rise in atmospheric CO_2 and CH_4 concentration with concomitant climate change and ocean acidification.[3] To solve all these issues, one spearhead in science is the so-called "functional" materials. In fact, all novel materials are functional and this tautology can be better defined as "materials chemically or physically designed for specific functions". Rationally designed porous materials possess high surface area, adjustable pore volume, and tunable chemical/physical functional groups to complete certain tasks. All these properties allow them to perform gas adsorption or storage,[4] purification and ion exchange,[5] to act as support for catalysts,[6,7] as semiconductors,[8] as electrodes or insulators, etc.[9,10] Depending on their pore size, they can be classified as (i) microporous (< 2 nm), (ii) mesoporous (2-50 nm), and (iii) macroporous (> 50 nm).[11] Some examples are zeolites, Periodic Mesoporous Organosilicas (PMOs), Metal-Organic Frameworks (MOFs), Conjugated Microporous Polymers (CMPs), or Covalent Organic Frameworks (COFs). The latter are crystalline porous materials based on organic building units linked by covalent bonds through reversible reactions.[12] Reversible covalent bond synthesis is required to self-correct any defects and thus, attain crystallinity. Disadvantageously, this reversibility translates into limited chemical and physical stability.[13]

Covalent Triazine Frameworks (CTFs) are a subclass of Conjugated Microporous Polymers (CMPs) that follow the same building block structure of COFs but are amorphous rather than crystalline. CTFs are synthesized by irreversible trimerization of cyano- groups forming triazine moieties that are the linkers between organic building units (see CTF-1 as an example in Figure 1). Thus, they are robust against high temperatures (> 250˚C) and chemicals (acids or bases).[13] Combined with their high surface area, they are ideal for catalysis, gas storage, and/or separation.[13]

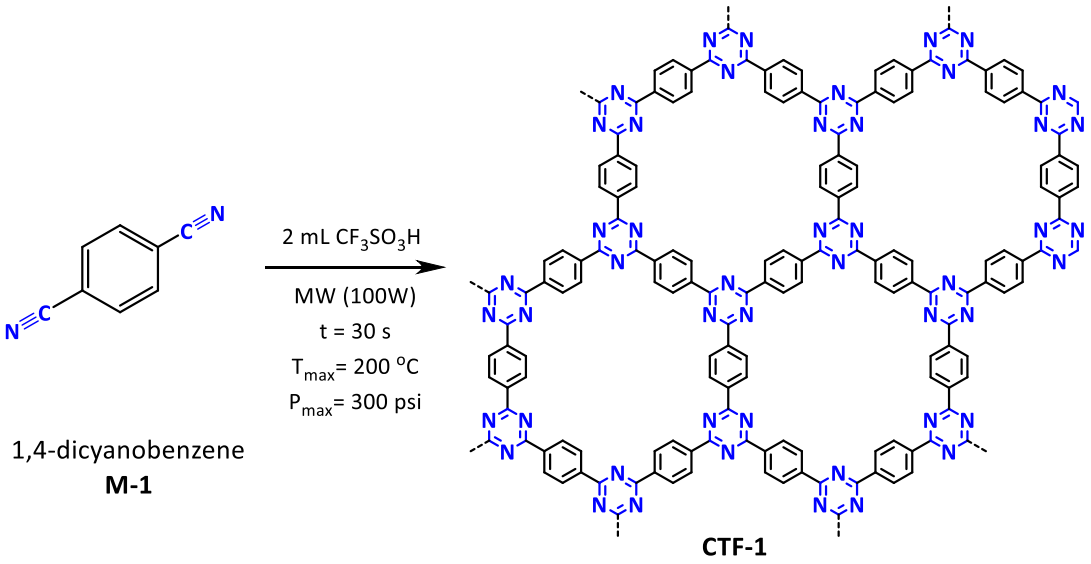

Figure 1. Schematic synthesis of CTF-1 through a microwave procedure reported by Cooper et al.[14]

A typical synthesis of CTF materials involves high temperatures (T > 500 ˚C) leading to side-products resulting from carbonization.[13] Recently, a new method based on microwave irradiation has been developed,[14] which requires lower temperatures avoiding char, paving the way to use CTFs for photocatalysis (Figure 1). Organic photocatalysts, unlike inorganic semiconductors, feature low-cost, earth-abundant, and low-toxic materials, easy fabrication for industrial applications, mechanical flexibility, chemical, and physical tunability, etc.[15] The emergence of organic or hybrid semiconductors (organic-inorganic) has led to improved light absorption in the visible solar spectrum, enhanced charge generation and transport, and higher surface areas.[16] Their main applications are the photooxidation of organic pollutants and in the field of artificial photosynthesis to promote light-induced transformations that store energy in the form of solar fuels.[16,17] Solar fuels such as H_2, CH_3OH, and CH_4 are products that can be obtained from the reduction of protons or CO_2 respectively. For both reductions, electrons and protons ideally derive from the oxidation of water, as it occurs in the Oxygen-Evolving Center of Photosystem II in the chloroplasts. Therefore, among all the reactions (Equations 1-3), water oxidation is one of the key reactions that need to be mastered. It is thermodynamically and kinetically more challenging than water reduction as denoted by the small amount of reported organic and/or inorganic photocatalysts for water oxidation.[16,18,19]

Oxidation half-reaction: $2H_2O \rightarrow O_2 + 4H^+ + 4e^-$ $E°$= 1.23 V *vs.* NHE, pH 0 (Eq. 1)

Reduction half-reaction: $4H^+ + 4e^- \rightarrow 2H_2$ $E°$= 0 V *vs.* NHE, pH 0 (Eq. 2)

$CO_2 + 6H^+ + 6e^- \rightarrow CH_3OH + H_2O$ $E°$= 0.03 V *vs.* NHE, pH 0 (Eq. 3)

In the field of organic photocatalysts, graphitic carbon nitrides (g-C_3N_4) and their derivatives have been the most extensively studied.[17] However, their synthesis at high temperatures (> 500 ˚C) is a drawback for chemical tailoring with different monomers or dopants.[20] Depending on the monomer or co-monomer composition, photophysical properties vary.[21] For example, the richer nitrogen content in CTFs compared to g-C_3N_4 affect their electronic structure and band alignment together with increased wettability and electroactive surface area.[13] The valence band (VB) position is dominated by the N 2p orbitals in the triazine units.[22,23] In the case of g-C_3N_4, N enrichment is in the form of –NHx groups, which contribute to n-π* transitions and not to the active π-π* transitions of the triazine units in CTFs. Hence, g-C_3N_4 show low water oxidation activity and stability,[24–27] being a drawback for achieving full light-induced water splitting. On the contrary, published CTFs by Tang and co-workers proved water oxidation and reduction.[8,23,28] The state-of-the-art was established in 2020 with the first CTF performing full water splitting without using sacrificial agents.[28] CTF-0, which was previously reported by the trimerization of 1,3,5-tricyanobenzene,[29] was post-functionalized with 6 wt% Co_3O_4 and 3 wt% Pt. As a result, 82 $\mu mol \cdot g^{-1} \cdot h^{-1}$ H_2 and 40 $\mu mol \cdot g^{-1} \cdot h^{-1}$ O_2 were produced in 18 hours, which draws the potentiality of CTFs in the field. However, high amounts of metal co-catalyst are needed,[23,28,30] which leads to higher costs and lower efficiencies, since all the surface is occupied by metal that hinders light absorption. Therefore, our focus of research is the incorporation of highly active molecular catalysts to increase the overall efficiency towards light-driven water oxidation, in line with the atom (circular) economy of the future.[31–33]

Herein we present a library of new CTFs with different functionalities, specifically designed to favor light absorption, charge transfer, and the anchoring of molecular Water Oxidation Catalysts (WOCs). Figure 2 displays the three different strategies that have been designed to explore these type of materials: (i) introduction of monomers (M) that act as capping agents (M-COOH, M-$CONH_2$); (ii) incorporation of electron-

withdrawing groups to modulate the bandgap and band position (M-F); (iii) addition of a dangling pyridine for post-functionalization with a molecular WOC (M-py). As shown at the top of Figure 2, the monomers M-COOH and M-$CONH_2$ only have one cyano-group, which will act as a capping agent in the polymerization process of 1,4-dicyanobenzene (M-1). As a result, lower molecular weight polymers will be synthesized which will increase their solubility in polar solvents. This feature will benefit the fabrication of homogeneous layers on photoelectrodes because insoluble polymers can lead to inhomogeneities on top of the electrodes generating short circuits, lower stabilities, higher charge recombination, and lower light-absorption efficiencies. Besides, soluble polymers may enhance their functionalization with molecular catalysts, because both will be in the homogenous phase. Moreover, the end –COOH and -$CONH_2$ groups can be used to anchor molecules and/or further influence band-gap energies due to the electron-withdrawing character of the acid and the amide groups. Following the latter strategy, the use of a monomer containing the electron-withdrawing fluorine group (M-F) will also be explored to build a fluorinated CTF structure. As shown by previous research, fluorination of g-C_3N_4 and graphitic materials can dramatically change the electronic and optical properties of the material by increasing the bandgap and shifting the bands to higher energies.[34,35] This should facilitate charge separation, electron transfer, higher thermodynamic driving force, and thus, the increase in photostability.[36] The final approach is the addition of a dangling pyridine for post-functionalization with proper WOC precursors. The use of molecular WOC in electrodes and photoelectrodes can significantly increase the water oxidation performance.[36–38] In line with the literature,[39,40,38] molecular photoanodes will be pursued by two anchoring methods: (i) π-π or CH-π stacking on CTF-COOH, CTF-F, and CTF-$CONH_2$, which takes advantage of the π-conjugated system of these materials; (ii) direct covalent bond to the dangling pyridine groups CTF-py. For the latter, the WOC precursor used is the reported [Ru^{II}(tda)(dmso)py] (tda^{2-} is [2,2':6',2''-terpyridine]-6,6''-dicarboxylate, dmso is dimethyl sulfoxide, and py is pyridine)[41] derivative from [Ru^{II}(tda)py_2], which stands out for its high activity or TOFs of 8,000 s^{-1} at pH 7.[42] The derivative employed in this work is useful for the liability of its axial (dmso) ligand, resulting in the perfect site to create a covalent bond between the complex and the (photo)electrode. On the other hand, π-π or CH-π interactions between Ru(tda) derivatives and multi-wall carbon nanotubes

resulted in robust (photo)electrodes for water oxidation.[37,38] Advantageously, these supramolecular interactions between the WOC and the (photo)electrode do not involve any chemical reaction. In this case, the WOC precursor used is the recently reported oligomeric version of $[Ru^{II}(tda)py_2]$, $[Ru(tda)(4,4'\text{-}bpy)]_{15}$ (bpy is bipyridine), which outstands by showing the highest current densities (240 $mA{\cdot}cm^{-2}$ at 1.86 V *vs.* NHE pH 7) and stabilities (over 12 h) for a published molecular anode up to date.[37]

6.2 Results and Discussion

6.2.1 Synthesis and characterization of a library of new CTFs

The synthesis of the CTF materials was adapted by a microwave procedure reported by Cooper and co-workers.[14] This methodology is based on using trifluoromethanesulfonic acid (triflic acid) as the catalyst in a microwave-assisted synthesis. The one-pot reaction introduced by Cooper's group is much faster, free of metal catalysts, and undergoes at lower temperatures compared to any other reported methodologies such as the ionothermal synthesis or vulcanization.[43] In this work, 1,4-dicyanobenzene was combined with a library of functionalized monomers (in a ratio of 5 to 1) in triflic acid (Figure 2). After 5 minutes of stirring for homogenization, the trimerization was triggered by microwave irradiation at 100 W for 30 s with a threshold of 200 ˚C and 300 psi. A brownish sluggish mixture was obtained, which was treated with 0.1 M NH_3 solution until a solid precipitated and the solution reached neutral pH. The mixture was filtered on a pore 5 frit filter and washed with water, followed by ethanol, ethyl acetate, acetone, and tetrahydrofuran. The white-yellowish solids were isolated in 50-70% yields and characterized without further treatment. As a reference, the published CTF-1 was synthesized,[8,14,23] with only 1,4-dicyanobenzene as a building block.

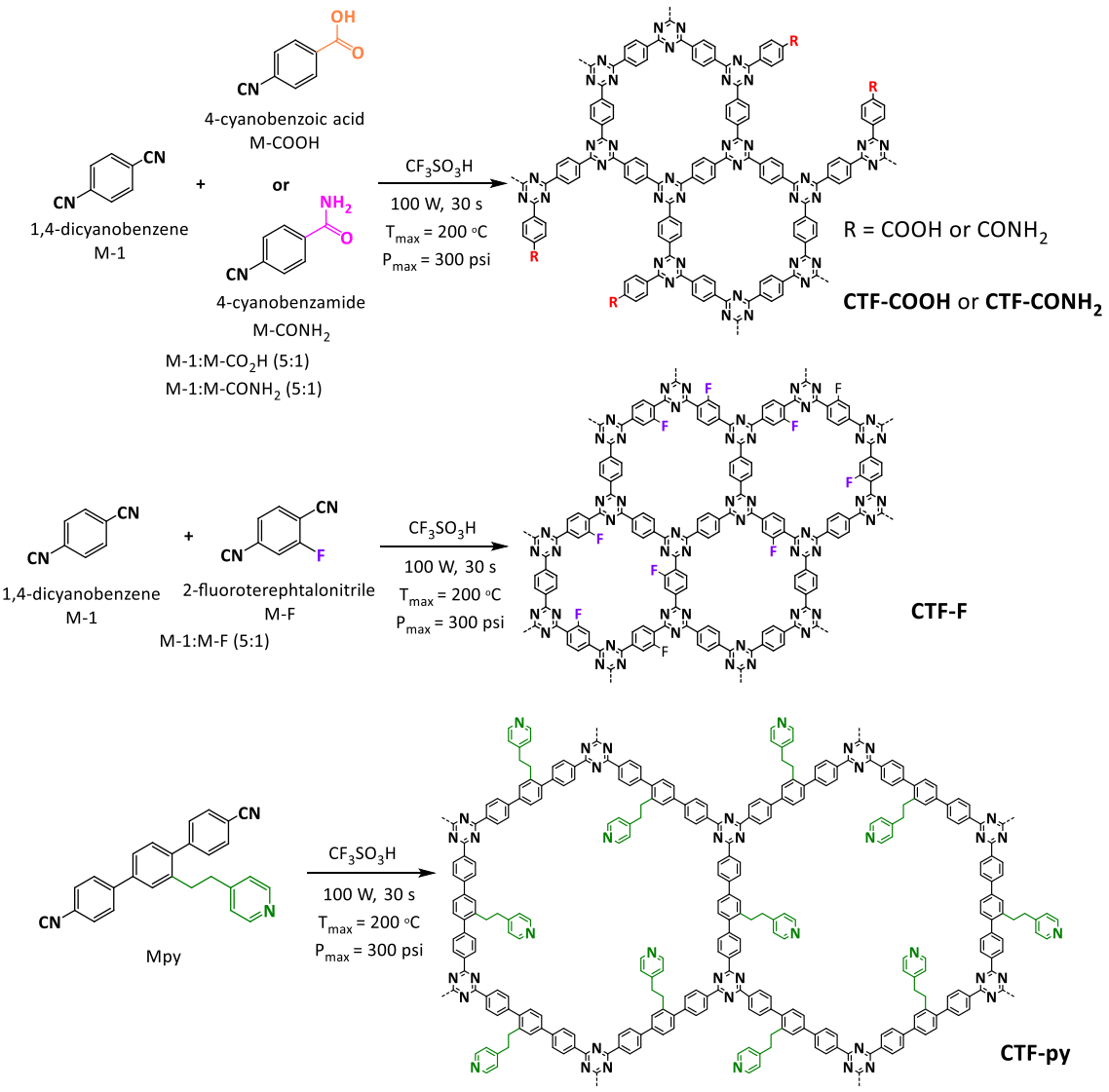

Figure 2. Three different strategies were designed to functionalize CTFs for photocatalytic water oxidation purposes. The first approach is represented by the top scheme, with the incorporation of 4-cyanobenzoic acid (M-COOH) and 4-cyanobenzamide (M-CONH₂) as capping agents of the polymeric layer (CTF-COOH, CTF-CONH₂). Secondly, the middle reaction shows the incorporation of an electron-withdrawing 2-fluoroterephthalonitrile (M-F) in the backbone to modulate band positions. Finally, the bottom scheme displays the trimerization of only M-py leading to CTF-py with dangling pyridines as anchoring sides for molecular complexes.

Following the work-up, Fourier-transform Infrared spectroscopy (FTIR) was performed to determine the end of polymerization. The spectrum of the monomers and the CTFs are given in Figure 3. One of the main features is the total disappearance of the -C≡N stretching bond at 2222 cm^{-1} in the CTF spectra (Figure 3 right) compared to the IR spectrum of the monomers (Figure 3 left), indicating a high degree of polymerization.[14] Besides, CTFs spectra display the triazine characteristic bands at 3100-3000 cm^{-1} (aromatic C-H stretching), 1600-1300 cm^{-1} (C=C bending), and ~800 cm^{-1} (aromatic C-H bending), which further proves the condensation of nitrile moieties into triazine rings.

For CTF-py (magenta, right), also preserves the bands associated with the alkyl linker (C-H stretching bands between 2975 and 2825 cm^{-1}) and the pyridine (C=C bending bands in the 1600-1400 cm^{-1} region) as seen in monomer M-py spectrum (magenta, left).

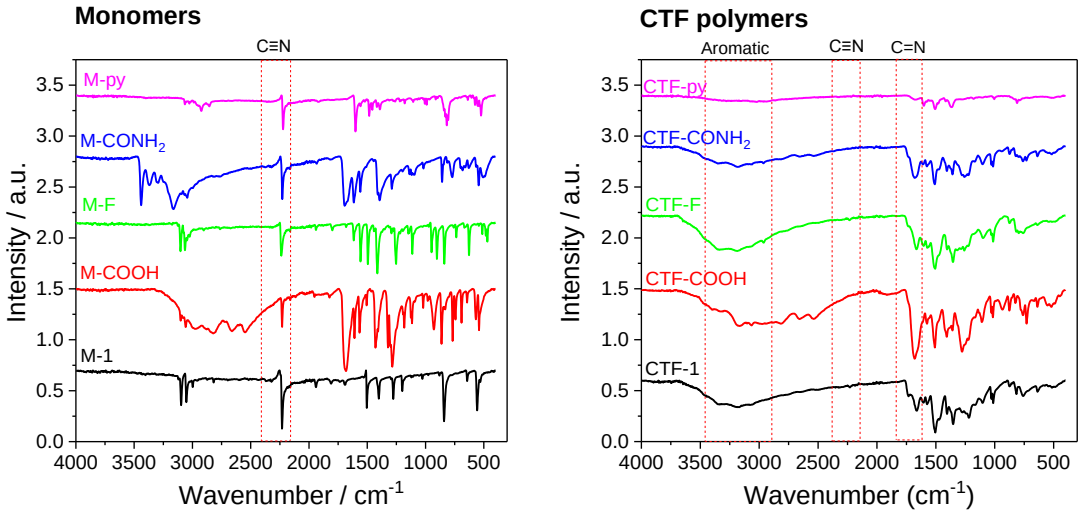

Figure 3. Fourier-transform Infrared spectroscopy (FTIR) for the different monomers employed (left) and the resulting CTFs (CTF-1, CTF-COOH, CTF-F, CTF-CONH2). The formation of CTF polymers (right) is justified by the disappearance of -C≡N bond shown in the monomers (left).

Later, morphological, optical, and electrochemical characterization techniques were performed. Some of them requested the deposition of the CTFs on top of solid and conductive surfaces, such as Transparent Conductive Oxides (TCO). Two strategies were employed to build the photoelectrodes: (i) drop-cast methodology, and (ii) doctor blading technique. Briefly, the first one consisted of dispersing 10 mg of CTF powder in 1 mL N,N-Dimethylformamide (DMF), or Dimethylsulfoxide (DMSO) solvent followed by sonication for 30 min. 50 µL of the CTF colloidal solution was dropped on clean Fluorine Tin Oxide (FTO) and dried on a hotplate at 50 ˚C. The same procedure was repeated twice to obtain the prepared CTF@FTO photoelectrodes. On the other hand, the doctor blade technique implied more preparation steps: (a) preparation of a viscous mixture by mixing 30 mg of CTF in 210 mg of DMF with 135 mg of α-terpineol and 22.5 mg ethylcellulose; (b) after stirring overnight, the sample was deposited on a clean FTO by using a doctor blade technique (see Figure S1); (c) finally, the freshly prepared photoelectrodes were dried in a muffle at 50 ˚C for 30 min, 100 ˚C for 20 min and 150 ˚C for 10 min. A picture of the resulting photoelectrodes can be found in Figure S1. Doctor blade photoelectrodes were employed for (photo)electrochemical techniques that demand robustness and homogeneity such as Mott-Schottky or Linear Sweep

Voltammetry (LSV). For the rest of the characterization techniques, drop-cast CTFs on FTO or only powder CTFs were used.

Figure 4 depicts the characterization techniques employed. All the results shown in this Figure correspond to CTF-$CONH_2$, yet the data for the rest of the CTFs are displayed in the supporting information (Table S1-S2 and Figures S2-S4).

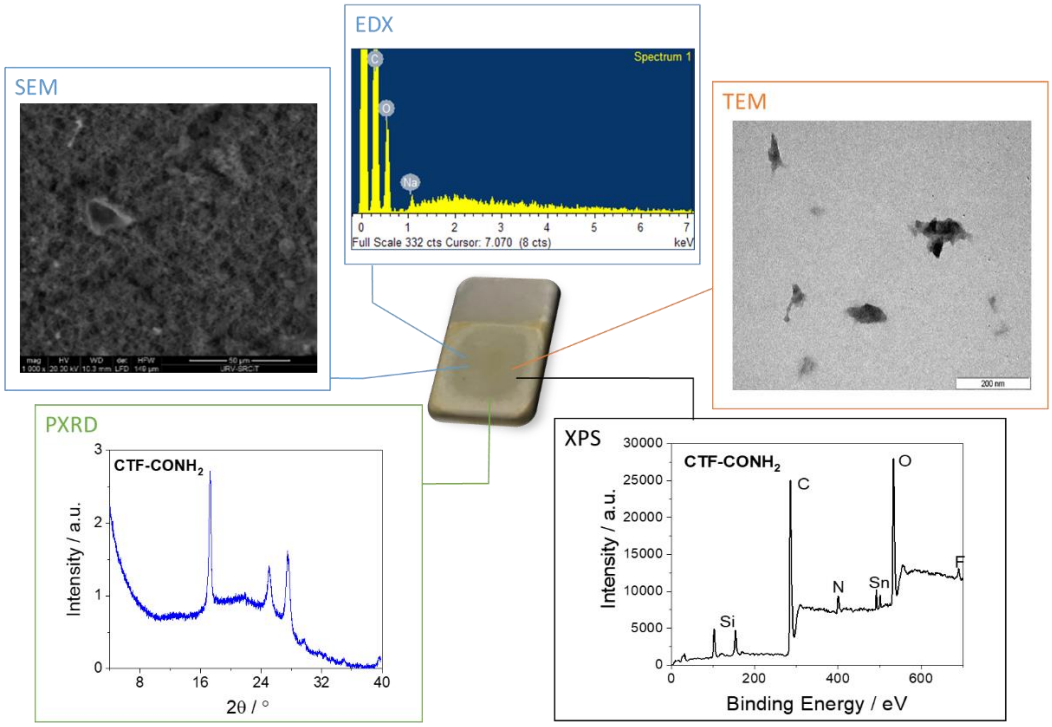

Figure 4. Swiss-knife characterization techniques employed for the CTF materials: Scanning Electron Microscopy or SEM; Energy Dispersive X-ray Spectroscopy or EDS; Transmission Electron Microscopy or TEM; Powder X-Ray Diffraction or PXRD; X-Ray Photoelectron Spectroscopy or XPS. All the depicted results are from the CTF-$CONH_2$ sample, see SI for data related to the rest of the CTFs.

Firstly, electron microscopy techniques were used to visualize qualitative macroscopic features. Transmission Electron Microscopy (TEM) images of freshly synthesized powders are shown in Figure 4 and Table S1. CTFs' powders displayed as tightly stacked irregular slices in the form of lamellar structures, which are similar to other reported CTFs.[44] In fact, these results are expected by the amorphous nature of CTFs.[11,13,19] These irregularities could be enhanced by the defects in the chemical structure introduced by the co-polymerization of 1,4-dicyanobenzene with M-COOH and M-$CONH_2$ as capping agents (top of Figure 2). This prevents the growth of the network in certain directions and thus, we expect them to generate more defective extended frameworks. However, no differences in the TEM images between all the presented CTFs can be visualized by

the naked eye (Table S1). On the other hand, Scanning Electron Microscopy (SEM) allowed the qualitative surface study of the photoelectrodes prepared by drop-casting. As seen in Figure 4 and Table S2, some of the prepared electrodes presented some cracks due to the fast evaporation of the solvent during the drop-cast procedure. Energy-Dispersive X-ray spectroscopy (EDX) was performed together with SEM, resulting C and O the main peaks in the EDX spectra. Another characterization technique employed was Powder X-Ray Diffraction (PXRD), which showed broad bands corresponding to the amorphous nature of the CTFs (Figure 4 and Figure S3). These patterns are in line with the ones reported in the literature by Tang and co-workers.[23] Despite the similar PXRD spectra, they seem to find somewhat of order in CTF-1, both in-plane and interlayer. Yet, as shown by their patterns, the bands are too broad to extract accurate conclusions. Finally, the outcome of the X-Ray Photoelectron Spectroscopy (XPS, Figure S4) survey spectra was the expected peaks for FTO (Si, Sn, F) and for CTF (C, N) with no significant differences between different samples.

One of the key aspects of this work was to determine if the electronic features of the new materials are thermodynamically suitable to be coupled to water oxidation catalysts. As depicted in Figure 5, optical band-gap (E_g) was determined by diffuse reflectance with concomitant Tauc plot analysis. Besides, conduction band edge (CB) was calculated to be *ca.* the flatband potential (E_{fb}), which was obtained from Mott-Schottky analysis (by Electrochemical Impedance Spectroscopy, EIS). This approximation comes from the assumption that E_{fb} is related to the Fermi energy,[45] which lays below the CB in n-type semiconductors. This is the case for CTFs, as shown by the positive slopes in Mott-Schottky plots, typical for n-type semiconductors. Valence band (VB) position was obtained by subtracting the E_g to the approximate value of CB. Detailed experimental data and band calculation for each CTF can be found in Table 1 and the supporting information (Figure S5 to Figure S9).

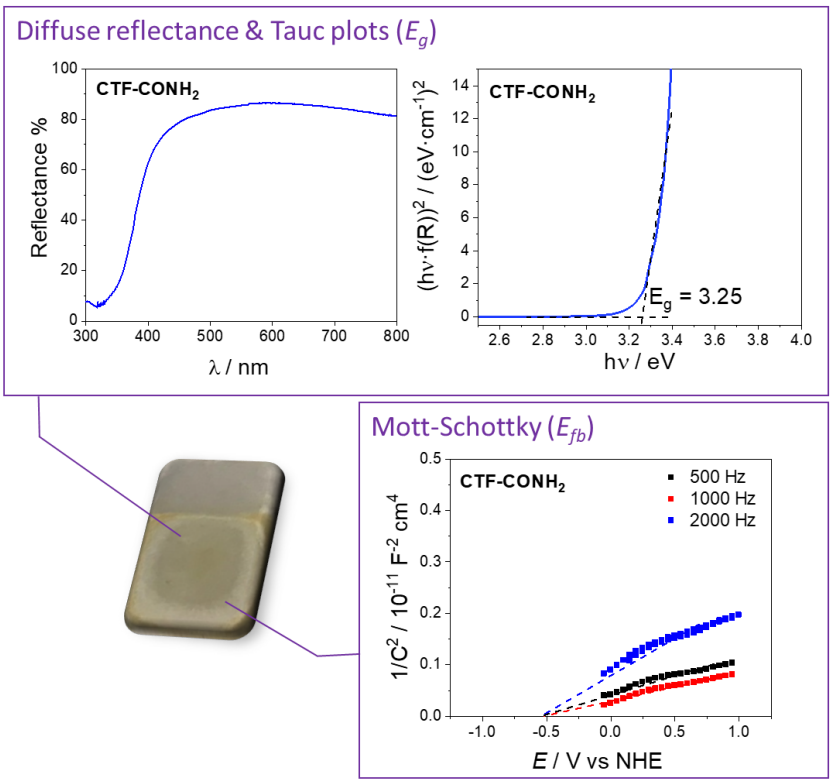

Figure 5. Optical characterization of CTF-CONH$_2$. The E_g = 3.25 V and the E_{fb} = -0.55 V vs. NHE (pH 7) were determined by diffuse reflectance (with Tauc plot transformation) and Mott-Schottky analysis respectively.

As summarized in Table 1 and illustrated in Scheme 1, all the synthesized CTFs present high oxidative potential energy in the range of 1.76-2.8 V, which make them suitable for water oxidation catalysis but also to be coupled to benchmarking molecular WOC with catalytic onset at E_{onset} = 1.2 V. All redox potentials in this work are reported *vs.* NHE at pH = 7.0. Interestingly, the effect of the substituents introduced in the CTF network is distinct. While the materials containing fluorine and amide groups show higher VB potentials compared to the reference CTF-1, presumably due to the electron-withdrawing effect of both groups, the VB potential of the carboxylic acid derivative is significantly lower. Considerable changes in the band-gap energy are also observed with CTF-COOH showing the lower bandgap among all. Ideally, the lower the bandgap the better, in order to absorb in the visible of the solar spectrum. On the other hand, it is important to have the CB as more reductive as possible to be able, in further research, to perform full water splitting or CO_2 reduction. As depicted in Scheme 1, thermodynamically, most of the CTFs synthesized could potentially perform both half-reactions for full water splitting. Only the CTF-py shows a potential below the H^+/H_2 couple and therefore is unlikely to perform full water-splitting according to our

measurement. In this case, it would be necessary to use a Z-scheme system that combines two materials to span the full range of required energy.[46,47] So far, only thermodynamic aspects have been considered, however, other characteristics such as charge generation and recombination or kinetic barrier of the chemical reaction are paramount for achieving efficient light-driven water oxidation or water splitting. The addition of specific catalysts for water oxidation and water reduction in combination with the photoactive material should overcome some of the abovementioned problems.

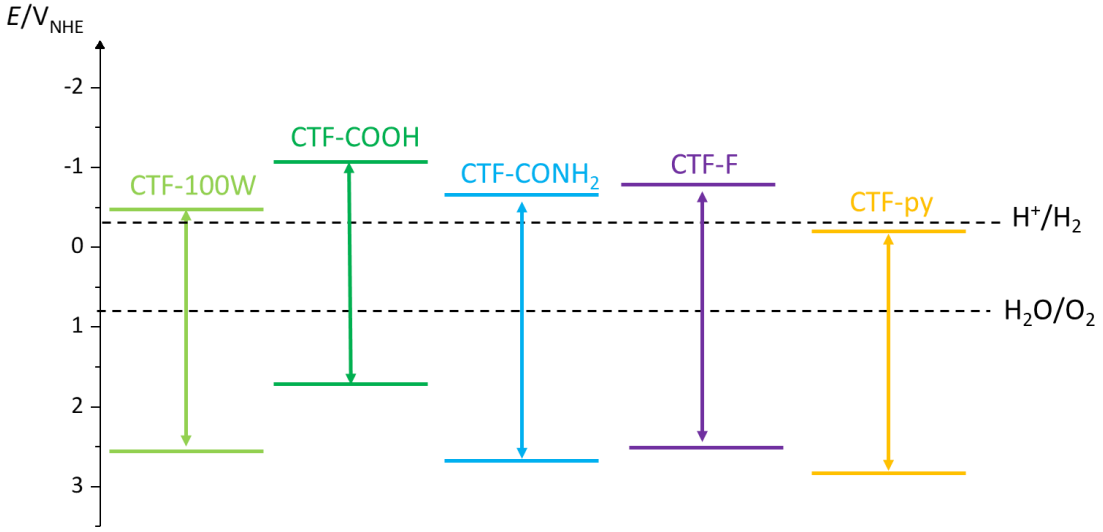

Scheme 1. Approximate positions of the conduction band edge and valence band edge of the CTFs prepared in this work (V vs. NHE at pH = 7.0), in comparison with the potentials required to conduct water oxidation and reduction (dashed lines). Scheme based on UV-Vis and Mott-Schottky spectroscopies with the required data treatment (see Table 1 and SI).

Monomers (ratio)	***CTF***	***Eg / V***	***CB / V***	***VB / V***
M-1:M-$CONH_2$ (5:1)	CTF-$CONH_2$	3.25	-0.55	2.7
M-1:M-COOH (5:1)	CTF-COOH	2.88	-1.12	1.76
M-1:M-F (5:1)	CTF-F	3.23	-0.61	2.63
M-py	CTF-py	3.1	-0.3	2.8
M-1	CTF-1	3	-0.47	2.53

Table 1. Summary of the results from optical characterization. Approximate energy levels of the conduction band edge (CB), valence band edge (VB) and bandgap of the studied CTFs, in V vs. NHE at pH = 7.0.

6.2.2 Water oxidation performance

As previously discussed, π-π or π-CH interactions between Ru(tda) derivatives and multi-wall carbon nanotubes generate robust electrodes and photoelectrodes for the water oxidation reaction.[37,38] However we have not managed to use CTFs as good supports for Ru-tda catalysts using the same strategy. Neither drop-casting nor adsorption in colloidal solution could achieve successful loading of the Ru-tda oligomer, $[Ru(tda)(4,4'\text{-bpy})]_{15}$, on the CTFs, probably due to the smaller surface area of the material accessible to the Ru(tda) complex or to the lower degree of conjugation of the CTF network compared to that of the carbon nanotubes. Despite it, photoelectrochemical experiments were performed on doctor blade photoelectrodes without WOC (herein labeled as CTF-COOH@FTO, CTF-F@FTO, and CTF-$CONH_2$@FTO) to determine potential photocatalytic activity and stability in water oxidation conditions. A home-made photoelectrochemical cell with a three-electrode configuration was employed (Figure S10), with the photoelectrodes as the working electrodes, Hg/Hg_2SO_4 as the reference electrode, and Pt coil as the counter electrode in pH 7 phosphate buffer (1 sun back illumination by a Xe lamp 150 W). Chopped Light Bulk Electrolysis (CL-BE) at 0.8 V (*vs.* NHE) of the new CTF electrodes display higher photocurrents than CTF-1@FTO used as a reference and other reported in the literature (Figure S11).[8,15,23,28] For instance, CTF-F@FTO shows photocurrents of 30 $\mu A \cdot cm^{-2}$ which is twice the photocurrents achieved by CTF-1@FTO. The rest presented photocurrents between 24-30 $\mu A \cdot cm^{-2}$, much higher than the 15 $\mu A \cdot cm^{-2}$ of CTF-1@FTO. To the best of our knowledge, it is the first time stable photoelectrodes with photocurrents > 10 $\mu A \cdot cm^{-2}$ over 60 min are reported.[8,28] Besides, the photoelectrodes display low currents in dark, i.e. short-circuit current, and no charge recombination, which is seen by the lack of spike current at the beginning of illumination. SEM analysis of the electrodes after the photoelectrochemical tests shows no significant differences in their morphology (Table S2). Subsequently, the Generator-Collector methodology was employed to detect oxygen in ranges of μA.[48] The Generator-Collector method consists of placing two electrodes very near to each other. One of them will perform water oxidation (Generator) while the other is set to reduce the oxygen that is produced (Collector) (Figure S12). By using this technique we could not detect any oxygen (Figure S14 in the

SI), maybe because of the low amounts produced and diffused, together with mass transport issues due to the presumed microporosity of the photoelectrodes. Alternative detection methods such as Clark electrodes were not sensitive enough to detect O_2 at this range (μA) either. Thus, although significant photocurrents are observed in chopped light BE experiments, we currently do not have proof of the water oxidation ability of the new CTF@FTO electrodes.

In parallel, another line of research was the covalent bonding of [Ru(tda)(dmso)(py)] to the dangling pyridine of CTF-py by refluxing both of them in ethanol/methanol (1:1) for three days (Figure 6 top). The successful functionalization of the material was confirmed by the Cyclic Voltammetry (CV) of a sample drop-cast on glassy carbon, which shows characteristic redox waves for the expected complex [Ru(tda)(py)$_2$] at $E_{1/2}(Ru^{III/II})$ = 0.6 V and $E_{1/2}(Ru^{IV/III})$ = 1.1 V (Figure 6 bottom, orange areas).[42] In addition, another set of waves are also observed, which are attributed to the [Ru(tda)(dmso)py] complex at $E_{1/2}(Ru^{III/II})$ = 0.8 V and $E_{1/2}(Ru^{IV/III})$ = 1.25 V (Figure 6 bottom in grey).[41] Therefore, the replacement of (dmso) and (py) axial ligands by CTF-py were competitive (Equations 4-5), and led to the two Ru species CTF-py-[Ru(tda)(py)] and CTF-py-[Ru(tda)(dmso)] in a ratio close to 1:1 according to the CV. Thus, the final product, herein labeled as CTF-py-Ru(tda), is the combination of both. XPS elemental analysis of the material results in 0.7 at% Ru in the sample.

CTF-py + [Ru(tda)(dmso)(py)] → CTF-py-[Ru(tda)(py)] + dmso (Equation 4)

CTF-py + [Ru(tda)(dmso)(py)] → CTF-py-[Ru(tda)(dmso)] + py (Equation 5)

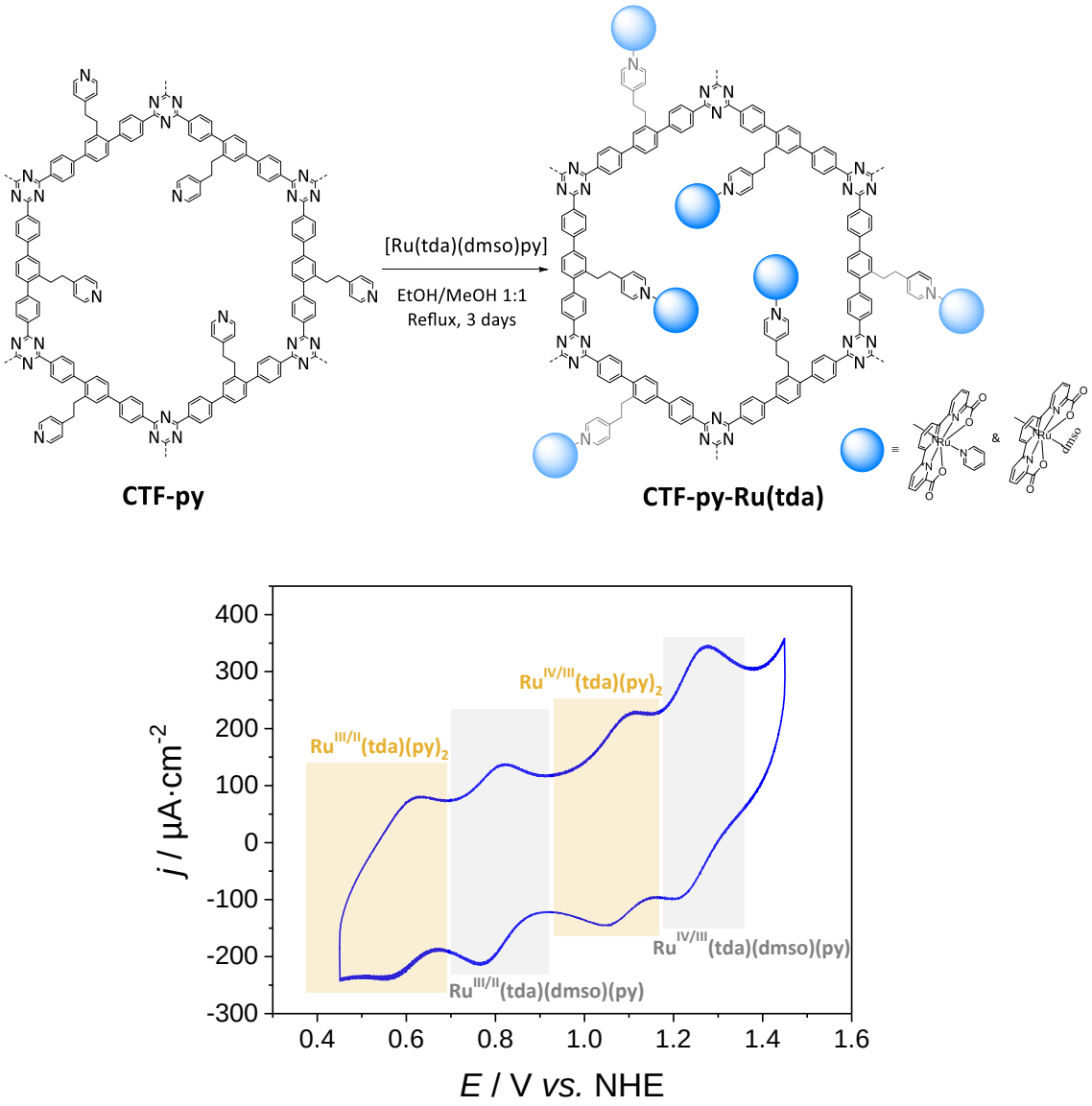

Figure 6. On the top, schematic loading of water oxidation catalyst on CTF-py to form the CTF-py-Ru(tda). On the right, cyclic voltammetry (CV) of the resulting CTF to demonstrate the catalyst loading. Two complexes are present in the CV: the anchored CTF-py-[Ru(tda)py] (orange) and CTF-py-[Ru(tda)(dmso)] (grey).

Figure 7 displays the photocatalytic activity of CTF-py-Ru(tda) as a suspended colloidal solution (2 mg·mL^{-1} in 2 mL pH 7 phosphate buffer, 25 mM) in the presence of a sacrificial electron acceptor (10 mM $Na_2S_2O_8$) under 1 sun illumination (Xe lamp 150 W). Upon light illumination, the complete photocatalytic system (red line in Figure 7) generates a significant amount of oxygen achieving 54 turnover numbers (TON) in about 3 h and 40 min (Equation S2). These results are remarkable when compared to the few related systems reported in the literature based on molecular water oxidation catalysts.[49] In the absence of Ru-WOC, CTF-py does not generate significant amounts of oxygen, proving the key role of the catalyst in driving the reaction (black trace in Figure 7). The bottom

part of Figure 7 represents a hypothetic reaction scheme for the studied sample that includes the thermodynamics involved in water oxidation and reduction (black lines). Firstly, the absorption of light promotes an electron to the Conduction Band (CB) of the material and creates a hole in its Valence Band (VB) (blue). The photogenerated holes will allow the generation of the active Ru^{V}=O species which will, in turn, oxidize water to dioxygen (E'_{ox}, green). On the other hand, the photogenerated electrons will rapidly reduce sodium persulfate into sodium sulfate, which acts as a sacrificial electron acceptor (red). To the best of our knowledge, this is the first example combining a carbon-based light-absorber covalently coupled with a molecular catalyst, which fulfills the needs of the future atom (circular) economy.[31–33]

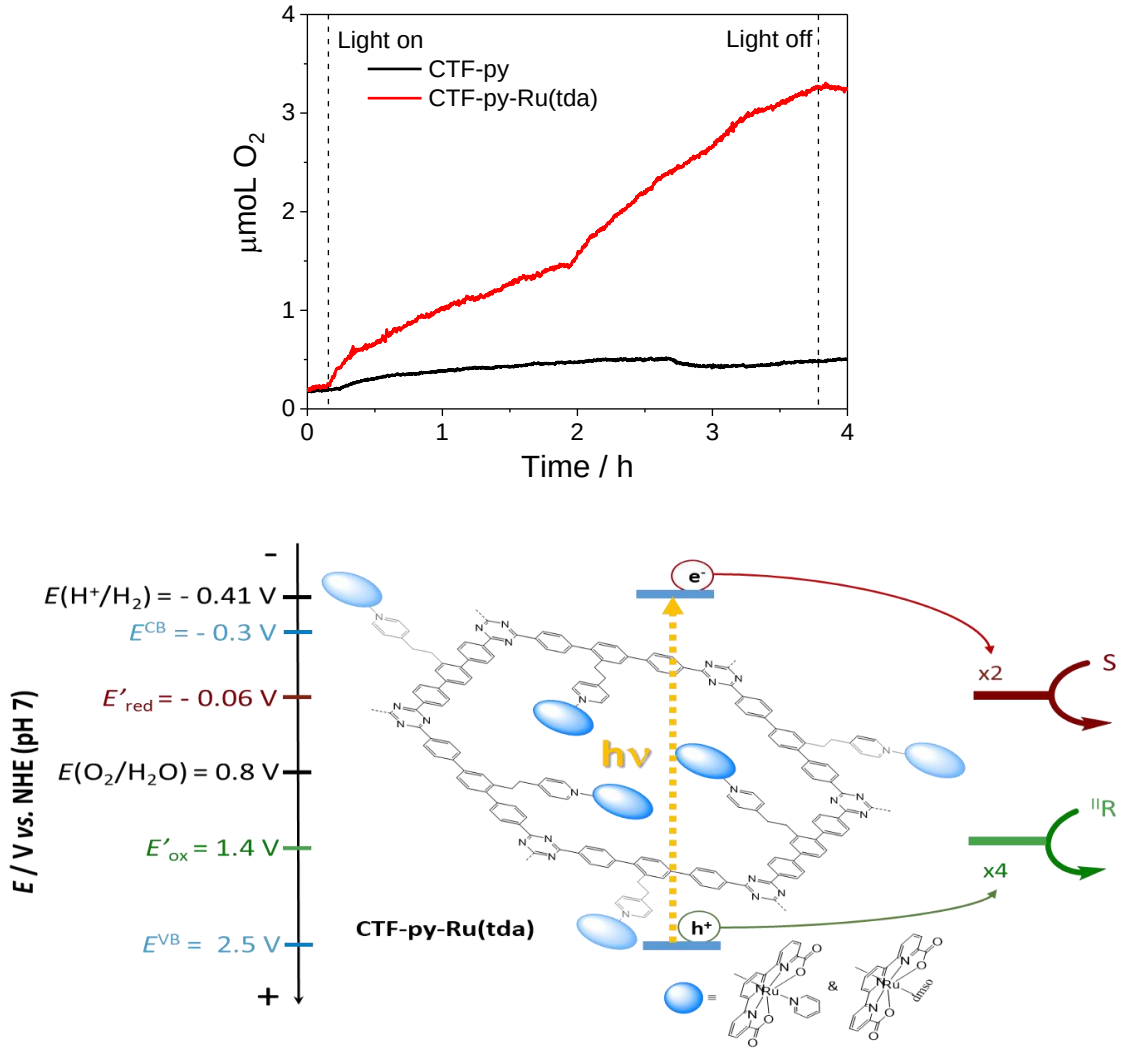

Figure 7. Top, oxygen evolution experiment of a colloidal solution of 2 mg·mL^{-1} CTF-py-Ru(tda) (red line) in 2 mL pH 7 phosphate buffer under 1 sun illumination (Xe lamp 150 W) in the presence of 10 mM $Na_2S_2O_8$. In black, the blank experiment using CTF-py without WOC. A Clark electrode for selective detection of O_2 in the gas phase (2 mL) was employed. At the bottom, schematic representation of the light absorption, charge transfer, and catalysis performed by CTF-py-Ru(tda) in the presence of a sacrificial agent.

6.3 Conclusions

Four novel CTFs have been reported. The synthesis was successfully performed together with their characterization by means of microscopy, spectroscopy, and electrochemical techniques. Besides, a new photoelectrode assembly procedure is presented. Compared to the literature, high and stable photocurrents for CTF-F, CTF-COOH, and CTF-$CONH_2$ were achieved. Despite all these advantages, oxygen measurements were difficult to perform. Therefore, for these samples, more sensitive O_2 detection techniques are in need. On the other hand, successful incorporation of a highly active Ru-based WOC has been attained in the case of CTF-py. CTF-py-Ru(tda) was designed based on the covalent bonding of Ru(tda)(dmso)py and the dangling pyridine in the CTF-py unit. The system proved to be active towards water oxidation with remarkable TONs of 54 and with just 0.7 at% Ru, which contributes to the lack of reported organic photocatalysts for light-driven water oxidation.

This is the first step towards the design of a cheap and available light-absorber capable of performing water oxidation photocatalysis thanks to the direct and rational incorporation of a highly active molecular catalyst for water oxidation. Further research is needed to study the catalyst loading influence in light absorption and/or catalysis rates, as well as to lower the bandgaps for a greater shift to the visible light absorption. Moreover, this structure allows the incorporation of first-row transition metal catalysts as well as catalysts for proton or CO_2 reduction.

6.4 References

(1) Steffen, W.; Rockström, J.; Richardson, K.; Lenton, T. M.; Folke, C.; Liverman, D.; Summerhayes, C. P.; Barnosky, A. D.; Cornell, S. E.; Crucifix, M.; Donges, J. F.; Fetzer, I.; Lade, S. J.; Scheffer, M.; Winkelmann, R.; Schellnhuber, H. J. Trajectories of the Earth System in the Anthropocene. *Proc. Natl. Acad. Sci. U. S. A.* **2018**, *115* (33), 8252–8259. https://doi.org/10.1073/pnas.1810141115.

(2) Waters, C. N.; Zalasiewicz, J.; Summerhayes, C.; Barnosky, A. D.; Poirier, C.; Ga uszka, A.; Cearreta, A.; Edgeworth, M.; Ellis, E. C.; Ellis, M.; Jeandel, C.; Leinfelder, R.; McNeill, J. R.; Richter, D. d.; Steffen, W.; Syvitski, J.; Vidas, D.; Wagreich, M.; Williams, M.; Zhisheng, A.; Grinevald, J.; Odada, E.; Oreskes, N.; Wolfe, A. P. The Anthropocene Is Functionally and Stratigraphically Distinct from the Holocene. *Science* **2016**, *351* (6269), 137–148. https://doi.org/10.1126/science.aad2622.

(3) Thuiller, W. Climate Change and the Ecologist. *Nature* **2007**, *448* (7153), 550–552. https://doi.org/10.1038/448550a.

(4) Dybtsev, D. N.; Chun, H.; Yoon, S. H.; Kim, D.; Kim, K. Microporous Manganese Formate: A Simple Metal-Organic Porous Material with High Framework Stability and Highly Selective Gas Sorption Properties. *J. Am. Chem. Soc.* **2004**, *126* (1), 32–33. https://doi.org/10.1021/ja038678c.

(5) Bae, Y. S.; Snurr, R. Q. Development and Evaluation of Porous Materials for Carbon Dioxide

Separation and Capture. *Angew. Chem. Int. Ed.* **2011**, *50* (49), 11586–11596. https://doi.org/10.1002/anie.201101891.

(6) Corma, A.; Garcia, H. Silica-Bound Homogenous Catalysts as Recoverable and Reusable Catalysts in Organic Synthesis. *Adv. Synth. Catal.* **2006**, *348* (12-13), 1391–1412. https://doi.org/10.1002/adsc.200606192.

(7) Taguchi, A.; Schüth, F. Ordered Mesoporous Materials in Catalysis. *Microporous Mesoporous Mater.* **2005**, *77* (1), 1–45. https://doi.org/10.1016/j.micromeso.2004.06.030.

(8) Bi, J.; Fang, W.; Li, L.; Wang, J.; Liang, S.; He, Y.; Liu, M.; Wu, L. Covalent Triazine-Based Frameworks as Visible Light Photocatalysts for the Splitting of Water. *Macromol. Rapid Commun.* **2015**, *36* (20), 1799–1805. https://doi.org/10.1002/marc.201500270.

(9) Thomas, A. Functional Materials: From Hard to Soft Porous Frameworks. *Angew. Chem. Int. Ed.* **2010**, *49* (45), 8328–8344. https://doi.org/10.1002/anie.201000167.

(10) Czaja, A. U.; Trukhan, N.; Müller, U. Industrial Applications of Metal–organic Frameworks. *Chem. Soc. Rev.* **2009**, *38* (5), 1284–1293. https://doi.org/10.1039/b804680h.

(11) Krishnaraj, C.; Jena, H. S.; Leus, K.; Van Der Voort, P. Covalent Triazine Frameworks-a Sustainable Perspective. *Green Chem.* **2020**, *22* (4), 1038–1071. https://doi.org/10.1039/c9gc03482j.

(12) Cote, A. P.; Benin, A. I.; Ockwig, N. W.; O'Keeffe, M.; Matzger, A. J.; Yaghi, O. M. Porous, Crystalline, Covalent Organic Frameworks. *Science* **2005**, *310* (5751), 1166–1170. https://doi.org/10.1126/science.1120411.

(13) Liu, M.; Guo, L.; Jin, S.; Tan, B. Covalent Triazine Frameworks: Synthesis and Applications. *J. Mater. Chem. A* **2019**, *7* (10), 5153–5172. https://doi.org/10.1039/c8ta12442f.

(14) Ren, S.; Bojdys, M. J.; Dawson, R.; Laybourn, A.; Khimyak, Y. Z.; Adams, D. J.; Cooper, A. I. Porous, Fluorescent, Covalent Triazine-Based Frameworks Via Room-Temperature and Microwave-Assisted Synthesis. *Adv. Mater.* **2012**, *24* (17), 2357–2361. https://doi.org/10.1002/adma.201200751.

(15) Jiang, X.; Wang, P.; Zhao, J. 2D Covalent Triazine Framework: A New Class of Organic Photocatalyst for Water Splitting. *J. Mater. Chem. A* **2015**, *3* (15), 7750–7758. https://doi.org/10.1039/c4ta03438d.

(16) Liras, M.; Barawi, M.; de la Peña O'Shea, V. A. Hybrid Materials Based on Conjugated Polymers and Inorganic Semiconductors as Photocatalysts: From Environmental to Energy Applications. *Chem. Soc. Rev.* **2019**, *48* (22), 5454–5487. https://doi.org/10.1039/C9CS00377K.

(17) Kosco, J.; Moruzzi, F.; Willner, B.; McCulloch, I. Photocatalysts Based on Organic Semiconductors with Tunable Energy Levels for Solar Fuel Applications. *Adv. Energy Mater.* **2020**, *10* (39). https://doi.org/10.1002/aenm.202001935.

(18) Yang, L.; Zhou, H.; Fan, T.; Zhang, D. Semiconductor Photocatalysts for Water Oxidation: Current Status and Challenges. *Phys. Chem. Chem. Phys.* **2014**, *16* (15), 6810–6826. https://doi.org/10.1039/c4cp00246f.

(19) Kong, D.; Zheng, Y.; Kobielusz, M.; Wang, Y.; Bai, Z.; Macyk, W.; Wang, X.; Tang, J. Recent Advances in Visible Light-Driven Water Oxidation and Reduction in Suspension Systems. *Mater. Today* **2018**, *21* (8), 897–924. https://doi.org/10.1016/j.mattod.2018.04.009.

(20) Meier, C. B.; Sprick, R. S.; Monti, A.; Guiglion, P.; Lee, J.-S. M.; Zwijnenburg, M. A.; Cooper, A. I. Structure-Property Relationships for Covalent Triazine-Based Frameworks: The Effect of Spacer Length on Photocatalytic Hydrogen Evolution from Water. *Polymer* **2017**, *126*, 283–290. https://doi.org/10.1016/j.polymer.2017.04.017.

(21) Lu, L.; Lv, Z.; Si, Y.; Liu, M.; Zhang, S. Recent Progress on Band and Surface Engineering of Graphitic Carbon Nitride for Artificial Photosynthesis. *Appl. Surf. Sci.* **2018**, *462*, 693–712. https://doi.org/10.1016/j.apsusc.2018.08.131.

(22) Wang, Y.; Silveri, F.; Bayazit, M. K.; Ruan, Q.; Li, Y.; Xie, J.; Catlow, C. R. A.; Tang, J. Bandgap Engineering of Organic Semiconductors for Highly Efficient Photocatalytic Water Splitting. *Adv. Energy Mater.* **2018**, *8* (24), 1801084. https://doi.org/10.1002/aenm.201801084.

(23) Xie, J.; Shevlin, S. A.; Ruan, Q.; Moniz, S. J. A.; Liu, Y.; Liu, X.; Li, Y.; Lau, C. C.; Guo, Z. X.; Tang, J. Efficient Visible Light-Driven Water Oxidation and Proton Reduction by an Ordered Covalent Triazine-Based Framework. *Energy Environ. Sci.* **2018**, *11* (6), 1617–1624. https://doi.org/10.1039/c7ee02981k.

(24) Maeda, K.; Wang, X.; Nishihara, Y.; Lu, D.; Antonietti, M.; Domen, K. Photocatalytic Activities of Graphitic Carbon Nitride Powder for Water Reduction and Oxidation under Visible Light. *J. Phys. Chem. C* **2009**, *113* (12), 4940–4947. https://doi.org/10.1021/jp809119m.

(25) Zhang, G.; Huang, C.; Wang, X. Dispersing Molecular Cobalt in Graphitic Carbon Nitride Frameworks for Photocatalytic Water Oxidation. *Small* **2015**, *11* (9-10), 1215–1221. https://doi.org/10.1002/smll.201402636.

(26) Lee, R.-L.; Tran, P. D.; Pramana, S. S.; Chiam, S. Y.; Ren, Y.; Meng, S.; Wong, L. H.; Barber, J. Assembling Graphitic-Carbon-Nitride with Cobalt-Oxide-Phosphate to Construct an Efficient Hybrid Photocatalyst for Water Splitting Application. *Catal. Sci. Technol.* **2013**, *3* (7), 1694. https://doi.org/10.1039/c3cy00054k.

(27) Pan, Z.; Zheng, Y.; Guo, F.; Niu, P.; Wang, X. Decorating CoP and Pt Nanoparticles on Graphitic Carbon Nitride Nanosheets to Promote Overall Water Splitting by Conjugated Polymers. *ChemSusChem.* **2017**, *10* (1), 87–90. https://doi.org/10.1002/cssc.201600850.

(28) Kong, D.; Xie, J.; Guo, Z.; Yang, D.; Tang, J. Stable Complete Water Splitting by Covalent Triazine-based Framework CTF-0. *ChemCatChem* **2020**, *12* (10), 2708–2712. https://doi.org/10.1002/cctc.201902396.

(29) Katekomol, P.; Roeser, J.; Bojdys, M.; Weber, J.; Thomas, A. Covalent Triazine Frameworks Prepared from 1,3,5-Tricyanobenzene. *Chem. Mater.* **2013**, *25* (9), 1542–1548. https://doi.org/10.1021/cm303751n.

(30) Bi, J.; Fang, W.; Li, L.; Wang, J.; Liang, S. Covalent Triazine-Based Frameworks as Visible Light Photocatalysts for the Splitting of Water. **2015**. https://doi.org/10.1002/marc.201500270.

(31) Roduner, E. Size Matters: Why Nanomaterials Are Different. *Chem. Soc. Rev.* **2006**, *35* (7), 583–592. https://doi.org/10.1039/b502142c.

(32) Vesborg, P. C. K.; Jaramillo, T. F. Addressing the Terawatt Challenge: Scalability in the Supply of Chemical Elements for Renewable Energy. *RSC Adv.* **2012**, *2* (21), 7933–7947. https://doi.org/10.1039/c2ra20839c.

(33) Stahel, W. R. The Circular Economy. *Nature* **2016**, *531* (7595), 435–438. https://doi.org/10.1038/531435a.

(34) Wang, Y.; Di, Y.; Antonietti, M.; Li, H.; Chen, X.; Wang, X. Excellent Visible-Light Photocatalysis of Fluorinated Polymeric Carbon Nitride Solids. *Chem. Mater.* **2010**, *22* (18), 5119–5121. https://doi.org/10.1021/cm1019102.

(35) Ha, T.-J.; Akinwande, D.; Dodabalapur, A. Hybrid Graphene/organic Semiconductor Field-Effect Transistors. *Appl. Phys. Lett.* **2012**, *101* (3), 033309. https://doi.org/10.1063/1.4737939.

(36) Niu, F.; Wang, D.; Li, F.; Liu, Y.; Shen, S.; Meyer, T. J. Hybrid Photoelectrochemical Water Splitting Systems: From Interface Design to System Assembly. *Adv. Energy Mater.* **2020**, *10* (11), 1–24. https://doi.org/10.1002/aenm.201900399.

(37) Hoque, M. A.; Gil-Sepulcre, M.; de Aguirre, A.; Elemans, J. A. A. W.; Moonshiram, D.; Matheu, R.; Shi, Y.; Benet-Buchholz, J.; Sala, X.; Malfois, M.; Solano, E.; Lim, J.; Garzón-Manjón, A.; Scheu, C.; Lanza, M.; Maseras, F.; Gimbert-Suriñach, C.; Llobet, A. Water Oxidation Electrocatalysis Using Ruthenium Coordination Oligomers Adsorbed on Multiwalled Carbon Nanotubes. *Nat. Chem.* **2020**, *12* (11), 1060–1066. https://doi.org/10.1038/s41557-020-0548-7.

(38) Creus, J.; Matheu, R.; Peñafiel, I.; Moonshiram, D.; Blondeau, P.; Benet-Buchholz, J.; García-Antón, J.; Sala, X.; Godard, C.; Llobet, A. A Million Turnover Molecular Anode for Catalytic Water Oxidation. *Angew. Chemie Int. Ed.* **2016**, *55* (49), 15382–15386. https://doi.org/10.1002/anie.201609167.

(39) Materna, K. L.; Crabtree, R. H.; Brudvig, G. W. Anchoring Groups for Photocatalytic Water Oxidation on Metal Oxide Surfaces. *Chem. Soc. Rev.* **2017**, *46* (20), 6099–6110. https://doi.org/10.1039/c7cs00314e.

(40) Garrido-Barros, P.; Matheu, R.; Gimbert-Suriñach, C.; Llobet, A. Electronic, Mechanistic, and Structural Factors That Influence the Performance of Molecular Water Oxidation Catalysts Anchored on Electrode Surfaces. *Curr. Opin. Electrochem.* **2019**, *15*, 140–147. https://doi.org/10.1016/j.coelec.2019.04.027.

(41) Matheu, R.; Benet-Buchholz, J.; Sala, X.; Llobet, A. Synthesis, Structure, and Redox Properties of a Trans -Diaqua Ru Complex That Reaches Seven-Coordination at High Oxidation States. *Inorg. Chem.* **2018**, *57*, 1757–1765. https://doi.org/10.1021/acs.inorgchem.7b02375.

(42) Matheu, R.; Ertem, M. Z.; Benet-Buchholz, J.; Coronado, E.; Batista, V. S.; Sala, X.; Llobet, A. Intramolecular Proton Transfer Boosts Water Oxidation Catalyzed by a Ru Complex. *J. Am. Chem. Soc.* **2015**, *137* (33), 10786–10795. https://doi.org/10.1021/jacs.5b06541.

(43) Kuhn, P.; Antonietti, M.; Thomas, A. Porous, Covalent Triazine-Based Frameworks Prepared by Ionothermal Synthesis. *Angew. Chem. Int. Ed.* **2008**, *47* (18), 3450–3453.

https://doi.org/10.1002/anie.200705710.

(44) Guo, L.; Niu, Y.; Razzaque, S.; Tan, B.; Jin, S. Design of D−A1−A2 Covalent Triazine Frameworks via Copolymerization for Photocatalytic Hydrogen Evolution. *ACS Catal.* **2019**, *9* (10), 9438–9445. https://doi.org/10.1021/acscatal.9b01951.

(45) Gim, S.; Bisquert, J. *Photoelectrochemical Solar Fuel Production*, 1st ed.; Giménez, S., Bisquert, J., Eds.; Springer International Publishing, 2016. https://doi.org/10.1007/978-3-319-29641-8.

(46) Fabian, D. M.; Hu, S.; Singh, N.; Houle, F. A.; Hisatomi, T.; Domen, K.; Osterloh, F. E.; Ardo, S. Particle Suspension Reactors and Materials for Solar-Driven Water Splitting. *Energy Environ. Sci.* **2015**, *8* (10), 2825–2850. https://doi.org/10.1039/c5ee01434d.

(47) Berardi, S.; Drouet, S.; Francàs, L.; Gimbert-Suriñach, C.; Guttentag, M.; Richmond, C.; Stoll, T.; Llobet, A. Molecular Artificial Photosynthesis. *Chem. Soc. Rev.* **2014**, *43* (22), 7501–7519. https://doi.org/10.1039/C3CS60405E.

(48) Grau, S.; Berardi, S.; Moya, A.; Matheu, R.; Cristino, V.; Vilatela, J. J.; Bignozzi, C. A.; Caramori, S.; Gimbert-Suriñach, C.; Llobet, A. A Hybrid Molecular Photoanode for Efficient Light-Induced Water Oxidation. *Sustain. Energy Fuels* **2018**, *2* (9), 1979–1985. https://doi.org/10.1039/C8SE00146D.

(49) Ventosa, M.; Oliveras, J.; Bastús, N. G.; Gimbert-Suriñach, C.; Puntes, V.; Llobet, A. Nanocrystal–Molecular Hybrids for the Photocatalytic Oxidation of Water. *ACS Appl. Energy Mater.* **2020**, *3* (10), 10008–10014. https://doi.org/10.1021/acsaem.0c01685.

6.5 Supporting information

6.5.1 Experimental

2-fluoroterephtalonitrile, 4-cyanobenzoic acid, and 4-cyanobenzamide were purchased from Abcr; 1,4-dicyanobenzene, benzonitrile, Na_2HPO_4, trifluoromethanesulfonic acid and ethyl cellulose were acquired from Sigma-Aldrich; α-terpineol and N, N-Dimethylformamide (DMF) was produced by TCI and Scharlab S.L. company, respectively. FTO substrates were purchased from Pilkington (FTO TEC 8, 8 $\Omega \cdot sq^{-1}$).

pH = 7.0 buffered solution (0.1 M ionic strength) was prepared by dissolving NaH_2PO_4 (2.3 g, 0.017 M) and Na_2HPO_4 (3.75g, 0.026 M) with Mili-Q water up to 1 L solution. The pH was measured by a pHmeter (Seven Compact pH meter from Mettler Toledo).

6.5.2 CTFs synthesis

CTFs were fabricated following a reported microwave procedure.[1]

CTF-1: 0.2 g 1,4-dicyanobenzene (0.48 mmol) and 2 mL trifluoromethanesulfonic acid (TFMS) were charged into a 10 mL glass reaction vessel (CEM, Discover and Explorer SP Vessels). The monomer was dissolved by using a rare earth stirring magnet, and the vessel was sealed with a PTFE pressure control cap (ActiVent Pressure Control Technology, CEM). The reaction was stirred and heated dynamically at a maximum of

100 W in a CEM Discover SP microwave to 110 °C and kept at this temperature for 30 min (internal pressure ≤ 300 psi). As a result, a red-brownish viscous liquid was obtained. The addition of 0.1 M ammonia solution generated a precipitate which was filtered with a frit (pore 5). Afterward, more ammonia was added to the solid until the filtered solution achieved pH neutrality. Subsequently, the powder was washed with water, ethanol, ethyl acetate, acetone, and tetrahydrofuran. The final powder was dried under vacuum (<10^{-1} mbar) at 180 °C for ∼10 h to remove residual solvent and traces of TFMS (70% yield)

CTF-COOH: A reaction mixture of 1,4-dicyanobenzene (200 mg, 1.56 mmol), 4-cyanobenzoic acid (45 mg, 0.31 mmol), and trifluoromethanesulfonic acid (2 mL, 22.4 mmol) was prepared in a 10 mL Sealed-Pressure vessel (Discover and Explorer SP Vessels, CEM). Same conditions for microwave synthesis and work-up were applied as for CTF-1. CTF-COOH (60% yield) was obtained as a light pale yellow powder.

CTF-$CONH_2$: 1,4-dicyanobenzene (200 mg, 1.56 mmol) was mixed with 4-cyanobenzamide (47.8 mg, 0.31 mmol), and trifluoromethanesulfonic acid (2 mL, 22.4 mmol) was prepared. The same microwave-treatment and work-up were performed as explained previously. CTF-$CONH_2$ (54% yield) was obtained as a light brownish powder.

CTF-F: 1,4-dicyanobenzene (200 mg, 1.56 mmol) was mixed with 2-fluoroterephtalonitrile (45.7 g, 0.31 mmol), and trifluoromethanesulfonic acid (2 mL, 22.4 mmol) was prepared. The same microwave-treatment and work-up were performed as explained in CTF-COOH. CTF-F (62% yield) was obtained as a light pale yellow powder.

CTF-py: In a 10mL microwave tube containing a stirring bar, 83 mg of monomer M-py and 1.0 mL of trifluoromethanesulfonic acid were added. The solution turned red immediately and it was kept stirring for 5 min. Then, it was put in the microwave reactor for 30 s at a constant 100 W power. After, the addition of 0.1 M ammonia generated a brown precipitate. Subsequently, the same work-up procedure as for previous CTFs (washing and drying steps) was applied to the solid. CTF-py was obtained as a grey solid (72% yield).

6.5.3 Preparation of photoelectrodes

After synthesizing CTF powders, photoelectrodes of each were prepared by two different methods, including drop-casting and doctor blade.

For the drop-casting method, 10 mg CTF powder were dispersed in 1 mL N,N-Dimethylformamide (DMF) or Dimethylsulfoxide (DMSO) solvent under sonication for 30 min. If CTF was soluble, the solution was used directly. If not, the dispersion was allowed to stand for 48h, and then the supernatant was used for drop-casting. 50 µL CTF solution was dropped on FTO and dried on a hotplate at 50 ˚C. The same procedure was repeated twice to obtain the prepared CTF@FTO photoelectrodes.

For the doctor blade method, a viscous CTF solution is necessary. Its preparation consists of three steps: (i) 30 mg CTF were dispersed in ~210 mg DMF stirred for 3 min; (ii) 135 mg α-terpineol were added inside the dispersion being stirred for 3 min, and (iii) 22.5 mg ethylcellulose were added to increase the viscosity, and then the mixture was stirred overnight. Figure S1a shows the prepared CTF paste. Next, 5 layers of scotch tape were used to fix the shape and the thickness of the CTF film, which was deposited on FTO by a doctor blade technique (Figure S1b). Finally, the CTF film was dried in a muffle under 50 ˚C for 30 min, 100 ˚C for 20 min and 150 ˚C for 10 min (Figure S1c).

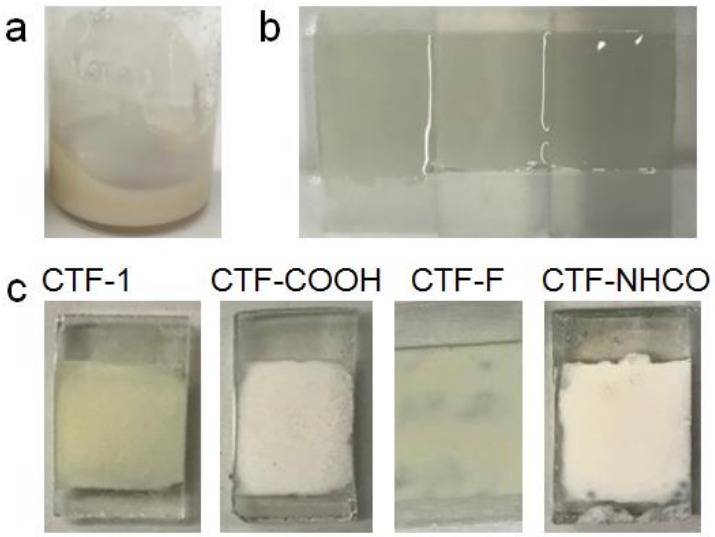

Figure S1. Photoelectrode preparation by doctor blade methodology. (a) Viscous liquid prepared from the mixture of CTF powder with DMF, α-terpineol, and ethyl cellulose under stirring overnight. (b) CTF layers spread on FTO by doctor blade. (c) Four types of CTF photoelectrodes were obtained after a dry process in a muffle.

6.5.4 Characterization techniques

Thermogravimetric analysis (TGA): was performed by using a differential scanning calorimeter (DSC) and a thermobalance (TG). Within a temperature range of 0 ˚C to 600 ˚C, 1 g of CTF was measured for phase transitions. A Mettler Toledo DSC822 with a 56-point Au-AuPd thermopile FRS5 sensor and a Mettler Toledo TGA/SDTA851 with a balance MT1 type were used.

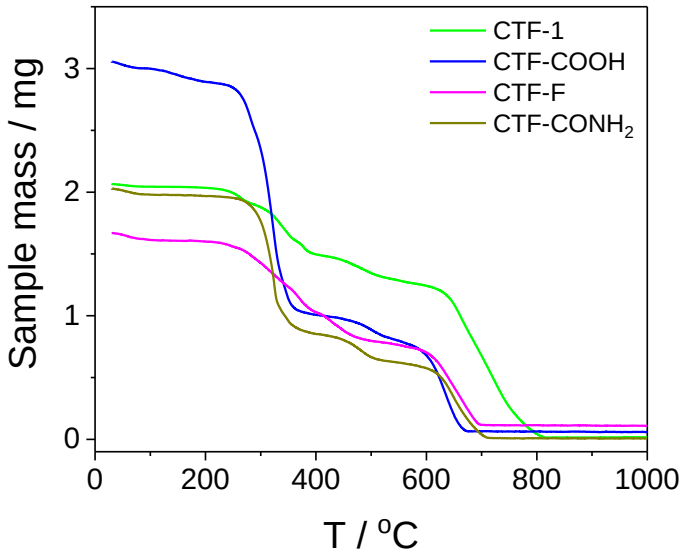

Figure S2. Thermal gravimetric analysis (TGA) for CTF-1, CTF-COOH, CTF-F, and CTF-$CONH_2$.

Fourier-transform infrared (FT-IR): Alpha Fourier-transform infrared spectrometer with the transmission accessory was used to acquire IR spectra. Small amounts of powder were used for characterization from 400 cm^{-1} to 4000 cm^{-1}.

Transmission electron microscopy (TEM): further morphological characterization was performed by using a JEOL TEM model 1011.

CTF	***x8K***	***x200K***
F	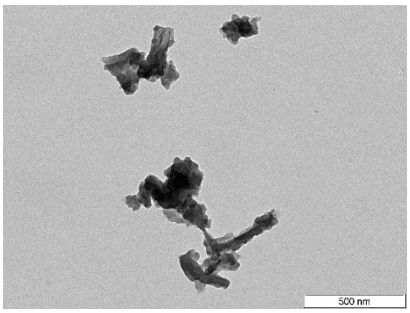	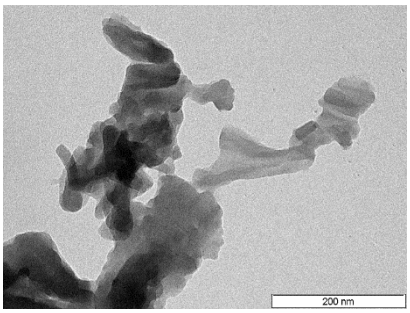
COOH	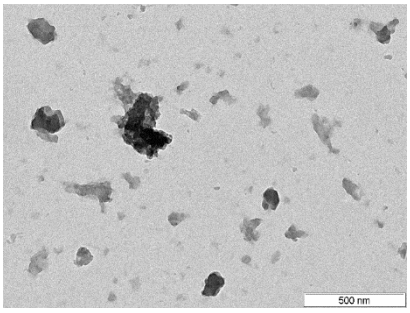	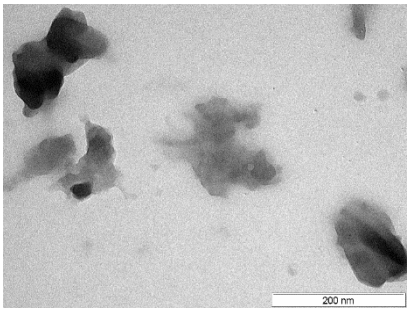
$CONH_2$	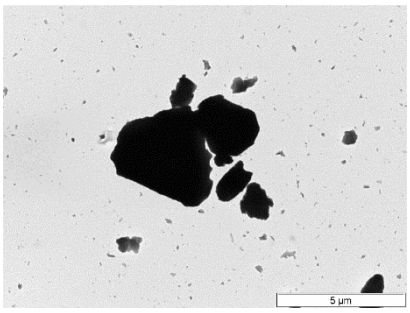	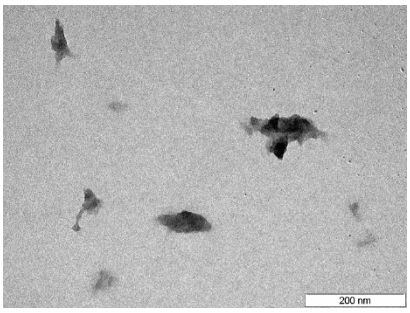
1	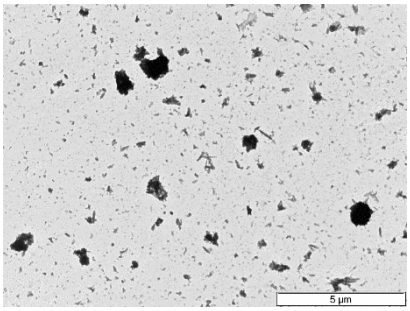	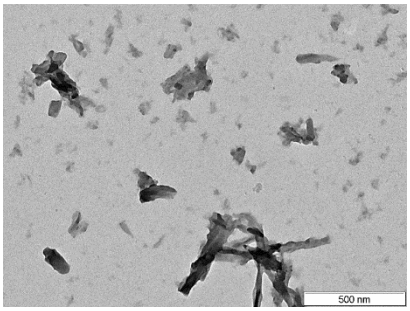

Table S1. Representative Transmission Electron Microscopy (TEM) images of as-synthesized powder CTF-F, CTF-COOH, CTF-$CONH_2$, CTF-1 in two magnification degrees. CTF-py is missing from this analysis.

Scanning Electron Microscopy (SEM): on JEOL SEM model JSM-6400 coupled with an Energy-Dispersive X-ray Spectroscopy (EDX) analyzer.

CTF	Fresh	After photoelectrocat.	EDX
F	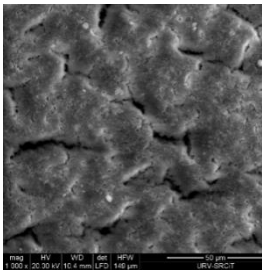	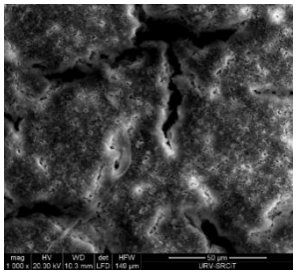	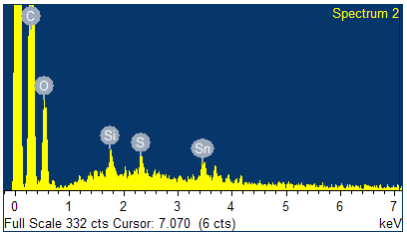
COOH	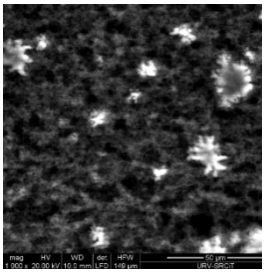	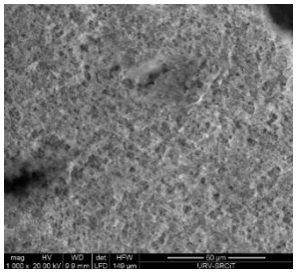	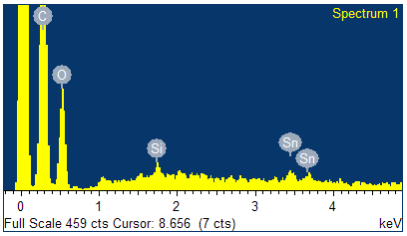
$CONH_2$	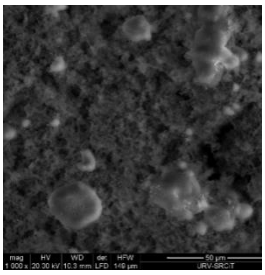	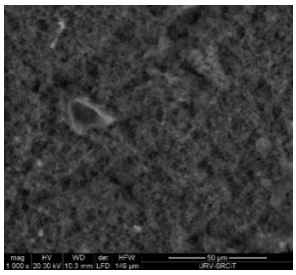	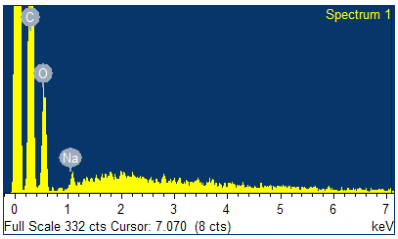
1	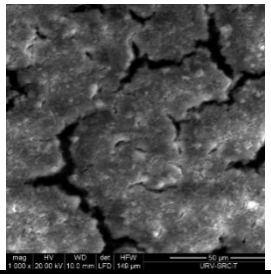	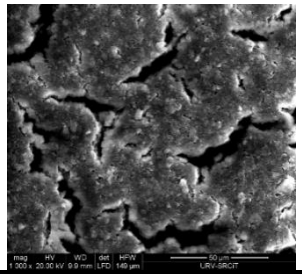	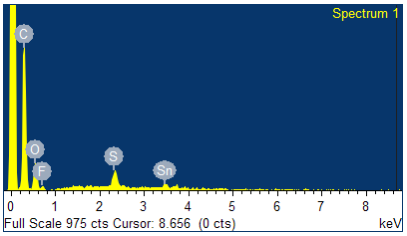

Table S2. Representative Scanning Electron Microscopy (SEM) images of photoelectrodes before and after photoelectrochemical use. EDX of the fresh samples on the right. CTF-py is missing from this analysis.

Powder X-Ray Diffraction (PXRD): D8 Advance Series 2θ/θ powder diffraction system in wide-angle X-ray scattering mode 2θ = 4–40 (wavelength 0.154 nm, Cu-Kα radiation).

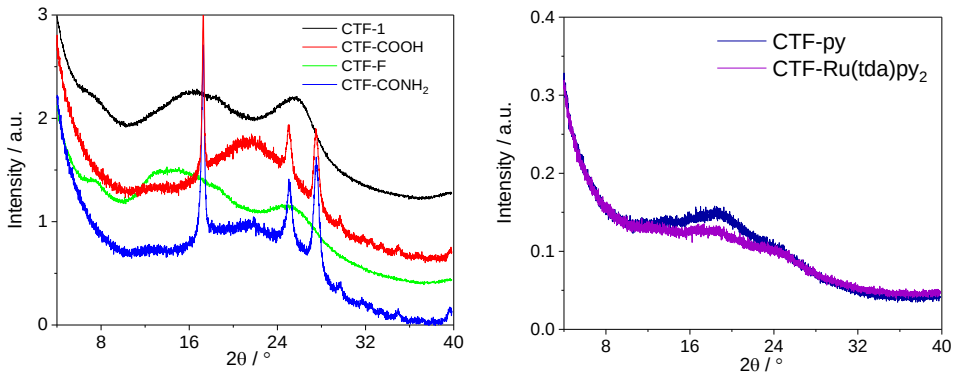

Figure S3. Powder X-ray diffraction (PXRD) patterns for CTF-1, CTF-COOH, CTF-F, CTF-$CONH_2$ on the left. On the right, CTF-py with and without Ru-WOC. As expected by the amorphous nature of CTFs, broadbands are predominant.

X-ray Photoelectron Spectroscopy (XPS): XPS measurements were performed at room temperature with a SPECS PHOIBOS 150 hemispherical analyzer (SPECS GmbH, Berlin, Germany)) in a base pressure of 5x10-10 mbar using monochromatic Al K_α radiation (1486.74 eV) as excitation source operated at 300 W. The energy resolution as measured by the FWHM of the Ag $3d_{5/2}$ peak for a sputtered silver foil was 0.62 eV.

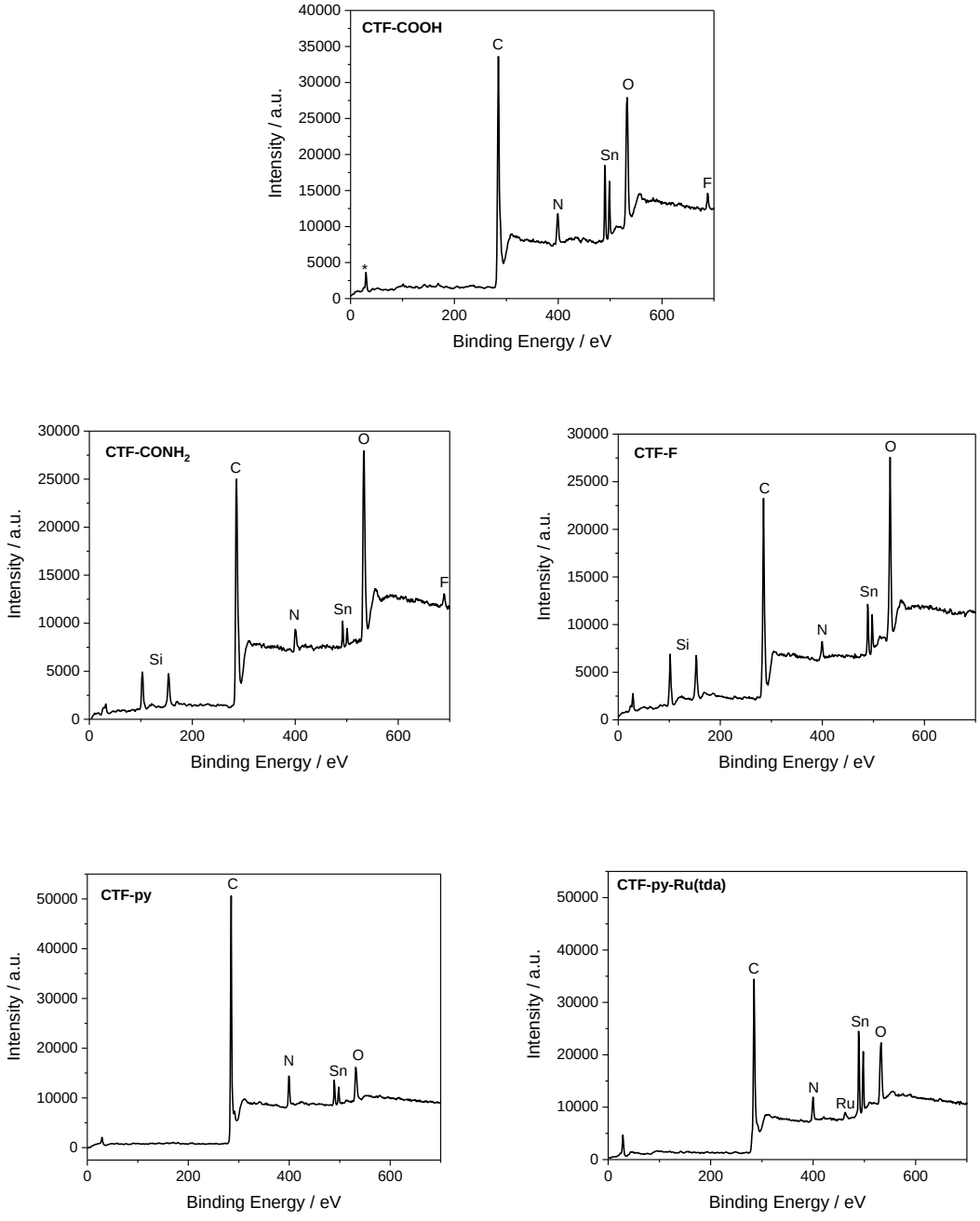

Figure S4. XPS surveys for CTF-COOH, CTF-F, CTF-CONH₂, CTF-py and CTF-py-Ru(tda). For the latter, elemental analysis resulted in 0.768% at. Ru. CTF-1 is missing from this analysis.

6.5.5 Optical bandgap characterization

Diffuse reflectance measurements: Lambda 1050 PerkinElmer spectrophotometer equipped with double beam optics, double monochromator, and D2 and W light sources were used together with a 150 mm Integrating Sphere with PbS and PMT detectors. Reflectance measurements were carried out on the photoelectrodes. Reflectance data were plotted as a Tauc plot by applying Kubelka–Mulk transformation.

Mott–Schottky analysis: curves were measured at a range of DC potential with an AC amplitude of 5 mV and a frequency of 500, 1000, and 2000 Hz under dark conditions in a conventional three-electrode cell. The measurements were carried out in the same potentiostat as previously described to calculate the flatband potential.

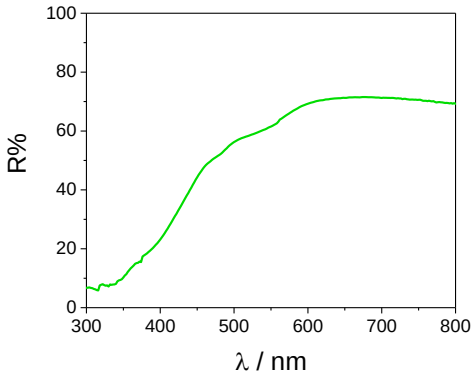

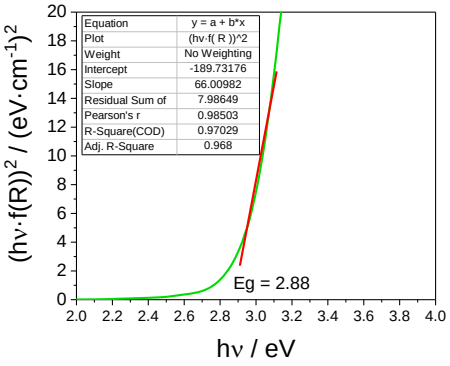

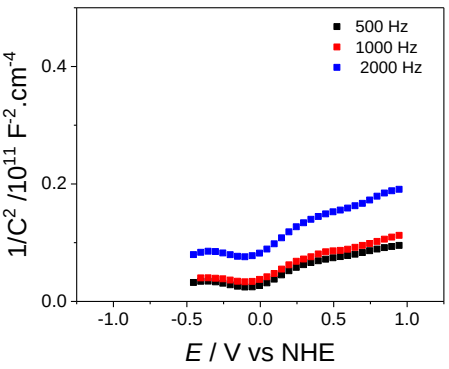

E_g	2.88 eV = 2.88 V
E_{fb} ≈ **CB**	-1.121 V vs NHE
VB	1.759 V vs NHE

Figure S5. Reflectance spectra (top left); Tauc plot and bandgap calculation (top right); Mott–Schottky plots of the CTF-COOH electrode in 0.1 M pH 7 phosphate buffer (bottom left), and the band structure of CTF-COOH (table).

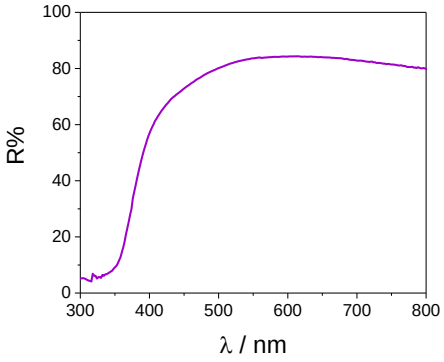

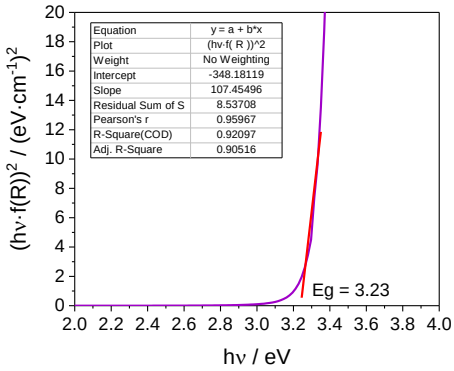

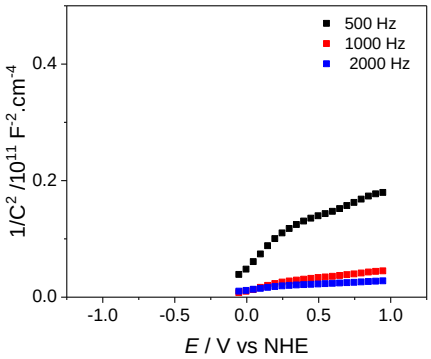

E_g	3.23 eV = 3.23 V
E_{fb} ≈ CB	-0.605 V vs NHE
VB	2.625 V vs NHE

VI

Figure S6. Reflectance spectra (top left); Tauc plot and bandgap calculation (top right); Mott–Schottky plots of the CTF-F electrode in 0.1 M pH 7 phosphate buffer (bottom left), and the band structure of CTF-F (table).

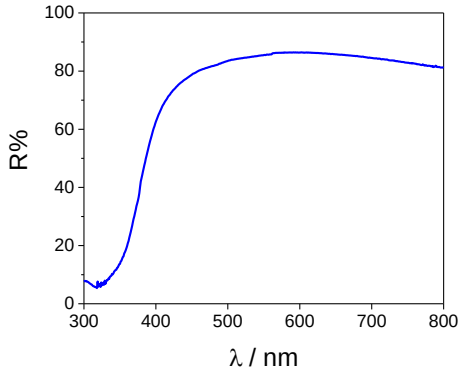

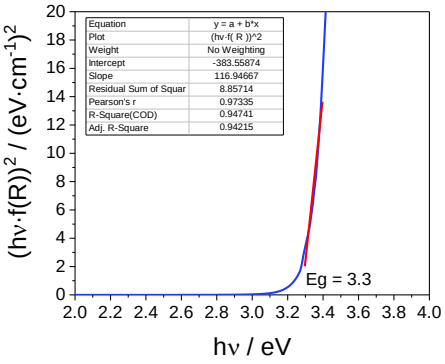

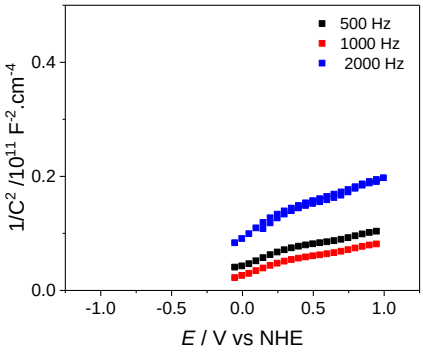

E_g	3.3 eV = 3.25 V
E_{fb} ≈ CB	-0.551 V vs NHE
VB	2.749 V vs NHE

Figure S7. Reflectance spectra (top left); Tauc plot and bandgap calculation (top right); Mott–Schottky plots of the CTF-CONH₂ electrode in 0.1 M pH 7 phosphate buffer (bottom left), and the band structure of CTF-CONH₂ (table).

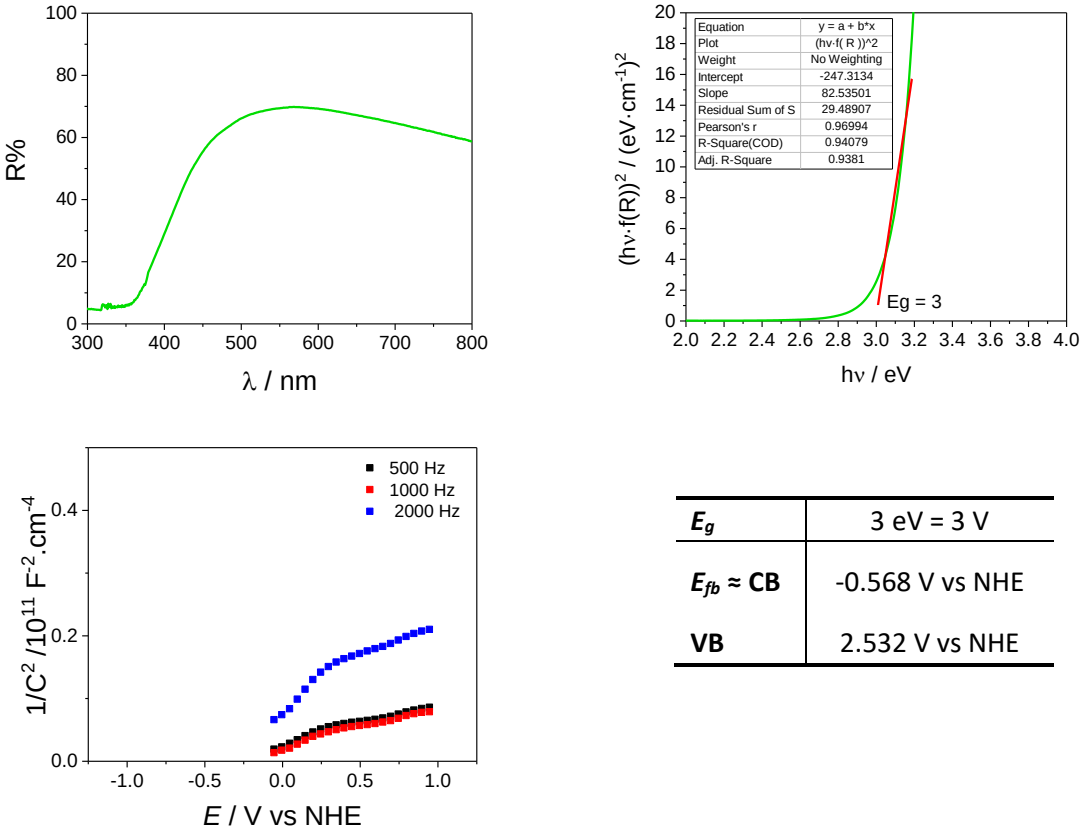

E_g	3 eV = 3 V
E_{fb} ≈ **CB**	-0.568 V vs NHE
VB	2.532 V vs NHE

Figure S8. Reflectance spectra (top left); Tauc plot and bandgap calculation (top right); Mott–Schottky plots of the CTF-1 electrode in 0.1 M pH 7 phosphate buffer (bottom left), and the band structure of CTF-1 (table).

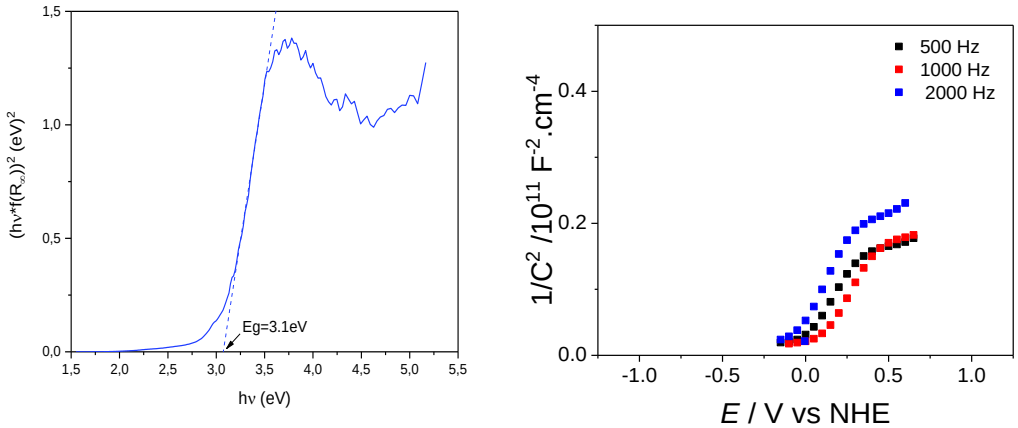

E_g	3.1 eV = 3.1 V
E_{fb} ≈ **CB**	-0.3 V vs NHE
VB	2.8 V vs NHE

Figure S9. Tauc plot and bandgap calculation (left); Mott–Schottky plots of the CTF-py electrode in 0.1 M pH7 phosphate buffer (right), and the band structure of CTF-1 (table).

6.5.6 (Photo)electrochemical characterization

Electrochemical characterization: by Bulk Electrolysis (BE), and Electrochemical Impedance Spectroscopy (EIS). All the electrochemical and photoelectrochemical experiments were performed in a pH 7 phosphate buffer (ionic strength = 0.1 M) and using a hand-made one-compartment Teflon cell. The prepared photoelectrodes were used as working electrodes (0.5 cm^2 exposed area), Pt wire as the counter electrode, Hg/Hg_2SO_4 (K_2SO_4 sat.) as the reference electrode. IJ-Cambria CHI-730D potentiostat was used to control the working system, and the copper tape pasted on the edge of FTO made the connection between the photoelectrodes and the potentiostat. A Xe lamp (150 W) from ABET technologies (Abet LS150) provided the light irradiating the samples, and the illumination intensity was calibrated by a commercial silicon photodiode at 100 $mW \cdot cm^{-2}$ (1 sun). Chopped light BE was performed at a constant potential of 0.8 V *vs.* NHE in 0.1 M pH 7 phosphate buffer electrolyte. The data for Mott–Schottky plots was obtained from applying a certain range of DC potential with an AC amplitude of 5 mV at a frequency of 500, 1000, and 2000 Hz under dark conditions in the same electrochemical set-up abovementioned.

Figure S10. Photography of the custom-made Teflon cell used for the (photo)electrochemical experiments (adapted from[2]).

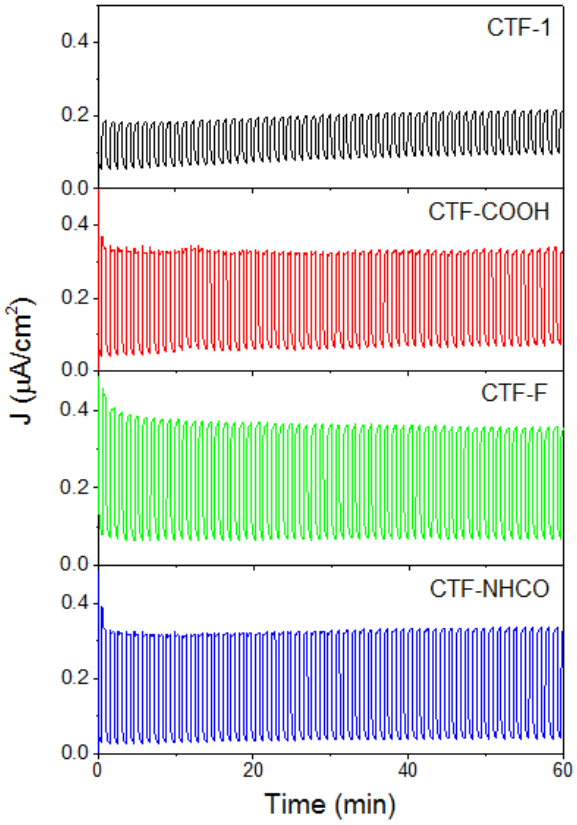

Figure S11. Bulk electrolysis with chopped light at the thermodynamic potential for water oxidation (0.8 V) for four types of photoelectrodes (CTF-1, CTF-COOH, CTF-F, and CTF-CONH₂) at pH 7 buffer electrolyte.

6.5.7 Loading of the water oxidation catalyst

CTF-py-Ru(tda): 25mg of CTF-py and 5mg of [Ru(tda)(dmso)py] catalyst were placed in a 25mL two-neck round bottom flask and vacuum-flushed with N_2. A degassed mixture of 5 mL of ethanol and 5 mL of methanol was added and the resulting solution was heated at reflux for 3 days. Afterward, a precipitated solid appeared, which was washed with methanol and centrifuged several times until the methanol was colorless. The powder was then washed with diethyl ether and dried at room temperature. Around 15mg of a brown solid was obtained.

Study of the loading by Cyclic Voltammetry (CV): Prior to experiment, the functionalized CTF was adsorbed on multi-walled carbon nanotubes (CNTs) to increase the signal's intensity. Firstly, a solution of CNT was prepared by sonicating 5 mg of CNTs in 5 mL of THF for 60 minutes. In parallel, 0.5 mg of CTF-py-Ru(tda) was sonicated in 0.2 mL of diethylether. Then, 0.2 mL of the CNT solution were added and sonicated for 10 min. Finally, the obtained mixture was drop-cast on glassy carbon (GC) electrodes and left to air dry. Afterward, CV experiments were performed with a CHI660D potentiostat in a

three-electrode one-compartment cell with CTF-py-Ru(tda)@CNT@GC as Working Electrode (WE), a platinum disk as the Counter Electrode (CE), and Hg/Hg_2SO_4 as the Reference Electrode (RE) in a pH 7 phosphate buffer solution. All the potentials are reported vs NHE by adding 0.65 V to the measured potential. The surface coverage (Γ) of the complex on the WE was estimated by applying the formula:

$$\Gamma\ (mol \cdot g^{-1}) = \frac{Q}{n \cdot m \cdot F} \qquad \text{(Equation S1)}$$

Q is the charge under the oxidative peak of the reversible, one-electron wave obtained by integration of the CV (Figure 6). *n* is the number of electrons involved in that oxidation process, which is 1 (Ru^{II} to Ru^{III}). *m* is the hybrid catalyst mass on the electrode and *F* is the Faradaic constant (96,485 $C \cdot mol^{-1}$).

VI

6.5.8 Oxygen evolution experiments

Irradiation was provided by a Xe lamp (150 W) from ABET technologies (Abet LS150), and the illumination intensity was calibrated by a commercial silicon photodiode at 100 $mW \cdot cm^{-2}$ (1 sun). The temperature was kept at 25 °C by a PolyScience temperature controller using water as a cooling agent.

Clark electrode: Experiments were conducted in a 4 mL cell closed with a septum and equipped with a mantle for temperature control. Oxygen evolution was measured in the gas phase using an NPOX709552 Clark electrode by Unisense. For a typical experiment, $2mg \cdot mL^{-1}$ in 2 mL phosphate buff pH 7 (25 mM aqueous) were sonicated until the formation of a homogeneous colloidal solution. Afterward, 10 mM of $Na_2S_2O_8$ was added in the dark. Then, the cell was closed with a septum and the solution was stirred and degassed by bubbling nitrogen for at least 30 min. Subsequently, the Clark electrode was introduced and the temperature control started (25°C). After equilibration of the system irradiation was started. After photocatalysis, the Clark electrode was calibrated. Calibration consisted of different injections of µL O_2 in the headspace. Calibrations were analyzed assuming that the ideal gas law applies. Initial Turnover Numbers (TONs) were calculated as the quotient of the total amount of O_2 produced and the amount of water oxidation catalyst at the start of the irradiation.

Turnover Number (TON): The turnover number is defined as the number of mols of substrate transformed by 1 mol of both forms of the Ru-tda present on the surface of the colloidal photocatalyst:

$$TON = \frac{\text{mols } O_2}{mols\ WOC} = \frac{3.1\ \mu\text{mols } O_2}{0.055\ \mu\text{mols WOC}} = 54 \quad \text{(Equation S2)}$$

Generator-Collector method:[2] The Generator-Collector method consists of placing two electrodes very near to each other (Figure S12). One of them will perform water oxidation (Generator) while the other is set to reduce the oxygen that is produced (Collector). In our setup, the photoanode (CTF) acts as an oxygen Generator. The Collector electrode consists of a clean FTO (sonicated for 15min in a saturated solution of KOH in 2-propanol, rinsed with water, and annealed for 30 min at 500 ˚C). Both electrodes are placed together with the conductive part facing the inner part of the set-up. Two small pieces of coverslip (Menzel-Gläser, 130-140µm of thickness) are used to keep a constant distance between both electrodes. Then the electrodes are covered with parafilm leaving lateral apertures on both sides to allow the solution to fill the inner space by capillarity forces (Figure S12). Finally, the reference electrode is placed as near as possible to one lateral aperture. To select the optimal potential to reduce molecular oxygen in solution, several CVs in pH 7 were performed in aired and degassed solutions. A reduction peak controlled by diffusion can be observed in aired solution, reaching the maximum intensity at -0.455 V *vs.* NHE (Figure S13).

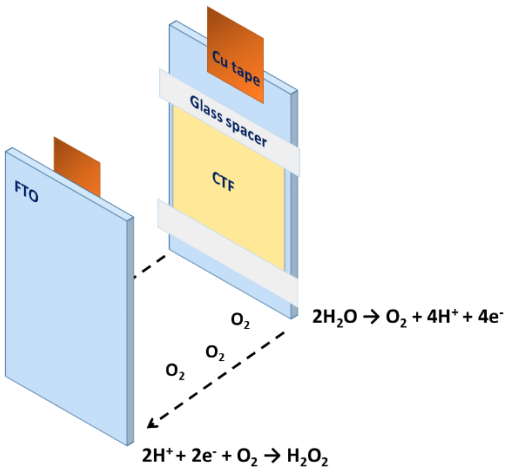

$$\eta(O_2) = \frac{-Q(WE2)}{Q(WE1)x\ \eta(calibration)} \quad \text{(Eq. S3)}$$

Figure S12. Generator CTF-X@FTO vs. FTO collector scheme illustrating the oxygen collection efficiency (described in Equation S3).

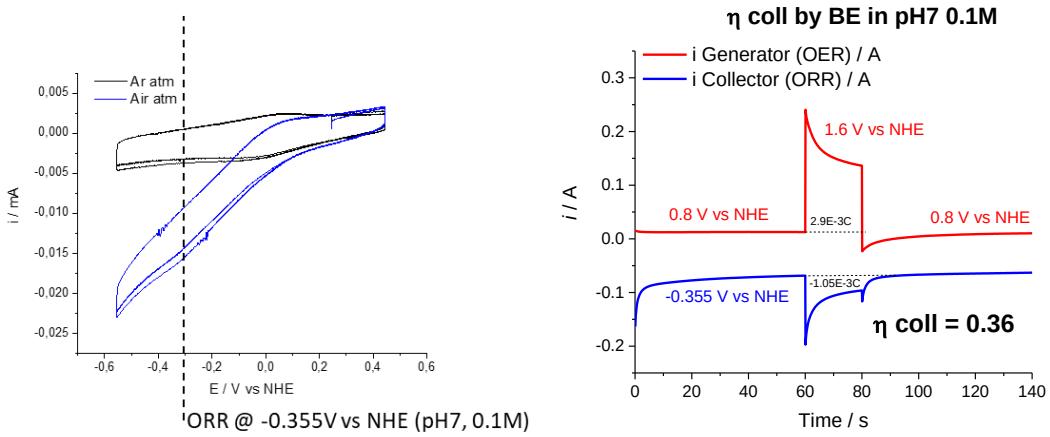

Figure S13. On the left, cyclic voltammetry of an FTO photoelectrode (WE) under argon (black) and air (blue) atmosphere to determine ORR potential (0.1 M pH 7 solution, Pt coil as CE and Hg/Hg_2SO_4 as RE). On the right, oxygen collection efficiency of 36% by comparing the charge passed through a CoOx@FTO generator (FE of 100%, in red) and the FTO collector (blue).

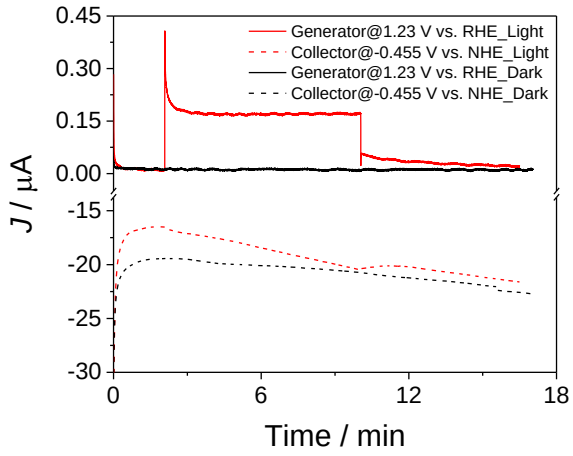

Figure S14. Generator CTF-COOH@FTO (straight lines) vs. FTO collector (dashed lines) under light (red) and dark conditions (black). The collector (FTO) always displayed greater amounts of charge compared to the generator.

6.5.9 References

(1) Ren, S.; Bojdys, M. J.; Dawson, R.; Laybourn, A.; Khimyak, Y. Z.; Adams, D. J.; Cooper, A. I. Porous, Fluorescent, Covalent Triazine-Based Frameworks Via Room-Temperature and Microwave-Assisted Synthesis. *Adv. Mater.* **2012**, *24* (17), 2357–2361. https://doi.org/10.1002/adma.201200751.

(2) Grau, S.; Berardi, S.; Moya, A.; Matheu, R.; Cristino, V.; Vilatela, J. J.; Bignozzi, C. A.; Caramori, S.; Gimbert-Suriñach, C.; Llobet, A. A Hybrid Molecular Photoanode for Efficient Light-Induced Water Oxidation. *Sustain. Energy Fuels* **2018**, *2* (9), 1979–1985. https://doi.org/10.1039/C8SE00146D.

Chapter 6.

VI

Chapter 7

Nanocrystal-molecular hybrids for the photocatalytic oxidation of water

The research results in this chapter are included in the following scientific publication:

Ventosa, M.; Oliveras, J.; Bastús, N. G.; Gimbert-Suriñach, C.; Puntes, V.; Llobet, A. Nanocrystal-Molecular Hybrids for the Photocatalytic Oxidation of Water. *ACS Appl. Energy Mater.* **2020**, *3* (10), 10008–10014. https://doi.org/10.1021/acsaem.0c01685.

Nanocrystal-molecular hybrids for the photocatalytic oxidation of water

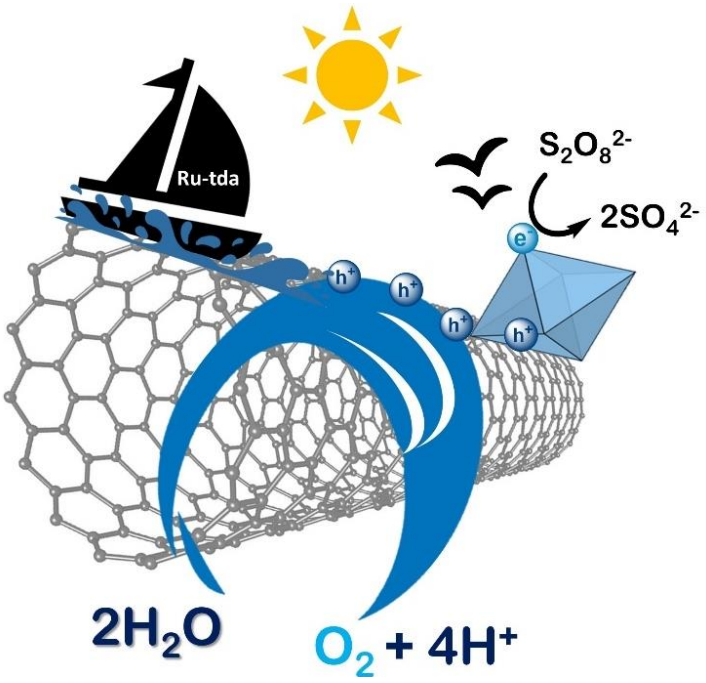

Abstract

A modular molecular hybrid colloidal photocatalyst composed by TiO_2 nanocrystals (TiO_2-NCs) as light-absorber and the molecular complex [Ru(tda)(pypyr)$_2$] (Ru-tda) as a water oxidation catalyst precursor, both anchored onto Single-Walled Carbon Nanotubes (SWCNTs) is described. This colloidal molecular hybrid photocatalyst, labeled as Ru-tda/SWCNT/TiO_2-NCs, is a robust material that can be easily prepared and scaled up. At neutral pH, in the presence of 3 suns illumination, the molecular hybrid material Ru-tda/SWCNT/TiO_2-NCs is capable of achieving the photocatalytic oxidation of water to dioxygen in the presence of persulfate, giving an unprecedented Turnover Number (TON) of 229.

Contributions:

Marta Ventosa synthesized [Ru(tda)(pypyr)$_2$], loaded it onto SWCNT/TiO$_2$-NCs, and characterized Ru-tda/SWCNT/TiO$_2$-NCs by photo(electro)chemistry.

7.1 Introduction

The health and the environmental impact of fossil fuel usage by modern societies have urged the scientific community to find alternative fuels that can sustain current energy demands using carbon-neutral, clean, and sustainable sources.[1] Inspired by nature, artificial photosynthesis aims at capturing and storing the energy from solar photons into chemical bonds, generating clean and sustainable fuels, that obtained in this manner are termed solar fuels.[2] Light-induced water splitting (hυ-WS), in which photons are stored into H-H and O-O bonds, can be considered a model case.[3] Many scientific challenges still need to be overcome to be able to implement hυ-WS as a widespread technology. One of the most critical challenges includes the performance of low-cost catalysts in terms of efficiency and stability, as well as their capacity to harmoniously interact with the light absorber.[4]

From a fundamental perspective, hυ-WS is a complex process involving a series of steps working in a synchronized manner, starting with the absorption of light, followed by charge separation, charge transfer, and finally, the corresponding Proton Reduction (PR) and Water Oxidation (WO) reactions. The WO reaction is particularly challenging because it involves the removal of four electrons and four protons from two water molecules and the formation of an O-O bond. Further, it is a thermodynamically very unfavorable reaction with a formal redox potential of 1.23 V *vs*. RHE.[5] Semiconductor Nanocrystals (NCs) with suitable bandgaps are excellent materials for light absorption and charge pair generation.[6] However, high quantum efficiencies are not always translated into high water splitting activity due to the slow kinetics of the coupled PR and WO. The slow chemical reactions act as a bottleneck that will ultimately lead to charge recombination and photodegradation of the semiconductor NCs.[7, 8]

Pure inorganic hybrid colloidal photocatalysts enclosed in aqueous reactor beds are highly promising due to their simplicity in reactor design, economic viability, and scalability.[9] These systems involve colloidal photocatalysts based on wide-bandgap semiconductor NCs on top of which specific metal oxide domains -such as iridium, ruthenium, nickel, or cobalt oxides- are deposited and employed as Water Oxidation Catalysts (WOCs), leading to improved Solar To Fuel conversion efficiencies (STF).[10-13]

Despite their interest, their functionality and stability are mostly limited to extreme pH,[14] which constraints their use in realistic scenarios.

To overcome these limitations, molecular catalysts based on transition metal complexes can be employed. For the case of WO, some coordination complexes have been reported with very high Turnover Frequencies (TOFs), up to 50,000 s^{-1}, and Turnover Numbers (TONs) higher than one million.[15-16] Their proper design also allows them to work at mild pH conditions, close or equal to neutral pH.[5] In this regard, the combination of highly active molecular catalysts and semiconductor NCs are promising candidates to perform solar-driven WO provided they have adequate electronic communication between them.[17] Besides, as has recently been shown for a related molecular hybrid system[18], the fast hole transfer between the absorber and the molecular catalyst can act as a protective shield for the absorbing material. Degradation can occur due to the highly reactive generated holes upon light-induced charge separation, avoiding the formation of reactive radical species, which are known to damage the TiO_2.[33, 36]

To combine molecular catalysts with semiconductor NCs different strategies have been employed. The most straightforward methodology involves the simple deposition (drop-casting, spin coating, etc.), which is based on van der Waal interaction. Despite its simplicity, it might suffer from catalyst leaching or bad electronic communication between components. A promising alternative is the direct linkage of the molecular catalyst on the surface of the semiconductor NCs employing organic linkers.[17,19] However, its performance will directly depend on the stability of the bond between the linker and the surface in aqueous solutions as has been described in the literature.[19, 20]

To overcome these limitations, we herein describe a molecular colloidal hybrid photocatalyst containing three different components, each selected according to its specific functionality (Figure 1). Suitable light-absorbing TiO_2-NCs[21] and an efficient molecular Ru complex[16] providing an efficient light absorption and fast WO kinetics were selected (Figure 1). Both were deposited onto Single-Walled Carbon Nanotubes (SWCNTs, see Figure S1), which work as charge transfer platforms favoring the catalytic process[22] due to their high conductivity (theoretically estimated to be 10^6 $S \cdot cm^{-1}$).[23]

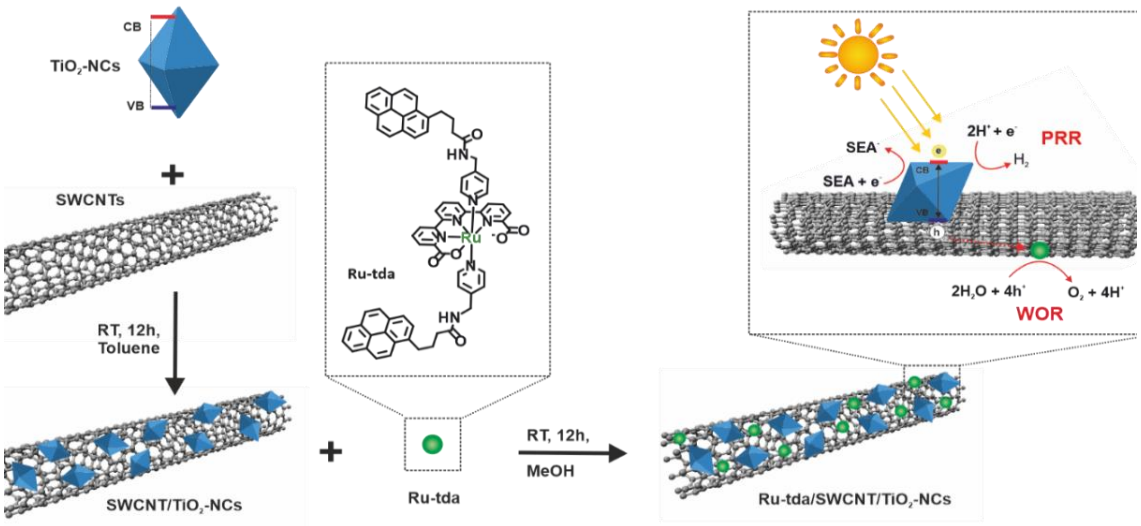

Figure 12. Schematic representation of the synthetic steps to obtain the colloidal photocatalyst Ru-tda/SWCNT/TiO_2-NCs, starting with the attachment of TiO_2-NCs to SWCNTs followed by the final loading of the molecular WOC. The upper right inset shows how the light-induced water oxidation reaction occurs on the particulates. TiO_2-NCs are responsible for absorbing the light and generate electrons and holes, which will diffuse through the SWCNT to the WOC and perform the desired water oxidation. On the other hand, the electrons will reduce protons, PR, or the sacrificial electron acceptor, SEA.

VII

7.2 Results and discussion

Highly monodisperse TiO_2 anatase tetragonally distorted square bipyramidal NCs of 9.3 ± 1.5 nm edge and 15.4 ± 1.8 nm diagonal (Figure S2-S4) with a high-intense UV light absorption spectra were synthesized following a non-aqueous surfactant-assisted approach previously reported by Murray and co-workers.[21] In that approach, TiO_2-NCs were obtained by injecting a 1:1 mixture of TiF_4:$TiCl_4$ solutions in a liquid mixture of surfactants and co-reagents under a controlled atmosphere. The use of TiF_4 as a precursor leads to reduced (substoichiometric) TiO_2 (TiO_{2-x}, $0 < x < 0.2$) NCs with a high percentage of highly active {101} facets and a large number of oxygen vacancies.[24] This is translated into a deep-blue color colloidal solution and reported as more photoactive than stochiometric TiO_2.[24-25]

Representative images of transmission electron microscopy (Figure 2A-B) of as-obtained TiO_2-NCs reveal highly uniform particles with well-defined morphologies. Optical characterization by UV-Vis spectroscopy shows a sharp absorption edge at 300 nm (3.2 eV), which broadens beyond this wavelength into the visible region, as manifested by the deep-blue color (Figure S3).[26, 27] Structural characterization by X-ray diffraction (Figure S4) shows well-defined peaks accordingly with the high crystallinity of the

sample. Crystal texture is observed in the relative enhanced intensity of 37.5° and 48° peaks, corresponding to the elongation of the "*a*" axis forming the bipyramids. Broadening of the peaks is attributed to finite crystal size and defects in the crystal structure as a result of the oxygen vacancies.[21, 25]

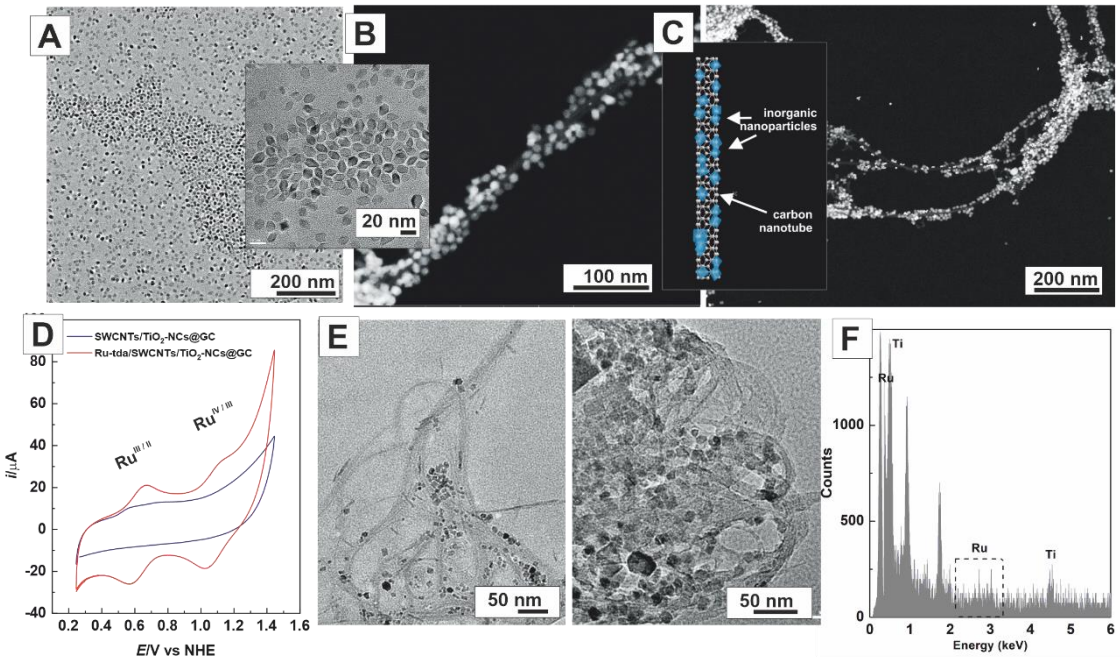

Figure 2. A) Representative Transmission Electron Microscopy (TEM) images of as-synthesized TiO_2 anatase square bipyramidal NCs. B) High magnification HAADF-STEM microscopy of the SWCNT/TiO_2-NCs. C) Schematic representation of the SWCNT/TiO_2-NCs hybrid structure. D) Cyclic Voltammetry at scan rate of 100 mV·s^{-1} in pH 7 phosphate buffer solution (I = 0.1M) from 0.25 to 1.45 V (vs NHE). In blue, a blank of SWCNT/TiO_2-NCs drop-cast on glassy carbon, GC, as the working electrode, and in red the freshly prepared Ru-tda/SWCNT/ TiO_2-NCs on GC as a working electrode. In both cases, Pt was used as the counter electrode and Hg/Hg_2SO_4 as the reference electrode. E) TEM microscopy of the Ru-tda/SWCNT/TiO_2-NCs hybrid structure. F) EDX spectra from the sample in E revealing the presence of atomic Ru in the hybrid structures.

After purification, TiO_2-NCs were mixed at room temperature with a suspension of SWCNTs in a methanolic solution. The decrease in surfactant concentration results in the progressive depletion of surfactant in the NCs' surface, destabilizing the system favoring aggregation. In a control experiment, NCs slowly aggregate in a relatively long period (> 6 h) in these conditions. The addition of SWCNTs to the system allows the NC naked surfaces to attach to them in a randomly distributed manner before aggregation takes place. As can be seen in Figures 2B and S5, the process leads to SWCNTs homogeneously coated with high densities of TiO_2-NCs ($3 \cdot 10^{15}$ NCs·mg^{-1} SWCNT), in the *c.a.* 80% of the SWCNT coated surface (see supporting information for details). Remarkably, the SWCNT/TiO_2-NCs structures can undergo ultra-sonication in a bath for up to 6 h without any observable NCs detachment or change in morphology. This

endurance experiment corroborates the stable and robust contact between both species indicating their direct contact, as microscopy analysis reveals (Figure 2B-C). The method is fast, straightforward, versatile, highly reproducible, and scalable, thereby representing an exciting approach for the modular development of inorganic carbon-supported hybrid structures.

As molecular Water Oxidation Catalyst (WOC) precursor in this work we used the Ru complex [Ru(tda)(pypyr)$_2$], where tda^{2-} = [2,2':6',2''-terpyridine]-6,6''-dicarboxylato and pypyr = 4-(pyren-1-yl)-N-(pyridin-4-ylmethyl)butanamide) reported earlier[9] and abbreviated as "Ru-tda" from here on (inset Figure 1). The tda^{2-} ligand coordinates equatorially to the Ru metal center and is the key for achieving TOFs in the range of 8.000 s^{-1} at neutral pH, thanks to the capacity of one of the carboxylate groups to act as an intramolecular proton acceptor during the O-O bond formation step.[28-29] The axial positions are occupied by two pyridyl ligands that are functionalized with pyrene units, which are responsible for the anchoring on the SWCNTs via π,π-stacking interactions (Figure 1).[16] The anchoring process, schematically represented in Figure S1, consists of soaking the SWCNT/TiO_2-NCs material in a 1mM methanolic solution of the Ru-tda catalyst precursor. After 8 h of stirring, the sample was centrifuged and washed with methanol. The resulting molecular hybrids Ru-tda/SWCNT/TiO_2-NCs were analyzed by Cyclic Voltammetry (CV), Scanning Electron Microscopy (SEM), and Energy-Dispersive X-ray spectroscopy (EDX) (Figure 2D-F), confirming the successful incorporation of the ruthenium complex without changing neither the morphology of the SWCNT/TiO_2-NCs nor the molecular structure of the catalyst precursor. Particularly for the latter, CV experiments were very useful to electrochemically corroborate the presence of the molecular Ru compound on top of the conductive SWCNTs. By drop-casting the Ru-tda/SWCNT/TiO_2-NCs molecular hybrids onto a glassy carbon working electrode (see supporting information for details) and carrying out a CV at pH 7, two redox waves at $E_{1/2}$ = 0.61 V and $E_{1/2}$ = 1.06 V (vs. NHE) appeared, corresponding to the characteristic Ru(III/II) and Ru(IV/III) couples, respectively (Figure 2D).[28] We calculated coverage of Γ = $2.18 \cdot 10^{-8}$ $mol_{Ru} \cdot g_{molecular\ hybrid}^{-1}$, based on the charge under the anodic Ru(III/II) wave, which accounts for a ratio of 10^4:1 TiO_2-NCs:Ru-tda (see SI). A high ratio of

semiconductor NCs versus catalyst is desirable to perform light-induced water oxidation efficiently, as previously observed in photocatalytic molecular systems.[30-32]

The capacity of the new molecular hybrid material, Ru-tda/SWCNT/TiO_2-NCs, to catalytically oxidize water to dioxygen induced by light was assessed in a thermostated reactor at 25 ˚C, under 3 suns irradiation, using peroxydisulfate ($S_2O_8^{2-}$) as a Sacrificial Electron Acceptor (SEA) in a pH 7 phosphate buffer solution. Figure 3A displays the oxygen evolution profile in the presence (red trace) and the absence (blue trace) of the Ru-tda catalyst precursor under dark (light off, grey area) and light on conditions (yellow region). Once the sample is illuminated, electrons and holes are generated at the photoactive TiO_2-NCs and are used to induce the chemical reactions that are responsible for final oxygen evolution (Figure 3B).

In the absence of the Ru-catalyst, the SWCNT/TiO_2-NCs material upon illumination generates an increasing amount of oxygen during the first 50 minutes, via hydroxyl radical formation and its evolution (see Equations 4-8 in Table 1) as it has been previously described in the literature.[24, 33, 36] Then, during the next 2.5 h, the oxygen production continuously decreases until it fades away (see Figure 3A, blue trace). This is consistent with the existence of a competing reaction pathway that degrades the TiO_2 or blocks its surface for further photoactivity in the present working conditions.

On the other hand, in the presence of the Ru-tda catalyst precursor, the molecular hybrid material Ru-tda/SWCNT/TiO_2-NCs generates no net molecular oxygen during the first 30 minutes when compared to the blank. However, and in sharp contrast, there is a sustained generation of O_2 over time afterward. This induction period is associated with the generation of the catalyst active species from the catalyst precursor as indicated in Equations 3a-c in Table 1, where the precursor is progressively oxidized from Ru(II) to Ru(IV). The latter coordinates to a solvent OH^- generating a Ru seven-coordinated species, [Ru^{IV}(O)(tda)(pypyr)$_2$] (abbreviated as Ru^{IV}(O)-tda), responsible for water oxidation catalysis. This is a process that has been described previously in the homogeneous phase and is known to be slow at pH 7.[28, 30] Therefore, the initial molecular hybrid material containing the catalyst precursor Ru-tda/SWCNT/TiO_2-NCs, is progressively transformed into a new catalytically active molecular hybrid material, Ru^{IV}(O)-tda/SWCNT/TiO_2-NCs, that is responsible for the light-induced water oxidation

catalysis. As mentioned earlier, the water oxidation to dioxygen reaction involves the removal of four H^+ and four e^- from two water molecules and the formation of an O-O bond. The sequence of reactions responsible for all these processes is outlined in Table 1, in Equations 3d-3h, and are shown in a simplified manner with the green arrows in the energy scheme illustrated in Figure 3B. The key for this fast WO reaction is the Ru-tda catalyst that is driven by the photogenerated holes from the valence band of the TiO_2-NCs. Electrochemically, the Ru-tda catalyst has been shown to turn at the range of 8.000 s^{-1} at pH 7. On the cathodic side, a large excess of peroxydisulfate is reduced to sulfate by the photoexcited electrons in the conduction band of the TiO_2 (Equations 4, 5a-c in Table 1 and solid red arrows in Figure 3B).

The fact that under the presence of Ru complex the photoactivity of the TiO_2 moiety is maintained throughout 2.7 h indicates that the Ru complex acts as a protecting agent for the surface of TiO_2. Firstly, by avoiding the formation of $HO^{\cdot}$ and secondly, by reacting very fast with the holes generated upon excitation, thus avoiding TiO_2 surface degradation. The latter is a phenomenon that has recently been reported that occurs in the time scale of 300 fs in related systems.[18]

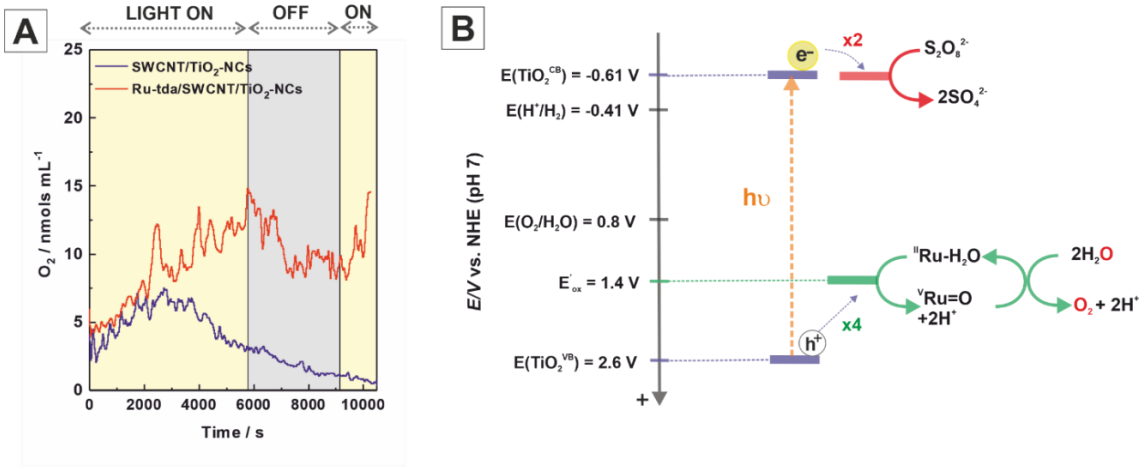

Figure 3. A) Oxygen evolution profile obtained during illumination of a mixture containing 2 mg·mL^{-1} Ru-tda/SWCNT/TiO_2-NCs (red) or 2 mg·mL^{-1} SWCNT/TiO_2-NCs (blue) in a photocatalytic reactor thermostated at 25 ˚C, under 3 suns irradiation, and using 10 mM $Na_2S_2O_8$ as a sacrificial electron acceptor in a pH 7 phosphate buffer solution (I = 0.1 M); B) schematic representation of the charge carrier dynamics and main reactions upon illumination.

	Reactions	*E / V vs NHE pH7*	*Eq.*
Water Oxidation (WO)	$2H_2O + 4h^+ \rightarrow O_2 + 4H^+$	0.82	(1)
Proton Reduction (PR)	$2H^+ + 2e^- \rightarrow H_2$	-0.41	(2)
Catalyst Precursor activation	Ru^{II}-tda + $h^+ \rightarrow Ru^{III}$-tda	0.61	(3a)
	Ru^{III}-tda + $h^+ \rightarrow Ru^{IV}$-tda	1.06	(3b)
WO Catalyst (WOC) generation	Ru^{IV}-tda + $OH^- \rightarrow Ru^{IV}$(O)-tda + H^+		(3c)
WO Catalytic Cycle	Ru^{IV}(O)-tda + $h^+ \rightarrow Ru^{V}$(O)-tda	1.43	(3d)
	Ru^{V}(O)-tda + $H_2O \rightarrow Ru^{III}$(OOH)-tda + H^+		(3e)
	Ru^{III}(OOH)-tda + $h^+ \rightarrow Ru^{IV}$(OO)-tda + H^+		(3f)
	Ru^{IV}(OO)-tda + $H_2O \rightarrow Ru^{II}(H_2O)$-tda + O_2		(3g)
	$Ru^{II}(H_2O)$-tda + $2h^+ \rightarrow Ru^{IV}$(O)-tda + $2H^+$		(3h)
Sacrificial Electron Acceptor (SEA)	$S_2O_8^{2-} + e^- \rightarrow SO_4^{2-} + SO_4^{\cdot-}$		(4)
	$SO_4^{\cdot-} + e^- \rightarrow SO_4^{2-}$		(5a)
	$S_2O_8^{2-} + 2e^- \rightarrow 2SO_4^{2-}$		(5b)
	$2SO_4^{\cdot-} + H_2O \rightarrow 2SO_4^{2-} + OH^{\cdot}$		(5c)
Hydroxyl radical evolution	$2\ OH^{\cdot} \rightarrow H_2O_2$		(6a)
	$H_2O_2 \rightarrow 2H^+ + O_2 + 2e^-$	-0.11	(6b)
Oxygen Reduction (OR) on TiO_2^{CB}	$O_2 + 2H^+ + 2e^- \rightarrow H_2O_2$	-0.33	(7)
1 and 2e^- WO on TiO_2^{VB}	$H_2O + h^+ \rightarrow HO^{\cdot} + H^+$	2.39	(8)
	$2H_2O + 2h^+ \rightarrow H_2O_2 + 2H^+$	1.37	(9)

Table 1. Set of reactions occurring on the Ru-tda/SWCNT/TiO_2-NCs molecular hybrid under light irradiation in the presence of a sacrificial electron acceptor in an aqueous phosphate buffer solution at pH 7.

Remarkably, the hybrid material Ru^{IV}(O)-tda/SWCNT/TiO_2-NCs achieves 229 TONs (20 nmols of O_2) based on the Ru catalyst amount (see supporting information), which is the highest reported for these type of systems.[18] The apparent quantum yield (AQY) of the water oxidation reaction at pH 7 and 25 ˚C was measured to be approximately 0.07% at the peak of absorbance of TiO_2-NCs at λ = 325 ± 25 nm (SI in section *7.5.5*). On the one hand, this low value can be attributed to the large excess of light absorber versus catalyst and, on the other hand, to the high complexity of these systems. Similar quantum yields, 0.10-0.27%, have been recently reported for related hybrid molecular photocatalytic material using a Ru complex as WOC and CdS as a light absorber,[18] although in this case, TONs were below 1.

The large absorber excess versus molecular catalyst (10^4:1 TiO_2-NCs:Ru-tda) could help in promoting the light-induced oxidation of the catalyst into high oxidation states by multiple sites which is reminiscent of the quantasome that operates in the photosystem II of green plants and algae.[34-35] Further, this cooperation will be favored by the high mobility of the catalysts within the SWCNT surface as recently proposed for related Ru complexes.[35] In fact, given the large excess of absorber *vs*. molecular catalyst, the AQY is relatively high. This can be explained by the fact that all the TiO_2 moieties that are not accessible by the highly mobile anchored Ru will progressively lose their photoactivity, as we have observed in the blank experiment. Thus, they will not be involved in the light-harvesting process.[33, 36] Further it is worth mentioning that the amount of highly active Ru catalyst used is extremely low (2.2 $\mu g_{Ru} \cdot g_{molecular\ hybrid}^{-1}$), in line with the scarcity of that element on Earth and the need of a better atom-(circular) economy for the future.[37,38]

The low quantum yield also reflects the complexity of the system studied here where a large number of reactions are operating at the same time. For instance, back electron transfer from the Conduction Band (CB) to the Valence Band (VB) upon light-induced charge separation, will consume photons but will not lead to productive reactions. An additional challenge of single colloidal devices, as compared to typical two-compartment photoelectrochemical cells (PECs), is that oxidation and reduction reactions are not spatially separated. Therefore, it can lead to non-productive redox reactions that again will be responsible for a decrease in quantum efficiency.

7.3 Conclusions

The system presented here is remarkable because it is capable of overcoming all the challenges just described at neutral pH. Under these conditions, the molecular hybrid material Ru^{IV}(O)-tda/SWCNT/TiO_2-NCs achieves a remarkable TON of 229 upon illumination, which is the highest reported for this type of device,[18] thanks to favorable overall kinetics. Furthermore, obtained results can be considered a proof-of-concept of a modular approach that paves the way to develop molecular-NC hybrid photocatalysts for the production of clean and renewable fuels. This unique architecture allows rational adjustments of each component independently. Based on this tunability, future work will be focused on optimizing the system by controlling the loading of semiconductor NCs and catalyst onto SWCNTs or other graphitic surfaces (e.g., graphene, 3D aerographites…), and on adding a hydrogen evolution reaction (HER) catalyst for full water splitting. The modular approach reported here establishes a very versatile platform. Each of the constituting entities, such as the light absorber, the holder/communicator, and the catalyst, can be easily and independently replaced. For this reason, it is an optimal and efficient methodology for device discovery to foster the production of clean and renewable fuels.

7.4 References

(1) Lewis, N. S.; Nocera, D. G. Powering the Planet: Chemical Challenges in Solar Energy Utilization. *Proc. Natl. Acad. Sci.* **2006**, *103* (43), 15729–15735. https://doi.org/10.1073/pnas.0603395103.
(2) Barber, J. Photosynthetic energy conversion: natural and artificial. *Chem Soc Rev* **2009,** *38 1*, 185-96. https://doi.org/10.1039/b802262n.
(3) Tachibana, Y.; Vayssieres, L.; Durrant, J. R. Artificial photosynthesis for solar water-splitting. *Nat Photonics* **2012,** *6 8*, 511-518. https://doi.org/10.1038/nphoton.2012.175.
(4) Office of Basic Energy Sciences. *Report of the Basic Energy Sciences Roundtable on Liquid Solar Fuels*; Rockville, 2019. https://doi.org/10.2172/1615599.
(5) Berardi, S.; Drouet, S.; Francàs, L.; Gimbert-Suriñach, C.; Guttentag, M.; Richmond, C.; Stoll, T.; Llobet, A. Molecular Artificial Photosynthesis. *Chem. Soc. Rev.* **2014**, *43* (22), 7501–7519. https://doi.org/10.1039/C3CS60405E.
(6) Maeda, K.; Domen, K. Photocatalytic Water Splitting: Recent Progress and Future Challenges. *Journal of Physical Chemistry Letters* **2010,** *1 18*, 2655-2661. https://doi.org/10.1021/jz1007966.
(7) Osterloh, F. E. Inorganic nanostructures for photoelectrochemical and photocatalytic water splitting. *Chem Soc Rev* **2013,** *42 6*, 2294-320. https://doi.org/10.1039/c2cs35266d.
(8) Hisatomi, T.; Kubota, J.; Domen, K. Recent advances in semiconductors for photocatalytic and photoelectrochemical water splitting. *Chem Soc Rev* **2014,** *43 22*, 7520-35. https://doi.org/10.1039/c3cs60378d.
(9) Pinaud, B. A.; Benck, J. D.; Seitz, L. C.; Forman, A. J.; Chen, Z.; Deutsch, T. G.; James, B. D.; Baum,

K. N.; Baum, G. N.; Ardo, S.; Wang, H.; Miller, E.; Jaramillo, T. F., Technical and economic feasibility of centralized facilities for solar hydrogen production via photocatalysis and photoelectrochemistry. *Energy & Environmental Science* **2013,** *6 7*, 1983-2002. https://doi.org/10.1039/C3EE40831K.

(10) Chen, X.; Shen, S.; Guo, L.; Mao, S. S., Semiconductor-based photocatalytic hydrogen generation. *Chem. Rev.* **2010,** *110 11*, 6503-70. https://doi.org/10.1021/cr1001645.

(11) Wang, Z.; Li, C.; Domen, K. Recent developments in heterogeneous photocatalysts for solar-driven overall water splitting. *Chem. Soc. Rev.* **2019,** *48 7*, 2109-2125. https://doi.org/10.1039/c8cs00542g.

(12) Kudo, A.; Miseki, Y. Heterogeneous photocatalyst materials for water splitting. *Chem Soc Rev* **2009,** *38 1*, 253-78. https://doi.org/10.1039/b800489g.

(13) Maeda, K. Photocatalytic water splitting using semiconductor particles: History and recent developments. *Journal of Photochemistry and Photobiology C-Photochemistry Reviews* **2011,** *12 4*, 237-268. https://doi.org/10.1016/j.jphotochemrev.2011.07.001.

(14) Kibsgaard, J.; Chorkendorff, I. Considerations for the scaling-up of water splitting catalysts. *Nature Energy* **2019,** *4 6*, 430-433. https://doi.org/10.1038/s41560-019-0407-1.

(15) Matheu, R.; Garrido-Barros, P.; Gil-Sepulcre, M.; Ertem, M. Z.; Sala, X.; Gimbert-Surinach, C.; Llobet, A. The development of molecular water oxidation catalysts. *Nature Reviews Chemistry* **2019,** *3 5*, 331-341. . https://doi.org/10.1038/s41570-019-0096-0.

(16) Creus, J.; Matheu, R.; Peñafiel, I.; Moonshiram, D.; Blondeau, P.; Benet-Buchholz, J.; García-Antón, J.; Sala, X.; Godard, C.; Llobet, A. A Million Turnover Molecular Anode for Catalytic Water Oxidation. *Angew. Chem. Int. Ed.* **2016**, *55* (49), 15382–15386. https://doi.org/10.1002/anie.201609167.

(17) Willkomm, J.; Orchard, K. L.; Reynal, A.; Pastor, E.; Durrant, J. R.; Reisner, E. Dye-sensitised semiconductors modified with molecular catalysts for light-driven H2 production. *Chem Soc Rev* **2016,** *45 1*, 9-23. https://doi.org/10.1039/c5cs00733j.

(18) Wolff, C. M.; Frischmann, P. D.; Schulze, M.; Bohn, B. J.; Wein, R.; Livadas, P.; Carlson, M. T.; Jackel, F.; Feldmann, J.; Wurthner, F.; Stolarczyk, J. K. All-in-one visible-light-driven water splitting by combining nanoparticulate and molecular co-catalysts on CdS nanorods. *Nature Energy* **2018,** *3 10*, 862-869. https://doi.org/10.1038/s41560-018-0229-6.

(19) Materna, K. L.; Crabtree, R. H.; Brudvig, G. W. Anchoring groups for photocatalytic water oxidation on metal oxide surfaces. *Chem Soc Rev* **2017,** *46 20*, 6099-6110. https://doi.org/10.1039/c7cs00314e.

(20) Hyde, J. T.; Hanson, K.; Vannucci, A. K.; Lapides, A. M.; Alibabaei, L.; Norris, M. R.; Meyer, T. J.; Harrison, D. P. Electrochemical Instability of Phosphonate-Derivatized, Ruthenium(III) Polypyridyl Complexes on Metal Oxide Surfaces. *ACS Appl Mater Interfaces* **2015,** *7 18*, 9554-62. https://doi.org/10.1021/acsami.5b01000.

(21) Gordon, T. R.; Cargnello, M.; Paik, T.; Mangolini, F.; Weber, R. T.; Fornasiero, P.; Murray, C. B. Nonaqueous synthesis of TiO2 nanocrystals using TiF4 to engineer morphology, oxygen vacancy concentration, and photocatalytic activity. *J Am Chem Soc* **2012,** *134 15*, 6751-61. https://doi.org/10.1021/ja300823a.

(22) Zhang, N.; Yang, M. Q.; Liu, S.; Sun, Y.; Xu, Y. J. Waltzing with the Versatile Platform of Graphene to Synthesize Composite Photocatalysts. *Chem Rev* **2015,** *115 18*, 10307-77. https://doi.org/10.1021/acs.chemrev.5b00267.

(23) McEuen, P. L.; Park, J. Y. Electron transport in single-walled carbon nanotubes. *Mrs Bulletin* **2004,** *29 4*, 272-275. https://doi.org/10.1557/mrs2004.79.

(24) Diebold, U. The surface science of titanium dioxide. *Surface Science Reports* **2003,** *48 5-8*, 53-229. https://doi.org/10.1016/S0167-5729(02)00100-0.

(25) Gharagozlou, M.; Bayati, R., Photocatalytic activity and formation of oxygen vacancies in cation doped anatase TiO2 nanoparticles. *Ceram. Int.* **2014,** *40 7*, 10247-10253. https://doi.org/10.1016/j.ceramint.2014.02.114.

(26) Choudhury, B.; Choudhury, A. Oxygen defect dependent variation of band gap, Urbach energy and luminescence property of anatase, anatase–rutile mixed phase and of rutile phases of TiO2 nanoparticles. *Physica E: Low-Dimensional Systems and Nanostructures* **2014,** *56*, 364-371. http://dx.doi.org/10.1016/j.physe.2013.10.014.

(27) Liu, G.; Yang, H. G.; Wang, X. W.; Cheng, L. N.; Lu, H. F.; Wang, L. Z.; Lu, G. Q.; Cheng, H. M. Enhanced Photoactivity of Oxygen-Deficient Anatase TiO2 Sheets with Dominant {001} Facets.

Journal of Physical Chemistry C **2009,** *113 52*, 21784-21788. https://doi.org/10.1021/jp907749r.
(28) Matheu, R.; Ertem, M. Z.; Benet-Buchholz, J.; Coronado, E.; Batista, V. S.; Sala, X.; Llobet, A. Intramolecular Proton Transfer Boosts Water Oxidation Catalyzed by a Ru Complex. *J Am Chem Soc* **2015,** *137 33*, 10786-95. https://doi.org/10.1021/jacs.5b06541.
(29) Matheu, R.; Neudeck, S.; Meyer, F.; Sala, X.; Llobet, A. Foot of the Wave Analysis for Mechanistic Elucidation and Benchmarking Applications in Molecular Water Oxidation Catalysis. *ChemSusChem* **2016,** *9 23*, 3361-3369. https://doi.org/10.1002/cssc.201601286.
(30) Francàs, L.; Matheu, R.; Pastor, E.; Reynal, A.; Berardi, S.; Sala, X.; Llobet, A.; Durrant, J. R. Kinetic Analysis of an Efficient Molecular Light-Driven Water Oxidation System. *Acs Catalysis* **2017,** *7 8*, 5142-5150. https://doi.org/10.1021/acscatal.7b01357.
(31) Duan, L.; Xu, Y.; Zhang, P.; Wang, M.; Sun, L. Visible light-driven water oxidation by a molecular ruthenium catalyst in homogeneous system. *Inorg Chem* **2010,** *49 1*, 209-15. https://doi.org/10.1021/ic9017486.
(32) Xu, Y.; Fischer, A.; Duan, L.; Tong, L.; Gabrielsson, E.; Akermark, B.; Sun, L. Chemical and light-driven oxidation of water catalyzed by an efficient dinuclear ruthenium complex. *Angew Chem Int Ed Engl* **2010,** *49 47*, 8934-7. https://doi.org/10.1002/anie.201004278.
(33) Linsebigler, A. L.; Lu, G. Q.; Yates, J. T. Photocatalysis on Tio2 Surfaces - Principles, Mechanisms, and Selected Results. *Chem. Rev.* **1995,** *95 3*, 735-758. https://doi.org/10.1021/cr00035a013.
(34) Bonchio, M.; Syrgiannis, Z.; Burian, M.; Marino, N.; Pizzolato, E.; Dirian, K.; Rigodanza, F.; Volpato, G. A.; La Ganga, G.; Demitri, N.; Berardi, S.; Amenitsch, H.; Guldi, D. M.; Caramori, S.; Bignozzi, C. A.; Sartorel, A.; Prato, M. Hierarchical organization of perylene bisimides and polyoxometalates for photo-assisted water oxidation. *Nat Chem* **2019,** *11 2*, 146-153. https://doi.org/10.1038/s41557-018-0172-y.
(35) Zhan, S.; Ahlquist, M. S. G. Dynamics and Reactions of Molecular Ru Catalysts at Carbon Nanotube-Water Interfaces. *J Am Chem Soc* **2018,** *140 24*, 7498-7503. https://doi.org/10.1021/jacs.8b00433.
(36) Setvin, M.; Aschauer, U.; Hulva, J.; Simschitz, T.; Daniel, B.; Schmid, M.; Selloni, A.; Diebold, U. Following the Reduction of Oxygen on TiO2 Anatase (101) Step by Step. *J Am Chem Soc* **2016,** *138 30*, 9565-71. https://doi.org/10.1021/jacs.6b04004.
(37) Roduner, E. Size matters: why nanomaterials are different. *Chem Soc Rev* **2006,** *35 7*, 583-92. https://doi.org/10.1039/b502142c.
(38) Vesborg, P. C. K.; Jaramillo, T. F. Addressing the terawatt challenge: scalability in the supply of chemical elements for renewable energy. *Rsc Advances* **2012,** *2 21*, 7933-7947. https://doi.org/10.1039/c2ra20839c.

VII

7.5 Supporting information

7.5.1 Synthesis of Ru-tda/SWCNT/TiO2-NCs

Single-Walled Carbon Nanotubes (SWCNTs), Titanium(IV) chloride ($TiCl_4$), Titanium fluoride (TiF_4), Oleylamine (OlAm, Technical Grade, 70%), Oleic Acid (OlAc, Technical Grade, 90%), Octadecanol (1-ODE) and 2-Propanol were purchased from Sigma-Aldrich and used as received. Toluene and Methanol, technical grade were purchased from Fluka.

Highly monodisperse (9.27 ± 1.5 nm in side and 15.4 ± 1.8 nm in diagonal) TiO_2-NCs were synthesized using the method proposed by Murray *et al*.[21] Shape-controlled synthesis of TiO_2-NCs was achieved by non-aqueous surfactant-assisted synthesis using standard

Schlenk line techniques under an inert atmosphere. Briefly, in a 125 mL flask, 30 mmol of cosurfactant (OlAm) 10.2 mL of 1-ODE, and 1.5 mmol of Oleic Acid (OlAc) are combined and degassed at 120 °C for 1 h. After degassing the flask, 1.5 mL of the titanium precursor is added at 60 °C under argon atmosphere. Titanium precursor is in this specific case a 1:1 mixture of TiF_4 and $TiCl_4$ stock solutions (0.2M halogenated titanium compound, 1M OlAc in 1-ODE each) which have been mixed at equal volume inside the glovebox prior to use. Then, the solution is quickly heated to 290 °C, and the temperature is held for 10 min to allow the formation of seed crystals. An 8 mL portion of the stock solution is then pumped into the flask kept at 290 °C at 0.3 mL min^{-1} using a syringe pump. Afterward, the heating mantle is removed and the flask is left to cool naturally to ambient temperature. After the synthesis, the reaction contents are first diluted with a small volume of toluene and centrifuged at 6000 rpm to separate the NCs. The NCs are then re-dispersed through the addition of toluene, 100 µL of OlAm and sonication. Insoluble surfactant and agglomerated particles are removed through centrifugation. A mixture of 2-propanol and methanol is added to precipitate the NCs, and centrifugation at 6000 rpm is used to recover the NCs. This washing process is repeated twice and adjusted to a final volume of 20 mL of toluene.

For controlled NCs deposition onto SWCNTs, as-synthesized NCs were purified by centrifugation up to four times following the procedure above described and finally resuspended in the original volume of 20 mL of toluene. After, 1 mL of the purified NCs are diluted in 2 mL of toluene. To this solution, 0.25 mL of a single-walled carbon nanotubes solution (100 mg in 20 mL of toluene) was added and then left under stirring for 12 h. This method has proved to be scalable up to a total volume of 50 mL solution.

The synthesis of Ru-tda water oxidation catalyst precursor is reported in the literature.[16]

The Ru-tda catalyst precursor was anchored by soaking and stirring the SWCNT/TiO_2-NCs material in a 1mM methanolic solution of Ru-tda for 8 h. Then, the sample was centrifuged, and the pellets were washed three times with methanol for purification from non-anchored catalyst (Figure S1).

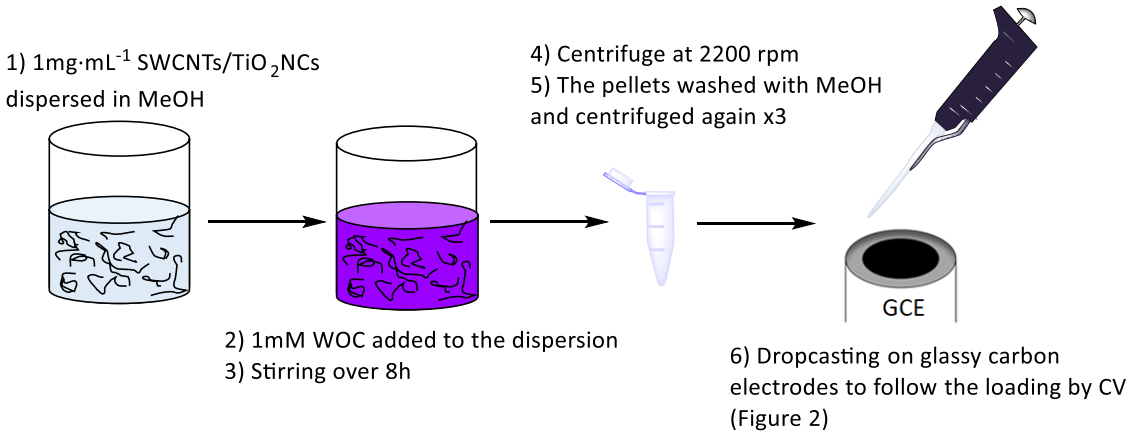

Figure S1. Sequence of operations followed for the preparation of catalyst precursor anchored on the graphitic area of the SWCNT/TiO_2-NCs.

7.5.2 Characterization techniques

The morphology of the TiO2-NCs was visualized using a JEM 1210, JEOL microscope in transmission mode operated at 120 kV. SWCNT/TiO_2-NCs and Ru-tda/SWCNT/TiO_2-NCs hybrids were observed by either using an FEI Magellan 400L XHR SEM, in transmission mode operated at 20 kV, or an FEI Tecnai G2 F20 HR(S)TEM operated at 200 kV in bright field mode. EDX of the sample was performed on an EDAX super ultra-thin window (SUTW) X-ray detector coupled to the Tecnai G2 F20 microscope.

Characterization of TiO2-NCs

The morphology of the NCs was visualized using a JEM 1210, JEOL microscope in transmission mode (TEM) operated at 120 kV. For the preparation of the sample, a droplet (10µL) of the sample was drop cast onto a piece of ultrathin carbon-coated 200-mesh copper grid (Ted-pella, Inc.) and left to dry in air. TEM images were used for the size distribution measurements. For each sample, the size of at least 100 particles was measured and the average size and standard deviation obtained (9.27±1.5 nm in side and 15.4±1.8 nm in diagonal), Figure S2 shows the size distribution histogram resulting from these measurements. UV–visible spectra were acquired with a Cary 60 spectrophotometer. A dilution of 1:10 in volume of as-synthesized NC solution in hexane was placed in a quartz cuvette and spectral analysis was performed in the 250–800 nm range at room temperature. Figure S2 shows TEM, High Angle Annular Dark Field – TEM (HAADF-TEM) and UV-Vis characterization of the samples. X-Ray Diffraction (XRD) data

were collected on a PANalytical X'Pert diffractometer using a Cu Kα radiation source (Figure S3).

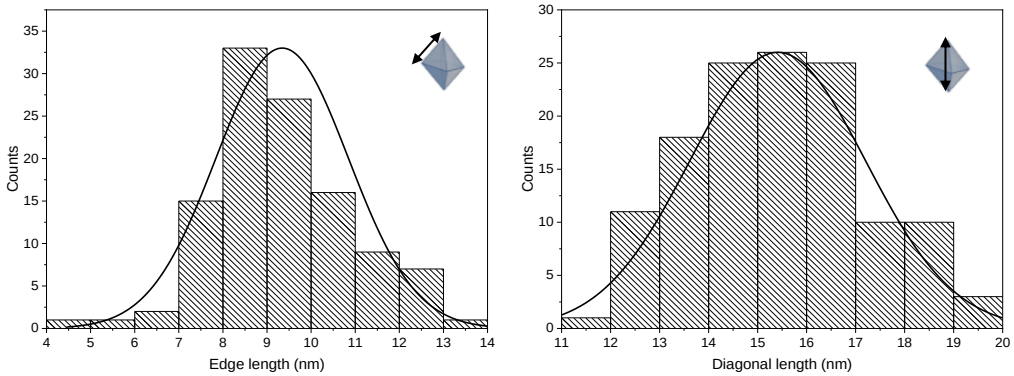

Figure S2. Histogram representing size distribution measurement for the TiO2-NCs side length (left) and diagonal (right).

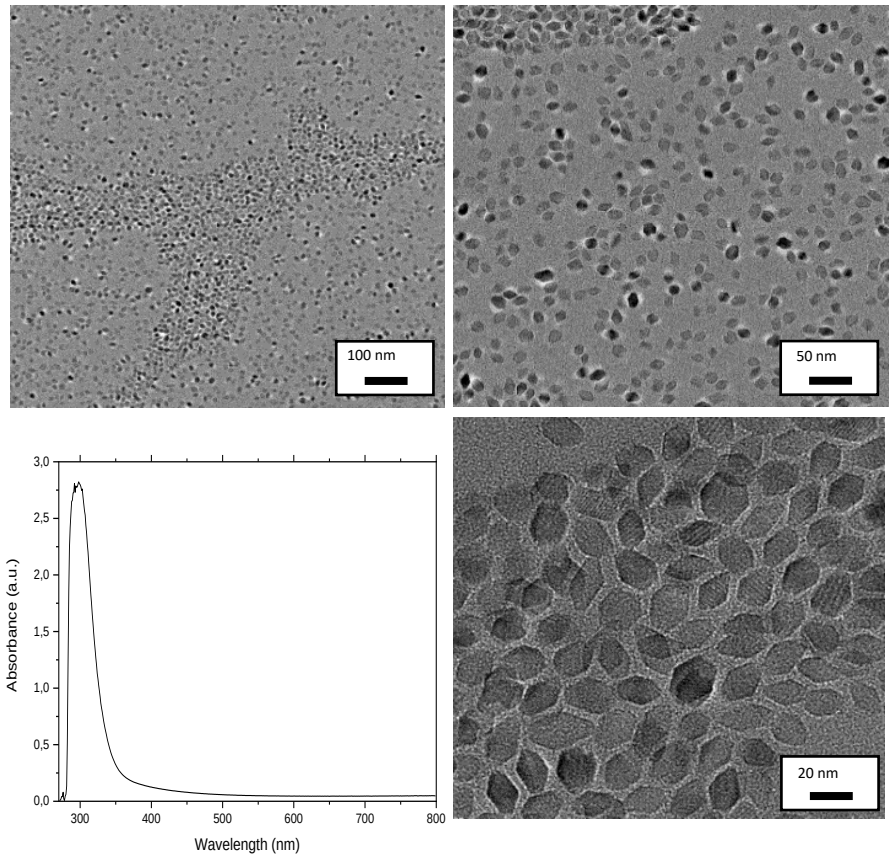

Figure S3. TEM (bright Field) of the TiO_2-NCs at different magnifications. At the bottom left, UV-Vis spectra of the sample.

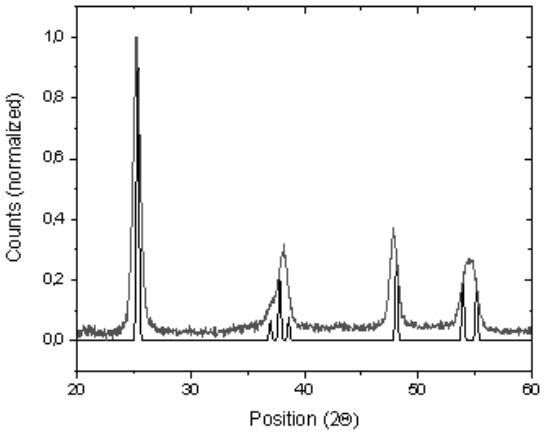

Figure S4. Experimental (gray trace) and theoretical (black trace) XRD Spectra of TiO_2 anatase NCs.

Characterization of SWCNT/TiO_2-NCs

The SWCNT/TiO_2-NCs were observed by TEM, as previously described, and by using an FEI Magellan 400L XHR SEM, in transmission mode operated at 20 kV. A droplet (10 µL) of a 1:5 dilution of the samples was ultrasonicated for 5 minutes, drop cast onto a piece of ultrathin carbon-coated 200-mesh copper grid (Ted-pella, Inc.) and left to dry in air.

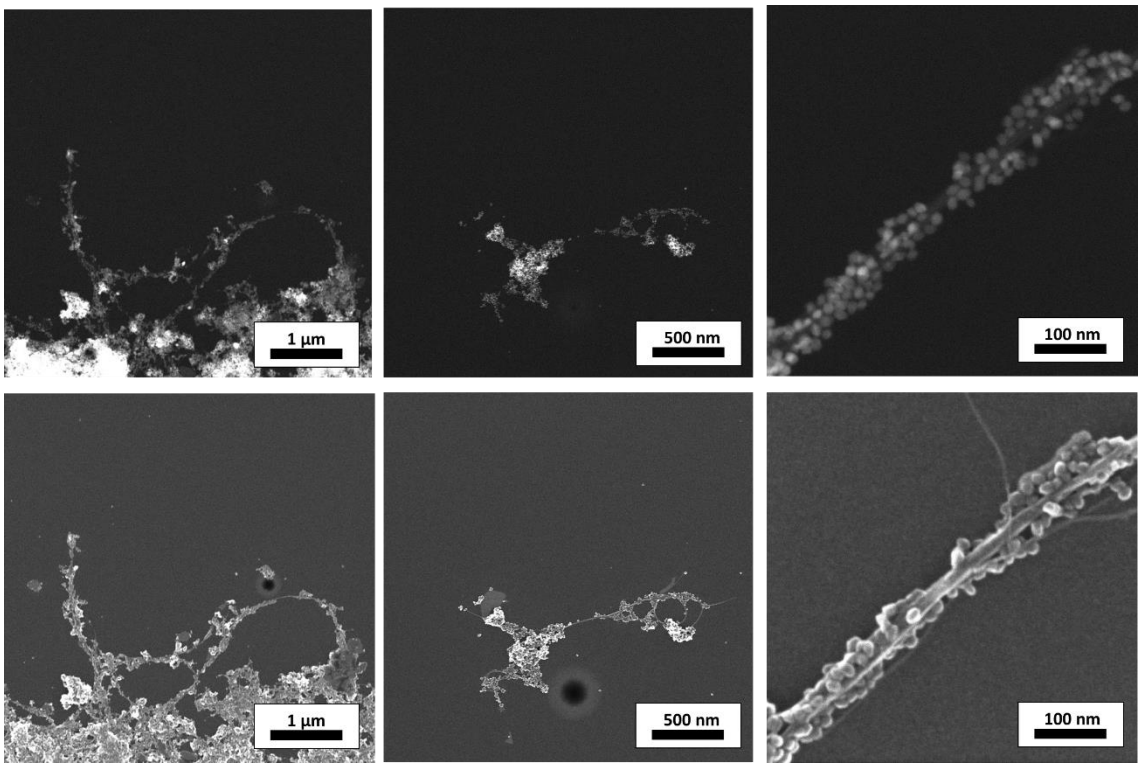

Figure S5. Top of the image: TEM HAADF imaging of the hybrid at different magnification. Corresponding SEM below.

Characterization of Ru-tda/SWCNT/TiO_2-NCs

The microscopy characterization before photocatalysis of the colloidal molecular hybrid is displayed in Figure 2 in the main manuscript. After photocatalysis, the integrity of the Ru^{IV}(O)-tda/SWCNT/TiO_2-NCs is shown in the SEM and EDX displayed in Figure S6.

The formation bundles and the appearance of metal traces might be due to the desiccation and preparation of the samples for characterization. Nevertheless, the latter are not responsible for O_2 generation as evidenced by blank experiments.

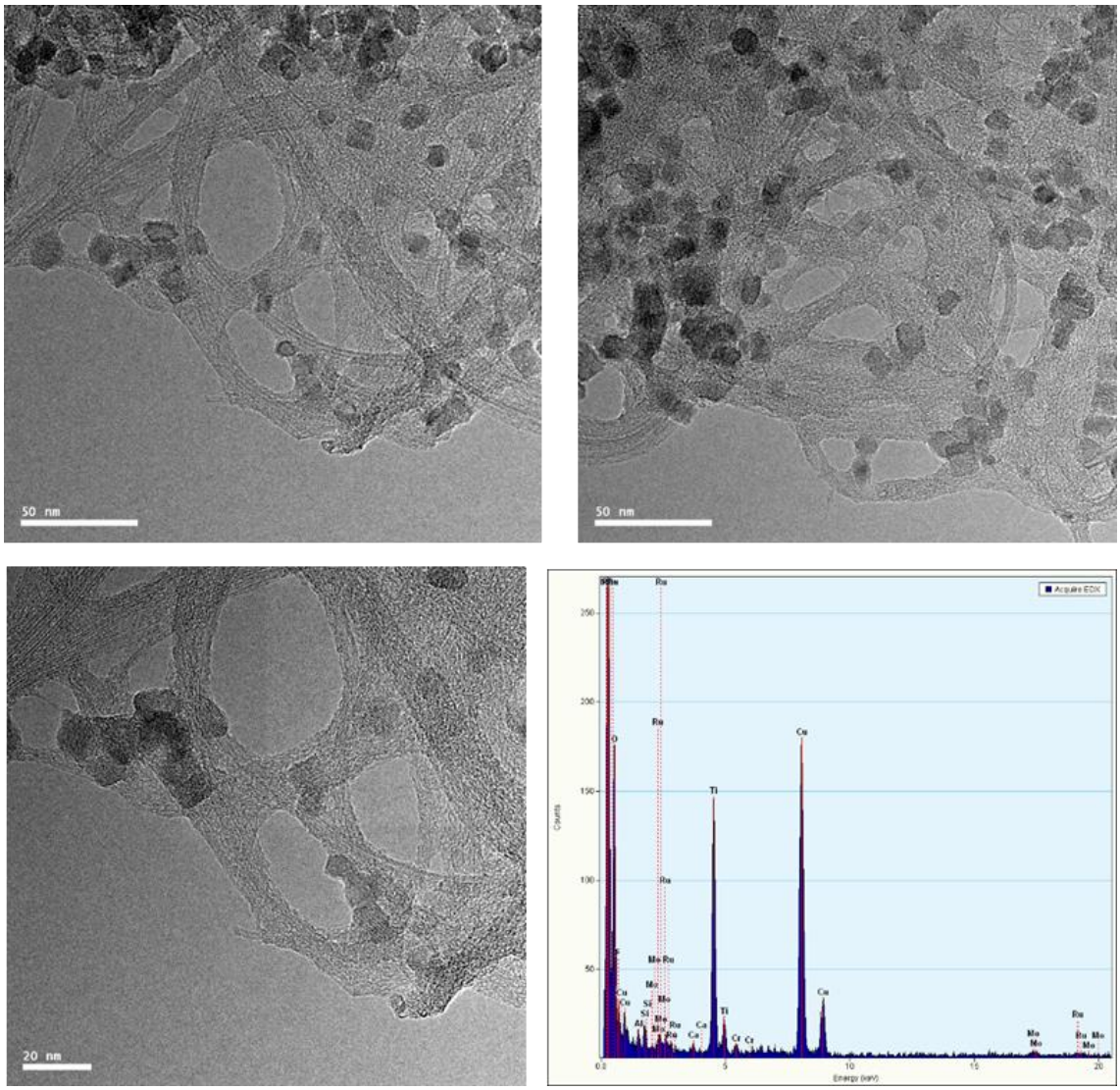

Figure S6. Top of the image: SEM of the TiO_2-NCs at different areas. Below, SEM at higher magnification and its corresponding EDX spectra.

7.5.3 Electrochemical methods

Buffer solutions at pH 7 were prepared with Na_2HPO_4 and NaH_2PO_4 and adjusted to 0.1 M ionic strength. Cyclic voltammetry experiments were performed with a CHI660D potentiostat in a one-compartment cell, three-electrode system using platinum disk as the counter electrode (Ø = 3 mm) and mercury-mercurous sulfate, Hg/Hg_2SO_4, as a reference electrode. The working electrode consisted of Ru-tda/SWCNT/TiO_2-NCs on top of a glassy carbon (GC) disk (Ø = 3 mm). The preparation of the working electrode was done following a dropcasting methodology. The as-prepared photocatalyst was dissolved in THF (50mg·mL^{-1}) and the colloidal solution was stirred until homogeneity. Subsequently, 25 µL of the solution were dropcasted 3 times onto previously polished glassy-carbon electrodes and left to air dry (Figure S1).

Photocatalytic experiments

O_2 detection was performed in a liquid phase by a Clark-type electrode (custom-made DW2/2 electrode chamber equipped with quartz glass, Hansatech Instruments®). The electrode was calibrated with saturated and non-saturated O_2 aqueous solutions at 25˚C before the photocatalytic experiment.

In a glass vial, 4 mg of Ru-tda/SWCNT/TiO_2-NCs or SWCNT/TiO_2-NCs were added to a 2 mL pH 7 phosphate buffer solution (25 mM). The mixture was sonicated until a dispersed colloidal suspension was formed. The suspension was transferred to a water-jacketed 2 mL chamber (Hansatech® Instruments) in the dark and $Na_2S_2O_8$ was added to give a final concentration of 10 mM and reaching a final ionic strength of the solution of 0.1 M. The cell was sealed with a Teflon cap with a double septum and the solution was bubbled with N_2. Afterward, the data was recorded both in the dark and under irradiation keeping the mixture at 25˚C. Post-normalization of the data was performed in order to subtract O_2 background.

The light source used was a 150 W Xe Arc Lamp previously calibrated to “3 suns” with a Si photodiode.

7.5.4 Ratios and concentration calculations

Calculation on the mass of a theoretical TiO2-NCs

Geometrical data (nm)			*Volume (nm^3) [$d_1 \cdot d_2 \cdot h/3$]*	*Density (mg/nm^3)*	*Mass of 1 NC (mg)*
d_1	d_2	h			
10	10	15	500	$4{,}23 \cdot 10^{-18}$	$2{,}115 \cdot 10^{-15}$

Table S1. Geometrical data given by the previous characterization and density of TiO2 allow the calculation of the mass of a single model TiO2 NCs.

Calculation of TiO_2-NCs in the colloidal solution

$$\frac{TiO_2NCs}{mL} = \frac{\frac{m_{TiO_2}}{m_{NC}}}{20mL} = \frac{\frac{91mg\ Ti\ in\ precursor \cdot \frac{79.866 \frac{mgTiO_2}{mmol}}{47.867 \frac{mg\ Ti}{mmol}}}{2.115 \cdot 10^{-15}}}{20mL} = 3.66 \cdot 10^{15} TiO_2NCs/mL$$

(Equation S1)

Calculations of SWCNT/TiO_2-NCs

$$\frac{TiO_2NCs}{mL\ hybrid} = \frac{3.66 \cdot 10^{15} TiO_2NCs}{mL\ colloid} \cdot \frac{1mL\ colloid}{3.25mL\ hybrid} \sim 1 \cdot 10^{18} TiO_2NCs/mL\ hybrid$$

(Equation S2)

Average superficial concentration of WOC on Ru-tda/SWCNT/TiO2-NCs

The surface coverage (Γ) of the complexes on the Ru-tda/SWCNT/TiO_2NCs was estimated by applying the formula:

$$\Gamma\ (mol \cdot g^{-1}) = \frac{Q}{n \cdot m \cdot F}$$

(Equation S3)

Q is the charge under the oxidative peak of the reversible, one-electron wave obtained by integration of the CV (Figure 2D), which is 9.1 x 10^{-6} C. *n* is the number of electrons involved in that oxidation process, which is 1 (Ru^{II} to Ru^{III}). *m* is the hybrid catalyst mass on the electrode and *F* is the Faradaic constant (96,485 C·mol^{-1}).

Ratio TiO_2-NCs:Ru-tda molecule

$$\frac{TiO_2NCs}{atom\ Ru} = \frac{1 \cdot 10^{18} TiO_2NCs}{1mL\ hybrid} \cdot \frac{1mL\ hybrid}{4.5\ mg\ hybrid} \cdot \frac{1\ g\ hybrid}{2.18 \cdot 10^{-8} mol\ RuWOC} \cdot \frac{1mol\ RuWOC}{6.02 \cdot 10^{23} molec\ RuWOC} \cdot \frac{1\ molec\ RuWOC}{1\ atom\ Ru} = \frac{1 \cdot 10^{4} TiO_2NCs}{atom\ Ru}$$

(Equation S4)

VII

Calculations on the TON_{Ru}

The turnover number, TON, is defined as the number of mols of substrate transformed by 1 mol of Ru-tda present on the surface of the colloidal photocatalyst[3]:

$$TON = \frac{\text{mols } O_2}{mols\ WOC} = \frac{20 \text{ nmols } O_2}{8.72 \cdot 10^{-11} \text{ mols WOC}} = 229.36 \qquad \text{(Equation S5)}$$

7.5.5. Apparent quantum yield (AQY)

Apparent quantum yield (AQY) is defined here according to the following formula[4]:

AQY (absorbed photons):

$$AQY(\%) = \frac{\text{Rate of reacted electrons}}{\text{Rate of absorbed photons}} \text{x} 100$$

$$= \frac{(4 \text{ x molecules } O_2)_t}{(absorbed\ photons)_t \cdot \text{area irradiated}}\ x\ 100 =$$

$$= \frac{4 \text{ x } 2 \cdot 10^{-8}\ mols\ O_2\ x\ 6.022 \cdot 10^{23} mols^{-1}}{3x(2.31 \cdot 10^{19}) photons \cdot s^{-1} \cdot m^{-2}} x100 = 0.07\%$$

(Equation S6)

The absorbed photons in the formula were estimated by integrating the solar spectrum (AM 1.5) in the 300-350 range, where the TiO_2-NCs absorber shows the maximum absorption and assuming full absorption in this range (UV-Vis in Figure S3). This assumption is based on the high extinction coefficient of the TiO_2-NCs and the relatively high amount of absorber in the reaction vessel (high concentration in each experiment, $1.2 \cdot 10^{16}$ TiO_2-NCs, and 1 cm of path length).

7.5.6 References

(1) Gordon, T. R.; Cargnello, M.; Paik, T.; Mangolini, F.; Weber, R. T.; Fornasiero, P.; Murray, C. B. Nonaqueous synthesis of TiO2 nanocrystals using TiF4 to engineer morphology, oxygen vacancy concentration, and photocatalytic activity. *J Am Chem Soc* **2012,** *134 15*, 6751-61. https://doi.org/10.1021/ja300823a.

(2) Matheu, R.; Ertem, M. Z.; Benet-Buchholz, J.; Coronado, E.; Batista, V. S.; Sala, X.; Llobet, A. Intramolecular Proton Transfer Boosts Water Oxidation Catalyzed by a Ru Complex. *J Am Chem Soc* **2015,** *137 33*, 10786-95. https://doi.org/10.1021/jacs.5b06541.

(3) Costentin C, Drouet S, Robert M, Saveant JM. Turnover numbers, turnover frequencies, and overpotential in molecular catalysis of electrochemical reactions. Cyclic voltammetry and preparative-scale electrolysis. *J Am Chem Soc*. **2012,** *134 27*, 11235-11242. https://doi.org/10.1021/ja303560c.

(4) Serpone N, Salinaro A. Terminology, relative photonic efficiencies and quantum yields in heterogeneous photocatalysis. Part I: Suggested protocol (Technical Report). *Pure Appl Chem*. **1999**, *71 2*, 303-320. https://doi.org/10.1351/pac199971020303.

Chapter 8

Conclusions

Chapter 8.

VIII

The current thesis presents the work in line with the three different technological strategies envisioned for photo(electro)chemical solar fuel generation. Chapter 3 results in a highly active electroanode with potential application in Photovoltaic-Electrolyzer technologies (PV-EC). Chapters 4 and 5 draw the preliminary steps towards the use of organic dyes in light-driven water oxidation in the form of Dye-Sensitized Photoelectrochemical Cells (DSPECs) or homogeneous catalysis. Finally, Chapters 6 and 7 display colloidal photocatalysts with remarkable water oxidation catalytic activities. Taking into consideration the independent nature of the three research lines, the conclusions and the outlook of each of the systems are highlighted as follows:

- A molecular electroanode has been achieved based on the thiophene electropolymerization of the synthesized Ru-tda derivative, [Ru(tda)(pyrS)$_2$] or **1,** to form **poly-1** on graphitic surfaces (Figure 1 left).

- The resulting electrode, **poly-1-OH**@CNT@GC (CNT is multiwall Carbon Nanotubes and GC is Glassy Carbon), reaches current densities of ~90 mA·cm^{-2} at 1.45 V *vs.* NHE (pH 7) (Figure 1 right). This translates into remarkable TONs of 20,000 for 4 h, ranking among the best molecular anodes described up to now.

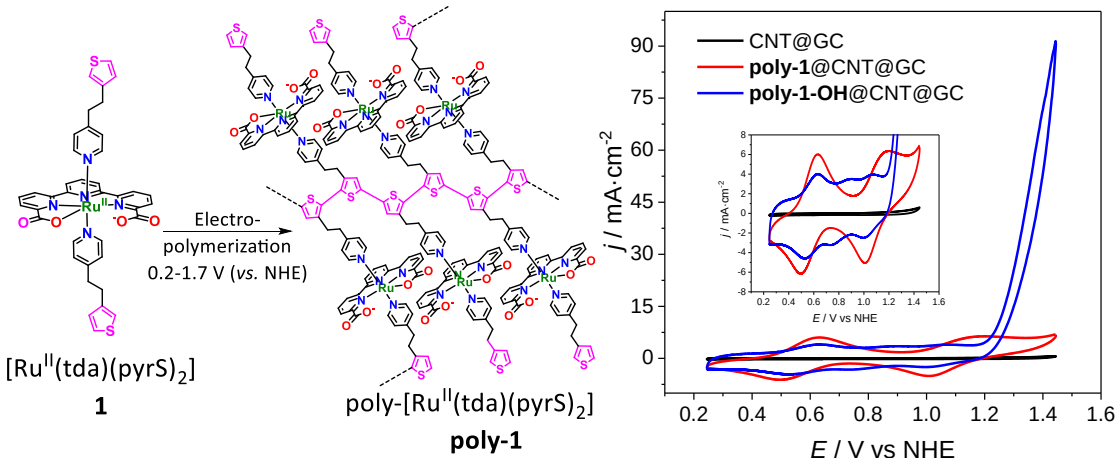

*Figure 1. On the left, scheme of the electropolymerization of **1** to **poly-1**. On the right, cyclic voltammetry experiments (v = 100 mV·s^{-1}) for **poly-1**@CNT@GC (red line), **poly-1-OH**@CNT@GC (blue line) and CNT@GC (black line) in a pH 7 phosphate buffer solution (Pt as counter electrode and Hg/Hg$_2$SO$_4$ as reference electrode), all under the same conditions except for **poly-1-OH**@CNT@GC that a 90% iR compensation was applied.*

- Towards light-driven water oxidation catalysis, two organic BODIPY dyes (**BDP1** and **BDP2**) have demonstrated photoactivated oxygen evolution in a fully homogeneous system without the presence of a sacrificial agent in combination with the state-of-the-art molecular water oxidation catalyst **Ru-(O)tPa** (Figure 2 left). Their stability is sufficient to produce TONs up to 14 (*vs.* BDP1) and 163 (*vs.* BDP2) within 4.5 h of irradiation (Figure 2 right).

- The lack of sacrificial agent leaves the reduction half-reaction with **BDP2**$^{-}$ as responsible for ORR to H_2O_2 through a $2e^-$ process. This hypothesis has been proven by iodometric methodology. The produced H_2O_2 converts **Ru(O)-tPa** to **Ru(O)-bPa** (Figure 2 left) with concomitant O_2 production without any light/potential bias.

- Further research is needed for photophysical characterization of the mechanisms, and to finally achieve homogeneous full water splitting photocatalysis and/or to adapt the system onto photoelectrodes.

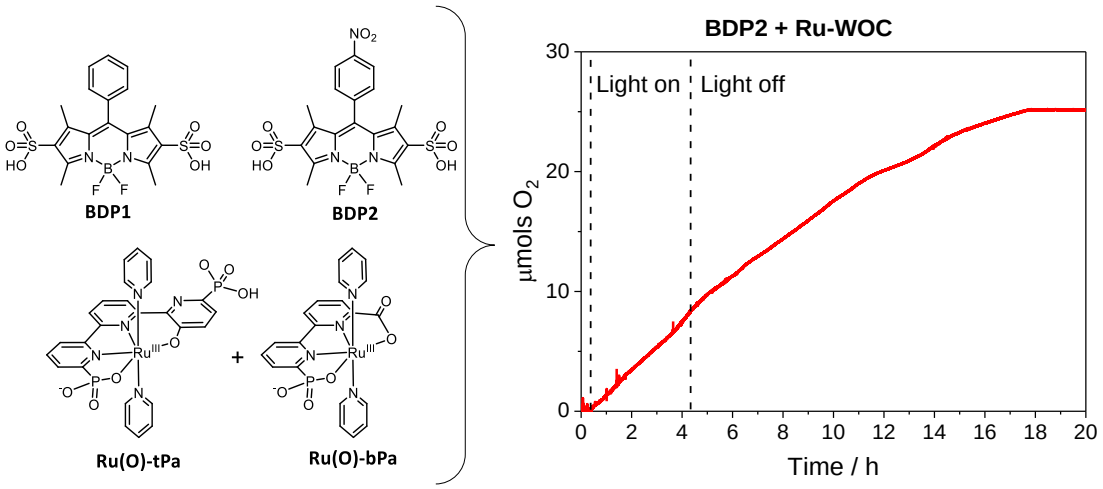

*Figure 2. On the left, chart with the structures and labeling for the organic dyes and molecular water oxidation catalysts employed in this work. On the right, oxygen detection experiment for the sample **BDP2** and **Ru(O)-tPa** without the presence of sacrificial agent under light/dark conditions (1.1 suns irradiation AM 1.5 G by Xe-lamp 150W with 400nm cut-off filter).*

- In the next step to build a DSPEC, a photoanode based on noble-metal-free components has been attained, consisting of a first-row transition metal water oxidation catalyst, Cu-MAC, and a PDI@ATO@FTO photoanode (where PDI is a dye from the perylene diimide family, ATO is Antimony doped Tin Oxide, FTO is Fluorine doped Tin Oxide, Figure 3 right).

- The final Cu-MAC/PDI@ATO@FTO demonstrates higher photocurrents than bare PDI@ATO@FTO electrodes (Figure 3 left). The interaction between Cu-MAC/PDI is proven by Nuclear Magnetic Resonance (NMR), UV-Vis, and X-ray Absorption Spectroscopy (XAS). XAS analysis also demonstrates the presence of molecular Cu-MAC after light-driven water oxidation.

- Despite the low Faradaic efficiency, Cu-MAC/PDI@ATO@FTO is the first example of a noble-metal-free DSPEC-photoanode reported to date. It represents a proof-of-concept for a broad field of research with high potential to achieve low-cost water oxidation photoelectrocatalysis.

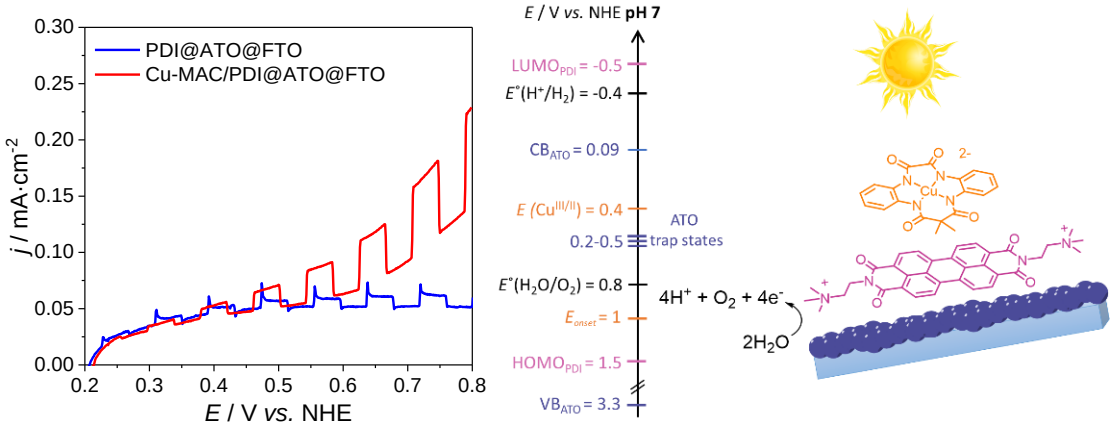

Figure 3. Left, chopped light linear sweep voltammetry (v = 10 mV·s^{-1}) of the photoelectrodes Cu-MAC/PDI@ATO@FTO (red) and the blank PDI@ATO@FTO (blue) in pH7 phosphate buffer and under 1 sun irradiation (AM 1.5 G by Xe-lamp 150W with 400nm cut-off filter). Right, band diagram of the studied photoanode.

- Finally, envisioning colloidal photocatalysis, four novel covalent triazine frameworks (CTFs) containing -F, -COOH, -$CONH_2$, or pyridine groups have been synthesized and fully characterized: CTF-F, CTF-$CONH_2$, CTF-COOH, CTF-py.

- Compared to the literature, high and stable photocurrents for CTF-F, CTF-COOH, and CTF-$CONH_2$ were achieved. Yet, attempted oxygen measurements led to conclude that incorporation of molecular catalysts is essential for these materials for photocatalytic purposes.

- In this line, CTF-py-Ru(tda) is synthesized based on the covalent bonding of [Ru(tda)(dmso)py] and the dangling pyridine in the CTF-py unit (Figure 4). The system proved to be active towards water oxidation with remarkable TONs of 54

and with just 0.7% Ru at neutral pH, which is to the best of our knowledge, the best of the few reported conjugated polymers for water oxidation.

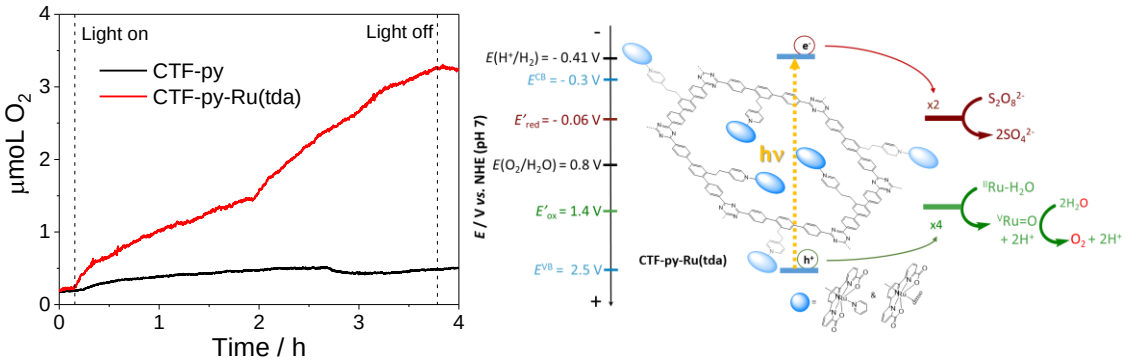

Figure 4. On the left, oxygen detection experiments of CTF-py-Ru(tda) (red) vs. CTF-py (black) by a Clark electrode in the headspace (1 sun irradiation AM 1.5G by Xe-lamp 150W). On the right, scheme of the light-driven water oxidation catalysis with band diagram.

- Alternatively, another type of molecular hybrid material has been prepared by combining a molecular catalyst (Ru-tda) and semiconductor Nanocrystals (TiO_2-NCs) on Single-Wall Carbon Nanotubes (SWCNT), herein labeled as Ru-tda/SWCNT/TiO_2-NCs.

- At neutral pH, it achieves a TON of 229 upon illumination, which is the highest reported for this type of device up to date (Figure 5).

- This modular approach allows that each of the constituting entities, such as the light absorber (TiO_2-NCs), the holder/communicator (SWCNT), and the catalyst (Ru(O)-tda), can be easily and independently replaced for optimization or wider applications.

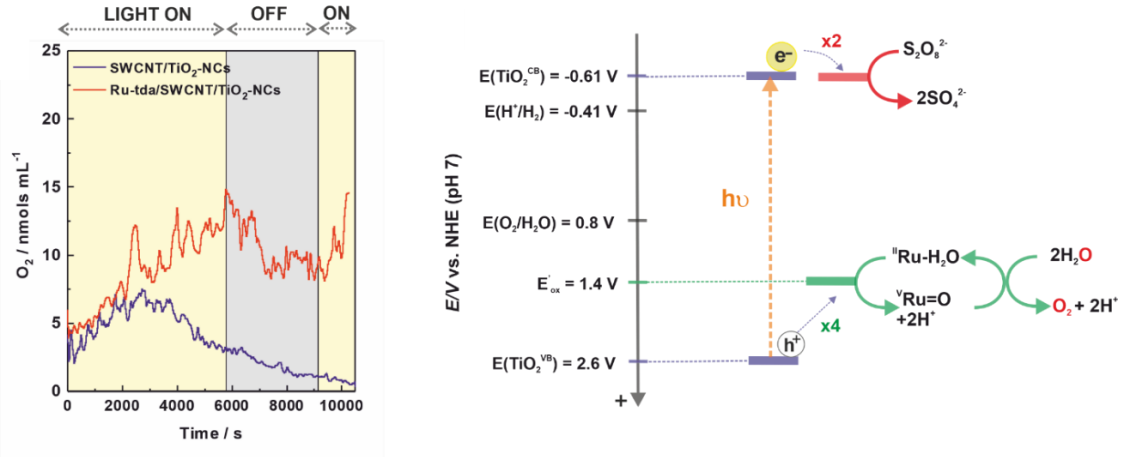

Figure 5. On the left, oxygen detected from Ru^{IV}(O)-tda/SWCNT/TiO_2-NCs (in red) and from bare SWCNT/TiO_2-NCs by Clark electrode in solution (3 suns irradiation AM 1.5G by Xe-lamp 150W). On the right, schematic representation of the charge carrier dynamics and main reactions upon illumination.

VIII

Chapter 8.

VIII

UNIVERSITAT
ROVIRA i VIRGILI